The synthesis, characterisation and sorptive properties of functionalised siliceous-MCM 41 materials

Thesis

THE SYNTHESIS, CHARACTERISATION AND SORPTIVE PROPERTIES OF FUNCTIONALISED SILICEOUS-MCM 41 MATERIALS

Submitted by

Udayshanker Singh

(MSc. Analytical Chem.)

as a Thesis for the degree of

Doctor of Philosophy

In the Faculty of Science

January 2003

I certify that all material in this thesis which is not my own work has been identified and that no material has previously been submitted and approved for the award of a degree by this or any other University.

Submission date: 30 January 200
Award date: 3 April 2003

ProQuest LLC.
789 East Eisenhower Parkway
P.O. Box 1346
Ann Arbor, MI 48106 – 1346

Dedicated to my beloved parents

ABSTRACT

A range of chemically-tailored mesoporous MCM 41 materials has been synthesised using two methods namely sol-gel synthesis, and post-synthetic grafting. Purely siliceous-MCM 41, a series of mesitylene-swollen MCM 41, metal-containing MCM 41 (Fe and Ti) and organically-modified (3-aminopropyl and Schiff base) MCM 41 were synthesised by the sol-gel synthesis method. Metal-grafted (Fe and Ti) MCM 41, organically-modified (3-aminopropyl, Schiff base and azodye) MCM 41 and the metal(Cu, Fe and Ni)-Schiff base-modified MCM 41 were prepared by the post-synthetic grafting method.

The materials were characterised using a number of techniques including powder-X-ray diffraction (*p*-XRD), infrared spectroscopy, CHN microanalysis, atomic absorption spectroscopy, nuclear magnetic resonance spectroscopy, X-ray photoelectron spectroscopy, transmission electron microscopy, and by the sorption of gases (N_2 and CO_2) and vapours (water, *n*-hexane, methanol, *n*-butanol, *t*-butanol).

p-XRD showed that all the materials synthesised possessed hexagonal periodicity apart from the sol-gel synthesised 3-aminopropyl-modified MCM 41 and the Schiff base-modified MCM 41 materials, in which the hexagonal structure collapsed after template removal.

The porosity of all the materials was confirmed by the Type IV (mesoporous) and Type I (microporous) isotherms yielded from nitrogen (77 K), CO_2 (195 K) and alcohols (303 K) sorption. A decrease in the surface area (1150 m^2g^{-1}), total pore volume (0.74 cm^3 g^{-1}) and average pore diameter (26 Å) of the parent Si-MCM 41 was observed following functionalisation.

The sorption of water on a number of synthesised materials yielded Type V isotherms and confirmed that the adsorption of the water molecules on the surface occurred *via* polar interaction with the surface hydroxyls. The adsorption of CO_2 was thought to occur by a different mechanism to N_2 sorption *i.e. via* interaction with polar groups on the surface rather than *via* monolayer formation. The nature of the *n*-hexane sorption showed the high organophilic character and water sorption demonstrated the hydrophobic character of the surface. The adsorptions of alcohols (MeOH, *n*-BuOH and *t*-BuOH) were found to be intermediate in character between those of water and *n*-hexane suggesting adsorption both by polar interaction with the hydroxyl groups, and by interaction of the alkyl groups of the alcohols with the surface.

Chemisorption of adsorptives, water and alcohols, of the Si-MCM 41 surface was confirmed by infrared spectroscopy. The numbers of surface hydroxyls were found to decrease following modification.

Sorption of two hexene isomers 1-hexene and 3,3-dimethyl-1-butene were carried out on a supplied sample of Ru-MCM 41 in order to investigate the observed enhanced catalytic activity following heat-treatment (at 623 K for 16 h under reduced pressure of $<10^{-5}$ torr). The Ru-MCM 41 material showed higher uptake of 1-hexene following heat-treatment. The adsorption of the isomer 3,3-dimethyl-1-butene was found be sterically hindered on the surface.

X-ray photoelectron spectroscopy was evaluated as an analytical technique to investigate the distribution of metal complexes within the pores and on the external surface of the Cu-Schiff base-modified MCM 41 materials. The argon etching technique showed that between 1/3 and 1/4 of the copper-Schiff base complex was located in the pores, whereas the remainder was present on the external surface, blocking some of the pores. The quantitative information obtained from XPS was found not to be reliable for this class of materials.

CONTENTS

1 Introduction

1.1 General 1

1.2 Green Chemistry in Context 2

1.3 Solid Supports 3

1.4 Porous Solids 4

1.4.1 M41S Materials 6

1.5 Modification of the MCM 41 Material 11

1.5.1 One Step, In-situ Modification via Sol-gel Synthesis Method 12

1.5.2 Post-synthetic Grafting 16

1.6 Aims of this Project 19

1.7 References 21

2 Techniques Used for Characterisation of Samples

2.1 Introduction 25

2.2 Powder X-ray Diffraction 27

2.2.1 The Crystal Lattice 27

2.2.2 Miller Indices 28

2.2.3 Theory of *p*-XRD 29

2.2.4 Experimental Details 31

2.3 Infrared Spectroscopy 31

2.3.1 General 31

2.3.2 Experimental Details 32

2.4 CHN Microanalysis 33

2.5 Atomic Absorption Spectroscopy 34

2.5.1 General 34

2.5.2 Experimental Details 35

2.6 X-ray Photoelectron Spectroscopy 36

2.6.1 General 36

2.6.2 Experimental Details 38

2.7 Transmission Electron Microscopy 40

2.7.1 General 40

2.7.2 Experimental Details 40
2.8 ^{57}Fe Mössbauer Spectroscopy 40
2.8.1 General 40
2.8.2 Experimental Details 42
2.9 Solid State Nuclear Magnetic Resonance Spectroscopy 42
2.9.1 General 42
2.9.2 MAS NMR Spectroscopy 43
2.9.3 Cross-polarization MAS NMR Spectroscopy 44
2.9.4 ^{29}Silicon NMR Spectroscopy 44
2.9.5 ^{13}C NMR Spectroscopy 46
2.10 Adsorption Studies: General 48
2.10.1 Type I Isotherm 50
2.10.2 Type IV Isotherm 52
2.10.3 Type V Isotherm 53
2.10.4 Determination of Specific Surface Area 54
2.10.5 Point B Method 55
2.10.6 BET Model 55
2.10.7 Pore Diameter 56
2.10.8 Pore Volume 57
2.10.9 α_s-Plots 58
2.11 Experimental Details: Volumetric Sorption 59
2.12 Experimental Details: Gravimetric Sorption 60
2.12.1 Sample Degassing 61
2.12.2 Adsorptive Degassing 61
2.12.3 Calibration of the Spring 62
2.12.4 Isotherm Measurment 62
2.13 References 65

3 Siliceous-MCM 41 (Si-MCM 41) Material

3.1 Introduction 68
3.2 Synthesis 68
3.2.1 Siliceous-MCM 41 70
3.2.2 Mesitylene-Swollen MCM 41 70
3.3 Results and Discussion: Physico-chemical Characterisation 72
3.3.1 *p*-X-ray Diffraction 72

3.3.2 Infrared Spectroscopy 74
3.3.3 CHN Microanalysis 78
3.3.4 X-ray Photoelectron Spectroscopy 79
3.3.5 Transmission Electron Microscopy 82
3.3.6 Nuclear Magnetic Resonance Spectroscopy 84
3.4 Sorption Studies: Results and Discussions 87
3.4.1 Nitrogen Sorption 88
3.4.2 Carbon Dioxide Sorption 93
3.4.3 Water Sorption 98
3.4.4 *n*-Hexane Sorption 102
3.4.5 Sorption of Alcohols 104
3.5 Conclusions 112
3.6 References 114

4 Metal-functionalised MCM 41 Materials

4.1 Introduction 117
4.2 Synthesis 119
4.2.1 Fe-MCM 41 119
4.2.2 Ti-MCM 41 123
4.2.3 Ru-MCM 41 125
4.3 Results and Discussions: Physico-chemical Characterisation 126
4.3.1 *p*-X-ray Diffraction 127
4.3.2 CHN microanalysis 129
4.3.3 Infrared Spectroscopy 130
4.3.4 X-ray Photoelectron Spectroscopy 134
4.3.5 ^{57}Fe Mössbauer Spectroscopy 138
4.4 Sorption Studies (Fe- and Ti-MCM 41): Results and Discussions 142
4.4.1 Nitrogen Sorption 142
4.4.2 Carbon Dioxide Sorption 146
4.5 Sorption Studies on Ru-MCM 41 150
4.6 Conclusions 154
4.6.1 Fe- and Ti-MCM 41 154
4.6.2 Ru-MCM 41 156
4.7 References 157

5 Organically-modified MCM 41 Materials

5.1 Introduction 160

5.2 Synthesis 164

5.2.1 3-Aminopropyl-functionalised MCM 41 164

5.2.2 Schiff Base-fuctionalised MCM 41 166

5.2.3 Azodye-fuctionalised MCM 41 169

5.3 Results and Discussions: Physico-chemical Characterisation 172

5.3.1 *p*-X-ray Diffraction 172

5.3.2 Infrared Spectroscopy 176

5.3.3 CHN Microanalysis 181

5.3.4 Nuclear Magnetic Resonance (NMR) Spectroscopy 183

5.3.5 UV/Visible Spectroscopy 191

5.4 Sorption Studies: Results and Discussions 193

5.4.1 Nitrogen Sorption 193

5.4.2 Carbon Dioxide Sorption 197

5.5 Conclusions 199

5.6 References 202

6 Metal-Schiff Base-modified MCM 41 Materials

6.1 Introduction 205

6.2 Synthesis 207

6.2.1 Synthesis of the Schiff Base Triethoxysilane Ligand 210

6.2.2 Post-synthetic Grafting of the Copper(II)-Schiff Base Complex on Si-MCM 41, Cu-Schiff-MCM-1.0 (8) 211

6.2.3 Post-synthetic Grafting of the Iron(II)-Schiff Base Complex on Si-MCM 41, Fe(II)-Schiff-MCM-1.0 212

6.2.4 Post-synthetic Grafting of Iron(III)-Schiff Base Complex on Si-MCM 41, Fe(III)-Schiff-MCM-1.0 213

6.2.5 Post-synthetic Grafting of Nickel(II)-Schiff Base Complex on Si-MCM 41, Ni-Schiff-MCM-1.0 214

6.3 Results and Discussions: Physico-chemical Characterisation 215

6.3.1 Powder-X-ray Diffraction 215

6.3.2 Infrared Spectroscopy 216

6.3.3 Nuclear Magnetic Resonance Spectroscopy 219

6.3.4 Atomic Absorption Spectroscopy 223

6.3.5 CHN Microanalysis 224
6.3.6 X-ray Photoelectron Spectroscopy 227
6.4 Gas Sorption Studies: Results and Discussions 238
6.4.1 Copper-Schiff Base-modified Materials 239
6.4.2 Iron-Schiff Base-modified Materials 265
. 6.4.3 Nickel-Schiff Base-modified Materials 269
6.5 Conclusions 273
6.6 References 277

7 Summary

7.1 Introduction 280
7.2 Si-MCM 41 Materials 281
7.3 Metal-functionalised MCM 41 Materials 282
7.4 Organically-modified MCM 41 Materials 285
7.5 Metal Schiff base-modified MCM 41 Materials 287

Appendices

A1 290
A2 291
A3 294
A4 298

ACKNOWLEDGEMENTS

I gratefully acknowledge to my two supervisors, Dr. Ruth Williams and Dr. Ian Salter for their expert advice, guidance and support. Special and sincere thanks to Dr. Ruth Williams for her encouragement and all of her help in this work.

Thanks to Adam Hazelwood for his friendship, co-operation and for his help in the laboratory.

I gratefully acknowledge:

- Prof. Frank Berry and Dr. Ibrar Iyub (The Open University) for their help with Mössbauer spectroscopic analysis.
- Naomi Williams (The Open University) for her help with TEM analysis.
- Dr. Richard Walton (University of Exeter) for his help with XRD and in laboratory.
- Dr. Mark Danks and Prof. Ducan Bruce (University of Exeter) for the supply of Ru-MCM 41 material.
- Dr. S. Ashbrook for her help with solid-state NMR analysis of azodye-functionalised MCM 41 material.
- Dr. Anne-Cecile Herve (University College London) for her help with solid-state NMR analysis of organically-modified and metal-Schiff base-modified MCM 41 materials.
- Dr. Henryk Herman (University of Surrey) for his help with solid-state UV/visible spectroscopic analysis.
- The University of Exeter technical staff for their help and University of Exeter for the use of its facility.
- The Open University for funding.

My parents and family members for their support.

GLOSSARY

MCM - Mobil Composite Material

Si-MCM 41 - Siliceous-MCM 41 material

Ms-MCM 41 - Mesitylene-swollen MCM 41 material

Mesitylene – 1, 3, 5-trimethyl benzene

CTMACl - Cetyltrimethylammonium chloride (C_{18}TMACl)

TEOS - Tetraethylorthosilicate

PEO-PPO-PEO – Alkylpoly-ethylene-propylene oxide

p-XRD - Powder-X-ray Diffraction

IR - Infrared Spectroscopy

NMR - Nuclear Magnetic Resonance

MAS - Magic Angle Spinning

CP MAS - Cross-polarisation Magic Angle Spinning

TMS - Trimethylsilane

TEM - Transmission Electron Microscopy

XPS - X-ray Photoelectron Spectroscopy

Azodye - 1-(4-bromo-phenylazo)-[2]naphthol

MeOH - Methanol

n-BuOH - *n*-Butanol

t-BuOH - *t*-Butanol

CHAPTER 1

INTRODUCTION

1.1 General

Increasing pollution from the chemical industries is a major concern for a modern world. A significant contribution to the waste produced in chemical processes arises from homogeneous catalysis, which involves the separation of the catalyst from the products in the reaction mixture.[1-9] This stage normally generates large volumes of salt wastes and toxic effluents. The environmental wastes could be minimised either by developing environmentally friendly processes (*e.g.* by eliminating the use of toxic solvents) and by developing solid catalysts (heterogeneous catalysts).[1, 2, 4, 5] The reduction of waste is one of the major goals of the 'Green Chemistry'. 'Green Chemistry',[6] as it has been called, involves the redesign of chemical processes so that the desired products from a reaction are produced with a minimal amount of waste. The main aim of this project is the development and characterisation of porous materials with the potential for heterogeneous catalysis.

The research work reported in this thesis involved the synthesis and characterisation of siliceous mesoporous MCM 41 type molecular sieves (discussed in Chapter 3) and their functionalisation with the potentially catalytically active transition metals (Fe and Ti) (discussed in Chapter 4), organic compounds (3-aminopropyl groups, Schiff base ligands and azodye) (discussed in Chapter 5), and metal complexes (Cu-, Ni- and Fe-Schiff base complexes) (discussed in Chapter 6). The work was also

intended to evaluate the effectiveness of the different synthesis methods used in the functionalisation of the mesoporous molecular sieves.

The mesoporous MCM 41 type silicas were used as solid supports in this work because of their potential advantage over microporous molecular sieves in the catalysis processes involving large organic molecules.

A number of analytical techniques were used in this research for the characterisation of the synthesised materials. In addition to the standard techniques *p*-X-ray diffraction, gas adsorption studies, nuclear magnetic resonance spectroscopy, atomic absorption spectroscopy and infrared spectroscopy, the technique X-ray photoelectron spectroscopy was also used to explore the location of metal complexes on the surface of the material. This is the first time the XPS technique has been used to analyse the distribution of metal complexes within the pores or on external surface of MCM 41 type material. General introductions to all these characterisation techniques are given in Chapter 2.

This Chapter (Chapter 1) aims to give a general introduction to porous materials with special attention being given to M41S type-solids. It discusses the original synthesis mechanism of the M41S material and the different methods that can be used for its functionalisation.

1.2 Green Chemistry in Context

In homogeneous catalysis, the traditional mineral acids (*e.g.* HF, H_2SO_4) and Lewis acids (*e.g.* $AlCl_3$) used in most of the alkylation and acylation reactions, and the transition metal complexes used in redox reactions are a major concern in producing toxic effluents.[1-5] The separation of products and catalyst in homogeneous catalysis can generate tremendous amounts of waste effluent. Sometimes the separation process may destroy the product or the catalyst, and most of the time the catalyst is not recycled.[1-9]

Thus, the elimination of this separation step to minimise the waste effluents is one of the major goals of 'Green Chemistry'.[1-7]

A general tendency in 'green' catalysis is to transform a homogeneous process into a heterogeneous one. The advantage of using solid catalysts is that they are in a different phase from both the reactants and the products and can be easily separated from the reaction mixture with the generation of minimal waste.[1, 9] In addition, solid catalysts can be easily recycled and are suitable for continuous processing and hence are environmentally friendly.[1, 9, 10]

1.3 Solid Supports

The type of solid support used can play a crucial role in the development and preparation of the solid catalysts.[4, 11]

The three main factors to be considered for employing a material as a solid support are:[1, 4, 11]

- The material should be stable, both chemically and thermally, to withstand the extreme reaction conditions of both pH and temperature.
- The structure of the support material should be such as that the active sites are well dispersed on its surface.
- The active sites should be easily accessible for the reactant molecules. This requires a reasonably high surface area, which is often achieved using porous supports.

For liquid phase reactions, a support with a mesoporous structure is desirable so that the reactant molecules can easily diffuse and access the active sites, and the product molecules can easily diffuse out.

Silica gel is one such material, which optimises these conditions. It offers high thermal and chemical stability, possess high surface area and can be synthesised with pores, which can be tailored easily within the microporous to mesoporous range.[1, 4, 11]

However, these materials do not have a narrow pore size distribution, nor are the pores open at both the ends. In contrast, the MCM 41 type materials used in the current work have well defined hexagonally arranged open-ended pores with a narrow pore size distribution.

1.4 Porous Solids

One of the interesting features of the supported catalysts is their high surface area, which is usually due to porosity. Thus, porous solids are ideal as a solid supports. Porous inorganic solids can be used as catalysts, supports for catalysts, adsorbents and molecular sieves.[7] They are classified according to their pore size into three different classes *i.e.* microporous, mesoporous and macroporous (Table 1.1).[12] Dubinin[13] first proposed this classification for inorganic porous materials and since then it has been officially adopted by the International Union of Pure and Applied Chemistry (IUPAC).[14]

Table 1.1 IUPAC classification of porous inorganic solids

Pore diameter / Å	**Classification**
< 20	Microporous
20 - 500	Mesoporous
> 500	Macroporous

Two classes of materials, which are extensively used as catalysts and sorption media, are microporous and mesoporous inorganic solids.[12, 15, 16] The structure of these materials allows molecular access to a large internal surface and associated active

catalytic sites within the cavities. This accounts for the utility of these materials as both catalysts and catalytic supports.[16, 17]

Porous solids can have valuable and very useful significance in shape-selective catalysis.[6, 18, 19] The molecular sieve action of the porous solids can be exploited to control the reaction of particular reactant molecules, which can have access to the pore structure and access the active sites. Similarly, the particular product formed may be controlled by virtue of the molecules having the appropriate shape and size to diffuse out through the pores. Preparation of *p*-xylene is a well-known commercial example of the shape-selective catalysis using the zeolite (discussed below), ZSM-5 as a catalyst. A mixture of all three isomers (*p*-, *m*-, *o*-xylene) is formed in the alkylation of toluene by methanol. However, the selectivity of the reaction for the desired *para*-isomer is achieved with the ZSM-5 catalyst. This is because of the high diffusion rate of the *para*-isomer from the pores of ZSM-5 compared with the other isomers, because of its less sterically hindered shape.[6, 18, 19]

Zeolites[17, 18, 19] are well known examples of microporous solids, which are widely used in chemical industries for their ion exchange, adsorption and catalytic properties. Zeolites are characterised by their open channels and pores of very well defined sizes. The frameworks forming the porous structure are constructed from the tetrahedral (TO_4) units of mainly silicon and aluminium (SiO_4 and AlO_4) linked together by corner sharing of oxygen atoms. However, zeolites with tetrahedral units of other elements (*e.g.* PO_4, BeO_4, ZnO_4) incorporated are also known. Zeolites are formed by the crystallisation of alumino-silicates around a single molecule, which acts as a template.[17]

Although, many industrially catalysed processes make use of zeolites, their use in the catalysis involving larger organic molecules is limited because of their small pore sizes,[6, 17, 20] and this is where the mesoporous materials have potential.

M41S-type[16, 17, 21] materials are an example of a class of mesoporous solids. These materials combines the well-defined pore structure of the zeolites with pore diameters in the mesoporous range (20 and 500 Å) and, hence, have potential as catalysts in reactions involving large organic molecules.[16, 17]

1.4.1 *M41S Materials*

In 1992, researchers of the Mobil group[22] developed a number of mesoporous materials, designated as M41S. The materials of this group are characterised by narrow pore size distributions, easily tunable pores, and large surface areas and pore volumes. These properties have attracted a great deal of interest from researchers throughout the world, because of the potential of M41S as catalysts involving the reaction of larger organic molecules. The main members of the M41S family are MCM 41 (Mobil Composite Material), MCM 48, HMS (Hexagonal Mesoporous Silica) and SBA-n (Santa Barbara-n), summarised in Table 1.2.

Table 1.2 Members of the M41S family[16, 17, 21]

Members of M41S family	**Type of template used in synthesis**	**Pore diameter / Å**	**Pore wall thickness / Å**
MCM 41	Cationic / anionic surfactant ($C_{16}H_{33}N^+(CH_3)_3$)	20 – 80	9 – 16
MCM 48	Cationic surfactant[17] ($C_{18}H_{37}N^+(C_2H_6)C_{12}N^+(C_2H_6)C_{18}H_{37}$	20 – 40	5 - 15
HMS	Neutral amines ($C_{16}H_{33}NH_2$)	20 – 60	17 - 30
SBA-n	Tri-block copolymers (PEO-PPO-PEO)	50 - 300	30 - 60

The four main components in the synthesis of the M41S materials are structure-directing surfactants, a source of silica, a solvent and a catalyst (an acid or a base). In

contrast to the synthesis of zeolites (where a single molecule is used as a template), the MCM 41, MCM 48 and HMS materials are formed *via* a liquid crystal-templating method,[17, 21, 22] where the micelles of the template molecules serve as a 'structure directing agent'. The pore diameters of these materials can be easily tailored by either changing the surfactant chain length,[17, 21] or by using a solubilising agent, such as mesitylene, to swell the micelle.[17, 21] It has been shown that by changing the surfactant/silica molar ratio each of the three different types of mesophase *i.e.* MCM 41, MCM 48 and MCM 50, may be formed (Table 1.3).[17, 21] However, the MCM 50 material formed is not stable and its structure collapses after template removal.[17]

Table 1.3 The types of mesoporous materials formed by changing the surfactant/silica molar ratio

Surfactant/silica ratio	Type of M41S material formed
< 1	MCM 41
1 to 1.5	MCM 48
> 1.5	Lamellar phase MCM 50 M41S

1.4.1.1 MCM 41

MCM 41[22] is a member of the M41S family, which possesses unidirectional channel-like pores with a narrow pore size distribution arranged in a regular hexagonal pattern. The pore diameter of these materials can be easily tailored between 20-80 Å, either by changing the surfactant chain length, or by using auxiliary chemicals, *e.g.* mesitylene. The characteristics of MCM 41 material are a high surface area of up to 1500 m^2g^{-1}, a pore volume of up to 1.4 cm^3g^{-1} and a high thermal and chemical stability.[5, 6, 7] It has been shown that the MCM 41 materials are formed *via* a liquid crystal-templating mechanism in which the surfactant molecules act as a template for the inorganic silica to

form a porous structure.[16, 17, 21, 22] Initial speculation on the mechanistic pathway for the formation of MCM 41 resulted in two proposed routes. One mechanism, proposed by Beck *et al.*,[16] (Fig. 1.1) suggests that the surfactant molecules aggregate into micellar rods, which in turn form an hexagonal array, which acts as a template for the inorganic silica.

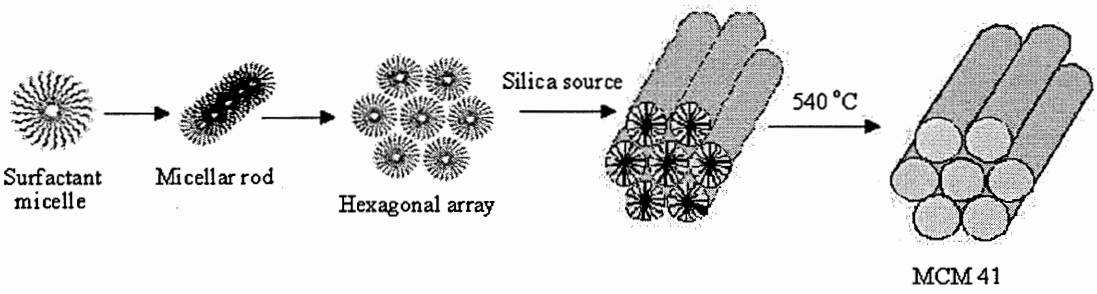

Figure 1.1 Mechanism for the synthesis of MCM materials suggested by Beck *et al.*[16]

The alternative mechanism, proposed by Vartuli *et al.*,[23] (Fig. 1.2) was proposed since the spontaneous aggregation of the surfactant molecules into a liquid crystal hexagonal array was thought to be unlikely at the working concentration of below the critical micelle concentration (CMC). The CMC is defined as the concentration above which monomers spontaneously self-assemble into micelles. CMC varies with the molecular structure according to the equation given below.

$$Log(CMC) = A\text{-}Bn_c \qquad \textit{Equation } 1.1$$

where A and B are constants, and n_c is the number of carbon atoms in the alkyl chain.[24] Thus, it was suggested by Vartuli that it is the addition of the silicate anions, by virtue of their charge balance with the cationic surfactant triggers the formation of micelles, which act as a template for the inorganic silica.

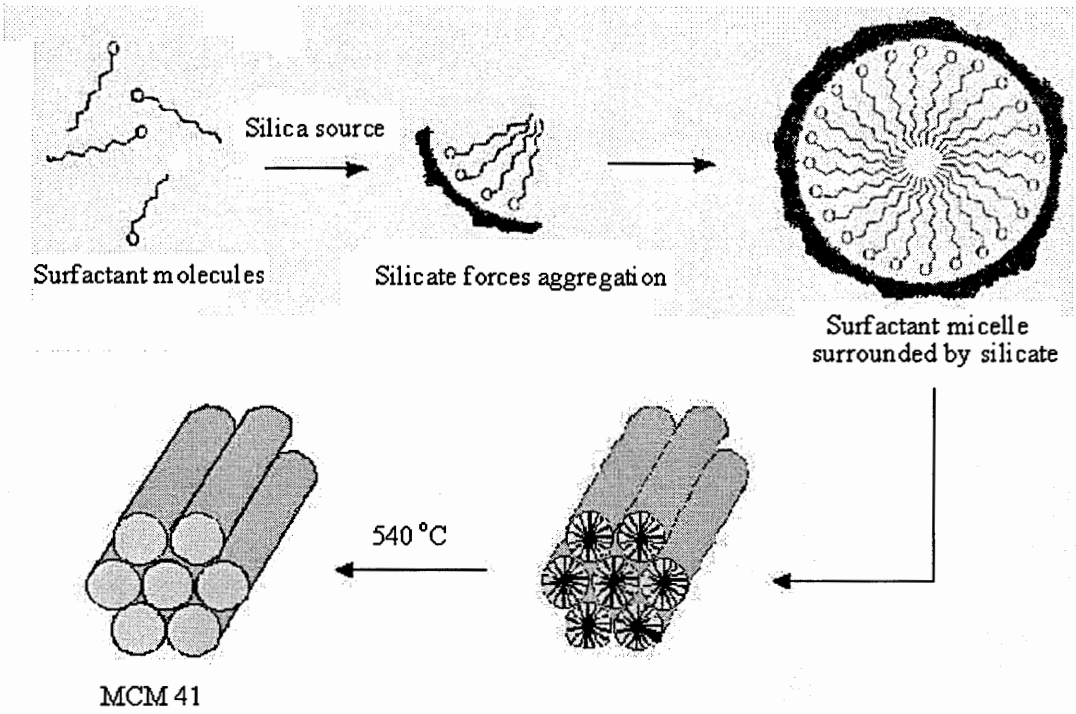

Figure 1.2 Mechanism for the synthesis of MCM 41 material, suggested by Vartuli *et al.*[23]

The synthesis of the MCM 41 material synthesised in this work follows the second mechanism suggested by Vartuli *et al.*[23]

1.4.1.2 MCM 48

MCM 48[24, 25,] is a mesoporous material, which has a three-dimensional, cubic ordered pore system with the space group Ia3d.[16] The MCM 48 materials are synthesised in a similar manner to the MCM 41 material using micelles of surfactant, which act as a template. The main difference in the synthesis of MCM 48, compared with that of MCM 41, is that the surfactant/silica ratio used is between 1 and 1.5. The advantage of MCM 48 over MCM 41 is that it has a three-dimensional pore system, which has several advantages in catalytic and separation processes, compared with the one-dimensional pores in MCM 41.

Monnier *et al.*[26] described MCM 48 as being remarkably similar to the Ia3d phase found in the water-cetyltrimethylammonium bromide (CTMABr) system. In the

water-CTMABr system, the solvated head groups of the surfactant meet near the minimal surface while the tails fill the rod structure and the water layer forms the gyroid surface. A minimal surface is the surface with principal curvatures, c_1 and c_2, that are equal in magnitude but opposite in sign. This gives a mean surface curvature of zero. In MCM 48, the silicate walls form the minimal surface with the head of the surfactant bound to the silicate. Alfredson *et al.*[27] have confirmed this structure by comparing experimental transmission electron micrographs with simulations based on the gyroid surface.

1.4.1.3 HMS (Hexagonal Mesoporous Silica)

HMS (Hexagonal Mesoporous Silica) is one of the family members of the M41S materials and was developed initially by Tanev and Pinnavaia in 1995.[28] The template used in the synthesis of HMS material is a neutral amine in contrast to the preparation of MCM 41 material, which employs cationic/anionic surfactants. HMS is formed by H-bonding interactions between electrically neutral surfactants and inorganic precursors (S^o I^o assembly pathway). These pathways normally afford mesostructures with a 'wormhole-like' framework.[29] Similar to MCM 41, the diameter of the pores in HMS can be tailored either using amines with different chain length or by using auxiliary chemicals. The surface properties can also be tailored by immobilisation of different functional groups on the surface (Section 1.5.2).

1.4.1.4 SBA-n (Santa Barbara-n)

SBA-n[30, 31] (Santa Barbara-n) materials were first reported by Stucky and co-workers[30, 31] in 1995. They are one of the family members of the highly ordered mesoporous silicas, which have been synthesised using non-ionic tri-block polymers [alkylpoly-ethylene-propylene oxide (PEO-PPO-PEO)], oligomeric surfactants and

poly(alkylene oxide) block copolymers] in acid media. The different types of SBA-n reported have cubic, hexagonal, or lamellar symmetries.[32]

The assembly of the inorganic and organic precursors into solid mesoporous materials takes place by a hydrogen-bonding (S^o H^+)(X^- I^+) pathway, where S is the PEO surfactant, I^+ is the protonated Si-OH moiety and H^+ and X^- are the hydrogen and halide ions for Coulombic interactions in the assembly process.

The hexagonal mesoporous silica synthesised by this approach showed a BET surface area of up to 1150 $m^2 g^{-1}$, a large uniform pore size (50 to 300 Å) with thicker pore walls (30 to 60 Å), and a large pore volume of up to 2.5 $cm^3 g^{-1}$ [32] compared with the MCM 41 material synthesised using a conventional low-molecular weight cationic surfactant. The SBA-n materials are highly stable due to their thicker pore walls.

1.5 Modification of MCM 41 Material

The as-synthesised MCM 41 material contains a substantial amount of organic template within its pores and the template needs to be removed for its application as a porous catalyst, so that the internal surface area is fully accessible. Purely siliceous-MCM 41 material possesses a neutral framework, which limits its application as a catalyst.[1, 4, 17] Thus, it becomes necessary to modify its framework/surface before it can be potentially used as a catalyst. The large surface area and tuneable pore structure of MCM 41 makes it a suitable support for the incorporation of catalytically-active species. Methodologies for modifying silica supports are:

- Impregnation[4, 7, 33] - filling the pores of a support with a solution of a reagent followed by evaporation of the solvent.
- Ion exchange[4, 34]
- Isomorphous substitution[4, 33, 34] - incorporation of potentially catalytically active metal ions, *e.g.* Al, Ti, and the organofunctional groups into the lattice framework by substitution of the framework silicon, in a sol-gel

synthesis process.

- One step, *in-situ* grafting of metal ions by using metal surfactants as a template,[35] *e.g.* ruthenium-MCM 41.
- Post-synthetic grafting of the metal ions, *e.g.* Al, Ti, on the pore surface.[4, 5, 33, 34]
- Post-synthetic tethering of organofunctional groups, *e.g.* 3-aminopropyl, and metal complexes, *e.g.* metal-Schiff base complexes, on the surface.[1, 4, 5, 34]

Some of the methods used for modifying the Si-MCM 41 material are described in the following sub-sections.

1.5.1 *One Step, In-situ Modification via Sol-gel Synthesis Method*

1.5.1.1 Incorporation of Metal Ions by Isomorphous Substitution of Framework Silicon

In the sol-gel synthesis of the MCM 41 material the catalytically active metal ions are added into the gel mixture, which leads to the isomorphous substitution of the framework silicon and results in the incorporation of the metal ions into the framework (Fig. 1.3). Isomorphous substitution of one element by another within the framework essentially alters many of the properties of the MCM 41 material. For example, the isomorphous substitution of some of the lattice silicon atoms by elements like aluminium or boron enhances the Brönsted acidity of the material synthesised and its potential as a solid acid catalyst.[34, 36, 37] In the past decade, the isomorphous substitution of bi-, tri-, tetra- and penta-valent elements such as Ti, V, Cr, Sn, Co and Cu into the framework of both siliceous and aluminosilicate MCM 41 materials has been reported.[38-42] The substitution by transition metal ions has extended the use of metallosilicate MCM 41 as a catalyst in many redox reactions.[43, 44]

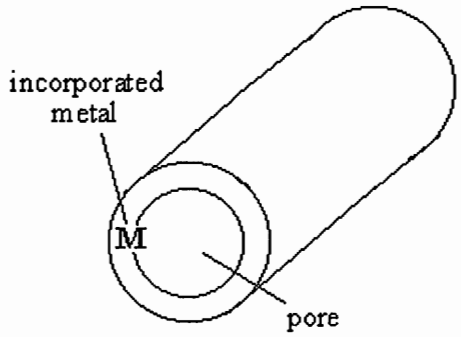

Figure 1.3 Diagram showing metal incorporated in framework lattice of the MCM 41 material.

1.5.1.2 Incorporation of Organofunctional Groups

In recent years, a wide variety of novel materials have been prepared by chemical modification of silica supports with organic functionalities. These materials have applications in chromatographic separation, selective removal of trace metals from aqueous systems and catalysis. For example 3-aminopropyl groups (discussed in Chapter 5) immobilized on a silica support have been used as a base catalyst in liquid phase organic reactions,[46] and in the removal of trace metal ions from aqueous systems.

Incorporation of organofunctional groups in the lattice framework of the MCM 41 material, carried out using the templated sol-gel methodology involves a 'one-pot' synthesis method in which an organotrialkoxysilane is co-polymerised with the silica precursor in the presence of a templating agent.[45-48] The organically-modified MCM 41 materials (Fig. 1.4) synthesised by this method are very stable.

However, the disadvantages of this method are:

- It is very difficult to control the surface area and porosity of the final material.
- There is a limit to the amount of organofunctional groups that can be incorporated, as too many organofunctional groups cause collapse of the hexagonal mesophase in the material.
- The limited availability of commercial organotrialkoxysilane species.

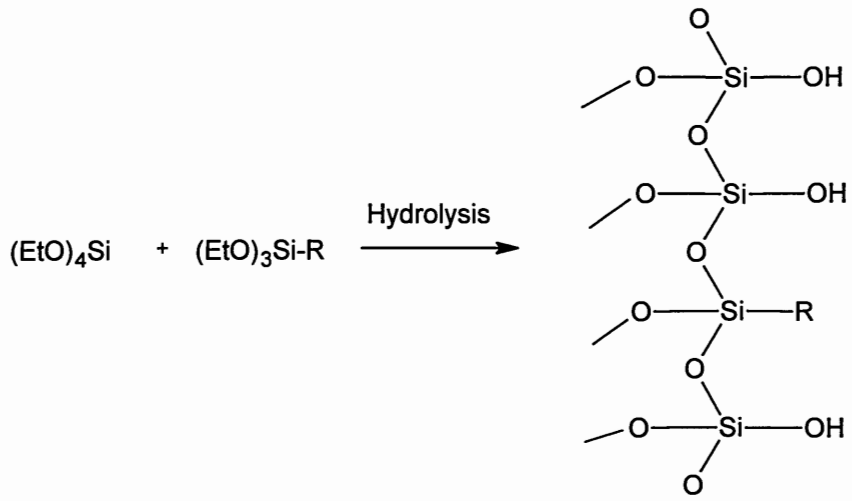

Figure 1.4 Preparation of organofunctionalised MCM 41 material *via* sol-gel methodology.

1.5.1.3 Pore Size Modification by Using Auxiliary Chemicals

Tethering of organfunctional groups or metal complexes within the pores of MCM 41 causes reduction in the pore diameters, as the incorporated groups protrude from the surface, as illustrated in Fig. 1.5.

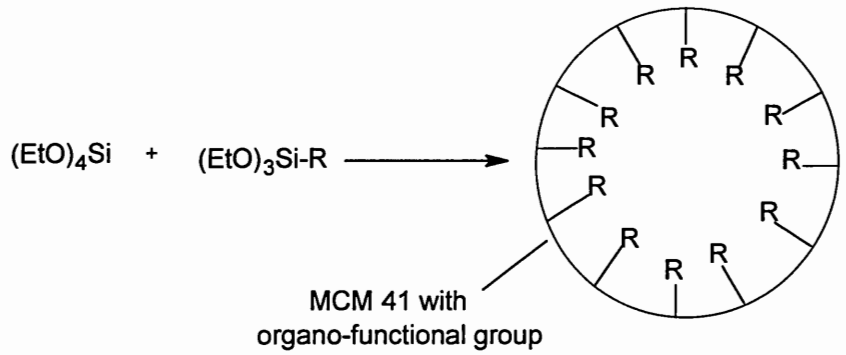

Figure 1.5 Schematic diagram showing reduction of the pore size due to the incorporation of organfunctional groups.

Thus, the organofunctionalised materials synthesised may show properties of microporous solids rather than mesoporous, as reported by Williams *et al.*[49] However, this can be overcome by swelling the pores in order to synthesise the organofunctionalised-MCM 41 or metal complex-functionalised MCM 41 materials with pores in a mesoporous range. Examples of auxiliary chemicals used to swell the pores are mesitylene and straight chain alkanes. Beck *et al.*[50] reported that when a mesitylene to surfactant molar ratio of 2.5 is employed an increase in pore diameter of 20 Å is observed. Thus, by using mesitylene (2,4,6 trimethyl benzene) as a solubilising agent the pores of the MCM 41 material can be expanded or swollen enough to accommodate organofuctional groups, while retaining the mesoporosity of the material.[49] Similarly, Ulgappan and Rao[51] used a straight chain alkane (Fig. 1.6) in an equimolar ratio with the surfactant to increase the pore diameter of the MCM 41 material.

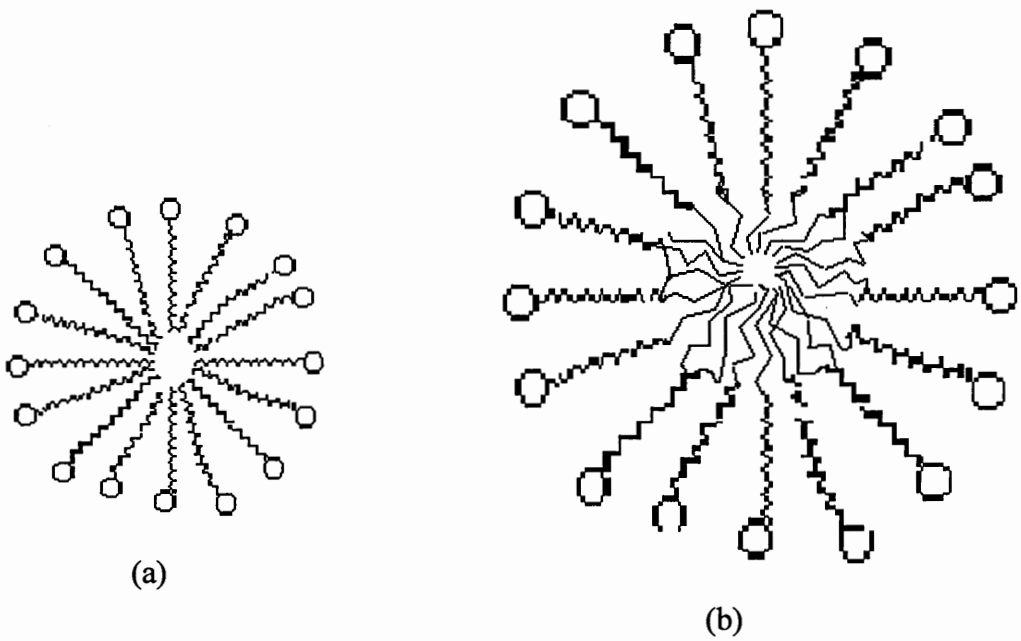

(a) (b)

Figure 1.6 Schematic diagram showing (a) a liquid crystal micelle and (b) a micelle swollen with straight chain alkanes (used as an auxiliary chemical).

1.5.2 *Post-synthetic Grafting*

1.5.2.1 Grafting of Metals[34, 42, 52-54]

The silanol and siloxane groups present on the surface of the MCM 41 materials are suitable for the chemical bonding of transition metals (Fig. 1.7). The transition metals, when immobilised on the pore surface of the solid support, can impart redox properties and the materials synthesised have a catalytic potential in many oxidation reactions. Oldroyd[55] observed that grafting of the metal ions gave better results in several oxidation reactions compared with materials prepared by isomorphous substitution into silica frameworks.

The materials synthesised by grafting are very stable at higher temperature but show leaching of metal ions during catalysis.[56, 57] Therefore, an alternative method, which will bind the metal ions firmly to the surface needed to be developed.

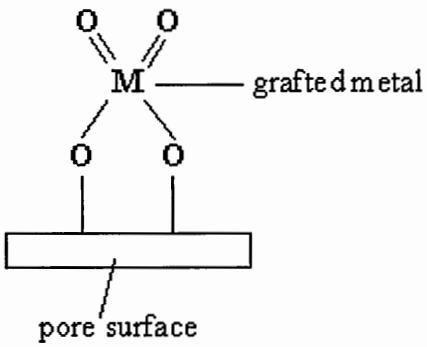

Figure 1.7 Metal tethered on the pore surface by the post-synthetic grafting methodology.

1.5.2.2 Tethering of Organic Compounds and Metal Complexes[58-61]

Organofunctional groups or metal complexes can be tethered onto the MCM 41 surface *via* covalent bond formation using surface silanol or siloxane groups. The materials synthesised by this method are very robust compared with materials prepared by grafting of metal ions and they show catalytic activity similar to their homogeneous

analogues.[1, 4, 5] Two significant features of the catalysts include their high selectivity and ability to retain the metal ions in harsh conditions.

The four different methods by which the organic compounds could be tethered onto the MCM 41 surface are:[2, 5]

1) Reaction of an aliphatic alcohol with the surface silanol groups, resulting in the formation of Si-O-C bonds (Fig. 1.8).

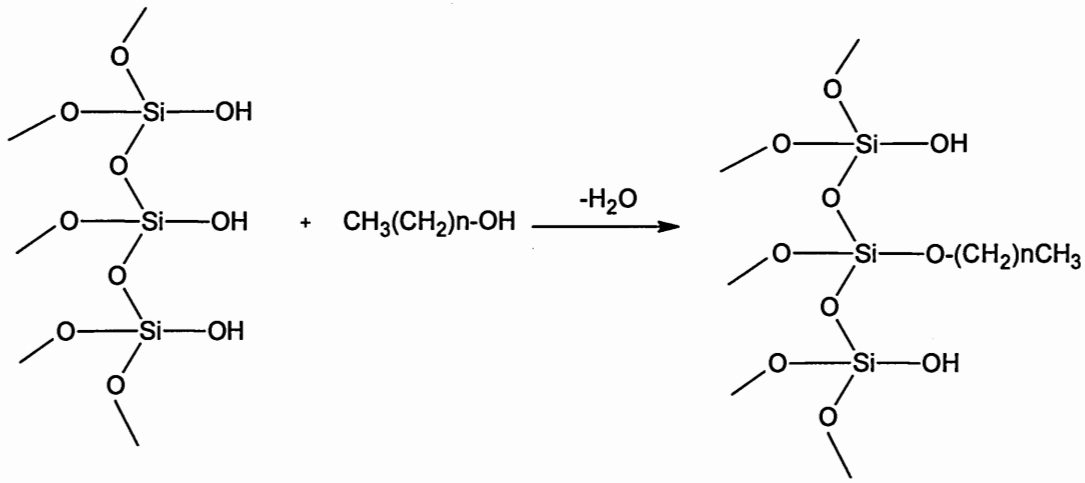

Figure 1.8 Tethering of the organofunctional groups to the silica surface by reaction with aliphatic alcohols.

2) Reaction of an organosiloxane or a metal-organosiloxane and the surface silanol (and siloxane) groups present on the MCM 41 surface (Fig. 1.9).

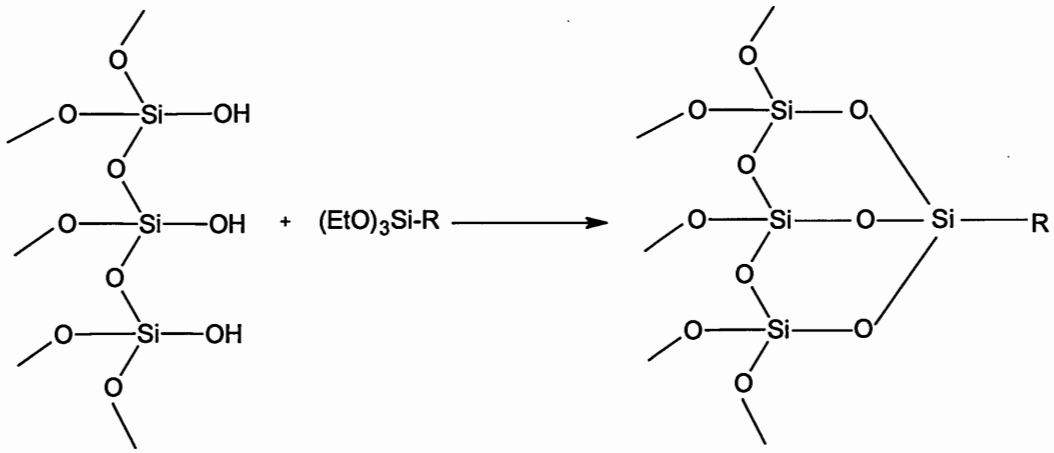

Figure 1.9 Tethering of organofunctional groups on a pore surface *via* the post-synthetic grafting methodology.

3) Chlorination of the silica surface followed by reaction of the chlorinated surface with an Grignard reagent (Fig. 1.10).

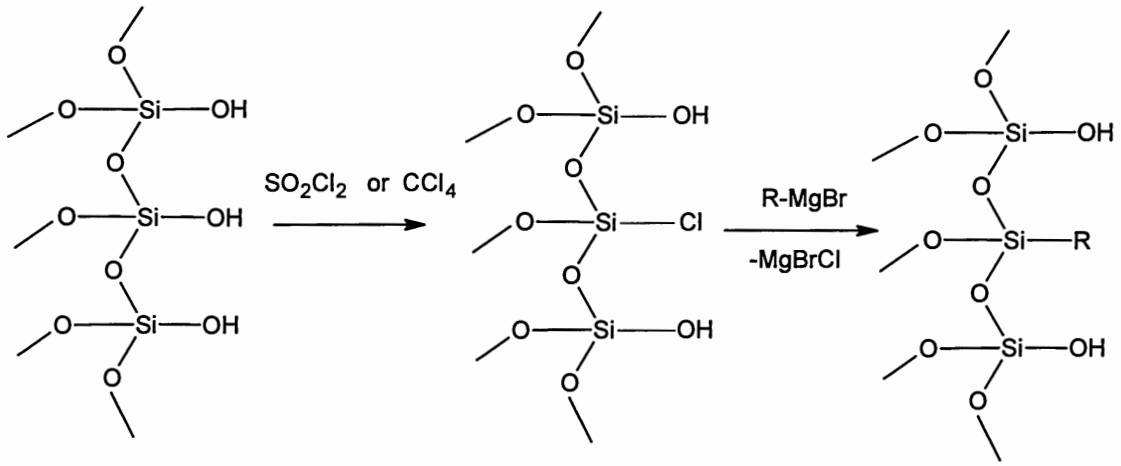

Figure 1.10 Chlorination of silica surface and subsequent modification with a Grignard reagent.

4) Coupling of an organic molecule with functional groups which have been previously grafted on the surface (Fig. 1.11).[62, 63]

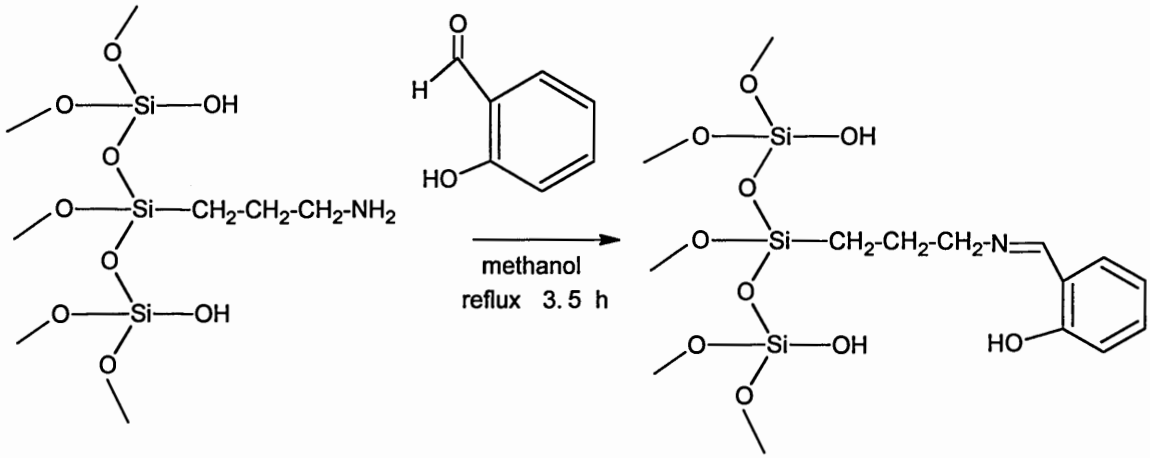

Figure 1.11 Modification of silica surface *via* the coupling of an organic molecule with previously grafted amino propyl functional group.

Advantages and Disadvantages of the four 'Tethering' Methods

The first method used for modification is environmentally friendly, but the method involves reaction between the surface silanol groups and aliphatic alcohols, resulting in the formation of Si-O-C bonds. However, this bond is unstable and readily cleaved at elevated temperatures.[1, 3, 4] The other method for modification of silica is the reaction of the surface hydroxyl groups with alkoxysilanes, forming a Si-O-Si bond. Thus, the Si-O-Si bond formed is more thermally and chemically stable than the Si-O-C bond. The material formed by this method is not very stable at extremes of pH and at very high temperatures.[1, 3, 4]

The third method (chlorination and Grignard reaction) involves the formation of highly stable Si-C bonds. This method makes use of either thionyl chloride or carbon tetrachloride as the surface-chlorinating agents. Both the reagents are hazardous and have to be carefully handled, and the by-products such as HCl, SO_2, Cl_2, CO evolved during the synthesis process are not environmentally friendly.[1, 3, 4]

The third method involves the coupling of previously grafted organofuctional groups with organic molecules. Higher loading of the organic compounds or the metal complexes can be achieved due to the easier access of the smaller reactant molecules to reactive sites in the pores, compared with the larger organic compounds or metal complexes involved in direct grafting. The disadvantage of this method for immobilisation of metal complexes is that some of the metal ions can react directly with the surface of the MCM 41 material.

1.6 Aims of this Project

The main aims of this study were the synthesis of novel, metal-functionalised MCM 41, organofunctionalised-MCM 41, and metal-complex-functionalised MCM 41 materials, which could potentially be used for catalysis. Different synthesis methods were used in

their preparation and evaluated with respect to the maximum loading achieved, and the mesoporosity of the synthesised material.

A number of standard analytical techniques were used for the characterisation of these synthesised materials. X-ray photoelectron spectroscopy was used for the first time in the characterisation of a metal-complex-functionalised MCM 41 material. Hence, evaluation of X-ray photoelectron spectroscopy as an analytical technique to investigate the distribution of metal complexes within the pores or on external surface in this class of materials was one of the aims of this work.

Sorption studies of N_2 and CO_2 gases and various vapours (water, methanol, *n*-butanol, *t*-butanol, *n*-hexane, 1-hexene and 3,3-dimethyl-1-butene) were carried out on the materials synthesised in order to explore the pore structure and surface characteristics following modification.

Exploring the effect of heat treatment on the sorption properties of the Ru-MCM 41 material (supplied by Bruce *et al.*[35]) with respect to hexane isomers was also one of the objectives of this work.

1.7 References

1. P. M. Price, J. H. Clark and D. J. Macquarrie, *J. Chem. Soc., Dalton Trans.*, 2001, 101.
2. W. F. Hoelderich, *Catalysis Today*, 2000, **62**, 115.
3. J. S. Rafelt and J. H. Clark, *Catalysis Today*, 2000, **57**, 33.
4. J. H. Clark and D. J. Macquarrie, *J. Chem. Soc., Chem. Soc. Rev.*, 1996, 303.
5. J. H. Clark and D. J. Macquarrie, *J. Chem. Soc., Chem. Commun.*, 1998, 853.
6. D. J. Macquarrie, *Phil. Trans. R. Soc. Lond. A*, 2000, **358**, 419.
7. A. Corma, H. Garcia and A. Leyva, *Appl. Catal. A: General*, 2002, **236**, 179.
8. K. Wilson, A. F. Lee, D. J. Macquarrie and J. H. Clark, *Appl. Catal. A: General*, 2002, **228**, 127.
9. J. H. Clark (Ed.), *Chemistry of Waste Minimisation*, Chapman and Hall, Glasgow, 1995.
10. H. Kosslick, I. Mönnich, E. Patezold, H. Fuhrmann, R. Fricke, D. Müller and G. Oehme, *Micropor. Mesopor. Mater.*, 2001, **44-45**, 537.
11. K. Smith (Ed.), *Solid Supports and Catalysts in Organic Reactions*, Ellis Horwood Ltd., Chichester, 1992.
12. S. J. Gregg, K. W. Sing, *Adsorption, Surface Area and Porosity*, 2nd Edition, Academic Press, London, 1982.
13. M. M. Dubinin, *Chem. Rev.*, 1960, **60**, 235.
14. IUPAC Manual of Symbols and Terminology, Appendix 2, Pt. 1, Colloid and Surface Chemistry, *Pure Appl. Chem.*, 1972, **31**, 578.
15. K.W. Sing, D.H. Everett, J. Rouquerol, *Pure and Appl. Chem.,* 1995, **267**, 865.
16. J.S. Beck, Vartulli, J.C. Roth, C. T. Kresge, K. D. Schmitt, S.B. McCullen, and J. L. Schlenker, *J. Am. Chem. Soc.* 1992, **114**, 1083.
17. A. Corma, *Chem. Rev.*, 1997, **97**, 2373.

18. L. Smart and E. Moore, *Solid State Chemistry*, 2nd Edition, Chapman and Hall, London, 1995.

19. M. T. Weller, *Inorganic Materials Chemistry*, Oxford Chemistry Primers, Volume 23, Oxford University Press, UK, 1994.

20. U. Ciesla and F. Schüth, *Micropor. Mesopor. Mater.*, 1999, **27**, 131.

21. G. Øye, J. Sjöblom, and M. Stöcker, *Adv. Coll. Interf. Sci.*, 2001, **89-90**, 439.

22. C. T. Kresge, M. E. Leonowicz, W. J. Roth, J. C. Vartuli and J. S. Beck, *Nature*, 1992, **359**, 710.

23. J. C. Vartuli, K. D. Schmidt, C. T. Kresge, W. J. Roth, M. E. Leonowicz, S. B. McCullen, S. D. Hellring, J. S. Beck, J. L. Schlenker, D. H. Olson, E. W. Sheppard, *Chem. Mater.*, 1994, **6**, 2317.

24. G. Øye, J. Sjöblom and M. Stöcker, *Micropor. Mesopor. Mater.*, 1999, **27**, 171.

25. V. Alfredsson, M. W. Anderson, T. Ohsuna, O. Terasaki, M. Jacob and M. Bojrup, *Chem. Mater.*, 1997, **9**, 2066.

26. A. Monnier, F. Schuth, Q. Huo, D. Kumar, G. D. Stucky, M. Krishnamurty, A. Firouzi and B. F. Chmelka, *Science*, 1993, **261**, 1299.

27. V. Alfredson and M.W. Anderson, *Chem. Mater.*, 1996, **8**, 1141.

28. P.T. Tanev and T. J. Pinnavaia, *Science*, 1995, **267**, 865.

29. T. R. Pauly and T. J. Pinnavaia, *Chem. Mater.*, 2001, **13**, 987-993.

30. Q. Huo, R. Leon, P. M. Petroff and G. D. Stucky, *Science*, 1995, **268**, 1334.

31. H. M. A. Hunter, P. A. Wright, *Micropor. Mesopor. Mater.*, 2001, 43, 361.

32. D. Zhao, Q. Huo, J. Feng, B. F. Chmelka, G. D. Stucky, *J. Am. Chem. Soc.*, 1998, **120**, 6024.

33. E. F. Vasant and P. Cool, *Colloids and Surfaces A: Physiochem. Eng. Aspects*, 2001, **179**, 145.

34. A. Tuel, *Micropor. Mesopor. Mater.*, 1999, **27**, 151.

35. H. B. Jervis, M. E. Raimondi, R. Raja, T. Maschmeyer, J. M. Seddon and D. W. Bruce, *J. Chem. Soc., Chem. Commun.*, 1999, 2031.

36. B. Lindlar, A. Kogelbauer and R. Prins, *Micropor. Mesopor. Mater.*, 2000, **38**, 167.

37. R. Mokaya, W. Jones, Z. Luan, M. D. Alba and J. Klinowski, *Catal. Lett.*, 1996, **37**, 113.

38. X. He and D. Antonelli, *Angew. Chem. Int. Ed.*, 2002, **41**, 214.

39. F. Chen and M. Liu, *J. Chem. Soc., Chem. Commun.*, 1999, 1829.

40. E. Armengol, A. Corma, V. Fornés, H. García and J. Primo, *Appl. Catal. A: General*, 1999, **181**, 305.

41. S. C. Laha and R. Kumar, *Micropor. Mesopor. Mater.*, 2002, **53**, 163.

42. Z. Zhu, Z. Chang and L. Kevan, *J. Phys. Chem. B*, 1999, **103**, 2680.

43. W. A. Alves, M. Wallau and U. Schuchardt, *J. Mol. Catal. A: Chem.*, 1999, **144**, 91.

44. I. Kohara, H. Fujiyama, K. Iwai, S. Nishiyama and S. Tsuruya, *J. Mol. Catal. A: Chem.*, 2000, **153**, 93.

45. S. R. Hall, C. E. Folwer, B. Lebeau and S. Mann, *J. Chem. Soc., Chem. Commun.*, 1999, 201.

46. D. J. Macquarrie, *Green Chemistry*, 1999, 195.

47. D. J. Macquarrie, D. B. Jackson, J. E. G. Mdoe and J. H. Clark, *New J. Chem.*, 1999, **23**, 539.

48. D. J. Macquarrie, *J. Chem. Soc., Chem. Commun.*, 1996, 1961.

49. C. M. Bambrough, R. C. T. Slade and R. T. Williams, *J. Mater. Chem.*, 1998, **8**, 569.

50. J. C. Vartuli and J. S. Beck. *Solid State & Mater. Sci.* 1996, **1**, 76.

51. N. Ulgappan and C. N. R. Rao, *J. Chem. Soc., Chem. Commun.*, 1996, 2759.

52. Z. Li, K. Xie and R. C. T. Slade, *Appl. Catal. A: General*, 2001, **205**, 85.

53. V. Parvulescu and B. L. Su, *Catal. Today*, 2001, **69**, 315.

54. S. T. Wong, J. F. Lee, S. Cheng and C. Y. Mou, *Appl. Catal. A: General*, 2000, **198**, 115.

55. R. D. Oldroyd, J. M. Thomas, T. Maschmeyer, P. A. MacFaul, D. W. Snelgrove, K. U. Ingold and D. M. Wayner, *Angew. Chem. Int. Ed. Engl.*, 1996, **35**, No. 23/24, 2787.

56. J. M. Fraile, J. I. Garaía, J. A. Mayoral, E. V.ispe, D. R. Brown and M. Naderi, *J. Chem. Soc., Chem. Commun.*, 2001, 1510.

57. V. Parvulescu and B. L. Su, *Catal. Today*, 2001, **69**, 315.

58. I.C. Chisem, J. Rafelt, M.T. Shieh, J. Chisem, J.H. Clark, R. Jachhuck, D.J. Macquarrie, C. Ramshaw and K. Schott, *J. Chem. Soc., Chem. Commun.*, 1998, 1949.

59. P. Sutra and D. Brunel, *J. Chem. Soc., Chem. Commun.*, 1996, 2485.

60. E. I. Iiskola, S. Timonen, T. T. Pakkanen, O. Harkki and J. V. Seppala, *Appl. Surf. Sci.*, 1997, **121-122**, 372.

61. S. Shyu, S. Cheng and D. L. Tzou, *J. Chem. Soc., Chem. Commun.*, 1999, 2337.

62. D. Brunel, F. Fajula, J. B. Nagy, B. Deroide, M. J. Verhoef, L. Veum, J. A. Peters and H. van Bekkum, *Appl. Catal. A: General*, 2001, **213**, 73.

63. C. Baleizao, B. Gigante, M. J. Sabater, H. Garcia and A. Corma, *Appl. Catal. A: General*, 2002, **228 (1-2)**, 279.

CHAPTER 2

TECHNIQUES USED FOR CHARACTERISATION OF SAMPLES

2.1 Introduction

This Chapter describes the different techniques used for the characterisation of both the siliceous MCM 41 (Si-MCM 41) and the modified MCM 41 materials. Several techniques were used in combination, in order to provide structural information on the materials synthesised. In general, these techniques fall into two distinct areas:

- Characterisation of physical structure (*e.g. p*-X-ray diffraction, sorption studies)
- Chemical composition (*e.g.* infrared spectroscopy, atomic absorption spectroscopy)

Reliable characterisation of the porous hexagonal structure of the MCM 41 materials requires three independent techniques *i.e.* X-ray diffraction (XRD), transmission electron microscopy (TEM) and gas adsorption studies.[1] However a wide variety of techniques was used for the characterisation of the modified MCM 41 materials. Table 2.1 summarises the analytical techniques[2] used and the information obtained in the characterisation of Si-MCM 41 and the modified MCM 41 samples prepared in the current work. All of the techniques used are discussed briefly in Sections 2.2 to 2.12. This Chapter is divided into two parts:

- Part A, Physico-chemical Characterisation (Section 2.2 to 2.9)
- Part B, Gas Adsorption Studies (Section 2.10 to 2.12)

Tables 2.4 and 2.7 at the end of Part A and Part B, respectively, detail the characterisation techniques used for the analysis of each of the samples synthesised.

Table 2.1 Analytical techniques[2] employed for the characterisation of the Si-MCM 41 and modified MCM 41 materials

Analysis	Technique	Information
Structure of MCM 41	XRD, TEM	Confirms hexagonal arrangement of pores.
Porosity	Gas adsorption	Determines microporosity and/or mesoporosity of the material and yields values for the surface area, the pore volume and the pore diameter.
Chemical composition	Atomic absorption spectroscopy,	Used for the metal-functionalised materials to determine the amount of metal loaded.
	X-ray photoelectron spectroscopy	
	CHN microanalysis,	Confirms the presence of organic groups on the modified materials.
	NMR spectroscopy	
	Infrared spectroscopy	
	Mössbauer spectroscopy	Used for the qualitative analysis of iron present in the modified sample.
Structure of immobilised species	Infrared spectroscopy,	Mainly used for the analysis of the organically modified materials.
	^{29}Si *CP MAS* NMR,	
	^{13}C *CP MAS* NMR,	
	UV/Visible spectroscopy	Used for the analysis of dye-functionalised MCM 41

PART A

Physico-chemical Characterisation

2.2 Powder X-ray Diffraction (*p*-XRD)

Powder X-ray diffraction (*p*-XRD) is widely used in the study of inorganic solids. It can provide useful information about the following:

- Structure
- Phase purity
- Degree of crystallinity
- Unit cell parameters
- Crystal size

However, in this study *p*-XRD was used to confirm the hexagonal periodicity of the pores in the MCM 41 material (phase purity).[2, 3] Some of the important terms used in XRD are described briefly in following subsections.

2.2.1 The Crystal Lattice

A crystal lattice is a regular, three-dimensional distribution of equivalent points (atoms) in a space. These are arranged so that they form a series of parallel planes separated from one another by a distance *d*, which varies according to the nature of material.[4] In the MCM 41 materials we are looking at the distribution of the pores and the distance *d*, between them.

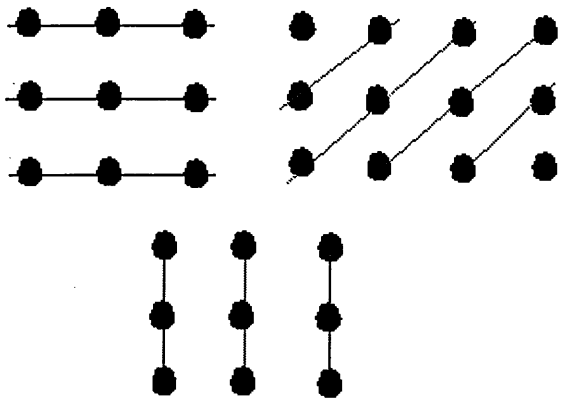

Figure 2.1 Two-dimensional array demonstrating lattice planes.

2.2.2 Miller Indices

Miller indices[4, 5, 8] are used to define lattice planes within the crystal structure. For a three-dimensional unit cell, three Miller indices are required, which are designated as *h*, *k* and *l*. The values of these indices are calculated by considering the position at which the planes intersect the axes of a unit cell.

The lattice plane shown in Fig. 2.2 has intercepts, 1/2 on x-axis, 1/3 on y-axis and 1 on z-axis. The fractional intersections are therefore, ½, ⅓, 1. The Miller indices are given by reciprocals of the fractional intercepts along each of the cell directions. Thus, by taking reciprocals of the fractions, the Miller indices of the plane shown in Fig. 2.2 is 231.

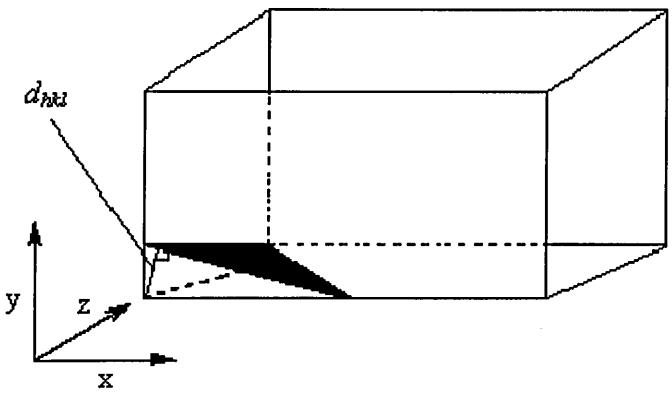

Figure 2.2 Lattice plane showing Miller indices for a unit cell

For any crystal, planes exist in a number of different orientations (see Fig. 2.1) each with its own specific *d*-spacing denoted as d_{hkl}. This term (d_{hkl}) is related to the Bragg angle, θ, by Bragg's equation (equation 2.1, as described in Section 2.2.3) and therefore can be determined.

2.2.3 Theory of p-XRD

X-ray diffraction is based on the principle of a crystallite acting as a diffraction grating.[5] For X-ray diffraction to take place, the scattering centres in the crystal must be separated by a distances comparable to the wavelength of the X-rays. The scattering of an X-ray beam by a crystal will give rise to a number of diffraction maxima, the position of which are related to the lattice parameters, the Miller indices and the X-ray wavelength. The diffraction maxima in X-ray diffraction were termed by Bragg as X-ray reflection. Bragg reflection from scattering planes, separated by a distance *d*, is shown in Fig. 2.3.

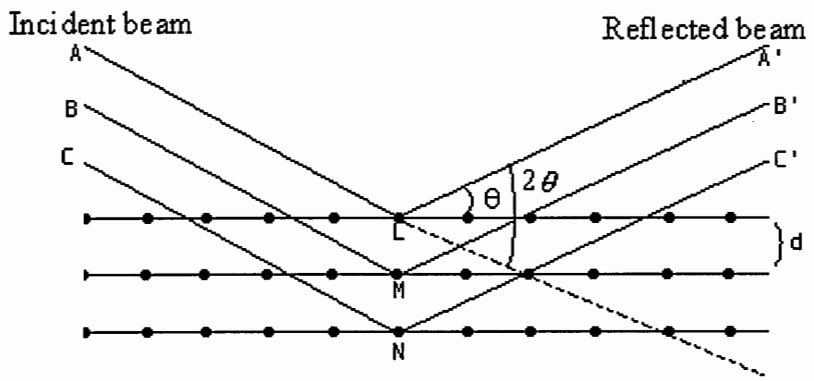

Figure 2.3 Schematic diagram showing scattering of X-rays by crystal lattice.

All crystalline material has an infinite number of lattice planes with different Miller indices, separated by a distance d_{hkl}. The relationship between the wavelength of X-rays (λ), the interplanar *d*-spacing in crystals (d), and the angle (θ) at which the

reflected X-rays are in phase (where the constructive interference of the waves occurs) is given by the Bragg equation:[4, 5, 8]

$$n\lambda = 2d_{hkl} \sin\theta \qquad \textit{Equation } 2.1$$

where n is an integer (the order of diffraction) and d, in this case, is the interplanar spacing between the adjacent pores (see Fig. 2.4).

Although, the MCM 41 materials are not crystalline at the atomic level and have amorphous pore walls, X-ray diffraction is an important tool in their characterisation.[1, 3] In this case, XRD has been used to investigate the periodicity of the pores arising from hexagonally arranged parallel cylindrical tubes of silica. This is shown schematically in Fig. 2.4, where d, is the height of the equilateral triangle and represents the interplanar spacing between the adjacent pores. The side of the triangle, a, which is the repeat distance of the hexagonal structure, represents the sample's pore diameter plus the pore wall thickness. The repeat distance, a, of the MCM 41 material is related to the d-spacing of the first XRD reflection (d_{100}) by an equation 2.2.

$$a = 2d_{100} / \sqrt{3} \qquad \textit{Equation } 2.2$$

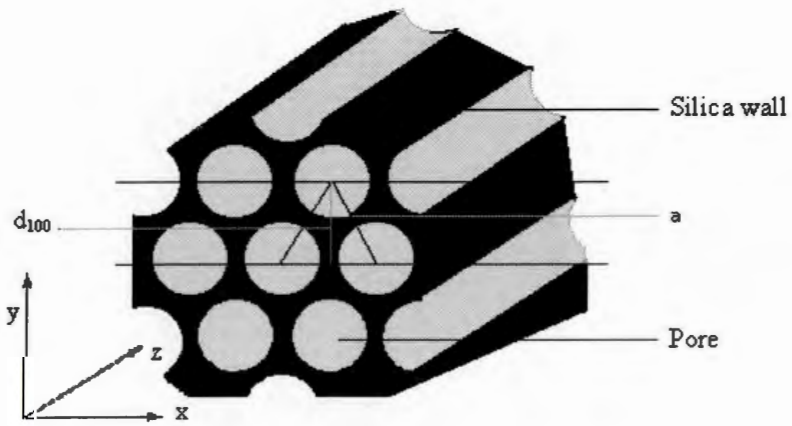

Figure 2.4 Schematic diagram showing the relationship between d, and the unit cell parameter, a.

Thus, if the pore diameter (D) of the material is known (obtained from N_2 adsorption, see Section 2.11.5) then the thickness (t) of the pore wall can be calculated by equation 2.3.

$$t = a - D \qquad \textit{Equation } 2.3$$

2.2.4 Experimental Details

Powder XRD patterns for the as-synthesised, the calcined and the modified MCM 41 materials were measured with a Philips PW 1050/81 diffractometer operating in Bragg-Brentano geometry with CrKα radiation (λ = 2.29 Å), (40 kV, 30 mA) and equipped with a diffracted beam monochromator. Data were collected in the 2θ range 2° – 10° with a step size of 0.05° and dwell time of 5 s per point. The samples were prepared as a thin layer on aluminium plates.

Initially, CuKα radiation (λ = 1.54 Å) was employed for the analysis. Problems arose while analysing samples with a larger pore diameter, because the d_{100} peak was obscured by the main X-ray beam, therefore CrKα radiation was subsequently used.

2.3 Infrared (IR) Spectroscopy

2.3.1 General

Infrared (IR) spectroscopy is an important tool for the analysis of molecules. The theory of IR spectroscopy is based on the change in dipole moment that arises from the "vibrations", which are caused by absorption of IR radiation.[6, 9, 10] Several classes of vibrational modes have been identified and may be classified as "stretching" (symmetric and asymmetric) or "bending" vibrations[7, 8, 9] (Fig. 2.5). An IR spectrum records the position of these vibrational bands (quoted in units of wavenumber, cm^{-1}) and allows identification of the functional groups contained in the sample.

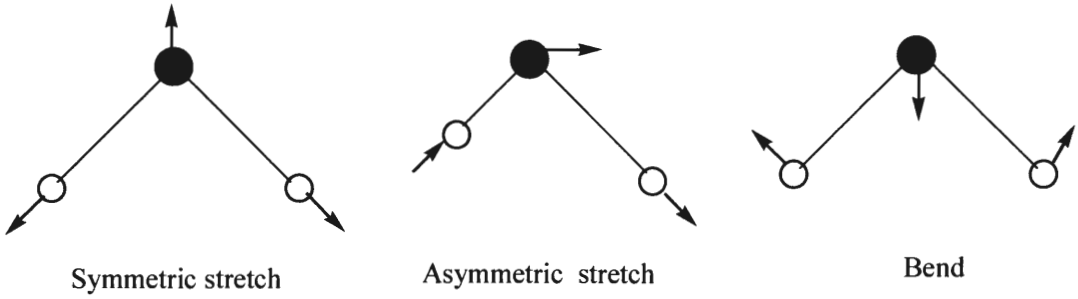

Figure 2.5 Some examples of modes of vibrations.

In this study, IR spectroscopy was used for the characterisation of the Si-MCM 41, organically-modified MCM 41 and metal-complex modified MCM 41 materials. The technique, along with CHN microanalysis and gas adsorption studies, provided useful information about the immobilisation of organic molecules and the metal complexes within the pores of the MCM 41 material. It was also used to monitor the removal of template from the as-synthesised MCM 41 materials and the chemisorption of vapours (*e.g.* water, methanol, butanol and *n*-hexane) on the Si-MCM 41 surface following sorption.

2.3.2 Experimental Details

The infrared spectrum of the Si-MCM 41 material and each of the modified MCM 41 materials were obtained using a Fourier Transform (FT) Infrared Nicolet Magna-IR^{TM} spectrometer 550, using the KBr self-supporting pellet technique. Samples were analysed by dispersing *ca.* 1% of the material in a KBr pellet and were scanned in the range from 4000 cm^{-1} to 400 cm^{-1}.

2.4 CHN Microanalysis

Elemental Analyser EA 1110 (from CE-instruments)[11] was used for the determination of the amount (% mass) of carbon, hydrogen, and nitrogen in both the Si-MCM 41 and modified MCM 41 samples. As the elements are present in trace amounts on the inorganic support (Si-MCM 41), 10 mg of sample were used for greater precision.

The procedure for the analysis is based on a number of sequential steps: the weighed sample contained in a tin capsule is first heated to 1000 °C to ensure quantitative and instantaneous combustion. The gas mixture from the combustion is then driven through an oxidation catalyst zone of CrO_3, and then through a copper zone, which acts as catalyst for the reduction of nitrogen oxide to elemental nitrogen. The mixture of these gases (N_2, CO_2 and H_2O) thus obtained is passed through a chromatographic column, where these gases are separated and are analysed by a thermal conductivity detector (TCD). The schematic of operation and the operation conditions are shown in Fig. 2.6.

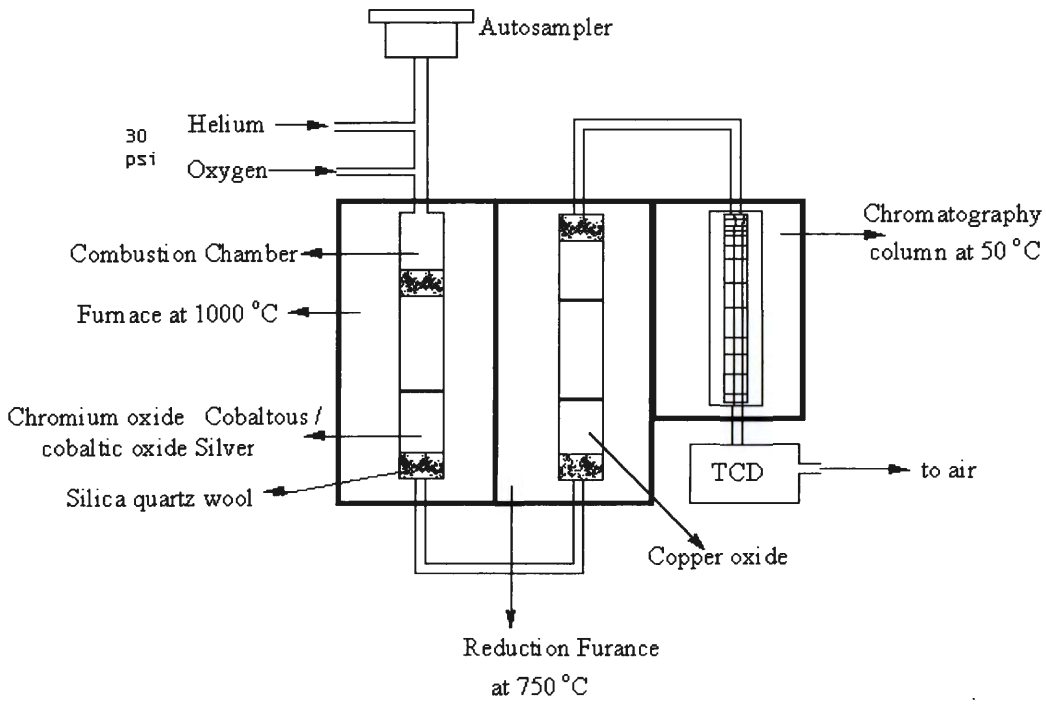

Figure 2.6 Schematic diagram of a CHN microanalysis reactor.

2.5 Atomic Absorption Spectroscopy (AAS)

2.5.1 General

Atomic absorption spectroscopy (AAS) is another useful tool in quantitative analysis of constituent elements (mainly metals) present in the materials. The technique uses "spectrum of a single element", *i.e.* a light of wavelength corresponding to the energy difference between an excited state and the ground state of an element, as a radiation source. The wavelength range extends from 180 nm to 800 nm and the actual wavelength depends on the type of the element to be analysed.[12]

When the free, neutral atoms are irradiated with a light of appropriate wavelength the energy is absorbed to raise electrons from the ground state to the excited state. The amount of energy absorbed is measured to give a quantitative result by means of a calibration curve.

The frequency of radiation absorbed, ν_{mn}, for a transition of an atom from the ground state, E_m, to the excited state, E_n, (illustrated schematically in Fig. 2.7) is given by Bohr's postulate, equation 2.4.[12]

$$\nu_{mn} = (E_n - E_m) / h \qquad \textit{Equation } 2.4$$

where h is Planck's constant.

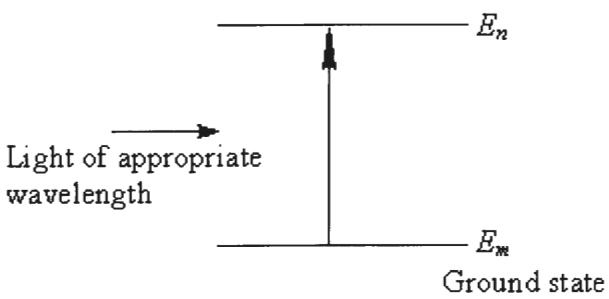

Figure 2.7 Schematic representation of the transition process of an atom in AAS.

2.5.2 Experimental Details

The quantitative analyses of the different metals immobilised within the pores of MCM 41 materials, were carried out by AAS using a Perkin Elmer Analyst 100. An air/acetylene fuel in a ratio of 3:1 litres per minute was used for analysis.

2.5.2.1 Sample Preparation

The metal ions were liberated from the samples by complete dissolution in either HF or HF/HNO_3 following a method similar to Armengol *et al.*[13] Details of the method used are as follows: A known mass of a sample (*ca.* 0.100 g), was dissolved either in HF (5 cm^3) or in 1:1 mixture of HF/HNO_3 (5 cm^3). The sample was left for 30 min to ensure complete dissolution followed by dilution with deionised water to 100 cm^3 in a standard volumetric flask.

2.5.2.2 Measurment of Absorbance

The free neutral atoms of the sample metal ions were obtained by aspiration of sample solution (prepared by the above procedure) as an aerosol into the flame, where it was vaporised and atomised, and irradiated with light of an appropriate wavelength. The amount of metal was determined using a calibration curve method. Table 2.2 summarises the details of the hollow cathode lamps used for the analysis of different metals.

Table 2.2 Hollow-cathode lamps used in AAS analysis

Samples	Lamp used	Wavelength / nm
Cu-Schiff MCM 41	Copper	324.8
Fe-Schiff MCM 41	Iron	248.3
Ni- Schiff MCM 41	Nickel	232.0

2.6 X-ray Photoelectron Spectroscopy (XPS)

2.6.1 General

X-ray photoelectron spectroscopy (XPS)[5, 8, 14] is a surface analytical technique where the sample is irradiated with monochromatic "soft" X-rays and the kinetic energy, *KE*, of the electrons emitted is analysed (see Fig. 2.8). This enables the determination of the binding energy, *BE*, of an emitted electron using Einstein's equation, 2.5.

$$KE = h\nu - BE - \phi_s \qquad \textit{Equation } 2.5$$

where $h\nu$, is the energy of the photons and ϕ_s is the spectrometer work function. The spectrum is a plot of electron detected per energy interval versus Binding energy.

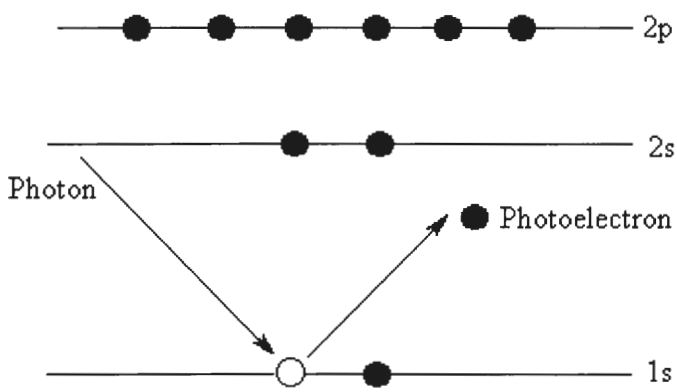

Figure 2.8 Schematic diagram showing the XPS emission process.

The "soft" X-rays used are Mg Kα (1253.6 eV) or Al Kα (1486.6 eV),[15] since these X-ray photons have energies up to several thousand eV, and they can therefore ionise both the valence electrons and the tightly bound core electrons. In practice, XPS concentrates almost exclusively on core level studies. When applied to solids, the mean free paths of the escaping electrons are equivalent to *ca.* 10 atom spacing and so XPS examines the near surface region only. This makes XPS a unique surface-sensitive technique for chemical analysis.

Core electrons are not directly involved in bonding. Hence, their binding energies are relatively insensitive to the chemical environment and are sufficiently characteristic of the parent atom. However, they do show chemical shift effects precisely and can be used to identify differences in bond polarisation and oxidation states. The chemical shift effect, which results from interaction between core and valence levels in a given atom, can be correlated with differences in valence electron density. The valence electron density depends on the bonding of an atom with a more electronegative or electropositive partner, which causes a change in the nuclear binding energy of all the electrons.

Quantitative analysis is less reliable because signal intensity from a given element is determined not only by concentration but also by factors such as the physical state of the sample and the orbital from which photoemission occurs. Nevertheless, for solids XPS can often give a reasonable quantitative estimate of surface composition and of change in composition with depth beneath the surface.[5, 15]

Auger electron spectroscopy,[5, 14, 15] like XPS, provides useful information in elemental analysis. Auger electrons are emitted when, after photoionisation, the ion is left with an electron missing from one of the core levels. In this unstable and electronically excited ion, an electron from higher energy level may relax into the core hole, which simultaneously releases a quantum of energy. This energy may be radiated as a photon or may be transferred to another electron in the ion. If this energy gained by the electron is greater than its binding energy, it is ejected from the ion as an Auger electron (See Fig. 2.9). Auger electrons have kinetic energies independent of the ionising radiation and appear at different positions in the binding energy plot. These Auger electrons emitted have a characteristic binding energy for each element and are useful in the characterisation of materials.

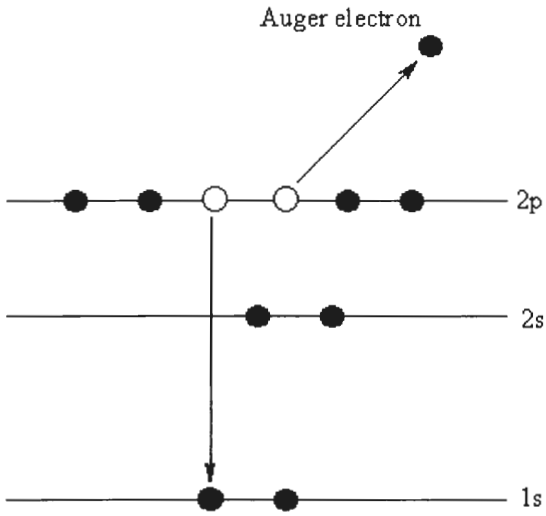

Figure 2.9 Schematic diagram showing the XPS Auger emission process.

2.6.2 Experimental Details

XPS was used to analyse the Cu-Schiff base-modified MCM 41 (see Chapter 6) and Si-MCM 41 materials synthesised in this work. For XPS analysis the samples were mounted on a stainless steel sample holder, using double-sided adhesive carbon tabs. A VG Scientific (East Grinstead, England) Escascope X-ray photoelectron spectrometer was used to acquire the data presented here using an MgKα X-ray source operating at 300 W (15 kV; 20 mA). The largest analysis area (*ca.* 4 mm × *ca.* 3 mm) was used to maximise the signal intensity. Wide-scan survey spectra, over the binding energy range 1000 - 0 eV, were acquired to identify the elements present, followed by higher resolution scans for the binding energy ranges of the elements identified from the wide-scans. The wide-scan spectra were obtained using an analyser pass energy of 50 eV, while high-resolution spectra of selected energy intervals were obtained using 30 eV pass energy. The C 1*s* peak from the adventitious hydrocarbon peak (this is the hydrocarbon peak always present in the XPS spectrum of a sample and can be used for charge correction), expected at 284.8 eV binding energy,[14] was used to correct binding energy for sample charging effects.[16] Quantification and peak fitting of the data were

performed using the VGS5250 software supplied with the spectrometer, based on the use of linear backgrounds beneath the peaks of interest and the quantification relative sensitivity factors supplied by the manufacturer.

Shallow take off angle analysis was performed by changing the angle between sample mounting with respect to the analyser input (below 90°), as shown in Fig 2.10. This technique enhances the surface selectivity of the analysis compared with the sample mounted at normal angle (0°). This effect can be used to estimate the depth of the layers in the surface. In this study, shallow take off angle analysis was used to explore the distribution of metal-Schiff base complex on the surface of MCM 41 material.

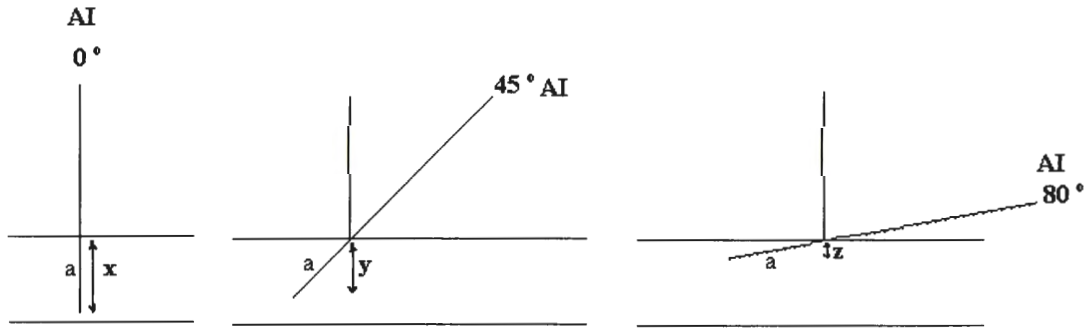

Figure 2.10 Schematic representation of shallow take off angle analysis, where AI is the position of analyser input at angle 0°, 45° and 80° and x, y and z are the distance from the sample surface from which the emitted electrons were analysed.

Argon ion etching is another technique used in XPS analysis. This technique involves using an argon ion beam to etch the surface of the sample so that analysis of the elements present below *ca.* 10 atomic distance of the original surface may be carried out. In this study, argon ion etching, at a rate of approximately 1 nm per minute for a total of 270 seconds, was used to examine the distribution of copper-Schiff base complex within the pores of the copper-Schiff base-modified MCM 41 materials. This corresponds to a total surface etching of *ca.* 4.5 nm depth from surface.

2.7 Transmission Electron Microscopy (TEM)

2.7.1 General

Transmission Electron Microscopy (TEM) is used extensively to investigate the ultra fine structure of the materials. TEM uses an electron beam, of wavelength between 0.0086 nm to 0.0025 nm, with accelerating voltages of 20 kV to 200 kV, respectively.

2.7.2 Experimental Details

The TEM analyses of both the Si-MCM 41 and modified MCM 41 materials were carried out at The Open University, using a JEOL 2000fx microscope operated at an accelerating voltage of 200 kV. The samples were suspended in ethanol and the suspension was deposited on a carbon grid for analysis.[18] Micrographs were taken using a standard, cut film TEM camera.

In this study, TEM was used to detect the hexagonal channels of the Si-MCM 41 material and to see the immobilised copper-Schiff base complex within the pores of the modified sample.

2.8 ^{57}Fe Mössbauer Spectroscopy

2.8.1 General

Mössbauer spectroscopy[6, 8] is a nuclear technique, which records transitions between energy levels within the nuclei of atoms. The technique involves measurements in the γ-ray region of the electromagnetic spectrum. It involves the absorption of the γ-rays by the sample under analysis, which are then emitted by an excited state nucleus when it returns to the ground state. A Geiger counter or scintillator counter can be used to detect the unabsorbed γ-rays. Fig. 2.11 shows the process schematically.

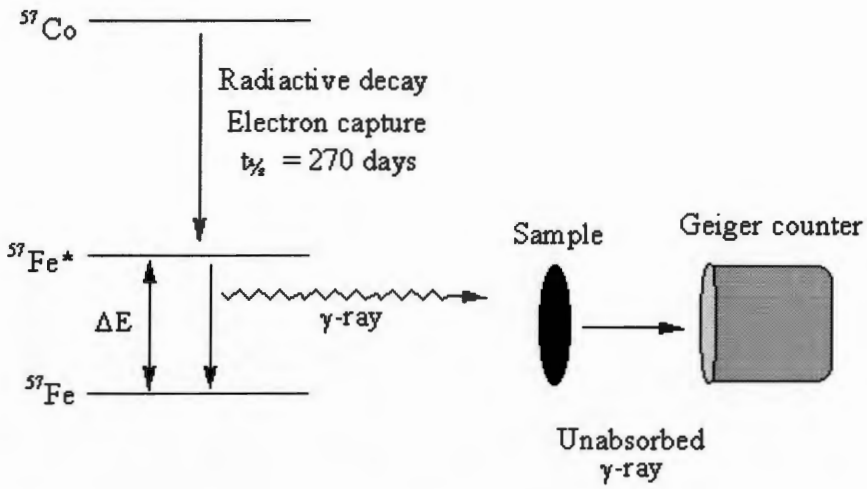

Figure 2.11 Energy level scheme showing generation of γ-rays by the decay of radioactive ^{57}Co and the absorption of γ-rays by the sample.

The absorption of γ-rays occurs only if the source material is moved relative to the sample. Therefore, the metal source (for γ-rays) is mounted on a coil through which an alternating current of a few cycles per second is passed so that the source oscillates back and forth. The sample specimen is left stationary to produce a Doppler shifting effect. The Geiger counter is used to detect unabsorbed γ-rays, where the data from each point of the source's movement are collected and summed over each cycle. The transitions due to absorbance of γ-rays are characterised by a change in the nuclear spin quantum number. The final spectrum is displayed as a plot of transmitted intensity (counts s^{-1}) of the Mössbauer γ-rays as a function of the relative velocity, v (mm s^{-1}).

Mössbauer analysis gives useful information about the valence state, coordination number and site symmetry of the observed nucleus in the material.[19] One of the greatest advantages of Mössbauer spectroscopy is that a particular source will detect only one element. Thus, for example in the analysis of iron, the spectrum will comprise contributions from each iron nucleus.[19] This permits quantitative

determination of the various iron environments present in the sample which is not possible from X-ray diffraction.

In this study, Mössbauer spectroscopy has been used to determine the valence state, its distribution (*i.e.* on a surface or in a crystal lattice) in the sample and the chemical environment(s) of iron nuclei present in the Fe-MCM 41 material.

2.8.2 Experimental Details

^{57}Fe Mössbauer spectra were measured at The Open University, at 298 K with a microprocessor controlled Mössbauer spectrometer using a *ca.* 25mCi (activity) ^{57}Co/Rh source. A Geiger detector was used for the measurement of unabsorbed γ-rays. The instrument was calibrated using a 25 mm natural iron standard. Isomer shift data are referenced to metallic iron.

2.9 Solid State Nuclear Magnetic Resonance Spectroscopy

2.9.1 General

Nuclear Magnetic Resonance (NMR)[20 - 24] is a powerful technique for investigating the structures, the motions, and the reaction of molecules. In principle, NMR can be used to investigate any isotope, which has a nucleus with non-zero nuclear spin quantum number. The nuclear spin is specified by quantum number, I (I = 1/2, 1, 3/2, 5/2). Nuclei with high spin numbers have a quadrupole moment, which leads to quadrupolar broadening of the absorption lines, which can often be severe.

In NMR, a strong and homogeneous magnetic field is used to split the degeneracy of the nuclear spin energy states, and then the sample is irradiated with radio frequency to cause the transitions between them (See Fig. 2.12).

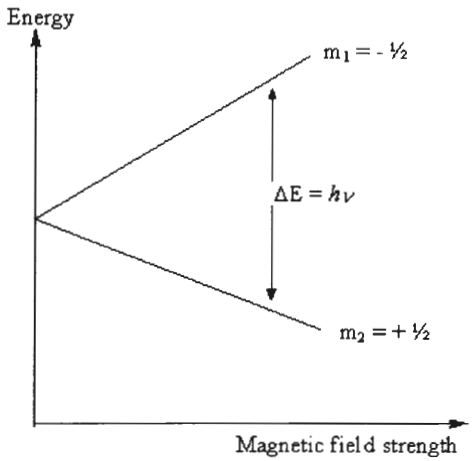

Figure 2.12 A schematic representation for the behaviour of the nuclear magnetic moment (m_1 *and* m_2) of a nucleus with spin $I = ½$ in an applied magnetic field.

2.9.2 Magic Angle Spinning Nuclear Magnetic Resonance (MAS NMR) Spectroscopy

In solids, the chemical shift anisotropy and the intermolecular interactions between the nuclear magnetic dipoles in addition to the interaction between them and external field, result in line broadening. As a consequence the information about chemical shifts and spin-spin coupling is often lost. The variation in the local magnetic field, ΔB, resulting from interaction between two nuclear magnetic moments separated by a distance, r, oriented at an angle, θ, to the direction of applied magnetic field, B_o, is given by equation 2.6.[20, 21]

$$\Delta B = \pm 3/2\, \mu\, (3\cos^2\theta - 1)\, r^{-3}\, \mu_o/4\pi \qquad \textit{Equation } 2.6$$

where μ_o is the permeability in free space.

In liquids, the factor $3\cos^2\theta$ -1 is zero. This normally gives sharp peaks with reasonable intensity. However, in solids, the dipolar interaction and chemical shift anisotropy between nuclei can be removed, when $\theta = 54^\circ\, 44'$ in equation 2.6. Spinning the sample around an axis that forms an angle β of $54^\circ\, 44'$ with the applied magnetic field multiplies these interactions by $(3\cos^2\beta - 1)$. When $\cos^2 54^\circ\, 44' = 1/3$ this term

becomes zero in equation 2.6. Thus, the rotation of sample at an angle 54° 44′, so called "magic angle", minimises the sources of line broadening and improves the resolution of spectra; the technique is called Magic Angle Spinning NMR spectroscopy.[23, 24]

2.9.3 Cross-polarization MAS NMR (CP MAS NMR) Spectroscopy

This technique is useful in the observation of less sensitive nuclei, such as ^{13}C in solids. These less sensitive nuclei are called 'rare spins' and are often surrounded by 'abundant spin nuclei' of high sensitivity, for example ^{1}H for organic solids. Both the spin systems are coupled by dipolar interaction. This technique involves the polarisation of 'rare spin nuclei' by spin order transfer from the 'abundant spins nuclei'. The resonance observed is by simultaneous decoupling of the 'abundant spins nuclei', to remove dipolar line broadening in NMR spectrum.[20] The technique is very useful in distinguishing two different carbon resonances in the spectrum when the chemical shift difference between them is small.

The nuclear properties of ^{29}Si is shown in Table 2.3.

Table 2.3 Nuclear properties of ^{29}Si and ^{13}C

Isotope	Abundance / %	Spin (I)	Magnetic moment (μ) / nuclear magnetons	NMR frequency / MH_z at field of 1 T
^{29}Si	4.7	½	-0.5548	8.460
^{13}C	1.1	½	0.7022	10.705

T = Tesla

2.9.4 ^{29}Silicon NMR Spectroscopy

Silicon-29[3, 22, 24] is the only naturally occurring isotope of silicon which has a spin quantum number, I = ½. It has a natural abundance of 4.7 %. The ^{29}Si nuclei have long spin-lattice relaxation times often more than 20 s, which makes recording of the

spectrum time consuming. The presence of a small amount, *ca.* 0.01 %, of a relaxation agent such as a metal compound can shorten the relaxation time.[22, 24]

The chemical shifts observed in a ^{29}Silicon MAS NMR spectrum gives information about the nature of SiO_4 tetrahedra in a silicate lattice *i.e.* isolated SiO_4 tetrahedra and SiO_4 tetrahedra joined through corner oxygen atoms, to either one, two, three or four other tetrahedral. Each silicon atom is usually assigned a 'Q value', ranging from zero to four, which represents the number of adjacent tetrahedra to which it is directly bonded. For each Q value, a characteristic range of chemical shift is observed in the spectrum allowing the identification of silicon environment present in the sample. The relative positions of these chemical shifts as a function of Q are shown in Fig. 2.13.[3, 25] The ^{29}Si chemical shift values for various silicon environments are found to be in the range of δ = -55 to -120 ppm with respect to TMS for silicates.

Q^0	Q^1	Q^2	Q^3	Q^4
O^- $^-O\ Si\ O^-$ O^-	O^- $^-O\ Si\ O^-$ O Si	Si O $^-O\ Si\ O^-$ O Si	Si O $Si\ O\ Si\ O^-$ O Si	Si O $Si\ O\ Si\ O\ Si$ O Si

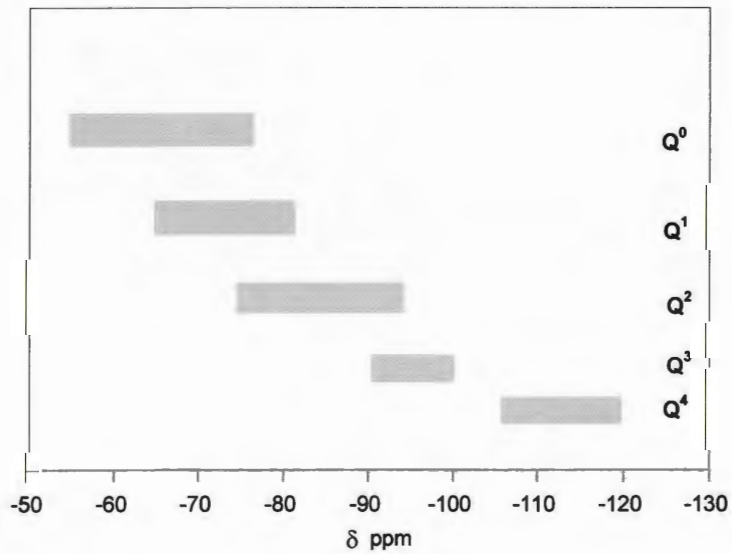

Figure 2.13 ^{29}Si chemical shift as a function of Q.

In the case of organically modified silicas, the chemical shifts are also influenced by the organic function attached to the silicon atom. In this case the silicons, attached to the organic function R, are described by "T-values" where $T^m = RSi(OSi)_mOH_{3-m}$ (m = 1-3).[3, 25] These T values also have a range of chemical shifts by which they can be recognised in a ^{29}Si spectrum, thus providing a means of determining functional-group incorporation in the material.

In this study, NMR spectroscopy was used to characterize framework and non-framework silicon atoms in modified MCM 41 materials. The materials modified with organic moieties and metal-Schiff base functions were expected to show the presence of two different types of silicon (*i.e.* framework and non-framework).

2.9.5 ^{13}C NMR Spectroscopy

Carbon-13[22, 24] is the only isotope of carbon which possesses a nuclear spin quantum number, $I = ½$, and can be studied by NMR spectroscopy. It has a natural abundance of 1.1 %. The low natural abundance, large relaxation times and poor natural sensitivity of ^{13}C nuclei, makes NMR spectroscopy analysis difficult. However, this can be offset by using a large sample size, high magnetic field and high radio frequency to increase the sensitivity for NMR analysis. The chemical shift range for ^{13}C nuclei is very wide (extends up to *ca.* 350 ppm) and the values of chemical shift are very sensitive to slight changes in the electronic environment of the carbon atom. In this study, Carbon-13 NMR Spectroscopy was used for the characterization of organically-modified MCM 41 materials.

Table 2.4

Sample	*p*-XRD	IR	AAS	XPS	TEM	Mössbauer	TGA	U/Visible	NMR
Si-MCM 41	✓	✓		✓	✓				✓
Ms-MCM 41	✓								
Fe-MCM 41									
i) Sol-gel synthesis	✓	✓				✓			
ii) Grafted	✓	✓				✓			
Ti-MCM 41									
i) Sol-gel synthesis	✓	✓							
ii) Grafted	✓	✓							
Organically-modified MCM 41 (Sol-gel synthesis)	✓								
Organically-modified MCM 41									
i) Aminopropyl-modified	✓	✓							✓
ii) Schiff base-modified	✓	✓							✓
iii) Azodye-modified	✓	✓							✓
iv) Metal-Schiff base-modified	✓	✓	✓	✓	✓	✓			✓

PART B

Sorption Studies

2.10 General

The term *adsorption* was introduced by Kayser[26] in 1881 to describe the condensation of gas on a free surface of powdered solids, either by capillary condensation or by surface adsorption. It is classified into two types, *physisorption,* and *chemisorption. Physisorption* involves weak forces, such as Van der Waals and hydrogen bonding and occurs in gas-solid systems. It can involve multilayer formation and in some ways resembles the condensation of a gas, whereas, *chemisorption* involves chemical bond formation, limited to certain systems and is confined to monolayer formation. The term *desorption* describes the depletion, *i.e.* negative adsorption, of the adsorbed gas from the surface of a solid. In 1909, McBain[27] used the term *sorption*, which describes the adsorption of a gas on a solid surface and its depletion from the solid.

A porous solid, when exposed to a gas in a closed space, can take up large volumes of a condensable gas. The amount of gas (*the adsorptive*) taken up by a solid (*the adsorbent*) is dependent on the mass and the nature of sample, as well as on the nature, adsorption temperature (T) and the pressure (p) of a gas. The quantity of gas, n, which is normally expressed in moles per gram of solid, is given by equation 2.7.[28]

$$n = f(p, T, \text{gas, solid}) \qquad \textit{Equation } 2.7$$

For a specific solid and gas at a fixed temperature the equation takes the form:

$$n = f(p)_{\text{T, gas, solid}} \qquad \textit{Equation } 2.8$$

This equation is an expression of the adsorption isotherm, which is the relationship at constant temperature between the amount of gas adsorbed by a solid and the pressure or the relative pressure, p/p^o, (p^o is the saturation vapour pressure of

adsorptive at the experimental temperature) of the adsorbate (adsorptive upon adsorption on adsorbent).[28]

IUPAC classifies sorption isotherms into six types, as shown in Fig. 2.14.[28] The five types of isotherm, Type I to Type V, in the classification were given by Brunauer, Demming, Demming and Teller (BDDT)[29] and are also referred to as the Brunauer, Emmett and Teller (BET) classification.[30] The sixth stepped isotherm, which is rarely observed, shows multilayer adsorption on a solid surface. In this study, Type I, Type IV and Type V isotherms are of particular interest, and are discussed briefly in Sections 2.10.1 to 2.10.3.

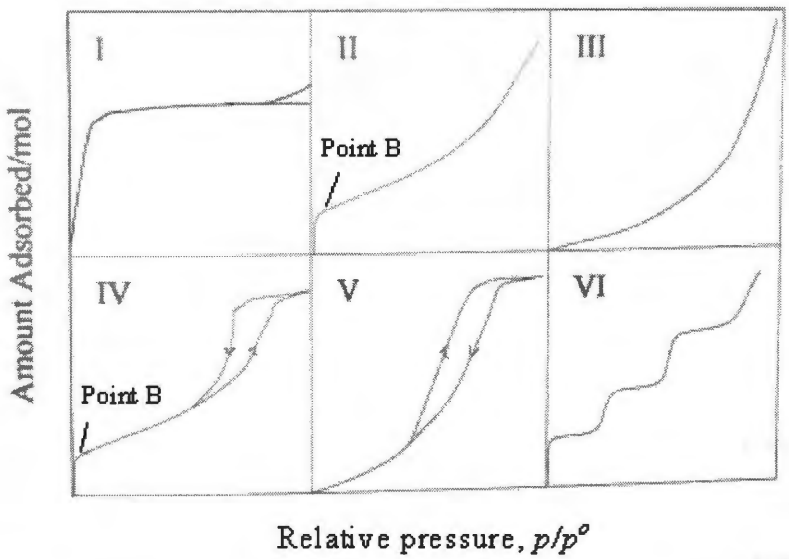

Figure 2.14 The five types of adsorption isotherms (Type I to Type V) given by BDDT together with Type VI, the stepped isotherm.[28]

Table 2.5 The characteristics described by the BDDT isotherm classification

Isotherm Type	Main pore characteristics
I	Microporous, or non-porous chemisorbed monolayer
II	Mainly non-porous or macroporous, but could still have some micropores
III	Characteristics of weak interaction between non-porous adsorbent and adsorptive
IV	Characteristic of mesoporous solids
V	Characteristic of weak adsorbent-adsorbate interaction on mesoporous solids
VI	Very rare-shows stepwise multilayer adsorption on a surface

The sorption of a number of gases and vapours was used to characterise the surface properties of the Si-MCM 41 and the modified-MCM 41 materials synthesised in the current work. The most useful information obtained from the adsorption isotherms are the surface area, the pore diameter and the pore volume of a material. However, different adsorbates for example water, methanol, *n*-hexane, on a same sample also give an indication of the nature of the interactions between the adsorptives and the adsorbent. The most commonly used sorptive for surface area determination is nitrogen at 77 K.

2.10.1 The Type I Isotherm

Type I isotherms are characteristics of microporous solids. The isotherm is characterised by a steep region at low relative pressure followed by a plateau at a limiting value of pressure. Microporous solids show enhanced adsorption at low relative pressure, as the narrowness of the pores causes the potential fields from neighbouring pore walls to interact to cause a distortion of the isotherm. According to the "classical"[31] view the limiting value at high p/p^o arises because the pores are so narrow that they

cannot accommodate more than a single molecular layer on their walls. The Type I isotherm was therefore assumed to conform to the Langmuir equation[31] (equation 2.9).

$$\frac{n}{n_m} = \frac{Bp}{1+Bp} \qquad \textit{Equation} \quad 2.9$$

where n is the amount adsorbed, n_m the monolayer amount, p is the pressure and

$$B = \frac{a_1 \kappa}{z_m v_1} e^{q_1/RT} \qquad \textit{Equation} \quad 2.10$$

where a_1 is the condensation coefficient (*i.e.* the fraction of incident molecules which actually adsorb), z_m is the number of absorption sites per unit area, v_1 is the frequency of oscillation of the molecule in a direction normal to the surface, q_1 is the isostearic heat of adsorption and κ is a constant given by the kinetic theory of gases, $\{\kappa = 0.5L/(MRT)^{1/2}\}$. In practice, B is a constant, which cannot be resolved experimentally *via* equation 2.10.

However, if relative pressure, p/p^o, is used in equation 2.9 instead of pressure, p, the equation takes a form:

$$\frac{n}{n_m} = \frac{c(p/p^o)}{1+c(p/p^o)} \qquad \textit{Equation} \quad 2.11$$

where c is the BET constant. Equation 2.11 may be written in a linear form (equation 2.12), and a plot of $(p/p^o)/n$ against p/p^o (BET plot) should yield a straight line with a slope of $1/n_m$.

$$\frac{p/p^o}{n} = \frac{1}{cn_m} + \frac{p/p^o}{n_m} \qquad \textit{Equation} \; 2.12$$

It is therefore possible to calculate the monolayer capacity, n_m, (from equation 2.12) of the solid from Type I isotherm, which when substituted in equation 2.13, yields specific surface, S_{sp}, area of a solid.

According to the postulate put forward by Pierce, Wiley and Smith[32] and, by Dubinin[33], the mechanism of adsorption in microporous solids is a pore filling process rather than a layer-by-layer build up of adsorbate on the pore walls. Thus, the uptake of adsorptive at saturation, n_p, may be used in equation 2.20 to determine the pore volume of an adsorbent

2.10.2 The Type IV Isotherm

The Type IV isotherm is characteristic of mesoporous solids. The mesopore range of the pore size is usually taken to be that range, which gives rise to a Type IV isotherm. The isotherm displays a region of steep adsorption at low relative pressure, which then plateaus and produces a sharp "knee", called Point B (see Section 2.10.5), which represents monolayer coverage of surface. The sharp 'knee' present in the isotherm represents monolayer formation and allows us to calculate the specific surface area, S_{sp} (m^2 g^{-1}). The second steep region in the isotherm represents the capillary condensation within the mesopores and is characteristic of mesoporous solids and is often accompanied by hysteresis. The shape of the hysteresis loop is used in the calculation of the pore diameter and also gives information about the shape of the pores present in the system. The final plateau of the isotherm at saturation pressure represents complete filling of the pores by liquid adsorptive and is used to determine the total pore volume, V_p (cm^3 g^{-1}) (Gurvitsch[34] volume) of the porous solid.

The hysteresis observed is a result of the formation, upon adsorption, of a meniscus from which a desorption will occur at relative pressures below those at which it is formed *i.e.* in each hysteresis loop the amount adsorbed on the adsorption branch at a particular relative pressure is always less than the adsorbed amount on the desorption branch at the same relative pressure. According to IUPAC, hysteresis loops are classified into four different types, designated as H1, H2, H3 and H4, as shown in

Fig. 2.15. Type H1 hysteresis is obtained from agglomerates or hexagonal pores of fairly uniform size and array. Type H2 hysteresis is associated with corpuscular systems, whereas Types H3 and H4 are shown by adsorbents with slit-shaped pores or plate like particles.[28] An interesting feature of the nitrogen isotherms determined for the MCM 41 materials at 77 K is the absence of hysteresis. The possible reason for this may be that the materials synthesised have pores closer to the microporous range (pores smaller than *ca.* 30 Å). The MCM 41 materials synthesised with large pores (greater than *ca.* 30 Å) do show the hysteresis.

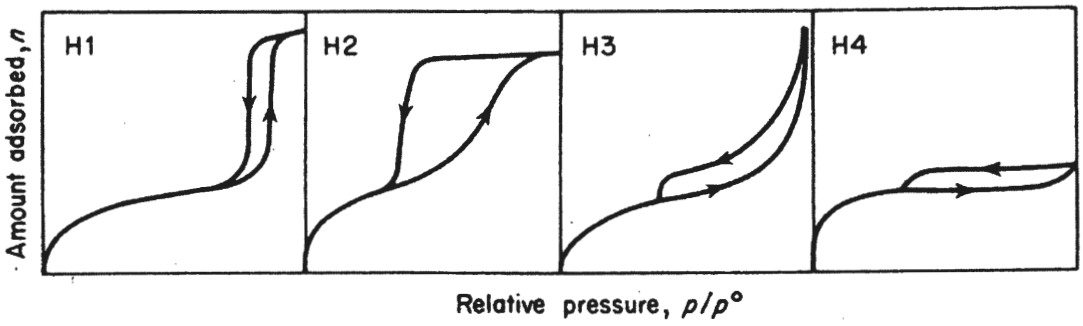

Figure 2.15 Types of hysteresis classified by IUPAC.[28]

2.10.3 The Type V Isotherm

The Type V isotherm is characteristic of weak adsorbate-adsorbent interaction, for example sorption of water on a hydrophobic porous surface. The isotherm is convex at low relative pressure due to the low uptake of adsorptive, followed by a point of inflection at high relative pressure (greater than *ca.* 0.5 p/p^o) arising from capillary condensation in mesopores and accompanying hysteresis. The isotherms do not show a distinct sharp 'knee' (Point B), thus, cannot be used to determine surface areas, but are useful in monitoring other surface characteristics such as the hydrophobic properties of a surface.

2.10.4 Determination of specific surface area

Three key types of information can be obtained from N_2 sorption at 77 K. These are the monolayer capacity of solid, n_m, the pore diameter, D, and the pore volume, V_p. The monolayer capacity of a solid, n_m (mol g^{-1}) is defined as the amount of gas that can be accommodated by a single molecular layer on the surface of one gram of a solid and is used to calculate the specific surface area, S_{sp}, (m^2 g^{-1}) of the solid. Equation 2.13 is used to calculate the surface area

$$S_{sp} = n_m L a_m \qquad \textit{Equation} \quad 2.13$$

where a_m is the cross sectional area of a liquid adsorbate molecule (16.2 $Å^2$ for nitrogen and 17.0 $Å^2$ for CO_2),[28, 35, 36] and L is the Avogadro constant.

Calculation of a_m (Equation 2.14) may be achieved by considering the density of the bulk liquid. This method, originally proposed by Emmett and Brunauer,[37] assumes that the molecules are arranged in the same manner when adsorbed on the surface, as they would be if placed on a plane surface within the bulk liquid *i.e.* in a close-packing arrangement

$$a_m = f(M/\rho L)^{2/3} \qquad \textit{Equation } 2.14$$

where f is a packing factor (1.091 for 12 nearest neighbours in the bulk liquid and six on the plane surface),[37] M is the molar mass, and ρ is the density of the adsorptive at the experimental temperature.

There are two methods to determine the value of n_m:

- The Point B method (Section 2.10.5)
- The BET model (Section 2.10.6)

2.10.5 Point B Method

The Type II and Type IV isotherms obtained experimentally show a sharp 'knee' at low relative pressure. The point in an isotherm, at which the curve tends to become linear after the sharp 'knee', was termed by Emmett and Brunauer[37] as "Point B" (see Fig. 2.14).[28, 38] The amount adsorbed at "Point B" in the isotherm, termed as n_B, is assumed to correspond to the completion of a monolayer on solid surface. The value of n_B may be substituted for n_m in equation 2.13 for the calculation of surface area.

2.10.6 BET Model

In isotherms with no distinct sharp 'knee', where the location of "Point B" becomes difficult, the BET model[28] may be used for calculating the monolayer capacity *i.e.* in most of the cases this is the preferred method for determing the monolayer capacity.

The equation most commonly used to describe multilayer adsorption is the BET equation (equation 2.14), formulated from the Langmuir equation[31] by Brunauer Emmett and Teller.[30] The BET equation was derived kinetically for a state of dynamic equilibrium, where the rate at which molecules condense from the gas phase onto the surface is equal to the rate at which molecules evaporate from the occupied sites. The equation (2.15) is shown below in its linear form:

$$\frac{p/p^o}{n(1-p/p^o)} = \frac{1}{n_m c} + \frac{c-1}{n_m c}\frac{p}{p^o} \qquad \textit{Equation } 2.15$$

where n is the amount adsorbed at equilibrium pressure p, p^o is the saturation vapour pressure at the experimental temperature, n_m is the monolayer capacity and c is the BET parameter, which is related to the net heat of adsorption, (q_1 = heat of adsorption in the first layer, q_L = heat of adsorption in subsequent layers), as shown in equation 2.16.

$$c = e^{(q_1 - q_L)R/T} \qquad \textit{Equation } 2.16$$

Plotting $(p/p^o) / n(1-p/p^o)$ against p/p^o should give a straight line with a slope, $(c-1/n_mc)$ and an intercept, $(1/n_mc)$. Thus, the monolayer capacity can be calculated from the relationship, $n_m=1/(slope+intercept)$. A BET analysis is generally considered applicable in the range of $0.05 \leq p/p^o \leq 0.30$ and is most accurate for Type II and Type IV isotherms. In this work, the BET model has been used for calculation of n_m. Specific surface areas in this work were determined using the BET model in the range $0.04 \geq p/p^o \geq 0.20$.

2.10.7 Pore Diameter

There are several methods to determine the pore size distribution of materials with cylindrical shaped pores. These are based on geometrical considerations, thermodynamics or a statistical thermodynamic approach. The traditional method for analysing pore size distribution in the mesopore range is the BJH (Barrett, Joyner, Halard) method, which is based on the Kelvin equation[39] (Equation 2.17)[28]

$$\ln\frac{p}{p^o} = \frac{-2\gamma V_L}{RTr_m}\cos\phi \qquad \textit{Equation} \quad 2.17$$

where p/p^o is the relative pressure of the vapour in equilibrium with a meniscus of radius of curvature, r_m, at temperature, T (K), γ is the surface tension of liquid adsorptive and V_L is the molar volume of the adsorbate in liquid form, and R is the gas constant.

Therefore, by applying the Kelvin equation at the inception of the hysteresis loop, the minimum pore radius in which capillary condensation can occur can be calculated. The usual pore diameter range between which capillary condensation occurs is 10 – 250 Å, and this is the range over which the Kelvin equation may be applied. Thus, by applying the Kelvin equation, the radius of curvature of the meniscus, r_m, can be calculated, which is related to the core pore radius of the material by equation 2.18

$$r = r_m + t \qquad \textit{Equation } 2.18$$

where t (Å), the thickness of the adsorbed film, is calculated from equation 2.19

$$t = (n/n_m)\sigma_t \qquad \textit{Equation } 2.19$$

where n is the amount of gas adsorbed at relative pressure, p/p^o, n_m is the monolayer capacity, and σ_t, is the thickness of each layer, allowing for close packing.

Another method employed to calculate the pore diameter is based on the simple relation between the surface area (BET derived), S_{sp}, and the pore volume, V_p, for cylindrical pores and is given by equation 2.20

$$D = \frac{4V_p}{S_{sp}} \qquad \textit{Equation } 2.20$$

The pore diameters calculated for the materials synthesised in the current work are based on these methods.

2.10.8 Pore volume

The final plateau in the Type IV and the Type I isotherms represents the complete filling of the pores by liquid adsorbate. Thus, the amount of liquid adsorbed in the pores can be calculated. The total pore volume, termed as the Gurvitsch pore volume, can be calculated from equation 2.21[3, 28, 38]

$$V_p = \frac{n_p M_w}{\rho} \qquad \textit{Equation } 2.21$$

where n_p is the limiting adsorption value obtained by extrapolation of the final plateau of isotherm to $p/p^o = 1$, M_w is the molar mass of the adsorbate, and ρ is the density of the liquid adsorbate. Thus the volume, V_p, is expected to be the same for all condensed sorptives on a particular solid provided that there are no packing effects or restricted

access to the pore space, as might be found in some narrow pore systems. The Gurvitsch rule is generally valid within a few percent for those systems yielding Type IV isotherms, but its accuracy is limited by the ease with which the plateau can be located.

2.10.9 α_s-Plots

The α_s-Plot was devised by Sing[28] and is used to detect microporosity and/or the mesoporosity present in the material. In an α_s-plot, the shape of the isotherm under test is plotted against a chemically equivalent non-porous reference (in this case hydroxylated silica was used). Sing observed that it was sufficient to take the amount adsorbed at some fixed relative pressure (n_s), in practice taken as $(p/p^o)_s = 0.4$, as the normalized factor. Thus, the α_s-plot is a plot of the amount of gas adsorbed for the test sample against α_s ($n/n_{0.4}$) obtained from the isotherm on a reference sample. If the plot is straight line passing through the origin, this suggests that the sample under test differs only in surface area and not in porosity. Mesoporosity and micrporosity present in the sample are denoted by deviation from linearity. The plot can also provide information on the micropore and the mesopore volumes of a material.

2.11 Experimental Details: Volumetric Sorption

Volumetric sorption of nitrogen (77 K) and carbon dioxide (195 K, 273 K and 286 K) were carried out using a fully automated and computer controlled Micromertics Tristar 3000 gas adsorption analyser. The analyser contains three ports for simultaneous analysis of three samples. For nitrogen sorption the sample tubes are immersed in a Dewar vessel of liquid nitrogen and are exposed to identical experimental conditions. For CO_2 sorption the sample tubes are immersed in an acetone-dry ice bath. The instrument uses a single rotary vacuum pump to achieve vacua < 20 μmHg at the instrument inlet. Sample masses as low as 0.1 g can be easily analysed. Prior to the

isotherm measurement the samples were degassed in a SmartPrep Degasser. The SmartPrep Degasser is a flowing-gas degassing unit in which samples may be heated to a maximum temperature of 673 K in the flow of nitrogen (50 cm^3/min) to remove moisture and other physisorbed contaminants without the use of a vacuum pump. The degasser has six heating stations so that six samples can be degassed simultaneously. The unmodified Si-MCM 41 samples were degassed at 423 K for 6 h, whereas, the modified MCM 41 samples (organically modified and metal-Schiff base modified MCM 41) were degassed at 373 K to minimise any possible decomposition of the samples.

Sorption data are displayed as an adsorption isotherm, which is a plot of the amount adsorbed (cm^3 g^{-1} (STP)) (y-axis) against the relative pressure (x-axis). Surface areas were obtained by the BET method. The BJH method and equation 2.20 were used to obtain the pore size distributions. Details of the two adsorptives used and their cross-sectional molecular areas [3, 35, 36, 38] are shown in Table 2.5.

Table 2.5 Sorptives, molecular area and temperatures of sorption measurment.[31, 32]

Adsorptive	**Molecular area a_m / Å^2**	**p^o, Saturated vapour pressure / mmHg**	**Temperature / K**
Nitrogen	16.2	760	77
Carbon dioxide	17.0	760 919	195 273

2.12 Experimental Details: Gravimetric Sorption

The conventional McBain and Bakr[40] method was used for gravimetric sorption of vapours (listed in Table 2.6) at 303 K. The system shown in Fig 2.16, designed and built in-house by Branton,[38] was constructed from Pyrex tubing and vacuum-seated Pyrex stopcocks.[3, 24, 40]

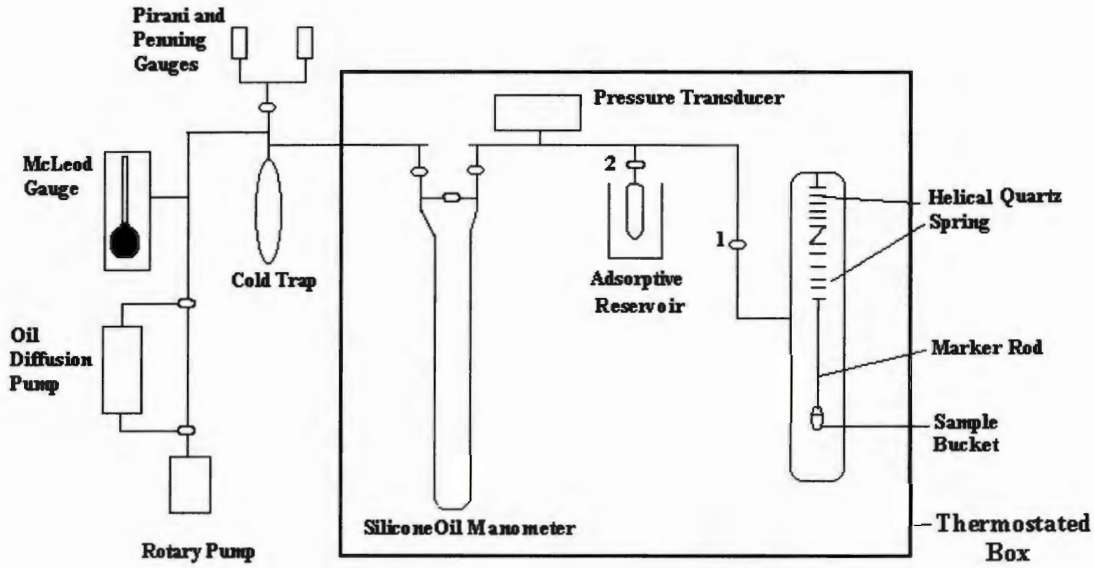

Figure 2.16 Schematic diagram of gravimetric sorption balance

The balance mechanism consisted of two calibrated helical quartz springs (connected in series to increase the sensitivity) suspended from a hook and the sample, housed in a silica bucket, was suspended from the spring *via* a series of silica rods. One of these rods, the marker rod, contained two blue glass reference markers. The spring along with the sample bucket was mounted in a condenser (to maintain their calibration), which was connected to the vacuum line.

The spring extension was monitored by a rack and pinion-type microscope, which was focused on the tip of one of the blue marker rods. The microscope was graduated to 0.01 microscope units. The sorptive pressure was measured using a silicone oil manometer and a pressure transducer. The pumping system consisted of a

water-cooled oil diffusion pump and a two-stage rotary pump. Pirani and Penninig gauges and a McLeod gauge were used to monitor the vacuum pressure. The adsorptive, contained in a pyrex reservoir, was located between the sample condenser and the silicone oil manometer. The temperature of the adsorptive was controlled by water and ice in a Dewar to achieve the required vapour pressure. The vacuum line, sample and reservoir were housed in a thermostatic box, where the temperature was maintained at 303 K by two thermistor-controlled carbon filament bulbs and an air-circulating fan.

2.12.1 Sample Degassing

It is necessary to remove any physisorbed water and volatile contaminants from the surface and the pores of a sample before analysis. This was done by heating the sample in a tube furnace under a reduced pressure $< 1 \times 10^{-5}$ torr. The temperatures used for degassing were similar to those used in volumetric analysis (see Section 2.11)[41] The low degassing temperature for the modified samples was used to minimise any possible decomposition of organic compounds.

2.12.2 Adsorptive Degassing

Analar grade adsorptive was loaded into a glass reservoir together with a plug of glass wool to prevent the cracking of the reservoir upon freezing in liquid nitrogen. In order to remove the dissolved gasses, the adsorptive was exposed to three "freeze-pump-thaw" cycles. This was done by first freezing the adsorptive in the reservoir using liquid nitrogen. The dissolved gases were then removed by opening the reservoir to the vacuum line. Following evacuation the reservoir was isolated and allowed to return to room temperature. The procedure was repeated twice more to ensure the complete removal of any dissolved gasses. The sorptives used in this work at 303 K are

summarized in Table 2.6 (Section 2.12.4) along with their cross-sectional molecular areas and saturated vapor pressures.

2.12.3 Calibration of the Spring

The calibration of the spring was carried out using the same procedure as described by other workers.[3, 38] The spring was calibrated under vacuum at 303 K by suspending a silica bucket containing aluminium beads of known mass. As the mass was increased the extension of spring was monitored by means of the rack and pinion type microscope, fitted with screw micrometer eyepiece focused on the tip of one of the blue reference markers. A plot (Appendix A-1) of spring extension against mass indicated the spring response to be linear and reversible with a sensitivity of 32.00 microscope units g^{-1}.

2.12.4 Isotherm Measurment

The system was evacuated to a reduced pressure of $< 10^{-5}$ torr and the thermostat box was maintained at 303 K. The adsorbate (sample) and adsorptive were degassed as described in Sections 2.12.1 and 2.12.2, respectively. The vapour pressure of the adsorptive was controlled by regulating the water temperature in a Dewar vessel surrounding the reservoir. Prior to adsorption, the microscope reading of the position of the blue reference marker was noted. The sample was isolated by closing tap 1 (Fig. 2.16) and the adsorptive reservoir was open to the transducer and silicone oil manometer *via* Tap 2 (Fig. 2.16), and the vapour pressure was noted. Tap 1 was then opened to expose the sample to the vapour. The change in both the pressure readings (pressure transducer and silicon oil manometer) and the extension of the spring (due to the increase in mass of the sample by adsorption) were closely monitored until the system reached equilibrium. Equilibrium was defined as the point at which no further

change in either pressure or spring extension was observed. Depending upon the type of adsorbent and adsorptive, equilibrium was reached in 0.5 to 24 h. A series of adsorption points was measured at increasing values of equilibrated relative pressures up to $p/p^o = 1$. Desorption points were obtained by exposing the sample to reduced vapour pressure (achieved by lowering the temperature of the reservoir). The adsorbate was allowed to desorb and equilibrate whilst open to the reservoir. Final equilibrium was achieved by isolating the sample from the reservoir. Calculation of the amount adsorbed, *n*/mol, was achieved using equation 2.22.

$$n = \delta / kM \qquad \textit{Equation} \quad 2.22$$

where δ is the spring extension, k is the sensitivity of the spring (32.00 microscope units g^{-1}) and M is the molar mass of the adsorptive.

Isotherms are presented as a plot of amount adsorbed (mmol g^{-1}) against relative pressure, p/p^o. The p^o (saturation vapour pressure) of water at 303 K measured *in-situ* was consistent with the literature value (38.4 mb).[35] The p^o value (at 303 K) for other adsorptives measured *in-situ* are summarised in Table 2.6.

Table 2.6 Sorptives, their molecular areas and saturated vapor pressures

Adsorptive	**Molecular area a_m† / Å^2**	**Saturated vapor pressure at 303 K, p^o/ mb**
Water	10.5	38.4*
1-Hexene	38.3	294.6
3,3-Dimethy-1-butene	39.0	666.5
Methanol	18.0	174.6
n-Butanol	31.0	11.6
t-Butanol	31.9	62.7
n-Hexane	39.3	211.3

† Molecular area (a_m) calculated from liquid density (ρ_L) using the equation[3] $a_m = (M/\rho_L L)^{2/3} \times 10^{16}$, where M is the molar mass (g mol^{-1}) and L is the Avagadro number. * References 35, 36

Table 2.7

Sample	Volumetric Sorption		Gravimetric Sorption						
	N_2	CO_2	H_2O	MeOH	*n*-BuOH	*t*-BuOH	n-hexane	1-hexene	3-3,dimethyl-1-butene
Si-MCM 41	✓	✓	✓	✓	✓	✓	✓	✓	✓
Ms-MCM 41	✓	✓							
Fe-MCM 41									
i) Sol-gel synthesis	✓	✓							
ii) Grafted	✓	✓							
Ti-MCM 41									
i) Sol-gel synthesis	✓	✓							
ii) Grafted	✓	✓							
Ru-MCM 41	✓							✓	✓
Organically-modified MCM 41									
i) Aminopropyl-modified	✓	✓							
ii) Schiff base-modified	✓	✓							
iii) Azodye-modified	✓								
iv) Metal-Schiff base - modified	✓	✓	✓	✓	✓	✓	✓	✓	✓

2.13 References

1. U. Ciesla and F. Schuth, *Micropor. Mesopor. Mater.*, 1999, **27**, 131.
2. P. M. Price, J. H. Clark and D. J. Macquarrie, *J. Chem. Soc., Dalton Trans.*, 2000, 101.
3. C. M. Bambrough, *PhD Thesis*, The Open University, 1994.
4. M. T. Weller, *Inorganic Materials Chemistry*, Oxford Chemistry Primers, Volume 23, Oxford University Press, UK, 1994.
5. Science: A 3rd Level Course. S342 Physical Chemistry: Principles of Chemical Change. Chapter 6, The Open University Press, Milton Keynes, 1985.
6. S. Walker and H. Straw, "*Spectroscopy*" Volume Two, Chapman and Hall Ltd., London, 1962.
7. D. P. Shoemaker, C. W. Garland and J. W. Nibler, "*Experiments in Physical Chemistry*", 5th Edition, McGraw-Hill Book Company, USA, 1989.
8. R. S. Drago, "*Physical Methods in Chemistry*", Saunders College Publishing, USA, 1977.
9. F. Daniels and R. A. Alberty, "*Physical Chemistry*", 2nd Edition, John Wiley and Sons, USA, 1962.
10. K. Nakamoto, "*Infrared and Raman Spectra of Inorganic and Coordination Compounds*", 4th Edition, John Wiley and Sons, USA, 1986.
11. *"Instruction Manual EA 1110 Elemental Analyser"*, Carlo Erba (CE) Instruments, September 1998.
12. G. F. Kirkbright and S. Sargent, "*Atomic Absorption and Fluorescence Spectroscopy*", Academic Press, London, 1974.
13. E. Armengol, A. Corma, V. Fornés, H. García and J. Primo, *Appl. Catal. A: General*, 1999, **181,** 305.

14. J. F. Moulder, W. F. Stickle, P. E. Sobol and K. D. Bomben, *"Handbook of X-Ray Photoelectron Spectra: A Reference Book of Standard Spectra for Identification and Interpretation of XPS Data"*, ed. by J. Chastain, Perkin-Elmer Corporation, Eden Prairie, Minnesota, USA, 1992.

15. Science: A 3rd Level Course. S342 Physical Chemistry: Principles of Chemical Change. Chapter 5 and 6, The Open University Press, Milton Keynes, 1996.

16. H. L. Siew, M. H. Qiao, C. H. Chew, K. F. Mok, L. Chan and G. Q. Xu, *Appl. Surf. Sci.*, 2001, **173**, 95.

17. S. Myra, J. A. A. Crossley and M. W. Barsoum, *J. Phys. Chem. Solids,* 2001, **62**, 811.

18. S. Schacht, M. Janicke and F. Schüth, *Micropor. Mesopor. Mater.*, 1998, **22**, 485.

19. G. J. Long and F. Grandjean, "*Mössbauer and Spectroscopy Applied to Magnetism and Material Science*", Volume 2, Plenum Press, New York, 1996.

20. R. W. Gleason, "*NMR Spectroscopy: An Introduction*", John Wiley and Sons, New York, 1980.

21. M. L. Levitt, "*Spin Dynamics: Basics of Nuclear Magnetic Resonance*", John Wiley and Sons, England.

22. G. A. Webb, "*Annual Reports on NMR Spectroscopy*", Volume 9, Academic Press, London, 1979.

23. J. M. Emsley, J. Feeney and L. H. Sutcliffe, "*High Resolution Nuclear Magnetic Resonance Spectroscopy*", Volume 2, Pergamon Press, Oxford, 1996.

24. Science: A 3rd Level Course. S343 Inorganic Chemistry: Nuclear Magnetic Resonance Spectroscopy. Block 5, The Open University Press, Milton Keynes, 1989.

25. S. L. Brukett, S. D. Sims and S. Mann, *J. Chem. Soc., Chem. Commun.*, 1996, 1367.

26. H. Kayser, *Wied. Ann.*, 1881, **14**, 451.

27. J. W. McBain, *Z. Phys. Chem.*, 1909, **38**, 471.

28. S. J. Gregg and K. S. W. Sing, *"Adsorption, Surface Area and Porosity"*, 2nd Edition, Academic Press, London, 1982.

29. S. Brunauer, L. S. Demming, W. S. Demming and Teller, *J. Am. Chem. Soc.*, 1940, **62,** 1723.

30. S. Brunauer, P. H. Emmett and E. Teller, *J. Am. Chem. Soc.*, 1938, **60**, 309.

31. I. Langmuir, *J. Am. Chem. Soc.*, 1916, **39**, 2221.

32. C. Pierce, J. W. Wiley and R. N. Smith, *J. Phy. Chem.*, 1952, **56**, 733.

33. M. M. Dubinin and E. D. Zaverina, *Zhur. Fiz. Khim.*, 1949, **23**, 1129.

34. L. Gurvitsch, *J, Phys. Chem. Soc. Russ.*, 1915, **47**, 805.

35. D.R. Linde, "*CRC Handbook of Chemistry and Physics*", 73rd Edition, CRC press, 1992 - 1993.

36. A. M. James and M. P. Lord, "*Macmillan's Chemical and Physical data*", The Macmillan Press Ltd., London, 1992.

37. P. H. Emmet and S, Brunauer, *J. Am. Chem. Soc.*, 1937, **59**, 1553.

38. P.J. Branton, *PhD Thesis*, University of Exeter, 1994.

39. W. T. Thomson, *Phil. Mag.*, 1871, **42**, 448.

40. J.W. McBain and A. M. Bakr, *J. Am. Chem. Soc.,* 1926, **48**, 690.

41. C.M. Bambrough, R. C. T. Slade, R. T. Williams, S. L. Burkett, S. D. Sims and S. Mann, *J. Colloid and Interface Sci.*, 1998, **201**, 220.

CHAPTER 3

SILICEOUS-MCM 41 (Si-MCM 41)

3.1 Introduction

This Chapter concerns the synthesis of the siliceous-MCM 41 (Si-MCM 41) material, which was used as a starting material in the synthesis of the metal-functionalised MCM 41 (Chapter 4), organically-modified MCM 41 (Chapter 5) and metal-Schiff base modified MCM 41 materials (Chapter 6). The MCM 41 material synthesised with a larger pore size using mesitylene (1,3,5-trimethyl benzene) as a pore-swelling agent, is also described. The mesitylene-swollen MCM 41 material (Ms-MCM 41) was used for the functionalisation of the surface with large organic molecules, which causes pore narrowing/blocking in unswollen-MCM 41. In the current work Ms-MCM 41 was used as a starting material in the functionalisation with azodye (Chapter 5, Section 5.2.3).

The preliminary work involved the characterisation of the synthesised Si-MCM 41 material using standard techniques *p*-XRD, IR spectroscopy, NMR spectroscopy, CHN microanalysis and nitrogen sorption together with new techniques XPS, vapour sorption of organic molecules (methanol, butanol, *n*-hexane).

3.2 Synthesis

The MCM 41 materials were synthesised using ordered micelles of surfactant molecules, below the critical micelle concentration (CMC), as a template to array the inorganic species into a regular mesostructure. It has been proposed that the

spontaneous aggregation of surfactant molecules into liquid crystal hexagonal arrays is unlikely at the working concentration (below CMC) and that it is the addition of silicate ions that triggers the micelle formation[1, 2] through the electrostatic interaction between the positively charged surfactants and the negatively charged silicate species.[3, 4] The condensation and polymerisation of the siliceous framework takes place around the micelles resulting in the formation of organic/inorganic composites.

The synthesis of the materials, used in this work, was based on a procedure described by Schmidt *et al.*[6-a], Hohenesche *et al.*[6-b] and Bambrough.[7] The synthesis method uses an organic surfactant, namely cetyltrimetylammonium chloride (C_{18}TMACl), as a template and tetraethyl orthosilicate (TEOS) as a source of silica. Sodium hydroxide was used as a base catalyst for hydrolysis and condensation of TEOS. The flow diagram for the general synthesis of MCM 41 is shown in Fig. 3.1.

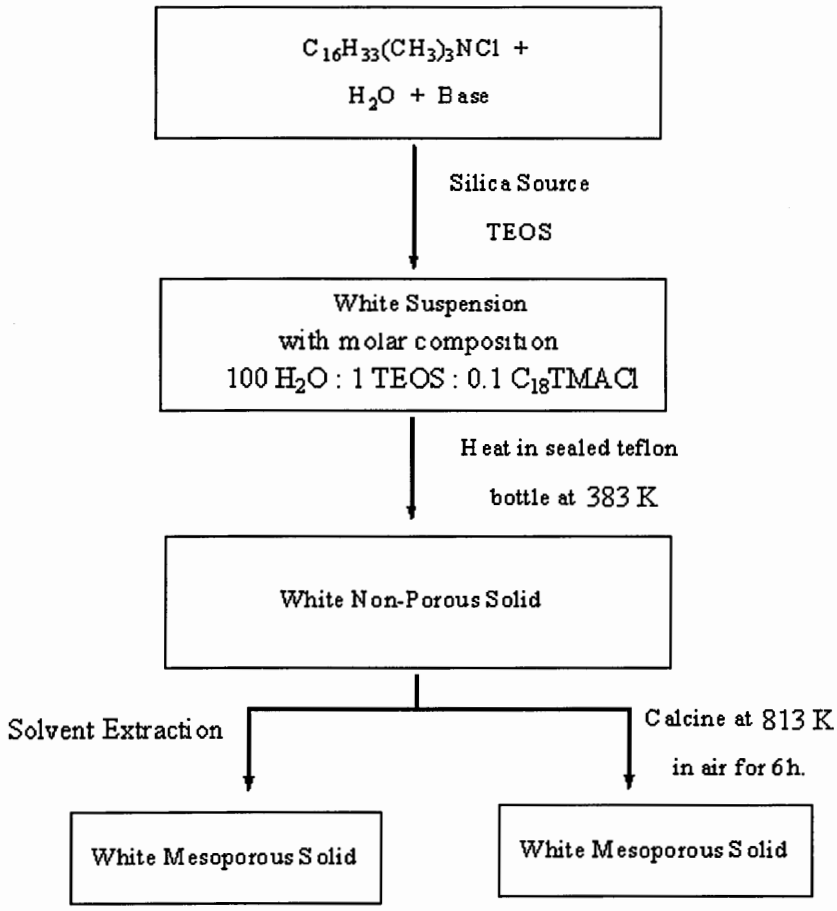

Figure 3.1 Flow diagram showing the general synthesis of the MCM 41 material.

3.2.1 Siliceous-MCM 41 (Si-MCM 41)

C_{18}TMACl (4.60 g, 3.80 mmol) was added to a solution of sodium hydroxide (0.70 g, 17.50 mmol) in a water (56 cm^3) and the resulting mixture was stirred for 10 min. TEOS (6.50 g, 32.10 mmol) was slowly added to the surfactant solution.[2, 8] The white suspension obtained was stirred for 48 h at room temperature and then transferred to a Teflon lined static autoclave. It was heated hydrothermally for 24 h at a temperature of 383 K. The white solid was filtered off and washed with deionised water (*ca.* 500 cm^3), dried under the vacuum and then in an oven at 323 K for 12 h.

Two different methods were used for the removal of the template namely:

i) Calcination,[9, 10] in which the as-synthesised sample was heated at a high temperature of 823 K for 6 h in air with the heating rate of 333 K h^{-1}

ii) Solvent extraction, in which the as-synthesised material (1.5 g) was suspended in a solvent (50 cm^3) and refluxed for 8 h. The porous solid was filtered, washed with 20 cm^3 of ethanol and then with 90-100 cm^3 of deionised water. The solvents used were concentrated HCl in ethanol (0.5 M solution)[11, 12] or ethanol.[13]

3.2.2 Mesitylene-swollen MCM 41 (Ms-MCM 41)[7, 14, 15]

Four different mesitylene-swollen MCM 41 samples (Ms-MCM 41) were synthesised using different amounts of mesitylene (see Table 3.1). A typical synthetic procedure is as follows: C_{18}TMACl (2.80 g, 2.20 mmol) was added to a solution of NaOH (0.37 g, 9.30 mmol) in water (60 cm^3). The resulting mixture was stirred for 15 min and TEOS (3.40 g, 16.30 mmol) was added to it followed by the addition of mesitylene (2.00 g, 16.60 mmol), as an auxiliary chemical to swell the micelle. The suspension formed was stirred for 48 h at room temperature and then heated in a sealed static autoclave for 24 h at 383 K. The white product obtained was filtered off, washed with deionised water

(*ca.* 500 cm^3). The material was dried in an oven at 323 K for 12 h and then calcined at 823 K for 6 h in air with the heating rate of 333 K h^{-1}.[9]

Table 3.1 Amount of mesitylene used in the synthesis of the Ms-MCM 41 materials

Mesitylene used / mmol / synthesis batch
0.0
8.4
12.5
16.6
33.4

3.3 Results and Discussion: Physico-chemical Characterisation

3.3.1 Powder-X-ray Diffraction (p-XRD)

3.3.1.1 Si-MCM 41

The hexagonal periodicity of the Si-MCM 41 material was confirmed by *p*-X-ray diffraction. The *p*-XRD patterns of both the as-synthesised and the calcined Si-MCM 41 materials are shown in Fig. 3.2.

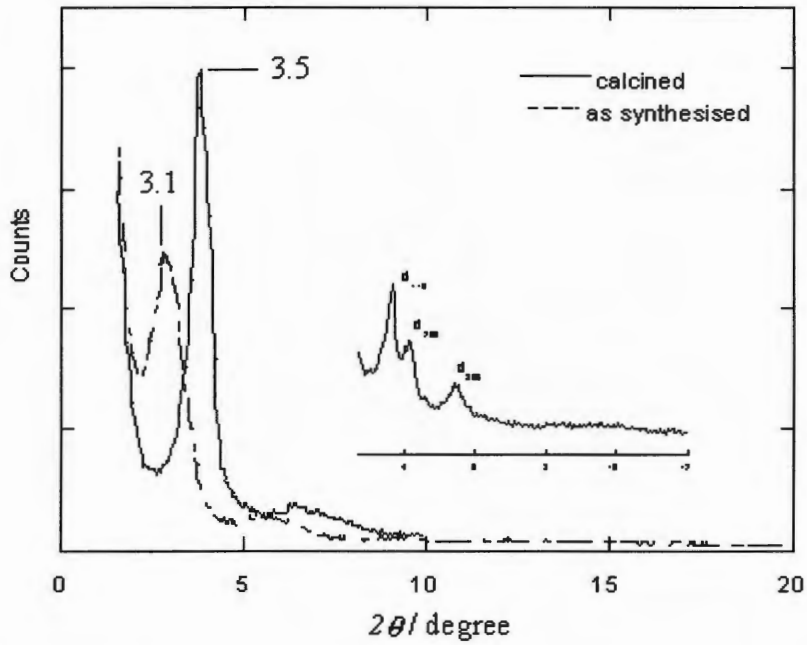

Figure 3.2 *p*-XRD patterns of as-synthesised and calcined Si-MCM 41 materials.

The materials exhibited a single, sharp and intense d_{100} peak and three weak peaks at low 2θ angle (below 10^{o}). These peaks were assigned to the (100), (110), (210) and (300) reflections of the hexagonal lattice of the mesophase, as described by Kresge *et al.*[8] and other workers.[6, 16, 17] Upon calcination of the as-synthesized material, the intensity of the d_{100} peak was found to increase and a slight shift towards a higher 2θ angle was observed. This suggested that there was a slight contraction in the pore diameter on removal of the template.[7]

The Table 3.2 shows the d_{100}-spacing and the unit cell parameter, a, for the calcined Si-MCM 41 material, obtained using CrKα and CuKα X-ray sources.

Table 3.2 The d-spacing and the unit cell, a, data for the Si-MCM 41 and Ms-MCM 41 samples obtained using copper and chromium X-ray sources

Sample	Kα Radiation	d_{100} / Å	a / Å
Si-MCM 41	Cu	36	42
	Cr	38	44

3.3.1.2 Mesitylene-swollen MCM 41(Ms-MCM 41)

The p-XRD pattern of the Ms-MCM 41 material was obtained, using CrKα radiation. Incremental addition of mesitylene (Table 3.1) resulted in proportional increase in the d-spacing of the material,[14] which are shown in Fig. 3.3.

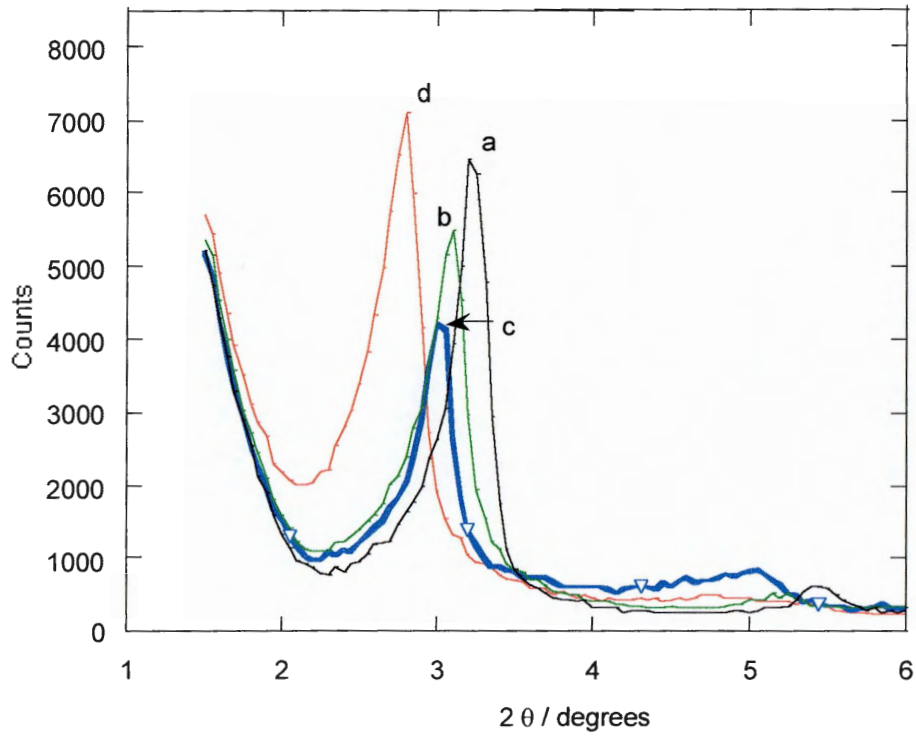

Figure 3.3 p-XRD patterns showing increase in the d-spacing with incremental addition of mesitylene.

Table 3.3 *p*-XRD results obtained using CrKα radiation for the Ms-MCM 41 materials

Peaks (Figure 5.2)	Mesitylene / mmol / batch	d_{100} peak at 2θ / degrees	d_{100}-spacing / Å	a / Å
a	0.0	3.3	40	46
b	8.4	3.1	42	49
c	12.5	3.0	43	50
d	16.6	2.8	47	54
--	33.4	--	--	--

The data in Table 3.3 show the increase in *d*-spacing and the unit cell parameter *a*, with the incremental addition of mesitylene used per synthesis batch.[7, 14, 18] The material synthesised with mesitylene (33.4 mmol) does not show any d_{100} peak as it is obscured by the main X-ray beam; the porosity of the material was confirmed by the nitrogen sorption results.

3.3.2 Infrared Spectroscopy (IR)

Fourier Transform (FT) infrared spectroscopic analysis was carried out on the as-synthesised, the solvent extracted, and the calcined Si-MCM 41 samples. A summary of the IR band wavenumbers and the band assignments for all the samples is given in Table 3.4, and the spectra are shown in Figs. 3.4 to 3.6.

Table 3.4 The IR band wavenumbers observed in the spectra of the as-synthesised, the solvent-extracted, and the calcined Si-MCM 41 samples[7, 19, 20, 21]

Approximate band wavenumber /cm^{-1}			Assignment
AS sample	**SE sample**	**Calcined sample**	
450 – 480	450 – 480	450 – 480	Si–O–Si $_{def}$
800	800	800	Si–O–Si$_{sym\ str}$
--	953	947	Si–O–H $_{vibration}$
1050–1100	1050–1100	1050–1100	Si–O–Si $_{asy\text{-}str}$
1243	1243	--	Si–O–C $_{str}$
1440	--	--	C–H $_{def}$
1642	1642	1642	O–H $_{def}$
2846, 2921	--	--	C–H $_{str}$
3400 - 3500	3400 - 3500	3400 - 3500	O–H $_{str}$

def – deformation (bending), *sym str* – symetrical stretching, *asy-str* – asymmetrical stretching, *AS* – as-synthesised, *SE* – solvent extracted (EtOH/HCl)

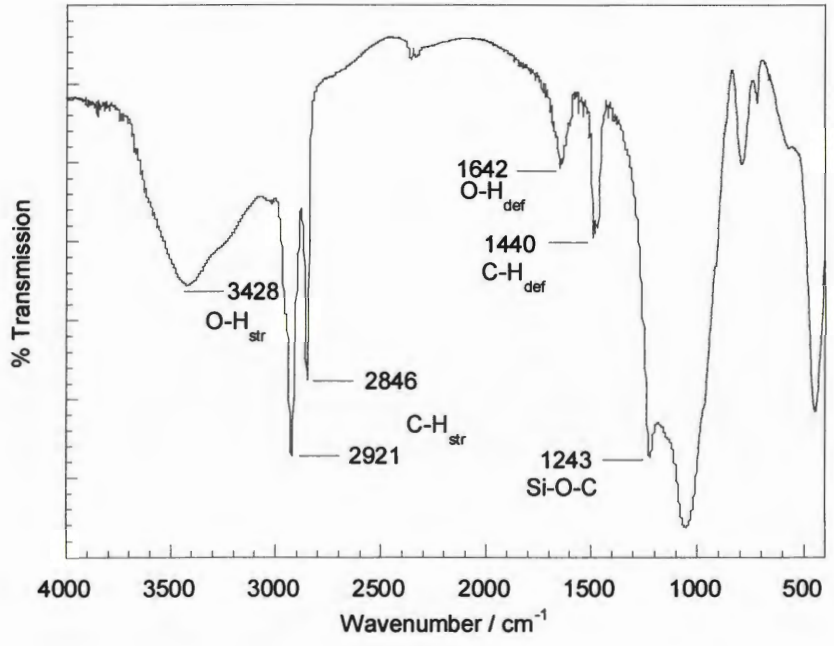

Figure 3.4 The IR spectrum of the as-synthesised Si-MCM 41 material.

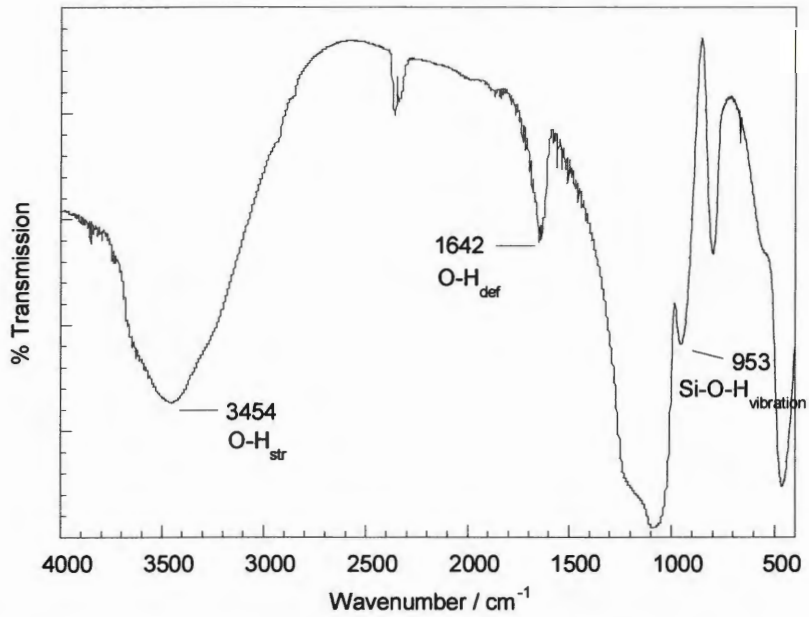

Figure 3.5 The IR spectrum of the solvent extracted Si-MCM 41 material.

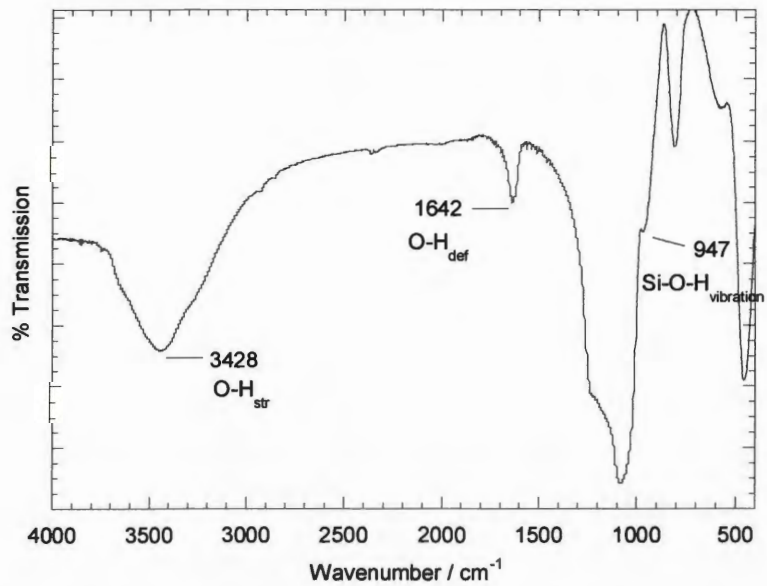

Figure 3.6 The IR spectrum of the calcined Si-MCM 41 material.

Fig. 3.4 shows the FTIR spectrum of the as-synthesised MCM 41 material. The spectrum shows prominent IR absorption bands at *ca.* 2921, 2846 cm^{-1} ($C–H_{str}$) and 1440 cm^{-1} ($C–H_{def}$)[7, 19, 20] corresponding to the presence of surfactant. The IR peak at

around 1243 cm^{-1} corresponding to the Si–O–C stretching vibration is more likely to be due to some unhydrolysed TEOS.[7] This band appears as a sharp peak in the as-synthesised material, whereas for the calcined material it is very weak and appears as a shoulder (Fig. 3.6). The broad absorption band centered at *ca.* 3400 cm^{-1} is due to the O–H stretching vibrations of the surface hydroxyl groups or may be due to the physisorbed water. The sharp absorption band at *ca.* 1642 cm^{-1} was assigned to the 'scissoring' deformation of water.[7]

The FTIR spectra of the solvent-extracted MCM 41 and calcined MCM 41 materials (after template removal) are shown in Fig. 3.5. and Fig. 3.6, respectively. The IR absorption bands corresponding to the surfactant (template) vibrations are absent in the IR spectra of both the samples. This confirmed the complete removal of the template by both the solvent extraction and the calcination methods.

Both the calcined and the solvent extracted MCM 41 samples show a prominent IR absorption band at *ca.* 1083 cm^{-1} due to asymmetric stretching vibration from the framework Si–O–Si, and a peak at *ca.* 470 cm^{-1} corresponds to the Si–O–Si deformation vibration. The band observed at *ca.* 800 cm^{-1} was assigned to the Si–O–Si symmetrical stretching vibration from the framework as reported earlier by Lazarev[22] and Flanigen *et al.*[23] The broad band centred at *ca.* 3400 cm^{-1} confirmed the presence of the surface hydroxyl groups (due to the stretching vibrations).[7] The band at *ca.* 970 cm^{-1} was assigned for the framework Si–O–H vibration[25] by Zhong *et al.*[24] A similar band appears at *ca.* 953 cm^{-1} and at *ca.* 947 cm^{-1} in the IR spectrum of the solvent extracted and calcined sample Si-MCM 41 materials, respectively. This band was found to be sharp and intense in the solvent extracted samples, whereas, it was weak and appears as a shoulder, with the main Si-O-Si asymmetric vibration band, in the spectrum of calcined Si-MCM 41 material (Fig. 3.6). A significant decrease in the broad signal, centred at 3400 cm^{-1} corresponding to the surface silanol groups, was observed upon

calcination. This suggested that after calcination at high temperature most of the surface hydroxyl groups were converted into four membered siloxane groups (due to dehydroxylation) as shown in Fig. 3.7.[7, 26]

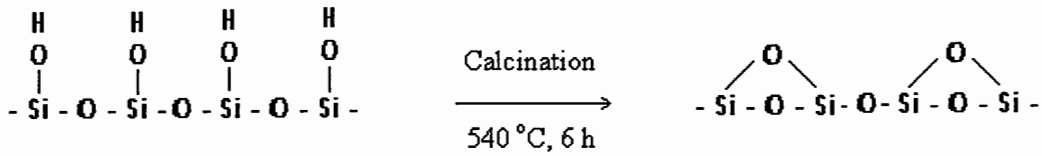

Figure 3.7 Diagram showing formation of the four-membered strained siloxane groups (rings) upon dehydroxylation at high temperature.

In conclusion, the IR spectroscopy confirmed the complete removal of template from the MCM 41 sample. It also implied the presence of siloxane groups in the calcined Si-MCM 41 samples.

3.3.3 CHN Microanalysis

The CHN microanalytical data for the as-synthesised and calcined Si-MCM 41 materials are shown in Table 3.5.

Table 3.5 CHN microanalysis data, in duplicate, for the as-synthesised and calcined Si-MCM 41 materials

Sample	**Carbon / % by mass**		**Hydrogen / % by mass**		**Nitrogen / % by mass**	
As-synthesised Si-MCM 41	36.2	36.0	8.6	8.7	2.1	2.1
Calcined Si-MCM 41	0.08	0.07	1.1	1.1	0.0	0.0

The as-synthesised material showed a much higher percentage (by mass) of carbon, hydrogen and nitrogen corresponding to the presence of template within the

material. Upon calcination the nitrogen content decreased to zero, which showed the template has been removed completely. This was consistent with the results obtained from IR analysis (Section 3.3.2). The amount of carbon present in the calcined sample was found to be negligible (carbon 0.08 %) indicating that the surface was almost free from organic debris. The calcined MCM 41 material showed 1.10 % of hydrogen, which corresponds to surface hydroxyl groups in the material. The CHN microanalysis data obtained for calcined Si-MCM 41 were used as a reference for the comparison with the modified MCM 41 samples (Section 5.3.3) and (Section 6. 3.5).

3.3.4 X-ray Photoelectron Spectroscopy (XPS)

X-ray photoelectron spectroscopic analysis on the Si-MCM 41 material was carried out at the Interface Analysis Center, University of Bristol. XPS is a surface analytical technique as discussed in Chapter 2, Section 2.6.1. One aim of this current work was to evaluate XPS as an analytical tool, for determining the distribution of metal-Schiff base complex in the modified MCM 41 material (Chapter 6). This section presents results from the Si-MCM 41 material, which was used as a reference for comparison with the modified samples.

Table 3.6 summarises the measured binding energy peak positions for the various elements as determined by XPS for the Si-MCM 41 sample. Charge correction of the measured binding energy peak was done to the adventitious hydrocarbon peak at 284.8 eV. Figs. 3.8 and 3.9 show the XPS spectra of the Si-MCM 41 material before and after argon etching, respectively. The spectra are displayed as plots of number of electrons (counts) versus the electron binding energy (eV).

Table 3.6 Binding energies and chemical environment as determined by XPS for the calcined Si-MCM 41 material. (HC = adventitious hydrocarbon [27] and $-CH_2-$ groups)

Elements	**Binding energy / eV**		
	Si-MCM 41	Si-MCM 41 (Shallow take-off angle analysis)	Si-MCM 41 (after argon etching)
Carbon	284.8 (HC)	284.8 (HC)	284.8 (HC) 287.2 (alcohol/ether) 289.0 (carboxyl)
Nitrogen	--	--	--
Oxygen	533.2 (SiO_2-type)	533.3 (SiO_2-type)	532.9 (SiO_2-type)
Silicon	103.8 (SiO_2-type))	104.0 (SiO_2-type))	102.2 (silicate) 103.7 (SiO_2-type)

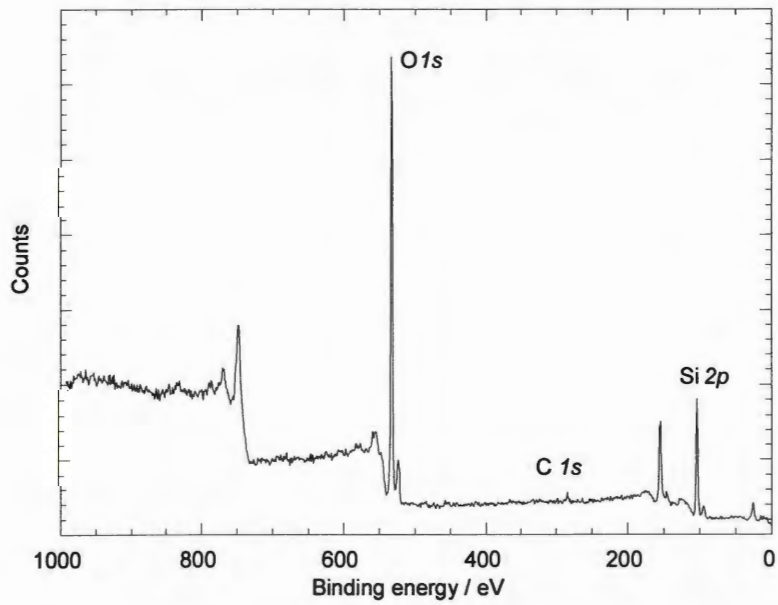

Figure 3.8 Wide scan XPS spectrum of the calcined Si-MCM 41 sample.

The spectrum (Fig. 3.8) shows the O 1*s* peak position at 533.2 eV, which is as expected for α-quartz (SiO_2 type material).[26] The Si 2*p* peak position observed at 103.8 eV is in agreement with the SiO_2-type material.[27] Ion etching (Fig. 3.9) appeared

to result in a decrease in this binding energy to 102.2 eV, which was more like that expected for silicates.

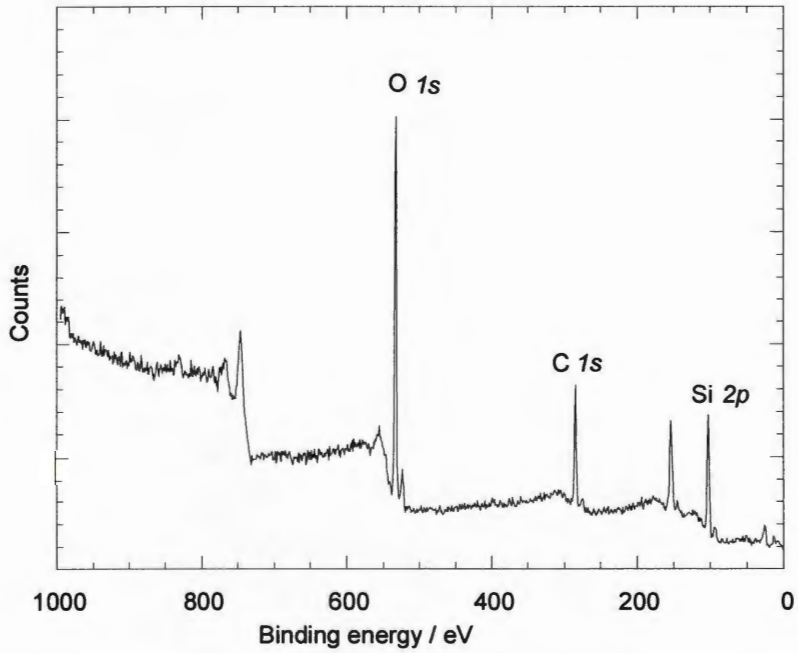

Figure 3.9 Wide scan XPS spectrum of the Si-MCM 41 material after argon etching.

The spectrum shows a very weak peak for carbon at a binding energy of 284.8 eV. This carbon peak became more intense following analysis after argon etching. The source of carbon in the Si-MCM 41 sample was presumed to come from the sticky tab used to mount the sample. Argon ion etching for a total time of 270 s (corresponds to *ca.* 4.5 nm surface etching at rate of 1 nm per min) was found to increase the measured carbon on the Si-MCM 41 sample (see Table 3.6), possibly through transporting adhesive material on to the sample surface, and as a result of the increased exposure of time in the spectrometer chamber.

Table 3.7 summarises the surface atomic concentrations as determined using XPS for the Si-MCM 41 sample. The oxygen-to-silicon ratio as determined by XPS was found to be 2.4 (which was slightly higher than the expected ratio of 2). However, on

argon etching the oxygen-to-silicon ratio reduced to 2.1. This may be because the surface hydroxyl groups were removed by argon etching causing a decrease in the oxygen-to-silicon ratio.

The sample angle was changed (from 0 to 45°) with respect to the analyser input to perform the shallow take-off analysis.[27] This technique enhances the surface selectivity of the analysis. No significant changes in the peak positions and the relative concentration of the elements Si and O were observed upon tilting the sample angle in order to reduce the analysis depth (see Table 3.7). The presence of a small percentage of carbon suggested that the surface was free from contaminant overlayers (silicate with adventitious carbon on the surface).

Table 3.7 Surface atomic concentrations of the Si-MCM 41 as determined by XPS.

Sample	Surface Concentration / Atomic % (at%)			
	Carbon	Nitrogen	Oxygen	Silicon
Si-MCM 41	3.3	--	68.5	28.3
Si-MCM 41 (shallow take-off angle)	6.4	--	65.5	28.0
Si-MCM 41 (after Ar^+ etching)	32.1	--	45.8	22.1

In conclusion, the XPS analysis showed the absence of nitrogen in calcined Si-MCM 41, which supported the results obtained from FTIR spectroscopy and the CHN microanalysis for the removal of template. The decrease in oxygen-to-silicon ratio from 2.4 to 2.1 suggests the presence of surface hydroxyl groups, which are removed by etching.

3.3.5 Transmission Electron Microscopy (TEM)

Transmission Electron Microscopy (TEM) was used to probe the hexagonal ordering of the pores, which can be directly observed using TEM. It gives useful information about

the pore diameter and the particle size of the MCM 41 material.[28] Apart from these advantages TEM has a limitation that only a small fraction of a sample is analysed, and it is difficult to assess how much of the material is really ordered, or apparently disordered. This is because the alignments of the hexagonal pores along the direction of the electron beam is not always achieved.[29]

Fig. 3.10 shows the TEM images of the Si-MCM 41 material with the hexagonal pores aligned in two different directions (parallel and perpendicular) to the direction of the electron beam. The TEM microscope used in this study was of low-resolution, and hence the image quality is not as good as that reported by the other workers, [28, 30, 31] where images were obtained using high-resolution microscopes. TEM studies showed that the material synthesised contained pores arranged hexagonally in a honeycomb fashion. This result was supported by the *p*-XRD analysis (Section 3.3.1) and from nitrogen sorption results (Section 3.4.1).

The part of Fig. 3.10 highlighted in the circle indicates the hexagonal arrangements of pores (although its not clear) along 100 directions, which is due to the projection of pores parallel to the direction of incident beam. This gives the cross-sectional view of the MCM 41 channels,[30] which could be useful in the evaluation of the pore diameter,[30] as shown by the other workers where high-resolution microscopy was used.[28, 30, 31] The pore diameter obtained by TEM analysis could be more reliable compared to the other methods used for the determination of pore diameter.[30]

The part of Fig. 3.10 highlighted in the square shows the cylindrical tubes of the Si-MCM 41 material oriented in a direction perpendicular to the incident beam. This image might suggest the presence of a lamellar phase. However, this can be ruled out as the lamellar phase is not stable and collapses following calcination.

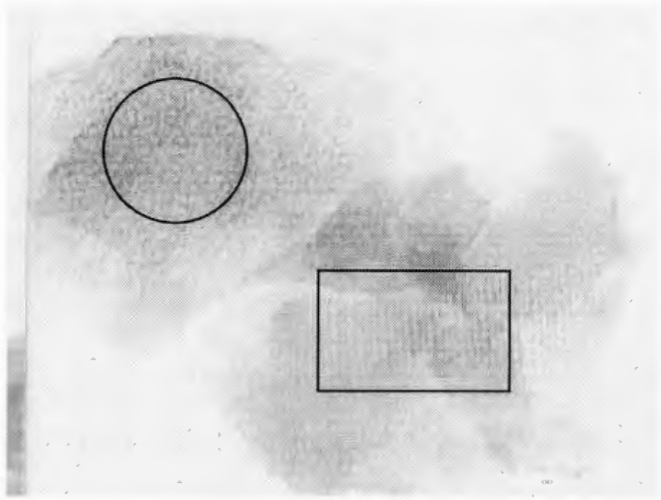

Figure 3.10 TEM image of the Si-MCM 41 material: (in circle) Pores parallel to the direction electron of beam, (in square) Pores perpendicular to the direction of electron beam.

3.3.6 Nuclear Magnetic Resonance (NMR) Spectroscopy

The ^{29}Si cross-polarisation magic angle spinning (CP MAS) NMR spectrum and the ^{29}Si magic angle spinning (MAS) NMR spectrum of the calcined Si-MCM 41 material are shown in Fig. 3.11 and Fig. 3.12, respectively. The observed peak positions for the Si sites in the sample are summarised in Table 3.8.

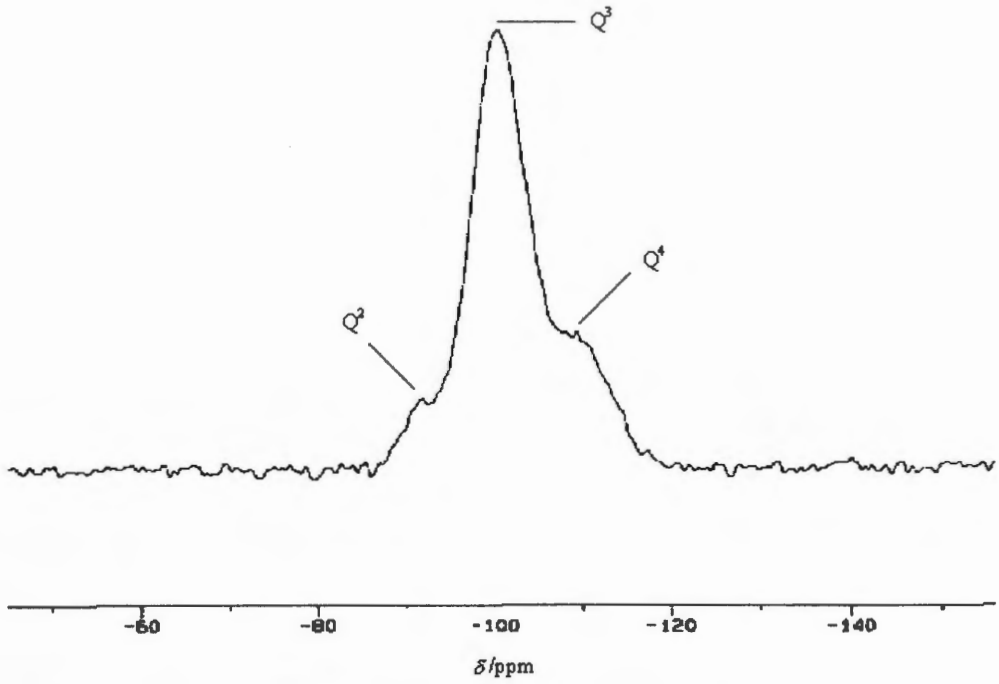

Figure 3.11 ^{29}Si CP MAS NMR spectrum of calcined Si-MCM 41.

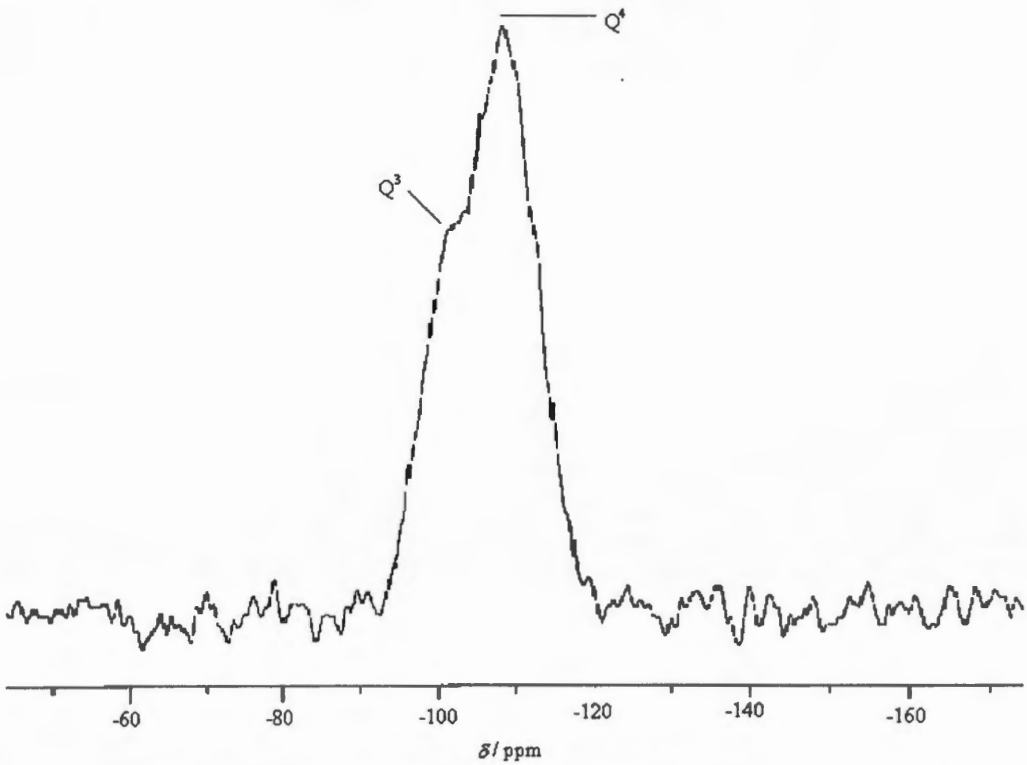

Figure 3.12 ^{29}Si MAS NMR spectrum of calcined Si-MCM 41.

Table 3.8 ^{29}Si MAS NMR spectroscopic results for the calcined Si-MCM 41 material

^{29}Si CP MAS NMR δ / ppm	^{29}Si MAS NMR δ / ppm	Branching‡	Unit
-91.9	--	Q^2	Middle group
-100.7	-101.2	Q^3	Branching group (Si-OH)
-109.3	-109.3	Q^4	Crosslinking group (SiO_4 tetrahedra)

**TMS as an external reference*
‡ Silicon environment (Chapter 2, Section 2.9.4)

The CP MAS NMR spectrum (Fig. 3.11) displays three resonances at δ = -109.3, -100.7 and -91.9 ppm, assigned to Q^4 (cross-linked), Q^3 and Q^2 species, respectively, of the silica framework [Q^n = $Si(OSi)_n$-$(OH)_{4-n}$].[33] The Q^3 resonance due to $(SiO)_3$Si-OH was intense compared with those from Q^4 and Q^2, both of which appear as shoulders. This indicated the presence of surface silanol (hydroxyl) groups on the MCM 41 surface, which was consistent with the results obtained from IR spectroscopy (Section 3.3.2).

In the ^{29}Si MAS NMR spectrum (Fig. 3.12), the two main peaks centred at δ = -109.3 and -100.7 ppm were assigned to the Q^4 and Q^3 Si sites, respectively. The signal due to Q^2 site was not observed, possibly due to an overlap of the Q^2 signal with the broad Q^4 and Q^3 signals, as reported by Marcos and co-workers.[34]

The ^{13}C CP MAS NMR analysis showed no peaks for carbon in the calcined Si-MCM 41 material.

3.4 Sorption Studies: Results and Discussions

Sorption studies were carried out on the Si-MCM 41 and Ms-MCM 41 materials using the adsorptives given below:

- nitrogen
- carbon dioxide
- water
- *n*-hexane
- methanol (MeOH)
- *n*-butanol (n-BuOH)
- *t*-butanol (t-BuOH)

The different adsortives were used to determine the surface area, the pore properties and the surface properties of the materials synthesized in the current work. The Table 3.9 summarises the different adsorptives, and the sorption conditions used to study the sorption properties of the Si-MCM 41 and Ms-MCM 41 materials. The sorption results are summarised in Table 3.10.

Table 3.9 Adsorptives, their molecular cross-sectional area, the sorption temperatures and the degassing times used to measure the sorption isotherms of the Si-MCM 41 and Ms-MCM 41 materials.

Adsorptive	**Technique used for sorption**	**Molecular cross-sectional area of adsorptive / Å^2**	**Sorption temperature / K**	**Degassing time / h at 423 K**
Nitrogen	Volumetric	16.2*	77	6
CO_2	Volumetric	17.0*	195	6
H_2O	Gravimetric	10.5*	303	1.5
MeOH	Gravimetric	18.0*	303	1.5
n-BuOH	Gravimetric	31.0†	303	1.5
t-BuOH	Gravimetric	31.9†	303	1.5
n-Hexane	Gravimetric	39.3†	303	1.5

* *Literature values* [7, 36, 47]

† *Derived from equation 2.14 (Chapter 2, Section 2.10.4)*

Table 3.10 Sorption isotherm results for the Si-MCM 41 and Ms-MCM 41 materials.

Sample	Adsorptive	Type of Isotherm	Surface Area / $m^2 g^{-1}$	Pore volume / $cm^3 g^{-1}$	Average Pore diameter / Å	
					§	†
Si-MCM 41	Nitrogen	IV	1150	0.74	26	25
	CO_2	IV	580	0.76	57	--
	H_2O	V	'70'	0.54	--	--
	MeOH	IV	640	0.70	--	--
	n-BuOH	IV	672	0.68	--	--
	t-BuOH	IV	840	0.69	--	--
	n-Hexane	*	800	0.57	--	--
Mesitylene-swollen MCM 41	Nitrogen	IV	338	0.30	36	39
	CO_2	Type II	200	--	--	--

** The isotherm was difficult to classify according to the IUPAC classification.*
§ = Pore diameter derived from eq. ($4V/S_{sp}$ by BET) and, † = BJH mean pore diameter.

3.4.1 Nitrogen Sorption

3.4.1.1 Si-MCM 41

The nitrogen sorption isotherm for the Si-MCM 41 material is shown in Fig. 3.13. The material showed a Type IV isotherm (according to IUPAC classification[7, 35, 36, 37], Chapter 2, Section 2.10), which is typical for this type of mesoporous material.[2, 17] The isotherm was reproducible and reversible with no hysteresis loop, which was characteristic of this type of material.[1, 2, 7, 37] A possible explanation for this is that the materials have pores bordering the microporous range. Secondly, it is thought to be due to the position of the capillary condensation step, p/p^o = *ca.* 0.4 (p/p^o = *ca.* 0.3 observed

in this case).[7] Under the sorption conditions it seems that this is the lowest p/p^o at which nitrogen can undergo the classical form of capillary condensation. This value of p/p^o represents a region of instability in the nitrogen meniscus[2, 7] and hence yields an isotherm with no hysteresis.

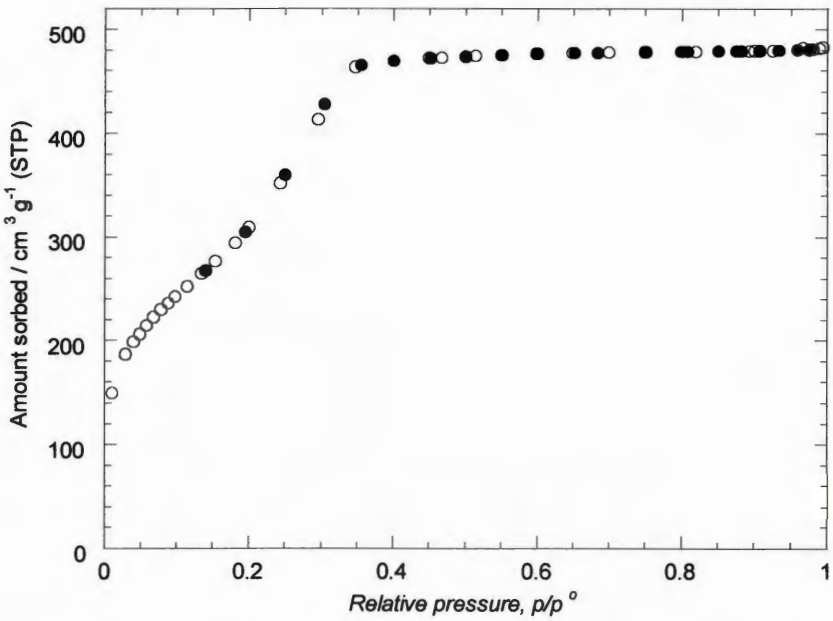

Figure 3.13 Nitrogen sorption isotherm (77 K) for the Si-MCM 41 material. Filled symbols denote desorption points.

The sharp 'knee' observed in the isotherm at lower relative pressure ($p/p^o < 0.1$), corresponds to the monolayer formation of adsorbed nitrogen on the pore walls of the mesopores. This monolayer coverage corresponded to a BET derived value of 11.9 mmol g^{-1} and specific surface area of 1150 m^2 g^{-1}. The isotherm shows a sharp inflection step at relative pressures between $0.25 < p/p^o < 0.35$, which was attributed to the capillary condensation of nitrogen in the mesopores. The sharpness in the step indicated that the material synthesised has a narrow pore size distribution.[3, 7, 37] The average pore diameter was 25 Å, derived from the BJH method (Chapter 2, Section 2.10.7), and 26 Å derived from *Eq.* $4V/S_{sp}$ (Chapter 2, Section 2.10.7). This confirmed

that the material synthesised was indeed mesoporous. The material showed a high Gurvitsch pore volume, V_p, of 0.74 $cm^3\ g^{-1}$.

The α_s-plot (Chapter 2, Section 2.10.9), constructed using nitrogen sorption data on non-porous hydroxylated silica, is shown in Fig. 3.14. The plot shows three well-defined regions:

- Region *A*, a linear region between $\alpha_s(n/n_{0.4})$ = *ca.* 0.4 to 0.75, due to the monolayer-multilayer adsorption on the pore walls.
- Region *B*, region between $\alpha_s(n/n_{0.4})$ = *ca.* 0.75 to 1.0, which shows deviation from the standard isotherm, due to the capillary condensation in the mesopores.
- Region *C*, another linear portion of the plot between $\alpha_s(n/n_{0.4})$ = *ca.* 1.0 to 1.6, shows multilayer adsorption on the external surface.

The extrapolation of region *A* to the origin confirmed the absence of any detectable micropore filling in the sample at low p/p^o.[35, 36, 37]

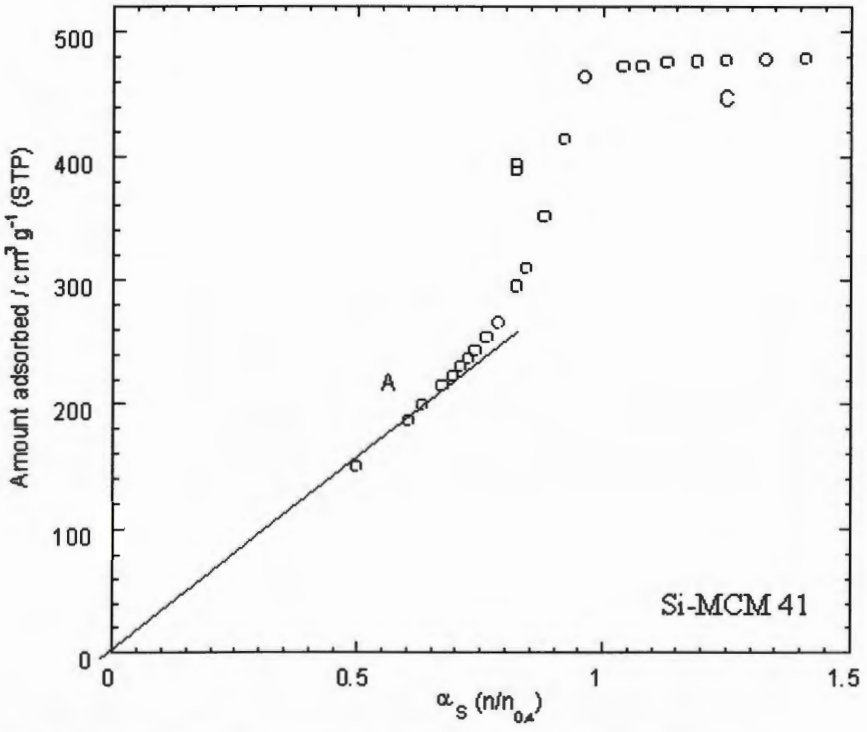

Figure 3.14 α_s-plot for the adsorption of nitrogen by Si-MCM 41.

3.4.1.2 Mesitylene-swollen MCM 41

Fig. 3.15 shows nitrogen sorption isotherm for mesitylene-swollen MCM 41.

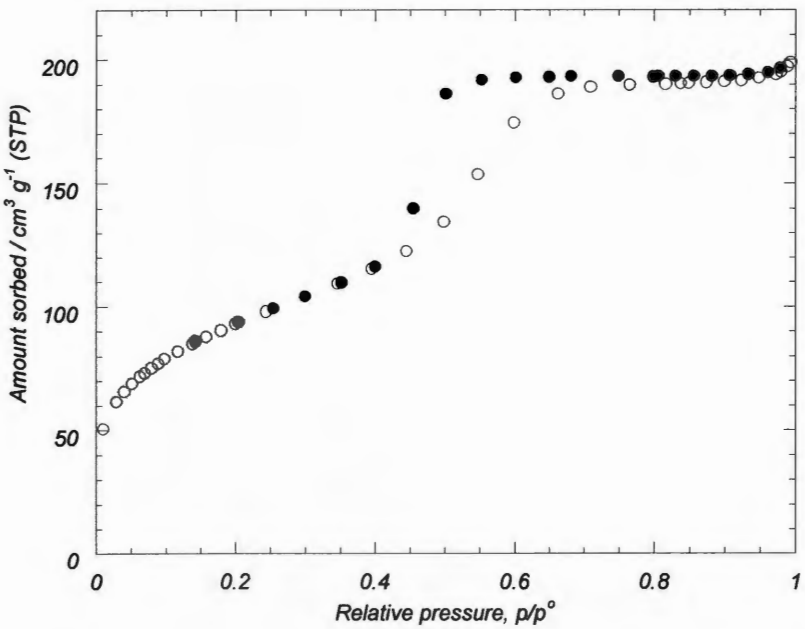

Figure 3.15 Nitrogen sorption isotherm (77 K) for the Ms-MCM 41 material. Filled symbols denote desorption points.

The isotherm shown, and the results discussed in this section are for the material synthesised with 33.4 mmol of mesitylene per synthesis batch (Table 3.1). The material yielded a Type IV isotherm, which was reproducible and shows an adsorption-desorption hysteresis loop, which is in contrast to the isotherm shown by the unswollen-Si-MCM 41 sample, where no hysteresis was observed. The inception in the isotherm due to capillary condensation is observed at p/p^o = *ca.* 0.5. The important feature of the isotherm is the hysteresis loop, and the pore condensation is observed at higher relative pressure (p/p^o = 0.6) compared with the unswollen-Si-MCM 41 material. This was as expected since the material possesses pores with a larger diameter (39 Å) compared with the pores of unswollen-Si-MCM 41 (26 Å).

The material yielded a BET derived specific surface area of 360 $m^2 g^{-1}$, and a Gurvitsch pore volume of 0.30 $cm^3 g^{-1}$, which were lower than 1150 $m^2 g^{-1}$ and 0.74 $cm^3 g^{-1}$, respectively, those yielded by the unswollen-Si-MCM 41 material. This decrease in both the surface area and pore volume of a material is consistent with the observation that as the diameter of the pores increases the number of pores per unit area decreases.[38] The results obtained were similar to those reported by other workers.[38, 39]

The calculation shown below suggests that the Ms-MCM 41 contains 1/5 the number of the pores compared with the unswollen sample and this is consistent with both decrease in surface area and in pore volume.

i) *The length (L) of cylindrical tube calculated for the unswollen-Si-MCM 41 material*

From surface area:

$$\pi DL = 1150\ m^2 g^{-1}$$

$$\therefore L = 1150 / \pi \times 26 \times 10^{-10}\ m$$

$$= 13.6 \times 10^{10}\ m\ g^{-1}$$

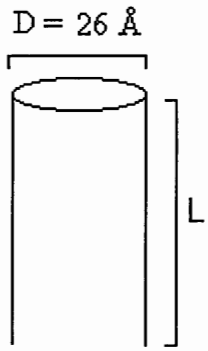

From pore volume

$$\pi D^2 / 4 \times L = 0.74\ cm^3 g^{-1}$$

$$\therefore L = 0.74 \times 10^{-6}\ m^3 g^{-1} \times 4 / \pi \times (26 \times 10^{-10})^2\ m$$

$$= 13.0 \times 10^{10}\ m\ g^{-1}$$

$\therefore$ L obtained from both methods is consistent.

ii) *The length (L) calculated for the Ms-MCM 41 material*

From surface area: (assuming external surface area is negligible)

$$\pi DL = 340\ m^2 g^{-1}$$

$$\therefore L = 2.78 \times 10^{10}\ m\ g^{-1}$$

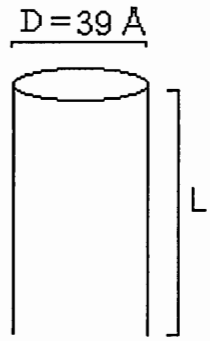

From pore volume

$$\pi D^2 / 4 \times L = 0.3\ cm^3 g^{-1}$$

$$\therefore L = 2.76 \times 10^{10}\ m\ g^{-1}$$

$\therefore$ L obtained from both methods is consistent.

The pore ratio:

Swollen : unswollen-MCM 41 material = 2.8 : 13, which is *ca.* 1: 5

3.4.2 Carbon Dioxide Sorption

Carbon dioxide (CO_2) sorption is often performed at elevated temperature (*e.g.* 273 K) and at high pressures, to obtain pore size distribution of narrow carbon micropores.[40] Due to the 'activated diffusion' of CO_2 at temperatures above 195 K, CO_2 can also penetrate 'ultramicropores' (pore diameter < 0.7 nm), which are often not accessible to nitrogen at 77 K. However, in this study the CO_2 sorption was carried out at 195 K, 273 K and 286 K using CO_2 pressures of less than 1 atmosphere on the Si-MCM 41 material and at 195 K on the Ms-MCM 41 material.

The sorption temperature of CO_2 *i.e.* 195 K is below its triple point (217 K, at pressure of *ca.* 3100 torr).[40] In principle, the adsorbed CO_2 phase can still be liquid like, when the fluid is confined to the narrow, micro- and meso-pores. It is a known that the triple point and the freezing temperatures of the fluids confined to narrow pores are different compared to the corresponding bulk system.[40] The triple point and the freezing temperature shift towards lower temperature for CO_2 adsorbed in narrow pores. This shift in temperature depends on the strength of the fluid-fluid and fluid-solid interactions and also on the pore diameter.[40] Thus, the smaller the pore diameter, the larger is the expected shift in the triple point temperature.

CO_2 sorption at 195 K on the Si-MCM 41 material yielded a Type IV isotherm (Fig. 3.16) and confirmed the mesoporosity of the material. The sharp step in sorption isotherm due to capillary condensation of CO_2 within the pores is observed at higher p/p^o (*ca.* 0.55) compared with that observed for nitrogen adsorption (p/p^o = 0.3) (Fig. 3.13). The CO_2 sorption isotherm shows a rounded 'knee' at low relative pressure, whereas for nitrogen adsorption a sharp 'knee' is evident at low relative pressure. A

possible explanation for this is that adsorption of CO_2 occurs by polar interaction with the surface because of its high quadrupole moment and is unlikely to proceed *via* monolayer formation. The lower value of the BET parameter, *c,* (10) obtained for CO_2 compared with nitrogen (45) supports this. The CO_2 sorption isotherm displays a Type H1 hysteresis loop[35] (Chapter 2, Section 2.10.2), which is absent in the N_2 sorption isotherm.

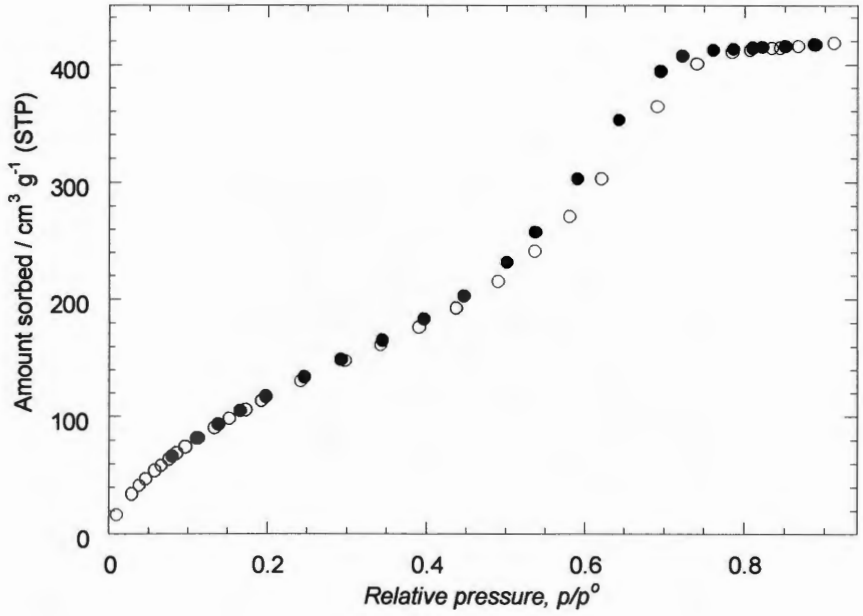

Figure 3.16 CO_2 sorption isotherm (195 K) for the Si-MCM 41 material (equilibration time = 15 s). Filled symbols denote desorption points.

Fig. 3.17 shows the α_s-plot for CO_2 sorption on Si-MCM 41. Similar to the nitrogen α_s-plot, three different regions, corresponding to initial adsorption on polar sites ('monolayer formation') (*A*), capillary condensation in the mesopores (*B*), and multilayer formation (*C*) are observed confirming the presence of mesopores in the material.[35, 36, 37] However, the inflection due to capillary condensation is not as sharp as that observed in the α_s-plot from the nitrogen (Fig 3.14). The linear region *A*, when

extrapolated (to $\alpha_s = 0$) shows a negative intercept on y-axis. This supports the earlier proposal that the sorption of CO_2 does not proceed *via* monolayer formation on the surface.[35]

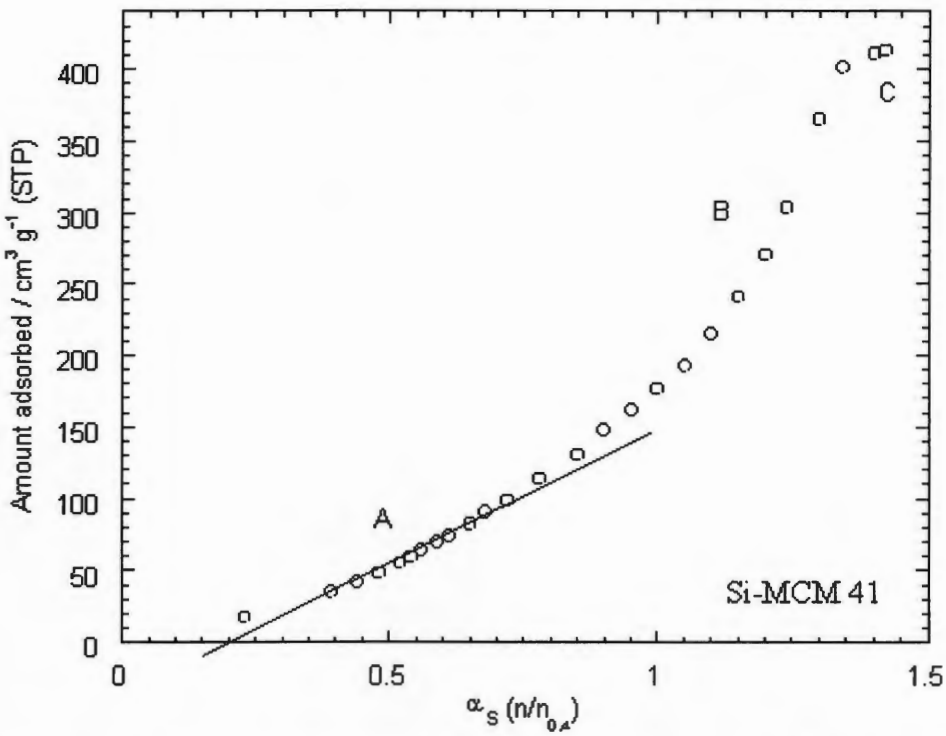

Figure 3.17 α_s-Plot for the adsorption of carbon dioxide by the Si-MCM 41 material.

The carbon dioxide adsorption isotherm for the Ms-MCM 41 material yielded a Type II isotherm (Fig. 3.18). It is apparent that the isotherm due to pore filling shows the start of the inflection point due to capillary condensation but the plateau has not been attained and suggests that the isotherm is incomplete as observed by Sing *et al.*[41] This may be explained by the presence of larger pores (39 Å) in Ms-MCM 41, which do not shift the triple point to sufficiently low temperature to cause capillary condensation below $p/p^o < 1.0$ under the working conditions, whereas the Si-MCM 41 with smaller pores (26 Å) shifts the triple point temperature sufficiently to enable capillary condensation (Fig. 3.16). As the complete filling of the pores by 'liquid CO_2' is not achieved, the validity of a calculated pore volume is questionable.

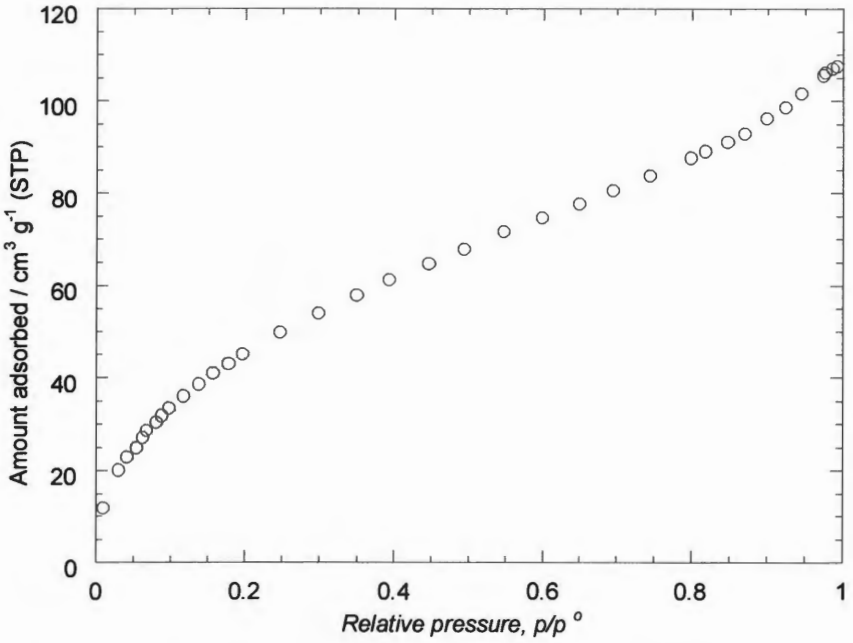

Figure 3.18 CO_2 adsorption isotherm (195 K) for the Ms-MCM 41 material (equilibration time = 15 s).

Isosteric Heat of Adsorption

Fig. 3.19 shows the CO_2 adsorption isotherm at elevated temperatures of 273 K and 286 K. However, at elevated temperature and at maximum achievable pressure, p^o, (effective saturation pressure) at *ca.* 1 atm, the isotherms correspond to only a narrow low relative pressure range, $0 < p/p^o$ 0.03, of the CO_2 sorption isotherm obtained at 195 K (the p^o for CO_2 at 273 K is 26140 torr). This low-pressure part of the isotherm is almost linear with very small uptake of CO_2, which decreases with increase in temperature (from 273 to 286 K).

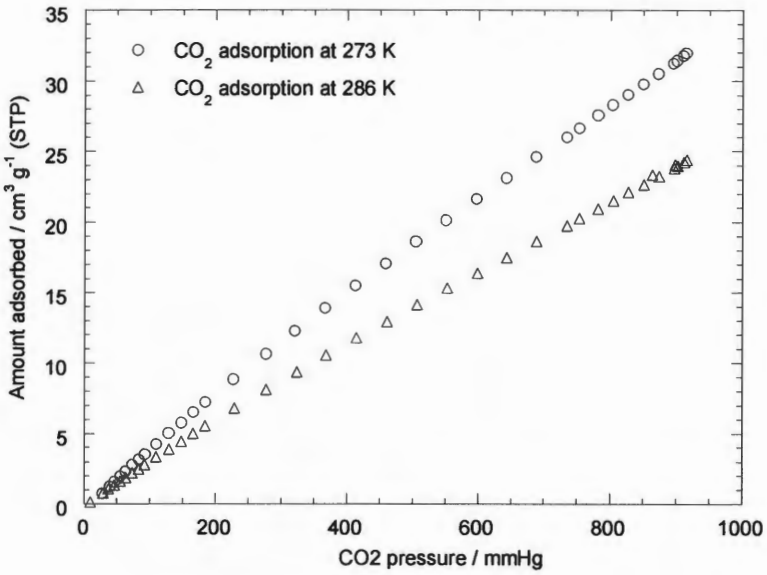

Figure 3.19 CO_2 adsorption isotherms at 273 K and 286 K for the Si-MCM 41 material.

The isosteric heat of adsorption (q^{st}) (Table 3.11) was calculated from the adsorption isotherm data at two temperatures *i.e.* 273 K and 286 K by using the Clausius-Clapeyron equation (Equation 3.1).

$$q^{st} = RT_1T_2/T_2\text{-}T_1\ (lnp_2\text{-}lnp_1)n_a \qquad \textit{Equation}\ 3.1$$

where p_1 and p_2 are the equilibrium pressures at temperatures T_1 and T_2, respectively, when the amount adsorbed is n_a.

Table 3.11 Isosteric heat of adsorption values at different surface coverages for the adsorption of CO_2 on Si-MCM 41.

Surface coverage, CO_2 on Si-MCM 41 / mmol g^{-1}	0.018	0.04	0.115	0.148	0.165
q^{st} / kJ mol^{-1}	7.5	12.5	15.0	15.5	15.6

The variation of heat of adsorption (q^{st}) with surface coverage for the adsorption of CO_2 on the Si-MCM 41 material is shown in Fig. 3.20. The isosteric heat of

adsorption was found to increase initially (up to a CO_2 coverage of 0.11 mmol g^{-1}), due to the surface-CO_2 interaction. However, it remains constant at higher CO_2 coverage, due to the interaction between the CO_2 molecules. The q^{st} value obtained (15.6 kJ mol^{-1}) was less than the theoretically estimated value of 28 kJ mol^{-1} for silicalite.[42] A drop in the heat of sorption from 28 to 22 kJ mol^{-1} and from 28 to 20 kJ mol^{-1} at a low loading of 0.12 mmol g^{-1} was reported by Graham *et al.*[43] and Choudhary *et al.*[44], respectively. However, it should be noted that in this work the CO_2 adsorption was measured at pressures below atmospheric pressure compared with the high pressure adsorption reported by other workers.[43, 44] The q^{st} data of the Si-MCM 41 material was used as a reference to compare with the copper-Schiff base-modified MCM 41 materials, discussed in Chapter 6 (Section 6.4.1.2).

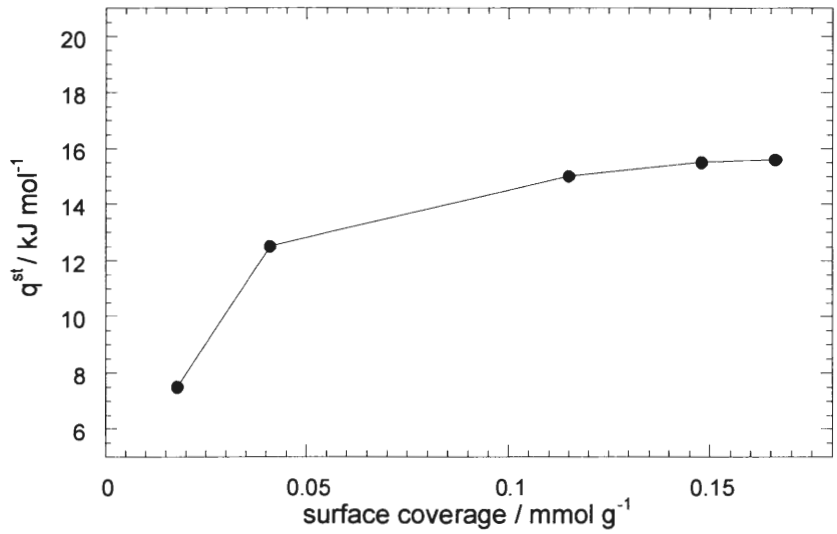

Figure 3.20 Variation of isosteric heat of adsorption, q^{st}, with surface coverage for the adsorption of CO_2 on Si-MCM 41.

3.4.3 Water Sorption

The sorption of water is highly specific and dependent on the surface chemistry of the adsorbent. The tendency of water molecules to form hydrogen bonds makes adsorption of water very sensitive to the degree of polarity (hydroxyl groups) present on the

adsorbent surface.[7, 35, 36] Therefore, it gives useful information about the hydrophilic and/or hydrophobic surface properties of a material. The water sorption isotherm at 303 K for the Si-MCM 41 material was obtained using the gravimetric technique (Chapter 2, Section 2.12).

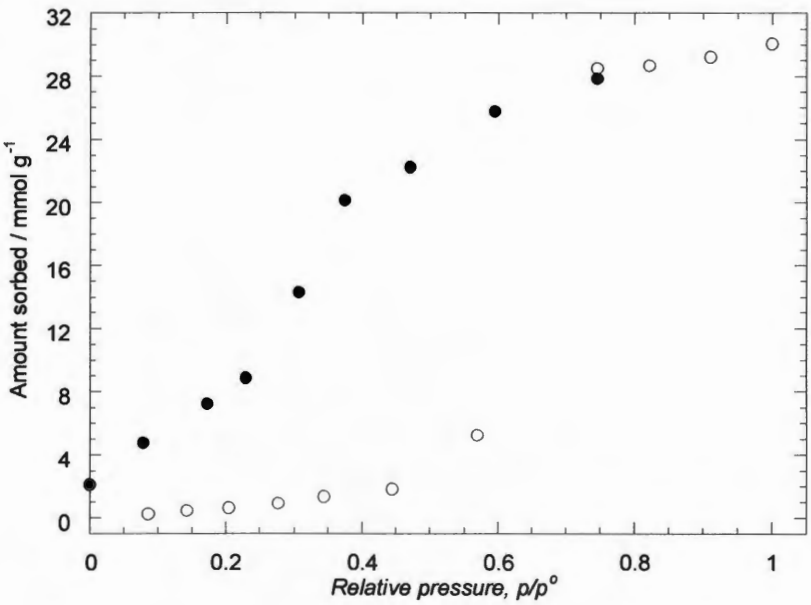

Figure 3.21 Water sorption isotherm (303 K) for the Si-MCM 41 material. Filled symbols denote desorption points.

The water sorption isotherm for the Si-MCM 41 material displays a Type V isotherm (Fig. 3.21) as reported by other workers.[7, 36, 39] The isotherm shows low initial adsorption up to p/p^o *ca.* 0.5, highlighted by the long plateau at the start of the isotherm. This low adsorption affinity can be attributed to the weak adsorbent-adsorbate interaction, which is associated with the hydrophobic surface. Capillary condensation in the mesopores starts at p/p^o *ca.* 0.6 and levels off at p/p^o *ca.* 0.75. The final plateau of the isotherm shows complete filling of the pores by water and yielded a Gurvitsch pore volume of 0.54 $cm^3\ g^{-1}$. The value obtained was lower than the nitrogen derived pore volume (0.74 $cm^3\ g^{-1}$) and the results obtained were similar to those reported by other

workers.[7, 36, 39] This behaviour was explained by Gregg and Sing[35] as the adsorbed water within the pore, which may exist in a less dense form compared with the ordinary water due to the differences in hydrogen bonding arrangements.

An interesting feature of the isotherm is the presence of hysteresis loop, which extends over the low-pressure region and does not close. The water 'remained' on the surface, even after exposing the sample to a high vacuum (*ca.* 10^{-5} torr), suggesting non-reversible adsorption of water on the Si-MCM 41 surface. This suggests that, initially, the Si-MCM 41 material, being in a partially dehydroxylated form, undergoes rehydroxylation following chemisorption of water. This is shown schematically in Fig. 3.22. This low-pressure hysteresis is similar to that reported by Bambrough[7] but is in contrast to the work reported by Branton[36] and Sing *et al.*,[41] where the isotherm was found to be reversible with no hysteresis.

The chemisorption represents 1:1 interaction of water with the surface hydroxyls/siloxanes and can be used to determine the number of hydroxyl groups present on the Si-MCM 41 surface, which yields a value of 1.0 -OH groups per nm^2 (*i.e.* total number of hydroxyl groups present on surface after sorption).

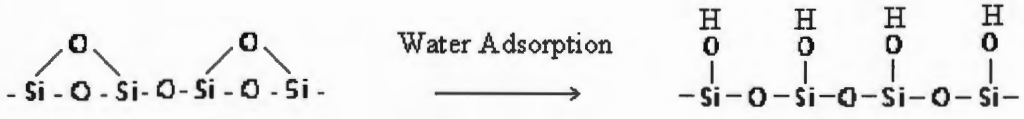

Figure 3.22 Diagram showing rehydroxylation of the surface siloxane groups following water adsorption.

The water sorption isotherm for the Si-MCM 41 material shows very low adsorption affinity at low relative pressure (see Fig. 3.21). This indicated that the sorption of water does not take place *via* monolayer formation on the pore surface.[35, 41]

It was explained by Gregg and Sing[35] that the physisorption of water is initiated by hydrogen bonding with surface hydroxyl groups, followed by cluster formation of water molecules, which grows with increasing relative pressure and finally shows pore filling by condensation at higher relative pressure. The BET derived monolayer capacity for water sorption represents the surface hydroxyl group concentration as the water molecules absorb on the surface in a 1:1 ratio with surface hydroxyl groups, as shown in Fig. 3.23. The sample showed a monolayer capacity of 1.2 mmol g^{-1}, and the surface area of the sample from nitrogen sorption (1150 m^2 g^{-1}) yielded a value of 0.63 -OH groups per nm^2. This value for the number of hydroxyl groups was less than the value derived from chemisorption (1.0 nm^2). However, in this work the number of hydroxyl groups (*i.e.* total number of hydroxyl groups present on surface after sorption) derived from chemisorption value are used for comparison with the modified samples.

Thus, water sorption provides useful information about the number of hydroxyl groups present on the surface. The number of hydroxyl groups was found to decrease in the modified samples, which will be discussed further in Chapter 6.

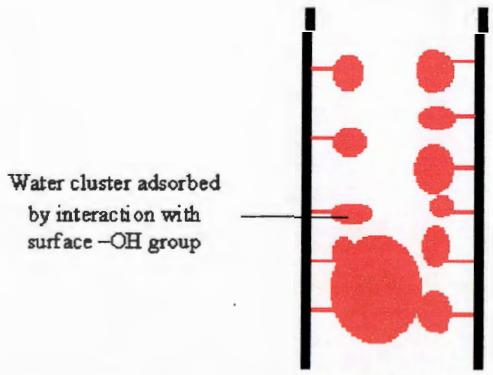

Figure 3.23 The diagram shows the sorption mechanism of water on Si-MCM 41.

The infrared spectrum of the Si-MCM 41 material after water sorption is presented in Fig. 3.24-a. The spectrum shows a more intense band at 3465 cm^{-1} when compared with the similar band in IR spectrum of Si-MCM 41 before water sorption.

The peak at 955 cm^{-1}, due to the surface silanol groups, is very intense and sharp after water sorption whereas a similar band (947 cm^{-1}) appears as a shoulder in the IR spectrum of the calcined Si-MCM 41 material before water sorption.

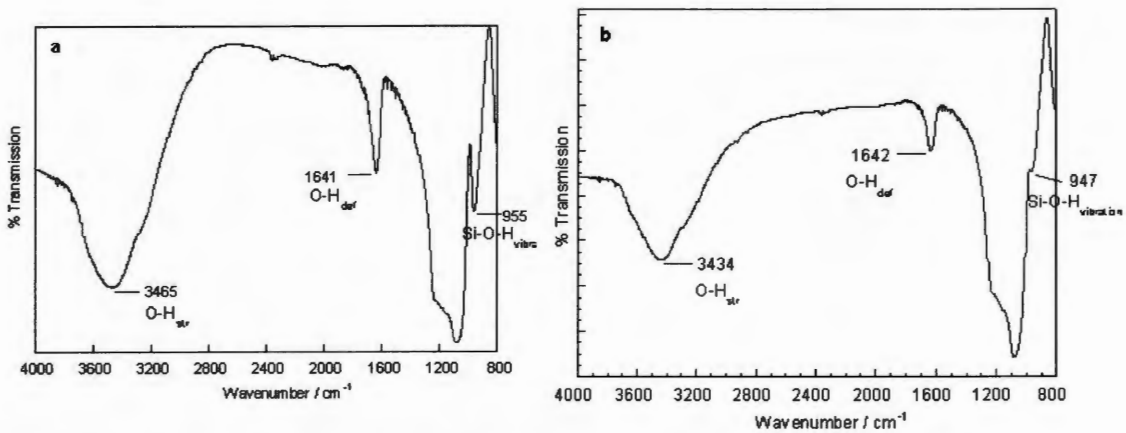

Figure 3.24 The IR spectrum of the calcined Si-MCM 41 material, (a) after water sorption, (b) before water sorption (Fig. 3.6 reproduced here for comparison).

3.4.4 n-Hexane Sorption

n-Hexane is a non-polar, hydrophobic molecule and its sorption isotherm could be useful in exploring the hydrophobic property of the surface. In the current work, the other adsorptives used are, water (polar molecule, to explore hydrophilic property of a surface) and MeOH, *n*-BuOH, *t*-BuOH (having both hydrophilic and organophilic nature) (Section 3.4.5). The sorption isotherms of water and *n*-hexane were used as two extremes (organophilic and hydrophobic ends) to study the sorption of MeOH, *n*-BuOH and *t*-BuOH.

Fig. 3.25 shows the sorption isotherm of *n*-hexane at 303 K for the Si-MCM 41 material. The isotherm was found to be difficult to classify according to the IUPAC classification (Chapter 2, Section 2.10), and similar to that reported by Hansen *et al.*[45] The isotherm is reversible with no evident hysterisis loop. No chemisorption of *n*-hexane on the pore surface is observed, as expected. The final plateau of the isotherm

yielded a Gurvitsch pore volume of 0.57 cm^3 g^{-1}, which was lower than those derived from other sorptives apart from water (See Table 3.10). A possible explanation for this is the larger size and the shape (straight chain) of the *n*-hexane molecule, which may restrict close packing and access of the molecules inside the pores. The validity of n_m (BET) is questionable since the BET plot was non-linear and therefore, the n_m value and the corresponding surface area derived from *n*-hexane isotherm may not be directly comparable with values derived from other adsorptives.

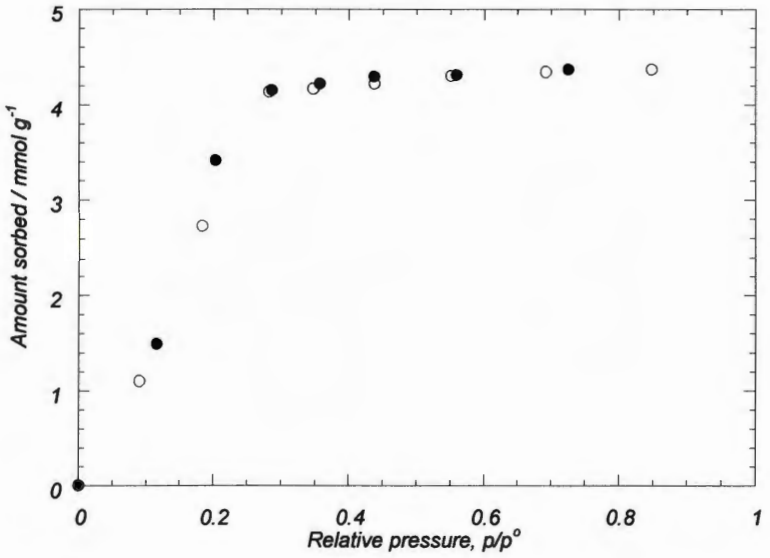

Figure 3.25 Sorption isotherm of *n*-Hexane (303 K) for the Si-MCM 41 material. Filled symbols denote desorption points.

The isotherm in Fig. 3.25 shows the absence of a sharp knee at low relative pressure but a sharp increase in the amount of *n*-hexane adsorbed is observed at p/p^o = 0.15, which levels off at p/p^o *ca.* 0.25 and represents condensation in the mesopores. The low initial uptake of *n*-hexane at low relative pressure suggested the restricted diffusion of *n*-hexane within the pores.[45] This may be explained by the hydrophobic nature of the Si-MCM 41 surface.

3.4.5 Sorption of Alcohols

This Section concerns the sorption of alcohols (MeOH, *n*-BuOH and *t*-BuOH) to study the surface characteristics and the pore properties of the Si-MCM 41 material. Sorption isotherms of the isomers *n*-BuOH and *t*-BuOH, a long chain molecule and a spherical shape molecule, respectively, enables exploration of the adsorption process *i.e.* whether its shape sensitive and whether the adsorption proceeds *via* the organophilic or hydrophilic interactions. They may also be used as a probe to study the porous nature of the material. The sorption isotherms of alcohols are compared with those of water (hydrophilic) and of *n*-hexane (organophilic), as the alcohol molecules possess both the characteristics. The surface area and the pore diameter values were compared with those derived from nitrogen (standard probe).

3.4.5.1 Methanol Sorption

Methanol sorption (MeOH) at 303 K for the Si-MCM 41 material yielded a Type IV isotherm as shown in Fig. 3.26. The isotherm has the characteristic shape shown by mesoporous solids *i.e.* monolayer-multilayer adsorption followed by capillary condensation. The isotherm is reproducible and reversible with no hysteresis loop present between the adsorption and desorption branch. Capillary condensation starts at higher relative pressure (p/p^o *ca.* 0.4) compared with that of nitrogen (p/p^o *ca.* 0.2), which levels off at p/p^o *ca.* 0.6 and shows complete complete filling of the mesopores by MeOH. The final plateau of the isotherm yielded a Gurvitsch pore volume of 0.70 $cm^3\ g^{-1}$, which is in good agreement with the nitrogen derived pore volume (0.74 $cm^3\ g^{-1}$). The material showed a BET surface area of 640 ± 50 $m^2\ g^{-1}$, which is much smaller when compared with the nitrogen (1150 $m^2\ g^{-1}$) and *t*-BuOH (840 $m^2\ g^{-1}$) derived surface areas. Although, the size of the MeOH molecule is smaller than *t*-BuOH it yields a smaller BET surface area *i.e.* indicating MeOH has restricted adsorption on

the surface. This suggested that the adsorption of MeOH was more influenced by its unhindered polar groups (–OH) compared with the *t*-BuOH, where the –OH group is embedded in the bulky methyl groups. Thus, for MeOH sorption the interaction of the polar –OH groups with the surface hydroxyl groups restricts complete monolayer formation on the pore walls resulting in a reduced value of the calculated surface area.

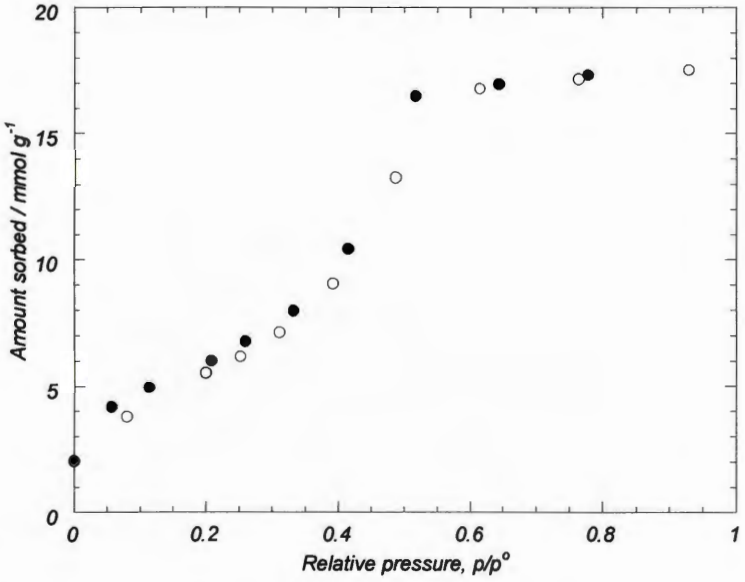

Figure 3.26 MeOH sorption isotherm (303 K) for the Si-MCM 41 material. Filled symbols denote desorption points.

The isotherm shows that the MeOH is retained on the surface, even after exposing the sample to a high vacuum (*ca.* 10^{-5} torr), and yielded a chemisorption value of 2.0 mmol g^{-1} (Table 3.12). The chemisorption of MeOH can be used to calculate the number of hydroxyl groups present on the surface. The number of hydroxyl groups derived from MeOH sorption (1.0 nm^2) was consistent with the number of hydroxyl groups derived from water sorption (1.0 nm^2). Table 3.12 shows the calculated monolayer capacity and the number of hydroxyl groups derived from different adsorptives for the Si-MCM 41 material.

Table 3.12 Summary of the chemisorption, monolayer capacity and the number of hydroxyl groups calculated for different adsorptives

Adsorptive	Chemisorption* / mmol g^{-1}	Monolayer† capacity / mmol g^{-1}	Number of –OH groups / nm^2	
			‡	§
Nitrogen	no	11.9	--	--
H_2O	2.0	1.2	0.63	1.0
MeOH	2.0	5.9	3.0	1.0
n-BuOH	2.8	3.6	1.9	1.5
t-BuOH	2.0	4.4	2.3	1.0
n-Hexane	no	3.4	--	--

* *Value after complete desorption and exposing to a vacuum of* $< 10^{-5}$ *torr.*
† *Monolayer capacity calculated from the BET plot.*
‡ *Hydroxyl groups derived from monolayer capacity.*
§ *Hydroxyl groups derived from chemisorption of adsorptive.*

The chemisorption of methanol on the Si-MCM 41 material was confirmed by FTIR spectroscopic analysis. The Fig. 3.27 shows an IR spectrum of Si-MCM 41 after methanol sorption. The spectrum shows the presence of an IR absorption band at 2860 cm^{-1} and 2960 cm^{-1} for the C–H stretching vibration of the $-CH_3$ group of methanol.[21, 46]

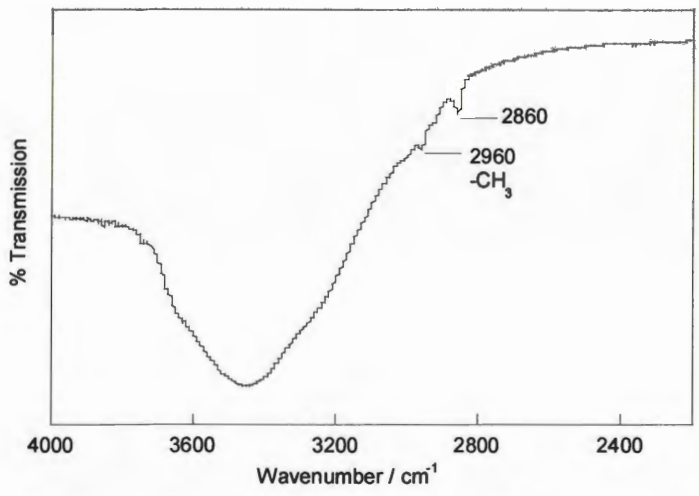

Figure 3.27 The IR spectrum of the calcined Si-MCM 41 material after methanol sorption.

3.4.5.2 n-Butanol Sorption

n-Butanol (*n*-BuOH) sorption at 303 K for the Si-MCM 41 material yielded a Type IV isotherm, as shown in Fig. 3.28.

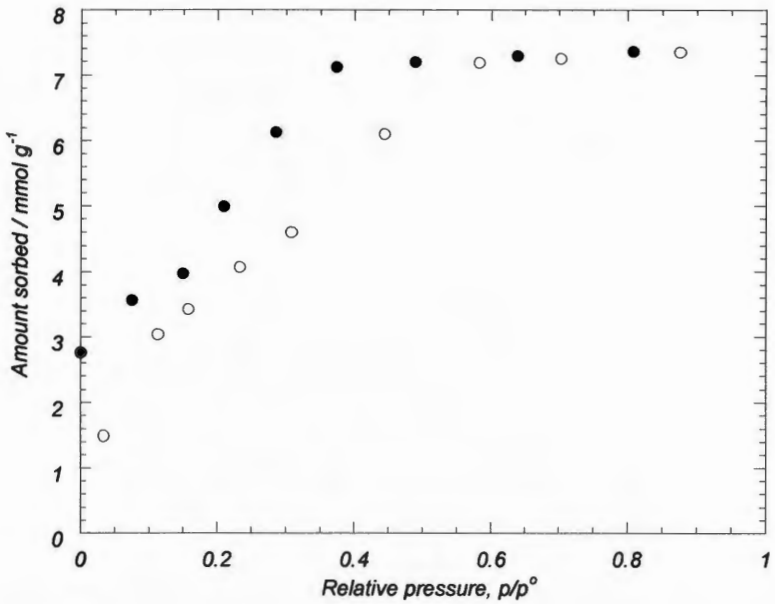

Figure 3.28 *n*-BuOH sorption isotherm (303 K) for the Si-MCM 41 material. Filled symbols denote desorption points.

The isotherm shows an inflection at p/p^o *ca.* 0.25 for capillary condensation, which levels off at p/p^o *ca.* 0.6. The capillary condensation step is not as sharp when compared with the MeOH and *t*-BuOH sorption isotherms and shows a gentle and gradual increase in the amount of adsorbed *n*-BuOH with increasing pressure. The isotherm shows a low-pressure hysteresis, which does not close and indicates chemisorption of *n*-BuOH on Si-MCM 41 surface (even after exposing the sample to a high vacuum, 10^{-5} torr). Thus, assuming that one *n*-BuOH molecule chemisorbs with one surface hydroxyl group, it is possible to calculate the number of hydroxyl groups per unit area (nm^{-2}). The n_m value derived from *n*-BuOH sorption is three times greater than that derived from water sorption (Table 3.12). This suggests that adsorption of

n-BuOH on a surface was favoured by both the organic end and the polar end of a molecule. Hence, the n_m value from *n*-BuOH sorption does not correspond with the number of hydroxyl groups on a surface. However, the chemisorption value can be used for the calculation of surface hydroxyl groups.

The material yielded a chemisorption value of 2.8 mmol g^{-1} (from *n*-BuOH sorption), slightly higher than the value, 2.0 mmol g^{-1}, derived from other adsorptives (Table 3.12). Thus, the number of hydroxyl groups derived from *n*-BuOH sorption (1.5 nm^2) was higher than the value derived from other adsorptives, 1.0 nm^2 (Table 3.12). The presence of low pressure hysteresis and the higher chemisorption value suggests that the adsorption of *n*-BuOH on the Si-MCM 41 surface was favoured by polar interaction whereas MeOH and *t*-BuOH are less so. The equilibration time required for the sorption of *n*-BuOH (3-5 h) was much longer compared with the *t*-BuOH (2-3 h), which suggested that the diffusion of *n*-BuOH is slower, because it has restricted access on the hydrophobic surface and within the pores, possibly due to the shape of the molecule.

3.4.5.3 t-Butanol Sorption

The sorption isotherm of *t*-butanol (*t*-BuOH) at 303 K for the Si-MCM 41 material is shown in Fig. 3.29. The shape of the isotherm from *t*-BuOH sorption is similar to that of the corresponding isotherm of MeOH (Fig. 3.24). However, the isotherm from *t*-BuOH shows a slight shift in the capillary condensation step towards a low relative pressure (p/p^o *ca.* 0.15), which levels off at p/p^o *ca.* 0.35. This could be due to the bulky, spherical shape of the *t*-BuOH molecule, which causes faster filling of the pores compared with the MeOH and *n*-BuOH. The isotherm is reversible with no hysteresis, similar to the methanol sorption, but is in contrast with the *n*-BuOH sorption isotherm (hysteresis present).

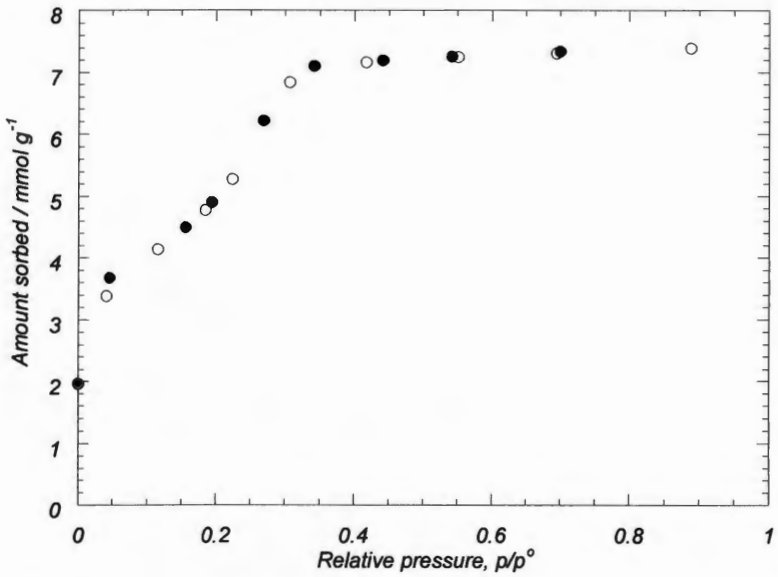

Figure 3.29 *t*-BuOH sorption isotherm (303 K) for the Si-MCM 41 material. Filled symbols denote desorption points.

The material yielded a Gurvitsch pore volume of 0.69 $cm^3\ g^{-1}$, which was in good agreement with the nitrogen, methanol and *n*-BuOH derived pore volumes (Table 3.10). The amount chemisorbed (2.0 mmol g^{-1}), obtained after complete desorption and exposing the sample to vacuum (< 10^{-5} torr) was found to be in good agreement with other adsorptives apart from *n*-BuOH (see Table 3.12). Again the number of hydroxyl groups (1.0 nm^2) derived from *t*-BuOH sorption was consistent with those values derived from other adsorptives apart from *n*-BuOH (1.5 nm^2).

A sharp 'knee' is clearly evident, at low relative pressure, in the sorption isotherm of *t*-BuOH, whereas it is somewhat rounded in the sorption isotherms of MeOH and *n*-BuOH. The monolayer capacity obtained from the sharp 'knee' was used for the calculation of BET surface area. The material showed a high surface area of 840 $m^2\ g^{-1}$ compared to 672 $m^2\ g^{-1}$ and 640 $m^2\ g^{-1}$ derived from *n*-BuOH and MeOH, respectively. However, for the calculation of surface area the value of a_m in this case was derived using equation 2.14 (Chapter 2, Section 2.10.4). The equation is based on a

model, which assumes spherical molecules and hexagonal-packing, that is inaccurate in the case for *n*-BuOH (a straight-chain alcohol). For this reason, it is the monolayer capacity which is of real interest for comparison here.

The *n*-BuOH derived BET monolayer capacity (n_m = 3.6 mmol g^{-1}) was lower than those derived from MeOH (n_m = 5.9 mmol g^{-1}) and *t*-BuOH (n_m = 4.4 mmol g^{-1}), but was much higher than the 'monolayer capacity' of water (n_m = 1.2 mmol g^{-1}). The results are summarised in Table 3.12. The higher value of n_m for all the alcohols compared with water indicated that the adsorptions of alcohols occurred *via* both the organic and the polar ends of the molecules. The higher n_m value for MeOH may be explained both by its smaller size (which takes up less space on the adsorption sites), and that its adsorption in the pores was less sterically hindered compared with the larger sizes of *n*-BuOH and *t*-BuOH molecules. The higher value of n_m for the *t*-BuOH compared with the *n*-BuOH suggested that the adsorption of *t*-BuOH occurred preferentially *via* organophilic interactions rather than hydrophilic interactions. This may be explained by the -OH groups in the *t*-BuOH molecule ('spherical' shape) being embedded within the bulky methyl groups, compared with the *n*-BuOH and MeOH where the –OH groups are free to interact with surface hydroxyls. The considerably lower value of n_m obtained for water sorption (1.2 mmol g^{-1}) compared with the other adsorptives (see Table 3.12) was explained by its localised adsorption on the surface due to the polar interaction with surface hydroxyl groups. The BET surface areas and the total pore volumes derived from all the adsorptives are summarised in Table 3.10.

The IR spectra of the Si-MCM 41 material after *n*-BuOH and *t*-BuOH sorption are presented in Fig. 3.30 and Fig. 3.31, respectively.

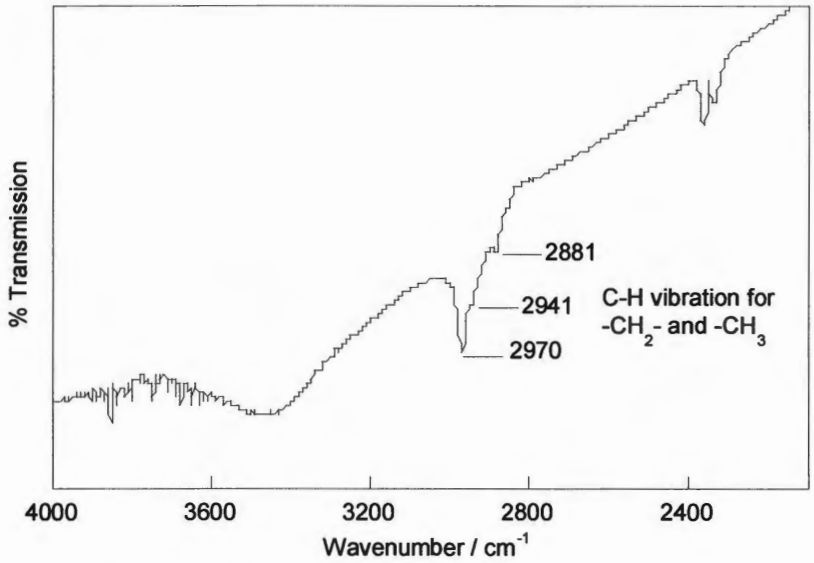

Figure 3.30 The IR spectrum of the calcined Si-MCM 41 material after *n*-BuOH sorption.

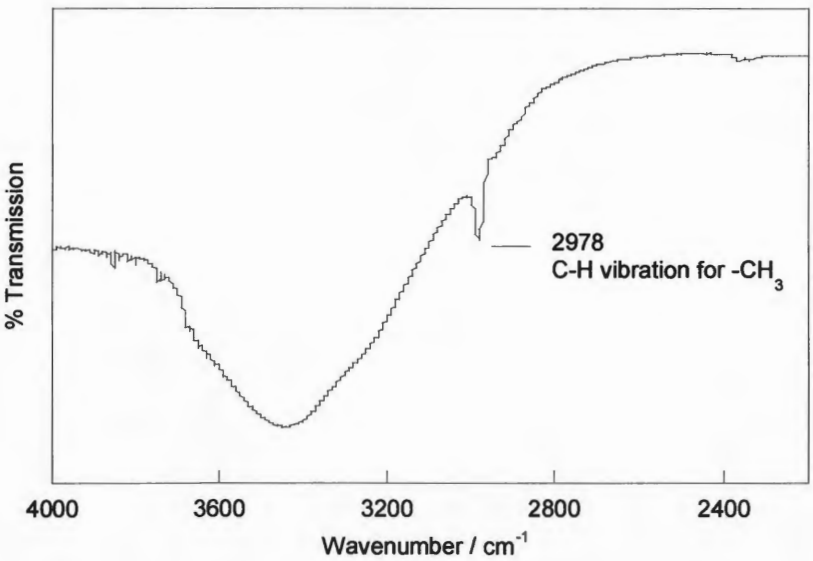

Figure 3.31 The IR spectrum of the calcined Si-MCM 41 material after *t*-BuOH sorption.

The spectra provided clear evidence for the chemisorption of *n*-BuOH and *t*-BuOH on the Si-MCM 41 surface. The IR spectrum for the *n*-BuOH sorption shows

two bands at 2881 cm^{-1} and 2941 cm^{-1}, assigned for the C-H stretching vibrations of the $-CH_2-$ and $-CH_3$ groups in *n*-BuOH. A marked decrease in the intensity of the band for surface hydroxyl groups at 3400 cm^{-1} is observed, which results from the chemisorption of *n*-BuOH. The IR spectrum for a sample after *t*-BuOH sorption shows a single and sharp band at 2978 cm^{-1}, which is assigned to the C-H stretching vibrations of the $-CH_3$ species of the *t*-BuOH molecule.[21, 46] These bands were absent before adsorption (see Fig. 3.6).

3.5 Conclusions

Standard methods were used to synthesise two types of Si-MCM 41 materials. The unswollen Si-MCM 41 material was synthesised by the method reported by Schmidt[6] and Bambrough[7]. Larger pore MCM 41 materials were synthesised using mesitylene as a pore-swelling agent, and characterised by *p*-XRD, IR spectroscopy, TEM, NMR spectroscopy, XPS, CHN microanalysis and by gas and vapour sorption. The Si-MCM 41 materials were used as solid supports for functionalisation and the characterisation results were used for comparison with the modified samples.

The hexagonal periodicity of the synthesised materials was confirmed by *p*-XRD, which shows an intense d_{100} peak and three less intense peaks below $2\theta = 10^{o}$. The shift in the d_{100} peak towards lower 2θ values in the *p*-XRD pattern of the mesitylene swollen MCM 41 reflected the incremental addition of mesitylene and this confirmed that the materials with larger pore diameters were formed.

The IR spectrum of the calcined Si-MCM 41 material showed a weak band at 947 cm^{-1} from siloxane groups present on the surface, suggesting that the surface dehydroxylates on calcination. The TEM analysis showed that the synthesised material has a tubular structure. The CHN microanalysis confirmed that the material was free from any organic contaminants.

The mesoporosity of the synthesised materials was confirmed by the Type IV isotherms obtained for nitrogen (77 K), CO_2 (195 K), MeOH, *n*-BuOH and *t*-BuOH (303 K) sorptions, and Type V isotherms for water sorption (303 K).

The Type V nature of the water sorption isotherm (303 K) confirmed that the material has a predominantly hydrophobic surface and adsorption of water is *via* polar interaction with the surface. The large degree of hysteresis extending in the low-pressure range ($0 < p/p^o < 0.60$) is due to rehydroxylation of the Si-MCM 41 surface following the chemisorption of water. The sorption isotherm of *n*-hexane is difficult to classify according to the IUPAC classification, which suggests restricted diffusion over the hydrophobic surface. The shape of the *n*-hexane sorption isotherm indicates the high organophilic character of the surface. The adsorption of alcohols was found to be intermediate in character between water and *n*-hexane. This suggests that adsorption of the alcohols takes place both by hydrophilic interactions involving –OH groups, and by organophilic interactions involving the alkyl groups with the surface.

The materials synthesised yielded high nitrogen-derived surface areas (*ca.* 1150 $m^2\ g^{-1}$), pore volumes (*ca.* 0.74 $cm^3\ g^{-1}$) and average pore diameters (*ca.* 26 Å), which are typical for mesoporous materials. The larger pore (39 Å) MCM 41 material (synthesised using 33.4 mmol of mesitylene/synthesis batch) showed an expected decrease in the surface area (360 $m^2\ g^{-1}$) and pore volume (0.3 $cm^3\ g^{-1}$) as the number of pores per unit area decreases with increase in the pore diameter.

The CO_2 adsorption showed a lower surface area (580 $m^2\ g^{-1}$) and a shift in capillary condensation towards higher p/p^o (*ca.* 0.60) compared with the nitrogen sorption (p/p^o *ca.* 0.30). This suggests that the adsorption of CO_2 proceeds *via* polar interaction with the MCM 41 surface, resulting in site-specific adsorption rather than *via* monolayer formation.

3.6 References:

1. J. S. Beck and J. C. Vartuli, *Solid State and Mater. Sci.*, 1996, **1**, 76.
2. G. Øye, J. Sjöblom and M. Stöcker, *Adv. Colliod and Interface Sci.*, 2001, **89-90**, 439.
3. M. Stöcker, *Micropor. Mesopor. Mater.*, 1999, **27**, 131.
4. A. Corma, *Chem. Rev.*, 1997, **97**, 2373.
5. G. S. Attard, J. C. Glyde and C. G. Göltner, *Nature*, 1995, **378**, 366.
6. (a) R. Schmidt, M. Stocker and D. Akporiaye, *J. Chem. Soc., Chem. Commun.*, 1994, 1493.

   (b) D. Kumar, K. Schumacher, C. Hohenesche, M. Grun and K. K. Unger, *Colloids and Surfaces A: Physiochem. Eng. Aspects*, 2001, **187-188**, 109.
7. C. M. Bambrough, *PhD Thesis,* The Open University, 1998.
8. J. C. Vartuli, K. D. Schmitt and C. T. Kresge, *Chem. Mater.*, 1994, **6**, 2317.
9. G. Brewer, J. Jasinski, W. Mahany, L. May and S. Prytkov, *Inorganica Chimica Acta.*, 1995, **232**, 183.
10. V. B. Fenelonov, V. N. Romannikov and A. Y. Derevyankin, *Micropor. Mesopor. Mater.*, 1999, **28**, 57.
11. C. Fowler, S. Burkett and S. Mann, *J. Chem. Soc., Chem. Commun.*, 1997, 1769.
12. C. Y. Chen, H. X. Li and M. E. Davies, *Micropor. Mater.*, 1993, **2**, 17.
13. R. J. P. Corriu, A. Mehdi and C. Reyé, *C. R. Acad. Sci. Paris,* 1999, 35.
14. J. C. Vartuli, J. S. Beck and W. J. Roth, *J. Am. Chem. Soc.*, 1992, **114**, 10834.
15. C. Bambrough, R. Slade and R. T. Williams, *J. Mater. Chem.*, 1998, **8(3)**, 569.
16. Z. Zhidong, Z. Chang and L. Kevan, *J. Phys. Chem. B*, 1996, **103**, 2680.
17. S. Schacht, M. Janicke and F. Schuth, *Micropor. Mesopor. Mater.*, 1998, **22**, 485.
18. N. Ulagappan and C. N. R. Rao, *J. Chem. Soc., Chem. Commun.*, 1996, 2759.
19. S. Burkett, S. D. Sims and S. Mann, *J. Chem. Soc., Chem. Commun.*, 1996, 1367.

20. D. J. Macquarrie, *J. Chem. Soc., Chem. Commun.*, 1996, 1961.

21. K. Nakamoto, "*Infrared and Raman Spectra of Inorganic and Coordination Compounds*", 4th Edition, John Wiley and Sons, USA, 1986.

22. A. N. Lazarev, "*Vibrational Spectroscopy and Structure of Silicates*", Plenum Press, New York, 1972.

23. E. Flanigen, H. Khatami and H. A. Szymanski, *Adv. Chem. Ser.*, 1971, **101**, 201.

24. Y. Y. Zhong, S. Q. Liu, T. H. Chen and L. Z. Wang, *J. Chem. Soc., Chem. Commun.*, 1995, 973.

25. G. Calleja, R. V. Grieken, R. Gracia, J. A. Melero and J. Iglesias, *J. Mol. Catal. A Chem.*, 2002, **182–183**, 215.

26. D. Brunel, A. Cauvel, F. Di Renzo, F. Fajula, B. Fubini, B. Onida and E. Garrone, *New J. Chem.*, 2000, **24**, 807.

27. J. F. Moulder, W. F. Stickle, P. E. Sobol and K. D. Bomben, "*Handbook of X-Ray Photoelectron Spectra- A Reference Book of Standard Spectra for Identification and Interpretation of XPS Data*", ed. by J. Chastain, Perkin-Elmer Corporation, Eden Prairie, Minnesota, USA, 1992.

28. P. Kooyman, M. Verhoel and E. Prouzet, *Stud. Surf. Sci. and Catal.*, **129**, 921.

29. S. Schacht, M. Janicke and F. Schüth, *Micropor. Mesopor. Mater.*, 1998, **22**, 485.

30. Z. Liu, Y. Sakamoto, T. Ohsuna, O. Terasaki and C. H. Ko, *Angew. Chem. Int. Ed.*, 2000, **39**(17), 3107.

31. V. Alfredson, M. Keung, A. Monnier, G. Stucky and K. Unger, *J. Chem. Soc., Chem. Commun.*, 1994, 921.

32. J. Aguado, D. Serrano and J. Escola, *Micropor. Mesopor. Mater.*, 2000, **34**, 43.

33. M. Pillinger, I. Goncalves, A. Lopes, J. Madureira, P. Ferreira, A. Valente, T. Santos, J, Rocha, J. F. Menezes and L. D. Carlos, *J. Chem. Soc., Dalton Trans.*, 2001, 1628.

34. Cabrera, J. Haskouri, S. Mendioroz, C. Guillen, J. Latorre, A. Beltrán-Porter, M. Marcos and P. Amorós, *J. Chem. Soc., Chem. Commun.*, 1999, 1679.

35. S. J. Gregg and K. S. W. Sing, *"Adsorption, Surface Area and Porosity"*, 2nd Edition, Academic Press, London, 1982.

36. P. J. Branton, *PhD Thesis*, University of Exeter, 1994.

37. P. Branton, P. Hall and K. W. Singh, *J. Chem. Soc., Chem. Commun.*, 1993, 1257.

38. C. G. Göltner, B. Smarsly, B. Berton and M. Antonietti, *Chem. Mater.*, 2001, **13**(5), 1617.

39. C. M . Bambrough, R. C. T. Slade, R. T. Williams, S. L. Burkett, S. D. Sims and S. Mann, *J. Colloid and Interface Sci.*, 1998, **201**, 220.

40. M. Thommes, R. Kohn and M. Froba, *Appl. Surf. Sci.*, 2002, **7843**, 1.

41. P. J. Branton, P. G. Hall, M. Treguer and K. S. W. Sing, *J. Chem. Soc., Faraday Trans.*, 1995, **91(13)**, 2041.

42. A. V. Kiselev, A. A. Lopatkin and A. A. Shugla, *Zeolites*, 1985, **5**, 261.

43. P. Graham, A. D. Hughes and L. V. C. Rees, *Gas Separation Technology*, Elsevier Science Publisher, Amsterdam, 1990, p. 215.

44. V. R. Choudhary and S. Mayadevi, *Zeolites*, 1996, **13**, 501.

45. F. Courivaud, E. W. Hansen, S. Kolboe, A. Karlsson and M. Stocker, *Micropor. Mesopor. Mater.*, 2000, **37**, 223.

46. D. Brunel, A. Cauvel, F. DiRenzo, F. Fajula, B. Fubini, B. Onida and E. Garrone, *New J. Chem.*, 2000, **24**, 807.

47. A. M. James and M. P. Lord, "*Macmillan's Chemical and Physical data*", The Macmillan Press Ltd., London, 1992.

CHAPTER 4

METAL-FUNCTIONALISED MCM 41 MATERIALS

4.1 Introduction

Si-MCM 41 material, discussed in Chapter 3, is used extensively as a solid support[1, 2, 3] and has the potential as a solid catalyst because of its high surface area, mesoporosity with narrow pore size distribution and high pore volume. Its application as a catalyst is currently limited (mild acidic property and a neutral framework) and, hence, has attracted the interest of researchers throughout the world to develop its catalytic potential. Some of the reported methods[4] used to enhance the catalytic properties of this material are:

- Incorporation of metal ions by isomorphic substitution of framework silicon with metal ions *via* a sol-gel synthesis method.
- Post-synthetic grafting of metal ions / organic functional groups / metal complexes.
- *In-situ* grafting of metal ions using metal surfactants.

This Chapter mainly concerns the synthesis of titanium- and iron- (Fe-II, Fe-III) functionalised MCM 41 materials by two of the above methods (sol-gel synthesis and post-synthetic grafting) and their characterisation using different techniques (discussed in Chapter 2). Samples of Ti-functionalised MCM 41 subjected to amnolysis (Section 4.2.2.3) were also studied in order to investigate the effect of changes in the surface characteristics of the materials.

This Chapter also discusses the results of sorption of nitrogen and the hexene isomers (1-hexene and 3,3-dimethyl-1-butene) by Ruthenium MCM 41 (Ru-MCM 41). This material was supplied by Bruce *et al.*[5] (University of Exeter), and was synthesised by *in-situ* grafting of metal using a ruthenium complex as the template. The synthesis exploits the dual functionality of the ruthenium complex as both the structure directing and catalytic site generation agent in the synthesis of Ru-MCM 41. The material synthesised had shown improved catalytic activity in the hydrogenation of 1-hexene to 1-hexane upon heat-treatment[6] (at 623 K for 16 h under reduced pressure of $< 10^{-5}$ torr). The work reported here is the study of the effect of heat-treatment on the sorption characteristics of Ru-MCM 41 by the adsorption of nitrogen (77 K), 1-hexene and 3,3-dimethyl-1-butene (303 K) before and after heat treatment of the material.

Table 4.1 summarises the metal-functionalised MCM 41 materials synthesised together with the analytical techniques used for their characterisation.

Table 4.1 Summary of the metal-functionalised MCM 41 synthesised and the different analytical techniques used for their characterisation

Materials	Abbreviations used	Physico-chemical Characterisation					V	G
		XRD	IR	XPS	CHN*	Mössbauer†		
Fe(II) MCM 41								
i) Sol-gel synthesis	Fe-MCM-**a**	✓	✓			✓	✓	
ii) Grafted MCM 41	Fe-MCM-**b**	✓	✓			✓	✓	
Fe(III) MCM 41								
i) Sol-gel synthesis	Fe-MCM-**c**	✓	✓			✓	✓	
ii) Grafted MCM 41	Fe-MCM-**d**	✓	✓			✓	✓	
Ti MCM 41								
i) Sol-gel synthesis	Ti-MCM-**e**	✓	✓	✓			✓	
ii) Grafted MCM 41	Ti-MCM-**f**	✓	✓	✓			✓	
iii) Amnolysis of Ti-MCM-**e**	Ti-MCM-**g**	✓	✓	✓	✓		✓	
iv) Amnolysis of Ti-MCM-**f**	Ti-MCM-**h**	✓	✓	✓	✓		✓	
Ru-MCM 41	Ru-MCM 41§						✓	✓

***V** = Volumetric sorption of nitrogen and CO_2, **G** = Gravimetric sorption of 1-hexene and 3,3-dimethyl-1-butene, * CHN microanalysis, † Mössbauer Spectroscopy*
§ Material supplied by Bruce et al.[5]
*Ti-MCM-**g** = Ti-MCM-**g**-773, Ti-MCM-**g**-823 and Ti-MCM-**g**-873 (Fig. 4.4)*

4.2 Synthesis

4.2.1 Fe-MCM 41[7, 8, 9]

4.2.1.1 Sol-gel Synthesis of Fe-MCM 41[8, 9] *(Samples, Fe-MCM-**a** and Fe-MCM-**c**)*

The Fe-MCM-**a** material was prepared as follows: Cetyltrimethylammonium chloride (CTMACl) (3.29 g, 2.60 mmol) was added to a solution of NaOH (0.65g, 16.30 mmol)

in water (45 cm^3). The resulting mixture was stirred for 15 min and TEOS (5.32 g, 25.60 mmol) was slowly added with stirring. When a white suspension started to form, $FeSO_4 \cdot 7H_2O$ (0.26 g, 1.00 mmol) was added. The brown gel formed was stirred for 48 h and then heated in a Teflon-lined autoclave for 24 h at 383 K. The brown product was filtered off, washed with water (300 cm^3) and then calcined at 823 K for 6 h in air at a heating rate of 333 K h^{-1}.[10]

For Fe-MCM-**c** material the synthesis procedure was similar to that for Fe-MCM-**a** as discussed above, using $Fe_2(SO_4)_3 \cdot 5H_2O$ (0.12 g 2.50 mmol) as the iron source. The flow diagram for the synthesis of Fe-MCM-**a** and Fe-MCM-**c** is shown in Fig. 4.1.

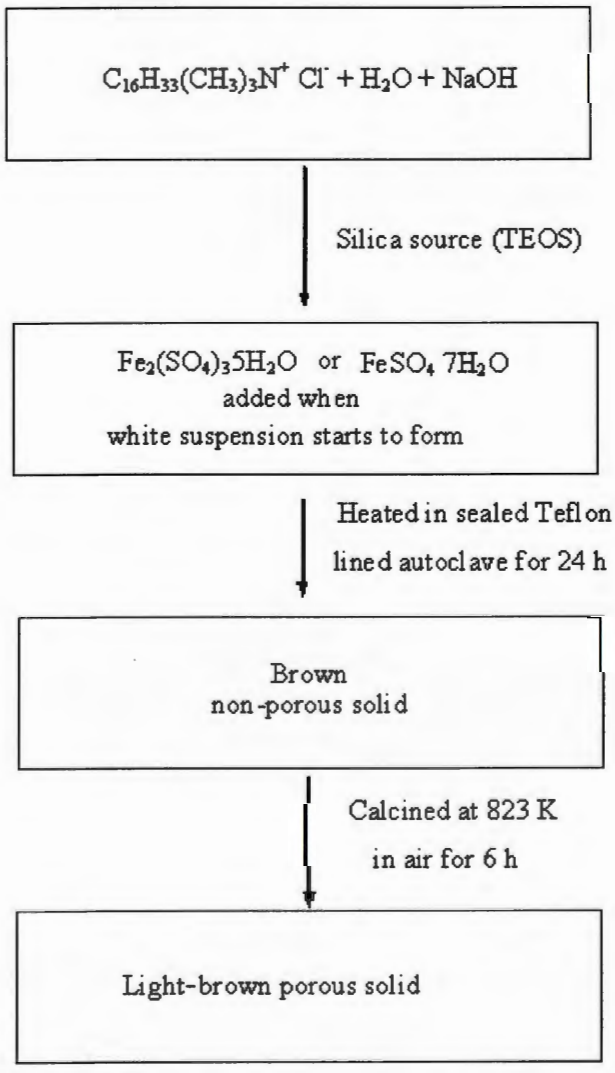

Figure 4.1 Flow diagram for the sol-gel synthesis of Fe-MCM 41.

4.2.1.2 Grafted Fe-MCM 41[11] *(Samples, Fe-MCM-**b** and Fe-MCM-**d**)*

Synthesis of the Salen Ligand [12]

A solution of ethylenediamine (0.63 g, 0.01 mol) in methanol (25 cm^3) was mixed with a solution of salicylaldehyde (2.46 g, 0.02 mol) in methanol (50 cm^3) and refluxed for 3 h. The yellow crystals obtained were filtered, washed with methanol (30 cm^3) and then dried, initially under reduced pressure, and finally in an oven at 323 K for 5 h. The product obtained was characterised by CHN microanalysis and IR spectroscopy.

Synthesis of the Fe-salen Complex[13]

The salen ligand (0.50 g, 1.55 mmol) was dissolved in hot ethanol (70 cm^3) with stirring. To this was added slowly (drop wise), $FeCl_2$ (0.29 g of 42.2 % Fe(II), 2.28 mmol) dissolved in ethanol (20 cm^3) followed by the addition of triethyl amine (0.41 g, 1.00 mmol) dissolved in ethanol (15 cm^3). The resulting mixture was refluxed for half an hour with stirring. The reaction mixture was then allowed to evaporate slowly for 12 h to form crystals. The chocolate brown crystals obtained were filtered and washed with ethanol (5 × 10 cm^3), dried under reduced pressure and then in a fumehood overnight. The product obtained was characterised by CHN microanalysis and IR spectroscopy. In the synthesis of the Fe(III)-salen complex, $FeCl_3 \cdot 6H_2O$ (0.42 g, 1.55 mmol) was used in place of $FeCl_2$ and the synthesis procedure was the same as that described for the Fe(II)-salen complex.

Post-synthetic Grafting of Fe on Si-MCM 41[10,11,13]

Calcined Si-MCM 41 (0.6 g) was added to toluene (30 cm^3) and the resulting suspension was refluxed for half an hour with stirring. To this was added Fe(II)-salen complex (0.20 g, 0.53 mmol) and the mixture was refluxed for further 3 h with continuous stirring. The light-brown product obtained was cooled, filtered, washed with

ethanol (25 cm^3), and then dried, initially under reduced pressure, and then in an oven at 323 K for 5 h. Finally it was calcined at 813 K for 2 h at a heating rate of 313 K h^{-1} to burn off the organic part (salen complex). In the synthesis of Fe(III)-grafted MCM 41, Fe(III)-salen complex (0.20 g, 0.53 mmol) was used in place of the Fe(II)-Salen complex and the synthesis procedure was the same as described for the Fe(II)-MCM 41. The flow diagram for the synthesis of Fe-MCM-**b** and Fe-MCM-**d** is shown in Fig. 4.2.

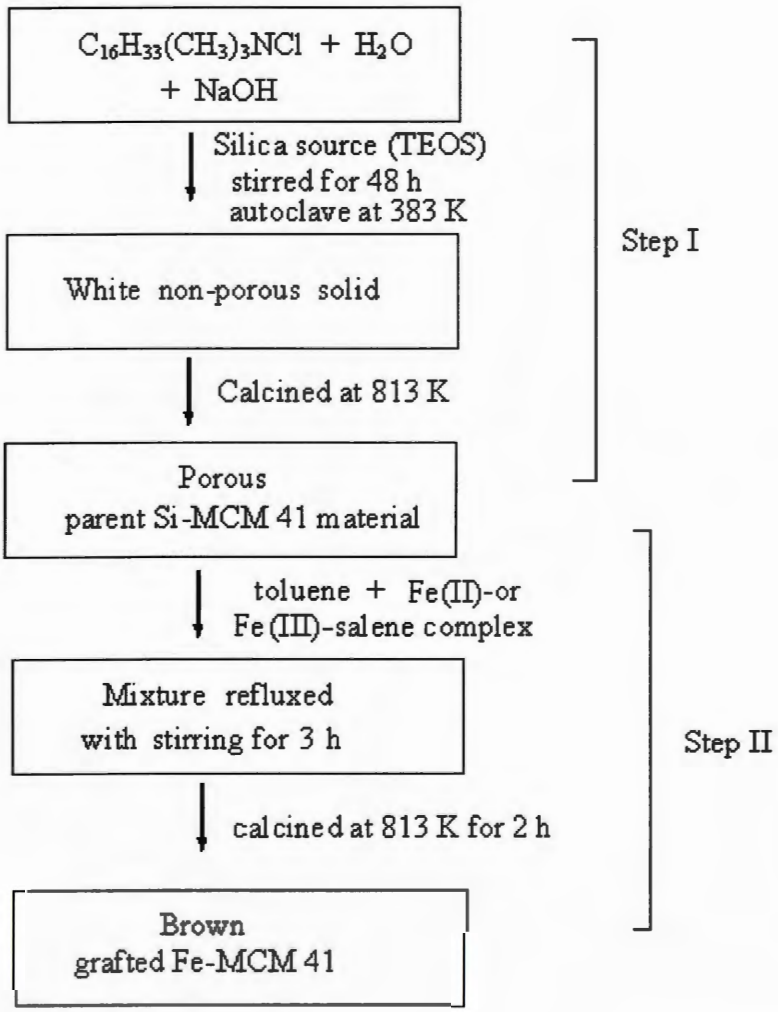

Figure 4.2 Flow diagram for the synthesis of grafted Fe-MCM 41.

4.2.2 Ti-MCM 41[14]

4.2.2.1 Sol-gel Synthesis of Ti-MCM 41[15,16] *(Ti-MCM-e)*

CTMACl (4.80 g, 3.75 mmol) was added to a solution of NaOH (0.75 g, 18.70 mmol) in water (60 cm^3), and the resulting mixture was stirred for 20 min. TEOS (7.19 g, 34.50 mmol) was slowly added and the stirring continued until a white suspension started to form at which point titanium (IV) butoxide (0.38 cm^3) was added slowly with stirring. The resulting white suspension (with Si:Ti ratio of 1:19) was stirred for 48 h at room temperature and then heated in an autoclave for 24 h at 383 K. The white product was filtered, washed with water (2 × 200 cm^3), dried overnight in an oven at 323 K and then calcined at 813 K for 6 h in air at a heating rate of 333 K h^{-1}.

4.2.2.2 Post-synthetic Grafting of Titanium on Si-MCM 41[15] *(Ti-MCM-f)*

Calcined Si-MCM 41 (1.50 g) was added to ethanol (40 cm^3, dried over calcium oxide) and the resulting suspension was stirred for one hour at 318 K under nitrogen. Titanium (IV) butoxide (0.51 cm^3) was then added and the suspension stirred for a further hour at 318 K. The product obtained was cooled, filtered, washed with ethanol (25 cm^3), and then dried, initially under reduced pressure and then in an oven at 323 K for 5 h. Finally it was calcined at 813 K for 4 h in air at a heating rate of 333 K h^{-1} to burn off the organic part (butoxide).

*4.2.2.3 Amnolysis of Ti-MCM 41 Material (*Ti-MCM-**g** and Ti-MCM-**h**)

Amnolysis of both the sol-gel synthesised and the grafted Ti-MCM 41 materials was carried out in a tube furnace at four different temperatures (773, 823, 873 and 923 K). This involved exposing the samples to flowing ammonia gas (flow rate 300 cm^3 min^{-1}) for 24 h at a high temperature. After amnolysis the product was cooled to room

temperature, without exposure to air, and the change in the mass was recorded. The types of reactions occurring during amnolysis are shown in Fig. 4.3.

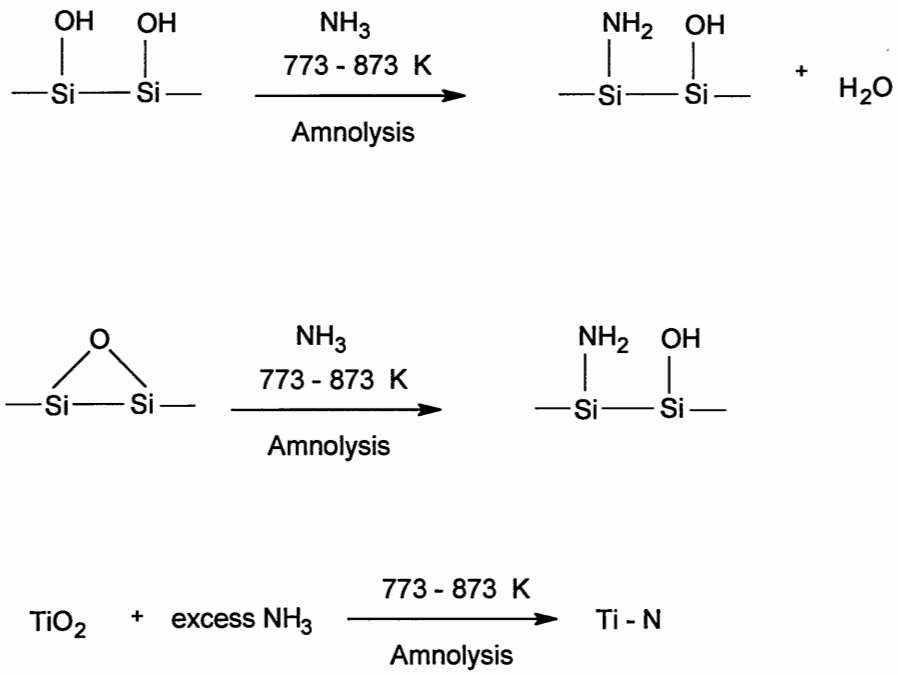

Figure 4.3 The reactions occurring during amnolysis.

Changes in the colour of the materials were observed on amnolysis from white (before amnolysis) to pale green or dark bluish grey colour (depending on the temperature of the amnolysis) for the sol-gel synthesised Ti-MCM 41, and from white to golden yellow for the grafted Ti-MCM 41. The colour changes are summarised in the schematic of amnolysis shown in Fig 4.4.

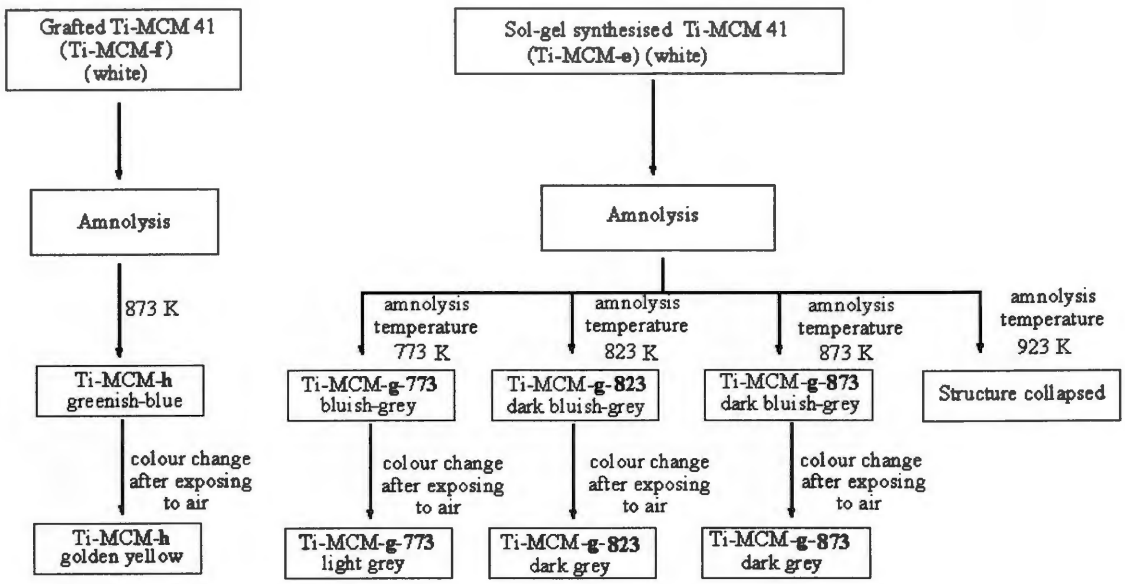

Figure 4.4 Schematic showing the changes in colour after amnolysis of the Ti-MCM 41 materials.

4.2.3 Ruthenium MCM 41 (Ru-MCM 41)

The ruthenium MCM 41 (Ru-MCM 41) material was supplied by Bruce *et al.* and the details of this synthesis are reported elsewhere.[5]

4.3 Results and Discussions: Physico-chemical Characterisation

4.3.1 Powder-X-ray Diffraction (p-XRD)

The MCM 41 materials synthesised with heteroelements (Fe and Ti) using the sol-gel synthesis method gave *p*-XRD patterns similar to the pattern from Si-MCM 41 (Chapter 3, Fig. 3.2), as shown in Figs. 4.5 and 4.6.

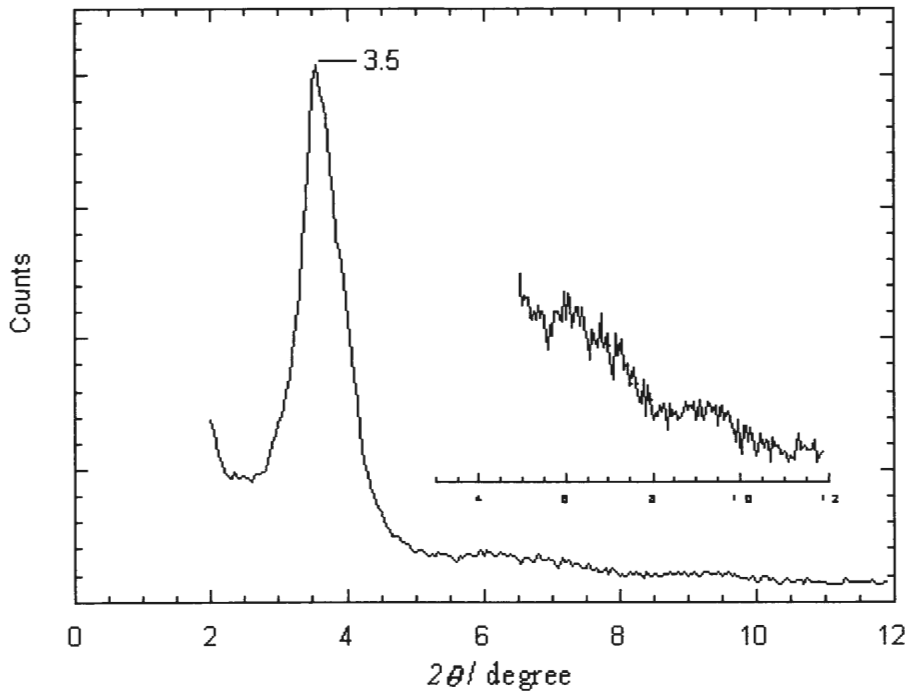

Figure 4.5 *p*-XRD pattern of sol-gel synthesised Fe-MCM 41(Fe-MCM-**a**).

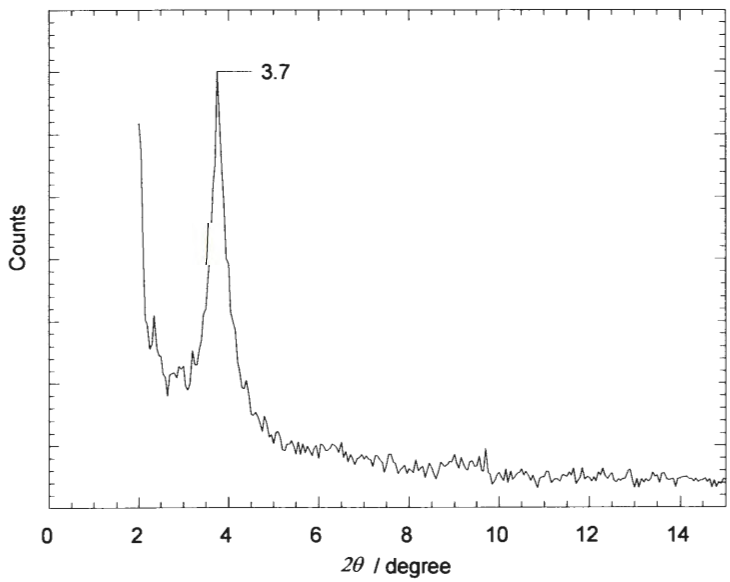

Figure 4.6 *p*-XRD pattern of sol-gel synthesised Ti-MCM 41(Ti-MCM-**e**).

Fig. 4.5 shows the *p*-XRD pattern of calcined Fe-MCM-**a**, which is similar to that observed for calcined Fe-MCM-**c** (*p*-XRD pattern in Appendix A2). Both the samples exhibited a well-defined d_{100} reflection at low 2θ angle. The (110) and (210) reflections observed at higher 2θ angles were very weak for these samples. The presence of all these peaks in the *p*-XRD pattern confirmed the hexagonal periodicity of the material.[15, 16] Table 4.2 summarises the calculated d_{100}-spacing and unit cell parameters for metal-functionalised MCM 41.

Table 4.2 Powder-XRD results obtained using CrKα radiation for the metal-functionalised MCM 41 materials

Samples	d_{100} peak position on 2θ scale	d_{100}-spacing / Å	a / Å
Si-MCM 41	3.5	38	44
Fe-MCM-**a**	3.5	38	44
Fe-MCM-**b**	3.5	38	44
Fe-MCM-**c***	2.5	36	42
Fe-MCM-**d**	3.5	38	44
Ti-MCM-**e**	3.7	36	42
Ti-MCM-**f**	3.5	38	44
Ti-MCM-**g**	3.7	36	42
Ti-MCM-**h**	3.5	38	44

** p-XRD analysis performed using CuKα radiation*

The *p*-XRD pattern of calcined Ti-MCM-**e** is shown in Fig. 4.6. The d_{100} reflection is evident, whereas the other reflections (110, 210) are absent in the *p*-XRD pattern. The presence of the d_{100} peak in the *p*-XRD pattern confirmed the hexagonal periodicity of the material, and this peak corresponded to a *d*-spacing of 36 Å, which was slightly lower than the value for the Si-MCM 41 material (38 Å). The results obtained for the sol-gel synthesised metal-functionalised MCM 41 materials were in

contrast to those reported by other workers,[15, 17, 18] where they observed a slight increase in the *d*-spacing due to the incorporation of metal.

Amnolysis, carried out on the Ti-MCM-**e** and Ti-MCM-**f** samples at a temperature of 923 K resulted in a collapse of the hexagonal structure, as evidenced by *p*-XRD pattern in which the d_{100} reflection was absent. There was no change in the *p*-XRD pattern for materials following amnolysis performed in a temperature range of 773 to 873 K. This confirmed that the material retained the hexagonal phase after amnolysis at temperatures up to 873 K.

The Fe- and Ti-grafted MCM 41 materials (Fe-MCM-**b,** Fe-MCM-**d** and Ti-MCM-**f**) also showed *p*-XRD patterns similar to that of parent Si-MCM 41. Fig. 4.7 shows the *p*-XRD pattern of Fe(II)-grafted MCM 41 (Fe-MCM-**b**), which suggests that the structural integrity of the Si-MCM 41 remains intact after the post-synthetic treatment. The d_{100} peak positions and the calculated *d*-spacing for grafted metal-functionalised MCM 41 materials are summarised in Table 4.2.

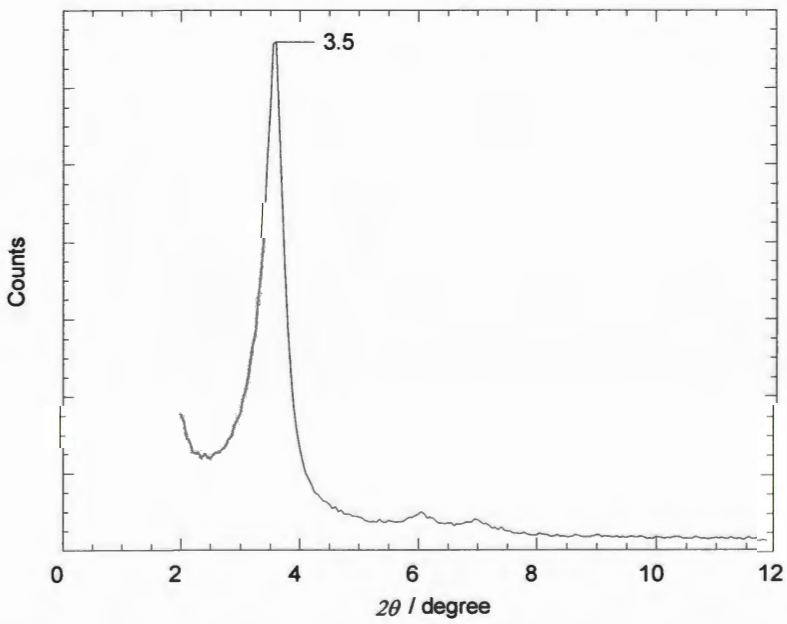

Figure 4.7 *p*-XRD pattern of Fe-grafted MCM 41(Fe-MCM-**b**).

4.3.2 CHN microanalysis

The CHN microanalysis results for the amnolysis products are summarised in Table 4.3.

Table 4.3 CHN microanalysis results of Ti-MCM 41 samples after amnolysis

Sample subjected to amnolysis	**Amnolysis temperature / K**	**Colour after amnolysis**	**After exposing to air**	**H / % (mass)**	**N / % (mass)**
Si-MCM 41 (white)	873	No change in colour (white)	No change in colour	1.6	1.2
Ti-MCM-**e** (white)	773	Bluish-grey (Ti-MCM-**g-773**)	Light grey	1.0	0.6
	823	Dark bluish-grey (Ti-MCM-**g-823**)	Dark grey	1.0	0.7
	873	Dark bluish-grey (Ti-MCM-**g-873**)	Dark grey	1.4	1.0
Ti-MCM-**f** (white)	873	Greenish-blue (Ti-MCM-**h-873**)	Golden yellow	1.7	0.8

A change in the colour of the titanium-functionalised samples was observed after amnolysis, whereas Si-MCM 41 did not show any change in the colour. This suggested that the change in the colour of the titanium-functionalised material was due to the formation of titanium nitrides and/or oxynitrides. The Si-MCM 41 sample showed 1.2 % nitrogen, which was due to the adsorbed NH_x (x = 1 or 2) on the surface, as shown by IR spectroscopic analysis (Section 4.3.3). Increasing the amnolysis temperature from 773 K to 873 K showed a slight increase in the amount of nitrogen, from 0.6 to 1.0 %, for the Ti-MCM-**g** samples (See Table 4.3). A small drop in H:N atomic ratio from 23:1 (for Ti-MCM-**g-773**) to 20:1 (for Ti-MCM-**g-873**) suggested that the formation of titanium nitride (Ti-N) increases with the increasing temperature.

4.3.3 Infrared (IR) Spectroscopy

The IR wavenumber and band assignments for the IR spectra measured on the metal-functionalised MCM samples are summarised in Table 4.4 below.

Table 4.4 The IR band wavenumber observed in the spectrum of the metal-functionalised MCM 41 samples

Approximate band wavenumber /cm^{-1}					**Assignment**
Fe-MCM 41 sol-gel	Fe-MCM 41 grafted	Ti-MCM 41 sol-gel	Ti-MCM 41 grafted	Ti-MCM 41 after amnolysis	
974	--	962	--	962	Si–O–M* vibration
1050–1100	1050–1100	1050–1100	1050–1100	1050–1100	Si–O–Si $_{asy\text{-}str}$
1642	1642	1642	1642	1642	O–H $_{def}$
--	--	--	--	1403	NH_4^+
--	--	--	--	3737	N-H $_{str}$
3400 - 3500	3400 - 3500	3400 - 3500	3400 - 3500	3400 - 3500	O–H $_{str}$
--	--	--	--	3200	Perturbed O–H groups

* *Metal (Fe and Ti)*

The Fourier Transform (FT) IR spectrum of Fe-MCM-**a** is shown in Fig. 4.8 and is similar to the spectrum of Ti-MCM-**e**.

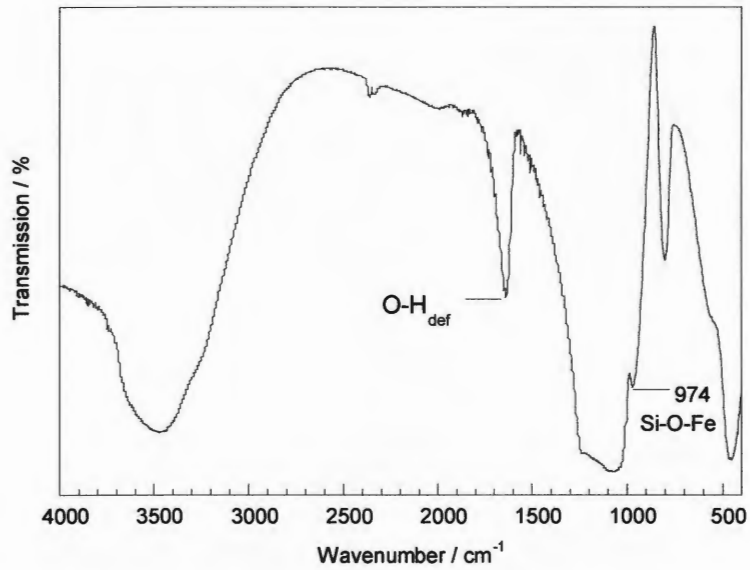

Figure 4.8 Infrared spectrum of sol-gel synthesised Fe-MCM 41 (Fe-MCM-**a**).

The incorporation of metal (Ti and Fe) in the Si-MCM 41 framework was supported by an increase in the intensity and a shift with respect to calcined Si-MCM 41 of the IR band at *ca.* 947 cm^{-1}.[17, 19] The stretching vibration band at 974 cm^{-1} observed in the IR spectrum of sol-gel synthesised Fe-MCM 41 supported the existence of a Si-O-Fe unit in the framework of the Fe-MCM 41 material.[15, 17, 19] The equivalent band appears at 962 cm^{-1} in the spectrum for Ti-MCM-**e** (spectrum in Appendix A2). This band was generally taken as a proof for the incorporation of Fe (or Ti) into the lattice of MCM 41 framework, since the band for the Si-OH groups appears at *ca.* 947 cm^{-1} in calcined Si-MCM 41 (see Chapter 3, Section 3.3.2). The sol-gel synthesised samples show a sharp and intense band at *ca.*1642 cm^{-1} (Fig. 4.8), which appears to be less intense in the spectra of the grafted samples (Fig. 4.9) and samples after amnolysis (Fig. 4.10). However, this band is possibly due to the bending vibrations of adsorbed water molecules.

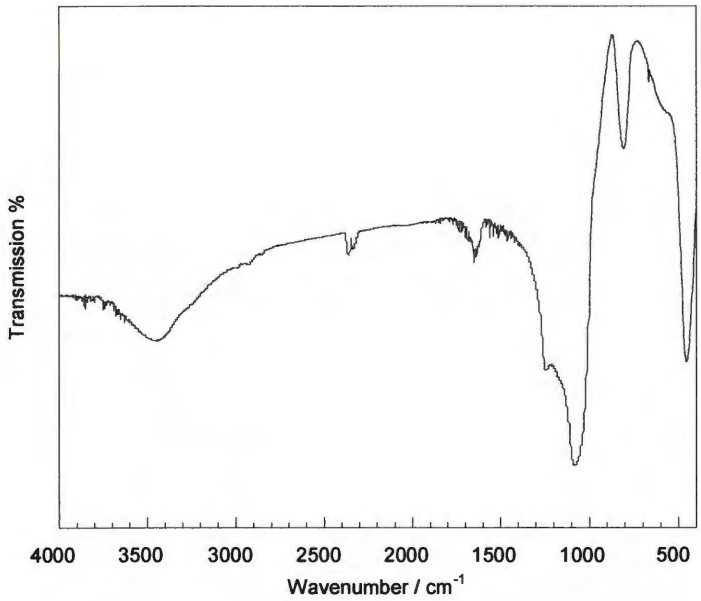

Figure 4.9 Infrared spectrum of the grafted Fe-MCM 41 (Fe-MCM-**b**).

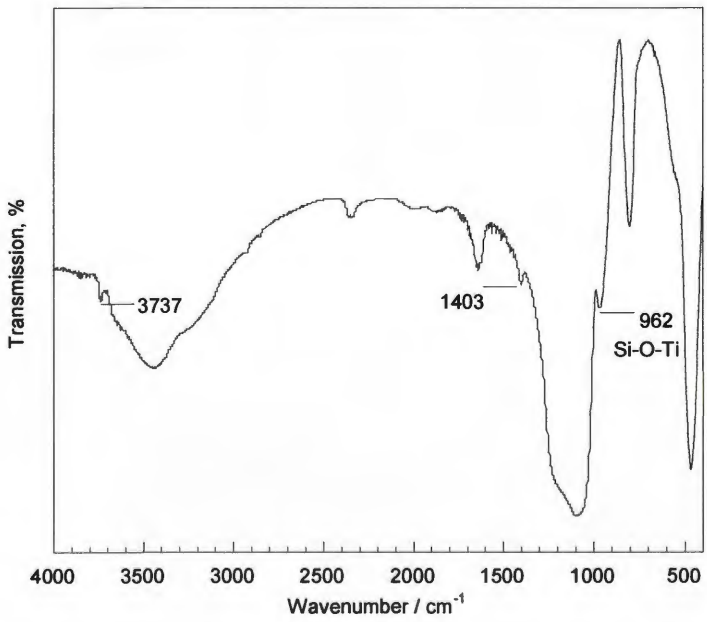

Figure 4.10 Infrared spectrum of the sol-gel synthesised Ti-MCM 41 after amnolysis (Ti-MCM-**g**)

The IR spectra of the grafted samples Fe-MCM-**b** (see Fig. 4.9) and Ti-MCM-**f** (Appendix A2) were found to be similar to that of Si-MCM 41. The IR spectrum of the

Fe-MCM-**d** sample was similar to that of the Fe-MCM-**b** sample. As expected the spectra do not show any IR band at *ca.* 947 cm^{-1}, as the surface hydroxyl groups (Si-O-H) are used up in the grafting of Fe and Ti species. A slight decrease in the intensity of a broad signal centred around 3400 cm^{-1} is observed, which is due to the surface silanol groups. The decrease in the intensity of this band may be explained by the involvement of some of the silanol groups in the grafting of the Fe and Ti species.

Fig. 4.10 shows the IR spectrum of the Ti-MCM-**g** sample (Ti-MCM-**e** sample after amnolysis). Following amnolysis the material showed all the IR bands as observed for Ti-MCM-**e** (parent material) with two additional bands at 1403 cm^{-1} and 3737 cm^{-1}. These bands were also observed in the spectrum of Ti-MCM-**h**. The absorption band at *ca.* 1403 cm^{-1}, which is due to the asymmetric deformation of adsorbed NH_4^+ ions,[20,21] is characteristic of the presence of NH_4^+ ions adsorbed on the surface. The hydroxyl groups present on the surface of the material are capable of protonating ammonia molecules, yielding ammonium ions. The band at *ca.* 3737 cm^{-1} was assigned to N–H stretching of the NH_2 groups arising from the dissociation of the ammonia molecules.[20,21]

The adsorption of ammonia on the surface hydroxyl groups to form NH_4^+ ions shows a band for perturbed hydroxyl groups at around 3200 cm^{-1} (see Fig. 4.10),[21] which appears as a shoulder along with the O–H stretching band centred at *ca.* 3400 cm^{-1}. This also gives an indication for the presence of hydroxyl groups (Brønsted acid centres) on a surface of the MCM 41 material.

XPS results (Section 4.3.4) indicated the presence of titanium nitrides and titanium oxynitrides. However the identification of the Ti–N bands in the amnolysed samples was difficult from IR spectroscopic analysis, due to the strong absorptions bands in the region 950–1300 cm^{-1} from the silica framework (SiO_4 unit). These

coincide with the Ti-N absorption bands (650 – 700 cm^{-1}, 950 – 1000 cm^{-1}, 1100 cm^{-1} and 1300 cm^{-1}).[22]

4.3.4 X-ray Photoelectron Spectroscopy (XPS)

X-ray photoelectron spectroscopy (XPS) was employed in the characterisation of the Ti-MCM 41 samples, before and after amnolysis. The technique was found to be very useful in determining the interaction of ammonia molecules with the MCM 41 surface and in the confirmation of the formation of titanium nitride (Ti-N bond). The XPS peaks measured were calibrated against the adventitious hydrocarbon peak at 284.8 eV.[23, 24]

The Si *2p* peak in the sol-gel synthesised material (Ti-MCM-**e**) was observed at a higher binding energy (104.6 eV) compared with the Si-MCM 41 (103.7 eV). This could be due to the incorporation of titanium in the lattice framework. Unfortunately, when XPS chemical shifts are obtained from solid compounds, the correlation with the electronegativity of the surrounding atom is much poorer, and this makes the interpretation difficult for spectra with small change in binding energy.[25]

The assigned binding energies and corresponding chemical environments are summarised in Table 4.5 and the XPS spectra of Ti 2*p* regions for the Ti-MCM 41 samples, before and after amnolysis, are shown in Figs. 4.11 and 4.12

Table 4.5 Binding energies and chemical environments for the Ti-MCM 41 samples, determined by XPS

Binding energy / eV				**Peaks**
Ti-MCM-**e**	Ti-MCM-**f**	Ti-MCM-**g**	Ti-MCM-**h**	
460.3	459.0	458.1	459.0	Ti 2*p*
465.6	464.7	463.0	464.8	
--	--	398.7	398.6	N 1*s*
--	--	398.4	397.8	
--	--	396.5 (Ti-N)	396.4 (Ti-N)	
--	--	395.8 (Ti-N)	--	

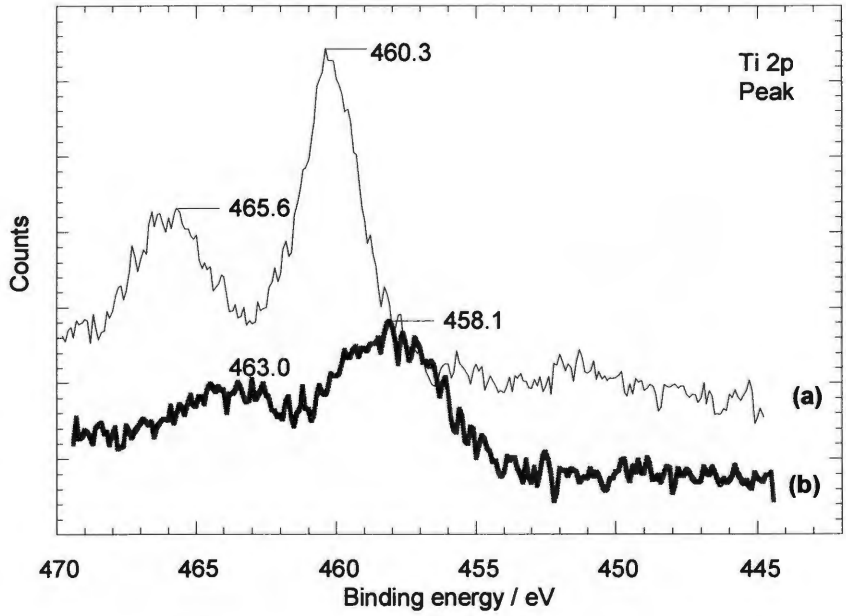

Figure 4.11 The Ti 2*p* region of XPS spectrum for sol-gel synthesised Ti-MCM 41, before and after amnolysis. (a) Ti-MCM-**e**, (b) Ti-MCM-**g**.

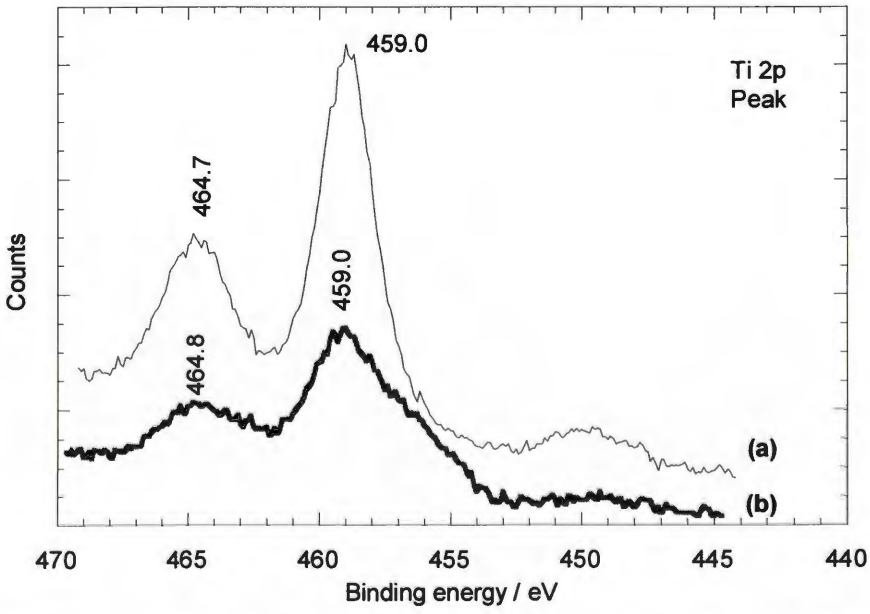

Figure 4.12 The Ti 2*p* region of XPS spectrum for grafted Ti-MCM 41, before and after amnolysis. (a) Ti-MCM-**f**, (b) Ti-MCM-**h**.

The sol-gel synthesised material, Ti-MCM-**e** shows the Ti 2*p* peak positions at slightly higher binding energy, 460.3 and 465.6 (Fig. 4.11) compared with grafted Ti-MCM-**f** (459.0 and 464.7 eV, respectively) (Fig. 4.12). This could possibly be explained as the Ti in Ti-MCM-**e** is present in the lattice framework, whereas in Ti-MCM-**f** it was grafted on the pore walls of the parent Si-MCM 41 material. In the samples after amnolysis, the Ti 2*p* peak shifted towards lower binding energy (Fig 4.11) for the Ti-MCM-**g** sample (sol-gel synthesised Ti-MCM 41 after amnolysis), whereas for the Ti-MCM-**h** (grafted Ti-MCM 41 after amnolysis) a broadening of Ti 2*p* peak (Fig 4.12) towards lower binding energy is observed when compared with Ti-MCM-**f** (sample before amnolysis). This could possibly be explained as the Ti 2*p* peaks in XPS spectra for samples after amnolysis contain contributions from both Ti-N and the unreacted Ti-O (after amnolysis). This shift/broadening of the Ti 2*p* peaks may be attributed to the presence of Ti-N in the samples after amnolysis.[24]

The N 1*s* XPS spectra for the Ti-MCM 41 samples, both before and after amnolysis, are displayed in Fig. 4.13 and Fig. 4.14. There are clear differences between the spectra of both the sol-gel and grafted samples before and after amnolysis. Both the samples Ti-MCM-**g** and Ti-MCM-**h** showed the presence of N 1*s* peak after amnolysis, whereas they are absent in Ti-MCM-**e** and Ti-MCM-**f**, prior to amnolysis (see Table 4.5).

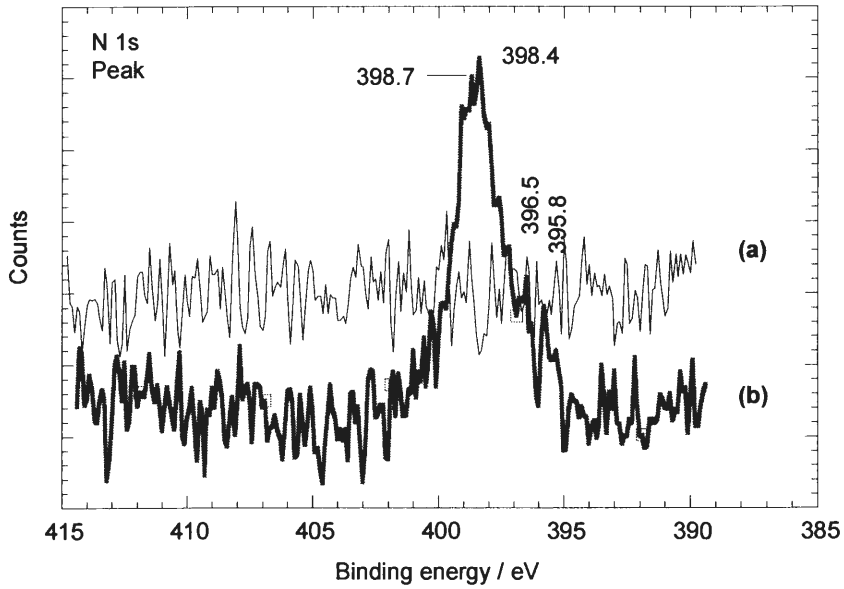

Figure 4.13 The N 1*s* region of XPS spectrum for sol-gel synthesised Ti-MCM 41, before and after amnolysis. (a) Ti-MCM-**e**, (b) Ti-MCM-**g**.

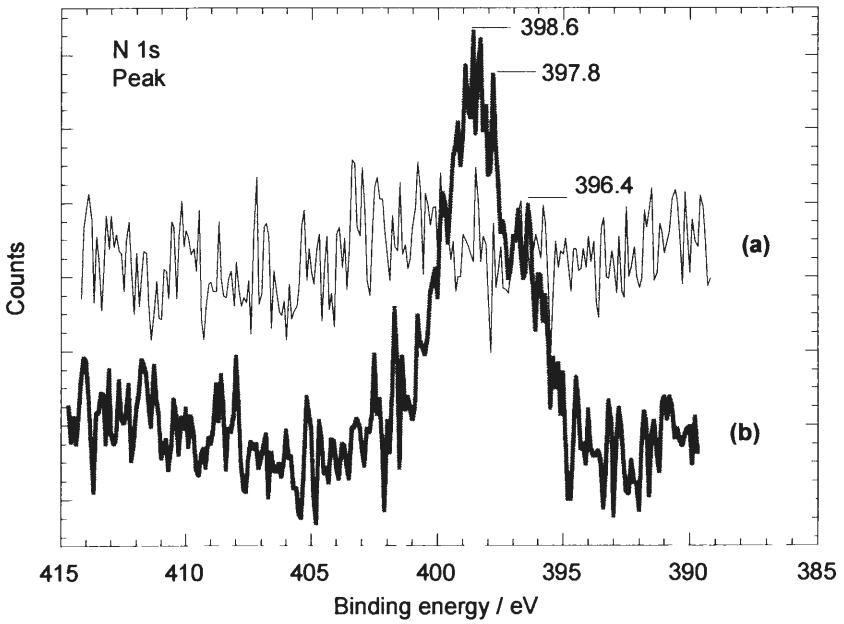

Figure 4.14 The N 1*s* region of XPS spectrum for grafted Ti-MCM 41, before and after amnolysis. (a) Ti-MCM-**f**, (b) Ti-MCM-**h**.

The spectra reveal the presence of different nitrogen species following amnolysis. The NH_3 adsorbed on the sample surface showed a splitting of the N *1s* peak into 2-3 maxima. The N 1*s* peak (*ca.* 398.6 eV) for the Ti-MCM-**g** sample shows two maxima at 398.7 eV and 398.4 eV and for the Ti-MCM-**h** sample they are observed at 398.6 eV and 397.8 eV. These maxima correspond to species such as NH_3 and NH_x (x = 1 or 2).[23, 24] However, the presence of physically adsorbed NH_3 can be ruled out under the analysis conditions (high vacuum). The peaks observed in the binding energy range 397.8 – 398.7 eV are assigned to NH_x, arising from the dissociative adsorption of NH_3 to NH_2 on the Ti/Si surface as reported by other workers.[24] This dissociative chemisorption of NH_3 on the Ti-MCM 41 surface is also supported by IR spectroscopy (see Section 4.3.3, Fig. 4.10). There was no peak observed for the presence of NH_4^+ species (expected in the range 402.2 – 402.6 eV[24]) as detected by IR spectroscopy. However, this may be explained as the desorption of NH_4^+ species was more likely under the high vacuum during analysis. The weak peaks observed at *ca.* 396.5 eV (Figs. 4.13 and 4.14) are in the range expected for nitrides,[23, 24, 26] and this confirmed the formation of Ti-N following amnolysis. This peak for Ti-N was observed at a slightly lower binding energy compared with the reported value of 397.1 eV by Siew *et al.*[24] This may be accounted for by the different source of X-rays (Mg) used in the current work (Al used by Siew *et al.*) Thus, XPS was found to be useful in the detection of the presence of Ti-N bond in the analysis of the amnolysed Ti-MCM 41 samples particularly, since, it was found to be difficult to detect Ti-N by CHN microanalysis and IR spectroscopy.

4.3.5 ^{57}Fe Mössbauer Spectroscopy

In this study, ^{57}Fe Mössbauer spectroscopy was used for the analysis of Fe-MCM 41 materials (Fe-MCM-**a** and Fe-MCM-**c**). The Fe-MCM-41 materials synthesised *via* the

sol-gel synthesis method, where the iron sources used were the salts of Fe(II) (Fe-MCM-**a**) and Fe(III) (Fe-MCM-**c**), respectively.

It is known that the large particles of α-Fe_2O_3 may be formed by precipitation in the sol-gel synthesis process and due to calcination at high temperature; the presence of α-Fe_2O_3 will give a sextet pattern in Mössbauer spectrum.[27] However, the Fe-MCM 41 samples do not show any evidence of a sextet pattern indicating the absence of large particles of α-Fe_2O_3 in the samples.

The analysis was also carried out for the identification of:

- The oxidation state of iron in the samples
- The environment in which the iron nuclei are embedded

4.3.5.1 Oxidation State of Iron

The ^{57}Fe Mössbauer spectra of Fe-MCM-**a** and Fe-MCM-**c** shown in Fig. 4.15 and Fig 4.16, respectively, confirms the incorporation of Fe in the material. The ^{57}Fe Mössbauer spectra ($\delta = 0.31$ mms^{-1}) of both the samples are characteristic of high-spin paramagnetic Fe^{3+}. The spectra show doublets with quadrupole splitting of *ca.* 0.86 mms^{-1}, which indicate the presence of Fe^{3+} in the samples. This suggests the oxidation of the Fe(II) to Fe(III) during the synthesis of Fe-MCM-**a**. This was as expected, since oxidation of Fe(II) to Fe(III) occurs readily in both air and water. This suggests that whatever the initial oxidation state of iron source (Fe(II) or Fe(III)) the final material synthesised is Fe(III)-MCM 41.

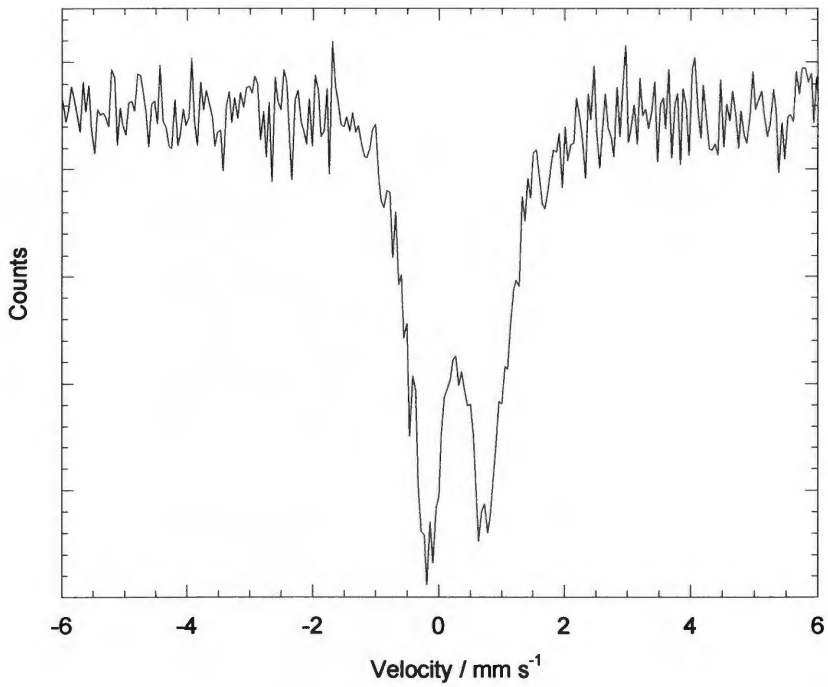

Figure 4.15 ^{57}Fe Mössbauer spectrum of the Fe(II)-MCM 41 sample (Fe-MCM-**a**).

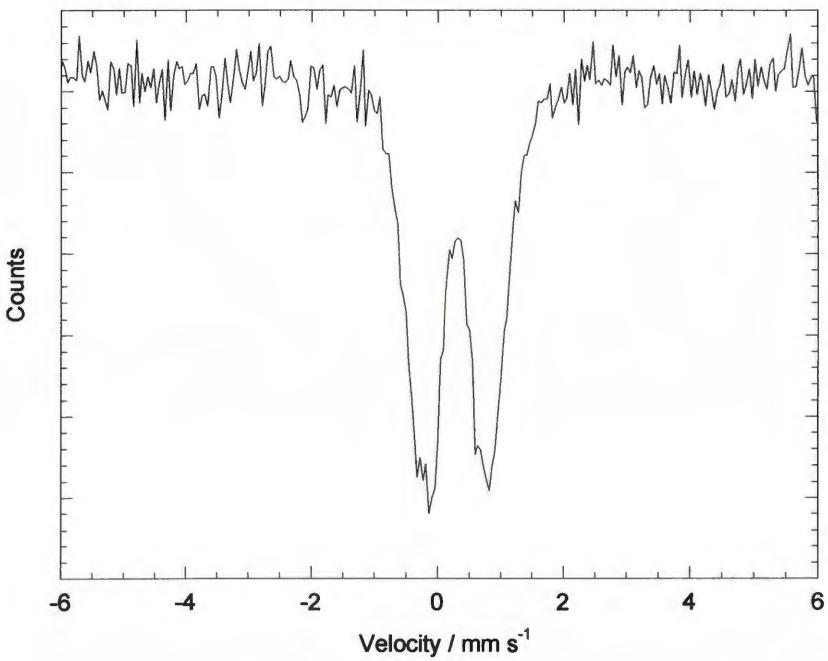

Figure 4.16 ^{57}Fe Mössbauer spectrum of the Fe(III)-MCM 41 sample (Fe-MCM-**c**).

4.3.5.2 Iron Environment

Each half of the doublet peak in each spectrum is split, and this indicates that two doublet sub-spectra are superimposed in each case (see Figs. 4.15 and Fig. 4.16).[27] The presence of these sub-spectra in both the samples, indicates the Fe^{3+} to be present in two different environments, which could be on the surface of pore walls, and within the lattice of the hexagonal framework. The observed quadrupole splitting in the spectra indicates the Fe^{3+} to be present in coordination with oxygen.

4.4 Sorption Studies: Results and Discussions

Sorption studies were carried out on all the metal-functionalised MCM 41 materials. The different adsorptives used are given below:

- nitrogen
- carbon dioxide
- 1-hexene
- 3,3-dimethyl-1-butene

Nitrogen (77 K) was used as a standard probe to study the surface area and pore parameters of the materials synthesised. Carbon dioxide was used, because of its high quadrupole moment, to investigate the change in surface characteristics after modification. 1-Hexene and 3,3-dimethyl-1-butene sorptions were carried out on Ru-MCM 41 to study the effects of heat-treatment on the sorptive properties of the material, as the material showed improved catalytic activity upon heat-treatment for the hydrogenation of 1-hexene.

4.4.1 Nitrogen sorption

The nitrogen sorption isotherm for Fe-MCM-**c** is shown in Fig. 4.17. The nitrogen sorption results for all the samples are also summarised in Table 4.6.

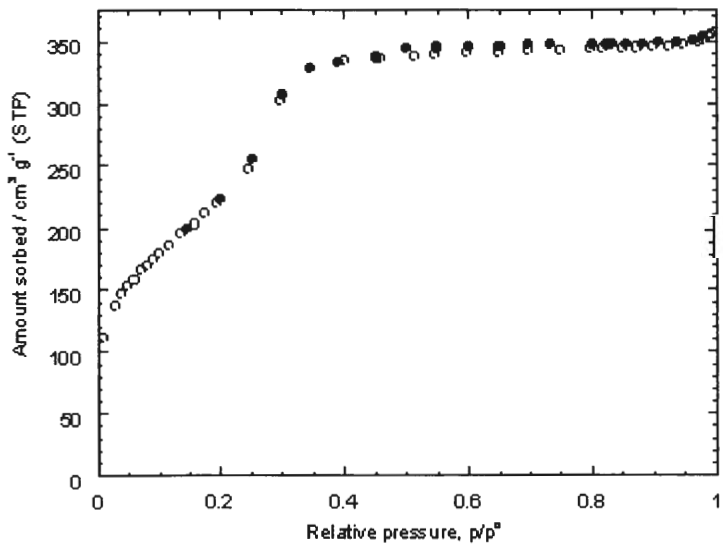

Figure 4.17 Nitrogen sorption isotherm (77 K) for sol-gel synthesised Fe(III)-MCM 41 (Fe-MCM-**c**). Filled symbols denote desorption points.

Table 4.6 Nitrogen sorption results on the metal-functionalised MCM 41 materials

Sample	Type of isotherm	BET, S_{sp} area / $m^2 g^{-1}$	Pore volume / $cm^3 g^{-1}$	Average Pore diameter / Å	
				†	§
Si-MCM 41	IV	1160	0.74	25	26
Fe-MCM-**a**	IV	820	0.54	27	26
Fe-MCM-**b**	IV	1110	0.51	23	18
Fe-MCM-**c**	IV	950	0.59	25	25
Fe-MCM-**d**	IV	1140	0.53	23	19
Ti-MCM-**e**	IV	800	0.45	27	22
Ti-MCM-**f**	IV	1097	0.67	23	20
Ti-MCM-**g** (873 K)	IV	690	0.35	27	21
Ti-MCM-**h** (873 K)	IV	770	0.43	26	22

§ = *Pore diameter derived from eq. ($4V/S_{sp}$ by BET) and,* † = *BJH mean pore diameter.*

Nitrogen sorption on both Fe-MCM-**a** (see Appendix A2) and Fe-MCM-**c** (sol-gel synthesised Fe-MCM 41) yielded Type IV isotherms. The isotherms were reproducible and reversible with no hysteresis present between the adsorption and desorption branches. A sharp step in each isotherm is observed in the range $0.25 < p/p^o < 0.35$, which corresponds to condensation in the mesopores.

The BET plots were found to be linear in the range $0.05 < p/p^o < 0.20$, and yielded specific surface areas of 820 m^2g^{-1} and 950 m^2g^{-1} for Fe-MCM-**a** and Fe-MCM-**c**, respectively. This represents reduction in the surface area compared to the Si-MCM 41 (1160 $m^2 g^{-1}$). The average pore diameter of 27 Å for Fe-MCM-**a** was slightly larger than that of Fe-MCM-**c** (25 Å). The materials yielded Gurvitsch pore volumes,[28, 29] V_p, of 0.54 $cm^3 g^{-1}$ and 0.59 $cm^3 g^{-1}$, respectively, listed in Table 4.6. The total pore volumes of the metal-functionalised samples were less than the parent Si-

MCM 41 material. This decrease in the surface areas and the pore volumes of the sol-gel functionalised Fe-MCM 41 materials suggested that some of the Fe ions may be grafted on the surface of pore walls. The sol-gel synthesised samples showed a slight increase in the average pore diameter (Table 4.6) compared with the Si-MCM 41 material, which indicated the incorporation of metal ions in the lattice framework. This is because the Si-O-M (M = Fe, Ti) bonds are longer than the Si-O-Si bonds.

The nitrogen sorption isotherms for the Fe- and Ti-grafted samples (Appendix A2) showed Type IV isotherms, similar to the parent Si-MCM 41 material (Chapter 3, Fig. 3.3) and the sol-gel synthesised materials. The isotherms were reversible, with no hysteresis loop present between the adsorption and desorption branches. It can be seen from Table 4.6 that grafting of metal species results in a decrease in the surface area, average pore diameter and pore volume of metal-functionalised MCM 41 compared with parent-MCM 41. The pore wall thickness for the samples (estimated by the difference between the unit cell parameter (a) and BJH pore diameter (D)) are summarised in Table 4.7. The materials showed an increase in the pore wall thickness upon grafting; this was not the case with the sol-gel synthesised samples. This increase in the pore wall thickness was possibly due to the smearing layer formed by grafting of metals onto the pore walls.

The nitrogen sorption isotherm on the sol-gel synthesised Ti-MCM-**e** yielded a Type IV isotherm (Fig. 4.18) with no hysteresis loop, which is characteristic of the MCM 41 material. The isotherm exhibits inflection in the isotherm in the range $0.15 < p/p^o < 0.30$, which indicates the condensation of the liquid adsorptive within the pores. However, this step was not sharp, and shows broad pore size distribution with an average pore diameter of 27 Å. The material synthesised yielded high BET derived surface area of 800 $m^2\ g^{-1}$, and a high Gurvitsch pore volume of 0.45 $cm^3\ g^{-1}$, typical for

mesoporous solids. These values are smaller than those of the parent Si-MCM 41 material (see Table 4.6).

Table 4.7 The pore wall thickness calculated from unit cell parameter and average pore diameter

Sample	Unit cell parameter, *a* / Å	Average pore† diameter, *D* / Å	Pore wall thickness / Å
Si-MCM 41	44	25	19
Fe-MCM-**a**	44	27	17
Fe-MCM-**b**	44	23	21
Fe-MCM-**c**	42	25	17
Fe-MCM-**d**	44	23	21
Ti-MCM-**e**	42	27	15
Ti-MCM-**f**	44	23	21
Ti-MCM-**g** (873 K)	42	27	15
Ti-MCM-**h** (873 K)	44	26	18

† = *BJH mean pore diameter*

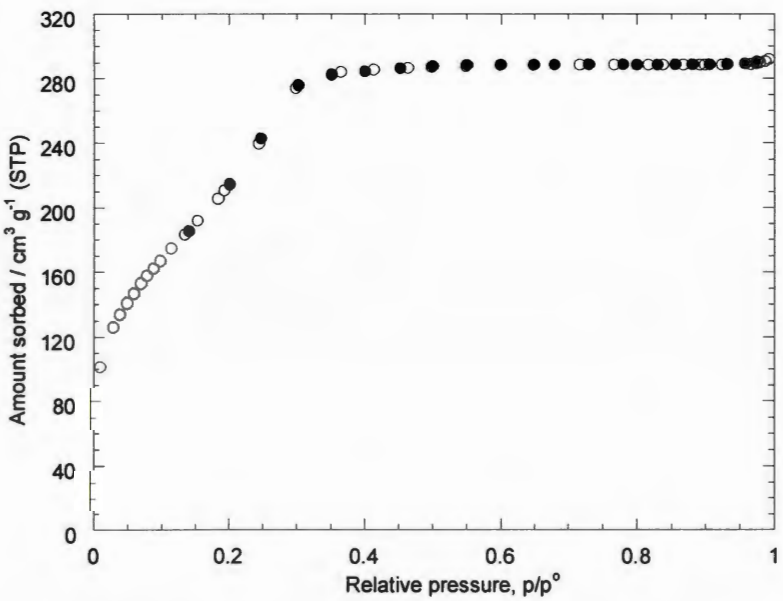

Figure 4.18 Nitrogen sorption isotherm (77 K) for sol-gel synthesised Ti-MCM 41 (Ti-MCM-**e**). Filled symbols denote desorption points.

Nitrogen sorption isotherms for Ti-MCM-**g** and Ti-MCM-**h** (materials after amnolysis) yielded typical Type IV isotherms (Appendix A2) with no hysteresis. Following amnolysis Ti-MCM-**h** material showed a considerable decrease of 390 $m^2 g^{-1}$ in the surface area whereas the Ti-MCM-**g** material showed a decrease of 110 $m^2 g^{-1}$ (see Table 4.6). The pore diameter of the Ti-MCM-**g** material remained unchanged, whereas an unexpected increase in the average pore diameter of the Ti-MCM-**h** material was observed. This increase in the average pore diameter of the grafted Ti-MCM 41 material (Ti-MCM-**h**) could be due to one of the following two reasons:

- The migration of the Ti from the pores at high temperature, and in the flow of ammonia gas during amnolysis (due to sintering).
- Sintering of Ti which may cause the smaller pores to become blocked and only the larger pores will then contribute to the determination of the pore diameter resulting in an increase in the average pore diameter of the Ti-MCM-**h** sample.

4.4.2 Carbon Dioxide Sorption

The adsorption isotherms of carbon dioxide were obtained at 195 K and at a maximum pressure of one atmosphere. Table 4.8 summarises the carbon dioxide adsorption data for the metal-functionalised MCM 41 materials.

Table 4.8 Carbon dioxide sorption results (N_2 values are given in bracket for comparision)

Sample	Type of isotherm	BET, S_{sp} area / $m^2\ g^{-1}$	Pore volume / $cm^3\ g^{-1}$
Si-MCM 41	IV	580 (1160)	0.76 (0.74)
Fe-MCM-**a***	II	210 (820)	0.20 (0.54)
Fe-MCM-**b**	--	--	--
Fe-MCM-**c**	IV	410 (950)	0.44 (0.59)
Fe-MCM-**d**	--	--	--
Ti-MCM-**e***	II	175 (800)	0.17 (0.45)
Ti-MCM-**f**	--	--	--
Ti-MCM-**g*** (873 K)	I	130 (690)	0.10 (0.35)
Ti-MCM-**h** (873 K)	IV	220 (770)	0.20 (0.43)

* *The final plateau of the isotherm was not achieved.*

It can be seen from Table 4.8, that the CO_2-derived surface area is smaller than the nitrogen-derived values (see Table 4.6). This is because the high quadrupole moment of CO_2 makes its adsorption 'more specific', *i.e.* it adsorbs preferentially on the polar groups or ions present on the surface of a solid.[29] Thus, the adsorption of CO_2 is unlikely to proceed by formation of a monolayer, thereby explaining the lower calculated surface area compared with the N_2 derived values (Table 4.6). The Fe-MCM-**c** material showed a Gurvitsch pore volume of 0.44 $cm^3\ g^{-1}$, which was less than the N_2 derived pore volume (0.59 $cm^3\ g^{-1}$). Since the final plateau of the isotherm was not achieved the CO_2 derived pore volumes for the Fe-MCM-**a** is not directly comparable with that from the N_2 sorption.

Fig. 4.19 shows the adsorption isotherms of CO_2 on the sol-gel synthesised Fe-MCM 41 materials. The Fe-MCM-**c** sample shows a Type IV isotherm with a condensation step at *ca.* $p/p^o = 0.7$, which levels off at *ca.* $p/p^o = 0.8$. Thus, the material shows mesoporous characteristics. A shift in the condensation step towards higher relative pressure was observed in the CO_2 sorption isotherm compared with the N_2 sorption (Fig. 4.17). The CO_2 sorption isotherm for the Fe-MCM-**a** sample shows a Type II isotherm, which is in contrast with the result obtained from N_2 sorption (Type IV isotherm). The differences observed in the CO_2 sorption for samples Fe-MCM-**a** and Fe-MCM-**c** are not clearly understood, and could be due to the difference in the nature of the surface possibly due to the amount of Fe incorporated (Fe-MCM-**a** =1.00 mmol, and Fe-MCM-**c** = 2.50 mmol used in synthesis).

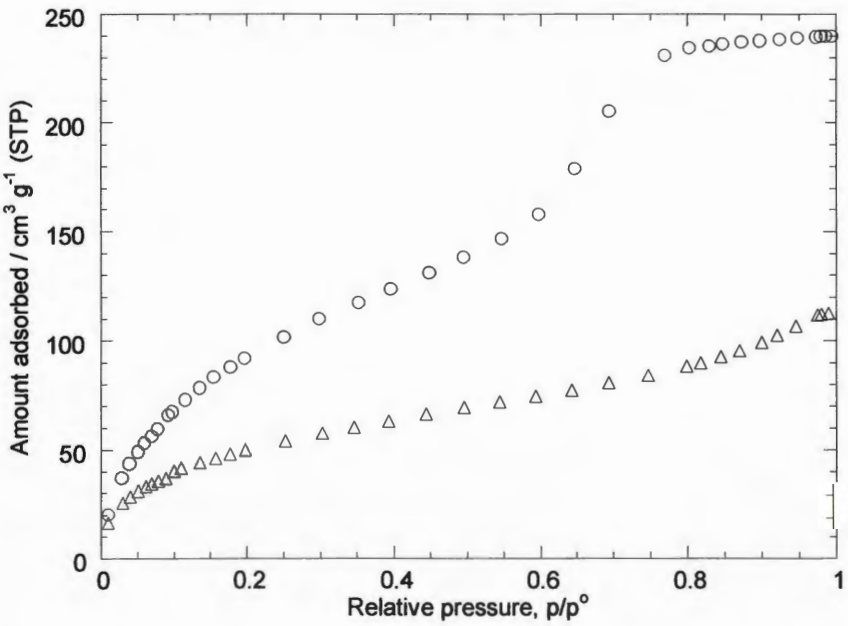

Figure 4.19 Carbon dioxide adsorption isotherms (195 K) for sol-gel synthesised Fe-MCM 41, (Δ) Fe-MCM-**a**, and (○) Fe-MCM-**c**.

Fig. 4.20 shows the CO_2 sorption isotherms for the Ti-MCM-**g** and Ti-MCM-**h** materials (samples after amnolysis). The Ti-MCM-**g** sample yields more of a Type I

isotherm compared with the Type II for Ti-MCM-**h**. The samples yielded lower CO_2 derived surface areas, 130 and 220 $m^2\ g^{-1}$, respectively, compared with the nitrogen derived surface areas (690 and 770 $m^2\ g^{-1}$, respectively). A decrease in the CO_2 derived surface area from 175 m^2g^{-1} for the parent Ti-MCM-**e** (isotherm in Appendix A2) to 130 m^2g^{-1} for the amnolysed Ti-MCM-**g** sample was also observed. This suggested that the modification of pore walls following amnolysis (possibly the formation of Ti-N) results in a decrease in the uptake of CO_2 *i.e.* Ti-N formation decreases surface polarity.

The final plateau in the CO_2 sorption isotherm was not achieved and hence the pore volumes obtained are not directly comparable with the nitrogen-derived values.

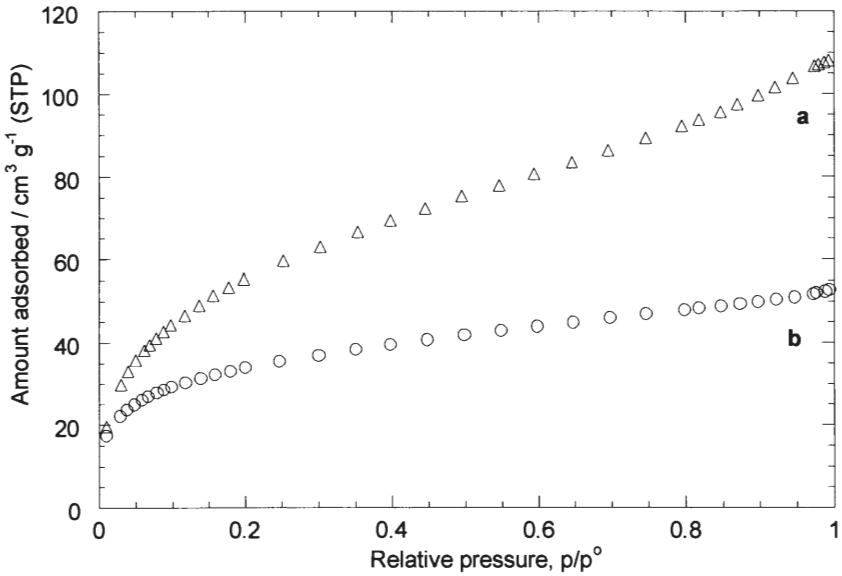

Figure 4.20 Carbon dioxide adsorption isotherms (195 K) for Ti-MCM 41 samples after amnolysis: (Δ) Ti-MCM-**h,** (○) Ti-MCM-**g**.

4.5 Adsorption Studies on Ru-MCM 41

This section is concerned with the adsorption studies of nitrogen, 1-hexene and 3,3-dimethyl-1-butene, before and after heat-treatment (at 623 K for 16 h under reduced pressure of $<10^{-5}$ torr) of ruthenium MCM 41 (Ru-MCM 41).

The sorption isotherm of nitrogen at 77 K is shown in Fig. 4.21.

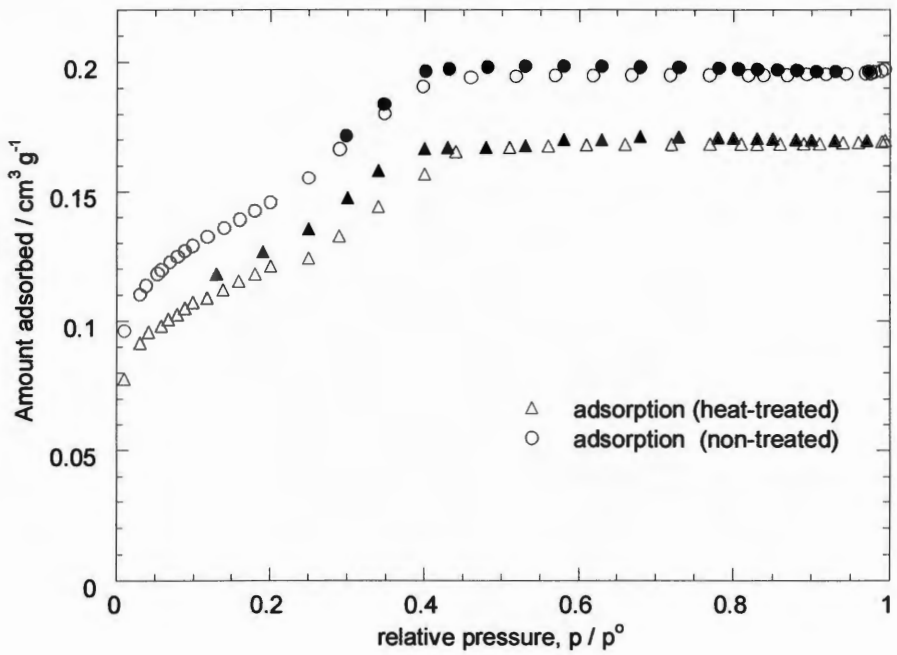

Figure 4.21 Nitrogen sorption isotherms (77 K), before and after heat-treatment of Ru-MCM 41. Filled symbols denote desorption points.

Nitrogen adsorption on both the non-treated and heat-treated samples yielded Type IV isotherms, indicating that these materials are mesoporous. The isotherm for the non-treated sample displays no desorption hysteresis, which is characteristic of nitrogen adsorption on MCM 41 materials.[30] The hysteresis observed in the nitrogen sorption isotherm for heat-treated sample suggested that heat treatment of the sample (at 623 K for 16 h under reduced pressure of $<10^{-5}$ torr) has resulted in a change in the nature of the surface characteristics.[31] A slight decrease in both the BET surface area (330 to

280 m^2g^{-1}) and the Gurvitsch pore volume (0.19 to 0.16 cm^3g^{-1}) as a result of the heat-treatment was observed for nitrogen sorption (see Table 4.9).

The *p*-XRD patterns for both the non-treated and the heat-treated sample displayed a d_{100} peak at a 2θ value of 3.7°. This confirmed that the material maintained its hexagonal periodicity after heat treatment.

Table 4.9 Summary of sorption results of nitrogen, 1-hexene and 3,3 dimethyl 1-butene for the Ru-MCM 41 material.

Adsorptives	**Molecular area of adsorptive / Å^2**	**BET derived surface area / m^2 g^{-1}**		**Pore volume / cm^3 g^{-1}**	
		Non-treated	Heat-treated*	Non-treated	Heat-treated*
nitrogen	16.2	330	280	0.19	0.16
1-hexene	38.2 †	145	295	0.12	0.16
3,3-dimethyl-1- butene	39.0 †	--	160	--	0.13

* Sample heated at 623 K under reduced pressure (< 10^{-5} torr) for 16 h.
† Molecular area (a_m) calculated using equation 2.14 (Chapter 2).

The adsorption of 1-hexene and 3,3-dimethyl-1-butene at 303 K on the Ru-MCM 41 samples yielded Type I isotherms, as shown in Fig. 4.22.

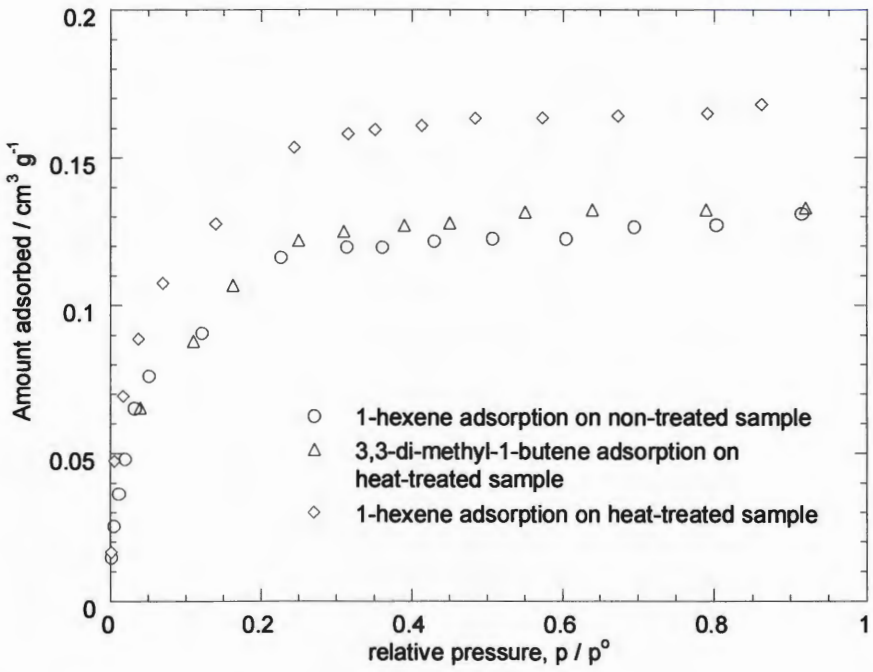

Figure 4.22 Adsorption isotherms of 1-hexene (at 303 K, before and after heat-treatment) and 3,3-dimethyl-1-butene (303 K) for the Ru-MCM 41 material.

The 1-hexene derived BET specific surface area of 144 m^2g^{-1} for the non-treated sample was found to be half the value of the heat-treated sample (295 m^2g^{-1}). The heat-treated material showed a high initial uptake of 1-hexene which levelled off around relative pressure of p/p^o = 0.25. The final plateau of the 1-hexene isotherms yielded Gurvitsch pore volumes of 0.12 cm^3g^{-1} and 0.16 cm^3g^{-1} for the non-treated and heat-treated samples, respectively. Heat-treatment was shown to result in improved accessibility of surface and pore to the 1-hexene molecules. This observed increase in the 1-hexene uptake without a corresponding change in the nitrogen BET surface area[31] (Table 4.9) may partly explain the observed increase in catalytic activity in hydrogenation of 1-hexene following heat-treatment of the Ru-MCM 41.[6] The larger

size of the 1-hexene molecule with respect to the nitrogen molecule may explain the lower uptake of 1-hexene (Table 4.9) compared with the nitrogen for the sample prior to heat-treatment.

The adsorption isotherm of the 3,3-dimethyl-1-butene at 303 K on the heat-treated sample yielded a Type I isotherm (Fig. 4.22).[31] The BET surface area value of 160 m^2g^{-1} obtained from 3,3-dimethyl-1-butene was lower than those derived from nitrogen and 1-hexene (see Table 4.9). The pore volume determined from this adsorptive was also lower (0.13 cm^3g^{-1}) than that for 1-hexene on the heat-treated sample. This suggested that adsorption of 3,3-dimethyl-1-butene, which approximates to a spherical shape (see Fig. 4.23) is sterically hindered,[32] whereas 1-hexene, which is a long chain molecule is less sterically hindered to interact with the pore surface.[31]

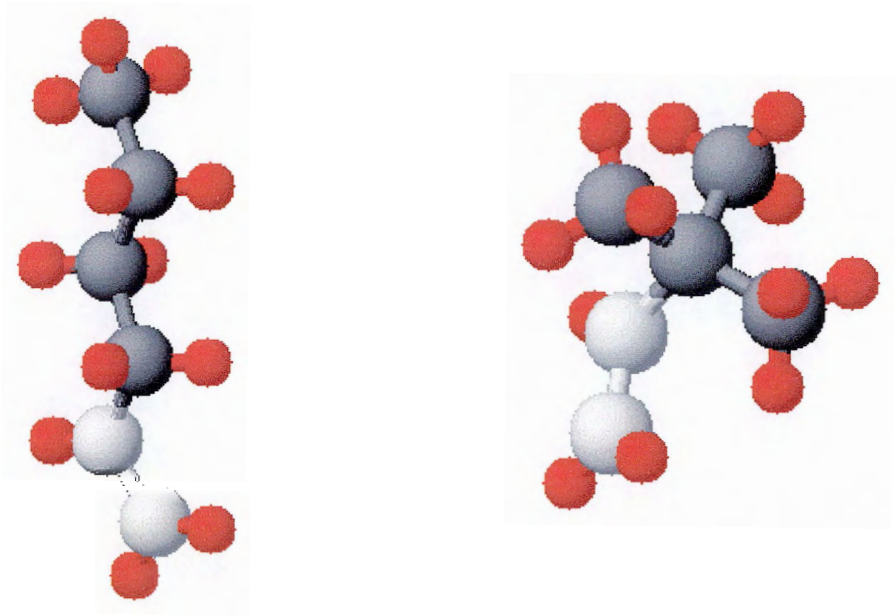

(a) (b)

Figure 4.23 Structure of (a) 1-hexene molecule (b) 3,3-di-methyl-1-butene.

4.6 Conclusions

4.6.1 Fe- and Ti-MCM 41

Fe and Ti were each incorporated into the Si-MCM 41 material to form Fe-MCM 41 and Ti-MCM 41, respectively. Fe-MCM 41 and Ti-MCM 41 were successfully synthesised by two different methods *i.e.* by the sol-gel method, and by the post-synthetic grafting method. Both Fe(II) and Fe(III) precursors were used for the synthesis of Fe-MCM 41. The ^{57}Fe Mössbauer spectrum of each sample showed a doublet with quadrupole a splitting of *ca.* 0.86 mms^{-1}, which demonstrated that Fe(III)-MCM 41 was synthesised irrespective of the initial source of iron [Fe(II) or Fe(III) salts] used in the synthesis. The surfaces of the Ti-MCM 41 samples were modified by amnolysis. The presence of a d_{100} peak in the *p*-XRD pattern of each of the metal-functionalised MCM 41 materials confirmed that the material synthesised exhibits hexagonal periodicity. The incorporation of Fe and Ti in the silica framework of the Fe-MCM-**a** and Ti-MCM-**e** (sol-gel synthesised materials), respectively, was confirmed by bands at 974 cm^{-1} and 962 cm^{-1}, respectively, in the IR spectra due to metal-oxygen stretching. The IR band at *ca.* 947 cm^{-1} for surface hydroxyls was not present in the grafted samples, which confirms the grafting of Fe and Ti involves reaction with the surface hydroxyls.

The mesoporosity of each of the synthesised materials was confirmed by the Type IV isotherms yielded by nitrogen sorption (77 K). A small decrease in both the surface area and total pore volume observed following grafting, was attributed to the immobilisation of the Fe and Ti species on the pore surface. The grafted Fe- and Ti-MCM 41 materials showed an increase in the pore wall thickness upon grafting but this was not the case with the sol-gel synthesised samples. This increase in the pore wall thickness (from 19 Å to 21 Å) was attributed to a smearing layer formed by metals grafted on the pore walls.

Incorporation of metal-functionalities resulted in a reduction in the surface areas (from 1160 to 1097 $m^2 g^{-1}$, and from 1160 to 800 $m^2 g^{-1}$, for the grafted and sol-gel synthesised samples, respectively) and pore volumes (from 0.74 to 0.45 $cm^3 g^{-1}$) of the modified samples. The loss in surface area was more pronounced for the sol-gel synthesised samples compared with the grafted samples. The grafted samples showed a reduction in the average pore diameter (from 26 Å to 18 Å) following functionalisation, whereas the sol-gel synthesised samples had pore diameters (*ca.* 25 Å) comparable with those of the parent Si-MCM 41 (26 Å). A significant decrease in the surface area (from 1160 $m^2 g^{-1}$ to 770 $m^2 g^{-1}$) and a slight increase in the average pore diameter (from 23 to 26 Å) for the grafted amnolysed Ti-MCM-**h** sample suggested sintering of Ti during amnolysis. However, for the sol-gel synthesised Ti-MCM-**g** sample, there was a slight decrease in the surface area (from 800 $m^2 g^{-1}$ to 690 $m^2 g^{-1}$) and no change in the pore diameter. This suggests that in the sol-gel synthesised sample the Ti was incorporated in the framework and was less likely to undergo sintering under amnolysis conditions compared with the grafted samples.

The condensation steps in the CO_2 sorption isotherms of all the modified samples were observed at higher relative pressures compared with N_2 sorption, and the CO_2 derived surface areas (between 130 and 580 $m^2 g^{-1}$) were found to be much smaller than the N_2 derived surface areas (between 690 and 1160 $m^2 g^{-1}$). This suggests that the CO_2 sorption occurs *via* a different mechanism to N_2 sorption *i.e.* by interaction with polar groups on the surface rather than monolayer formation.

The presence of titanium nitride in the amnolysed Ti-MCM 41 samples was suggested by the XPS. The detection Ti-N by the IR spectroscopy was not possible as the bands arising from the framework SiO_2 mask the expected Ti-N bands. The presence of adsorbed NH_4^+ and NH_2 groups in the amnolysed Ti-MCM 41 samples was confirmed by the IR spectroscopy.

4.6.2 Ru-MCM 41

The ruthenium-MCM 41 (Ru-MCM 41) material was supplied by Bruce *et al.*[5] The effect of heat-treatment (under reduced pressure of $< 10^{-5}$ torr, at 623 K) on the sorption characteristics of Ru-MCM 41 by the adsorption of nitrogen (77 K), 1-hexene and 3,3-dimethyl-1-butene (303 K) was studied. Heat-treatment of Ru-MCM 41 was shown to alter the surface characteristics of the material with respect to the sorption of both nitrogen and hexene isomers, 1-hexene and 3,3-dimethyl-1-butene, though the changes are more marked for 1-hexene. Nitrogen adsorption yields a Type IV isotherm, before and after heat-treatment, with hysteresis observed in the isotherm of the heat-treated sample. A slight decrease in the BET surface area (330 to 280 m^2g^{-1}) and pore volume (0.19 to 0.16 cm^3g^{-1}) as a result of the heat-treatment was observed for nitrogen adsorption. However, adsorption of 1-hexene yields a Type I isotherm and doubling of the monolayer uptake of 1-hexene was observed following heat-treatment, which was equivalent to an increase in both BET surface area (145 to 295 m^2g^{-1}) and pore volume (0.12 to 0.16 $cm^3\ g^{-1}$). For this sample, the heat-treatment resulted in improved accessibility of 1-hexene molecules to the surface and the pores. This increase in the 1-hexene uptake without a corresponding change in nitrogen BET surface area partly explains the observed increase in catalytic activity for 1-hexene hydrogenation following heat-treatment of Ru-MCM 41 sample. The adsorption of the hexene isomer 3,3-dimethyl-1-butene (303 K) after heat-treatment showed a Type I isotherm and yielded a BET surface area of 160 m^2g^{-1}, *i.e.* about half of the value derived from 1-hexene (295 m^2g^{-1}). The pore volume (0.13 cm^3g^{-1}) measured was also lower than that of 1-hexene (0.16 $cm^3\ g^{-1}$) on the heat-treated sample. The lower uptake of 'spherical' 3,3-dimethyl-1-butene, compared with the 'long chain' 1-hexene suggests that the 3,3-dimethyl-1-butene was more sterically hindered on the adsorption sites of the Ru-MCM 41 sample.

4.7 References

1. V. R. Choudhary and K. Mantri, *Micropor. Mesopor. Mater.*, 2000, **40**, 127.
2. S. Shyu, S. Cheng and D. Tzou, *J. Chem. Soc., Chem. Commun.*, 1999, 2337.
3. T. Maschmeyer, R. D. Oldroyd, G. Sankar, J. M. Thomas, I. J. Shanon, J. Beattie and R. Catlow, *Angew. Chem. Int. Ed. Engl.,* 1997, **36**, No. 15, 1639.
4. J. Clark and D. J. Macquarrie, *J. Chem. Soc., Chem. Soc. Rev.*, 1996, 303.
5. H. B. Jervis, M. E. Raimondi, R. Raja, T. Maschmeyer, J. M. Seddon and D. W. Bruce, *J. Chem. Soc., Chem. Commun.*, 1999, 2031.
6. M. Danks, *PhD Thesis*, The University of Exeter, 2002.
7. G. Katovic, B. Giordano, B. Onida, E. Garrone and P. Lentz, *Micropor. Mesopor. Mater.*, 2001, **44-45**, 275.
8. Y. Y. Zhong, Q. L. Shu, H. C. Tie, Z. W. Jing and X. L. He, *J. Chem. Soc., Chem. Commun.*, 1995, 973.
9. C. M. Bambrough, *PhD Thesis*, The Open University, 1998.
10. G. Brewer, J. Jasinski, W. Mahany, L. May and S. Prytkov, *Inorganica Chimica. Acta.*, 1995, **232**, 183.
11. M. Stockenhuber, R.W. Joyner, J. M. Dixon, M. J. Hudson, and G. Grubert, *Micropor. Mesopor. Mater.*, 2001, **44-45**, 367.
12. G. Kim, and S. Kim, *Catal. Lett.*, 1999, **57**, 139.
13. A. Böttcher, M. W. Grinstaff, J. A. Labinger, and H. B. Gray, *J. Mol. Catal. A: Chemical*, 1996, **113**, 191.
14. G. Calleja, R. van Grieken, R. Garcia, J. A. Melero and J. Iglesias, *J. Mol. Catal. A: Chemical*, 2002, **182-183**, 215.
15. W. Ahn, D. Lee, T. Kim, J. Kim, G. Seo and R. Ryoo, *Appl. Catal. A: General*, 1999, **181**, 39.
16. K. Koyano and T. Tatsumi, *Micropor. Mater.*, 1997, **10**, 259.

17. A. Tuel, *Micropor. Mesopor. Mater.*, 1999, **27**, 151.

18. Y. Kuang, N. He, J. Wang, P. Xiao, C. Yuan and Z. Lu, *Colloids and Surfaces A: Physicochem. Eng. Aspects*, 2001, **179**, 177.

19. Z. Zhu, Z. C. Chang and L. Kevan, *J. Phys. Chem. B*, 1999, **103**, 2680.

20. A. H. Vavydov, "*Infrared Spectroscopy of Advanced Species on the Surface of Transition Metal Oxides*" John Wiley and Sons, New York, 1990.

21. A. A. Tsyganenko, D. V. Pozdnyakov and V. N. Fvmonov, *J. Mol. Structure*, 1975, **29**, 299.

22. K. Nakamoto, "*Infra-red and Raman Spectra of Inorganic and Co-ordination Compounds*", 4th edition, John Wiley and Sons, New York, 1986.

23. J. F. Moulder, W. F. Stickle, P. E. Sobol and K. D. Bomben, "*Handbook of X-Ray Photoelectron Spectra- A Reference Book of Standard Spectra for Identification and Interpretation of XPS Data*", ed. J. Chastain, Perkin-Elmer Corporation, Eden Prairie, Minnesota, United States of America, 1992.

24. H. L. Siew, M. H. Qiao, C. H. Chew, K. F. Mok, L. Chan and G. Q. Xu, *Appl. Surface Sci.*, 2000, **173**, 95.

25. Science: A Third Level Course. S342 Physical Chemistry: Principal of Chemical Change, Block 6, Chapter 3, The Open University press, Milton Keynes, 1985.

26. S. Myhra, J. A. A. Crossley and M.W. Barsoum, *J. Phy. Chem. of Solids*, 2001, **62**, 811.

27. Personal communication, Prof. Frank J. Berry (The Open University), 2002.

28. P. J. Branton, *PhD thesis*, The University of Exeter, 1994.

29. S. J. Gregg and K. S. W. Sing, *"Adsorption, Surface Area and Porosity"*, 2nd Edition, Academic Press, London, 1982.

30. P. J. Branton, P.G. Hall, and K. S. W. Sing, *Adsorption*, 1994, **1**, 77.

31. U. Singh, R. T. Williams and I. D. Salter, K. R. Hallam, *Studies in Surface Science and Catalysis 144*, Elsevier Science, 2002, p-633.

32. C. M. Bambrough, R. C. T. Slade and R. T. Williams, *Phys. Chem. Chem. Phys.*, 2000, **2**, 3499.

CHAPTER 5

ORGANICALLY-MODIFIED MCM 41

5.1 Introduction

This Chapter summarises the synthesis and characterisation of a number of organically functionalised (organic-inorganic hybrid type materials[1, 2, 3]) MCM 41 materials; these are summarised in Table 5.1 at the end of this Section. A number of possible methodologies have been reported for attaching organic functionality to the surface of the silica support.[4] This Chapter describes the different routes used for the covalent attachment of organic moieties onto the Si-MCM 41 surface. The three different methods used in the current work are:

- The one-step, sol-gel synthesis method[3, 7, 8]
- The two-step, post-synthetic grafting of a functional groups[5, 6, 7, 8]
- The multi-step method, post-functionalisation by coupling with existing organic surface groups[4, 7, 8]

and these are discussed below.

5.1.1 The One Step Sol-gel Synthesis Method

The one-step method was carried out by co-hydrolysis and polymerisation of 3-aminopropyltriethoxysilane or Schiff base triethoxysilane along with the hydrolysis of tetraethyl orthosilicate. Cetyltrimethylammonium chloride (CTMACl) was used as the template in a solution of concentration less than that of the liquid crystal mesophase.

Mesitylene (1,3,5-trimethyl benzene) was used as the pore-swelling agent. Fig. 5.1 shows the flow diagram for the synthesis of the 3-aminopropyl and the Schiff base-modified MCM 41 materials.

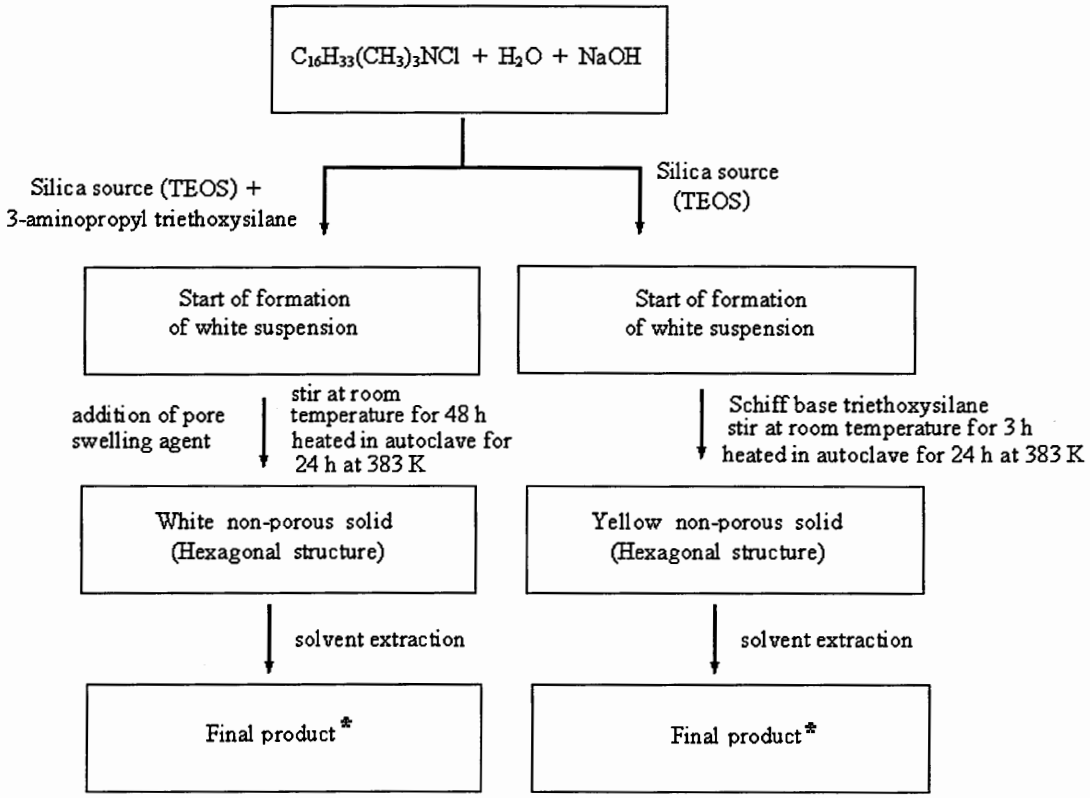

Figure 5.1 Flow diagram describing the synthesis of the organically-functionalised MCM 41 material by sol-gel synthesis method. * Structure collapsed after template removal.

5.1.2 The Two-Step, Post-synthetic Grafting of Organic Moiety

The immobilisation of organic molecules by post-synthetic grafting is a two-step method. The first step involves synthesis of the parent Si-MCM 41 material and then the second step involves its functionalisation with organic moieties. The 3-aminopropyltriethoxysilane and the Schiff base triethoxysilane are the two different organic moities immobilised on the parent Si-MCM 41 material. Fig. 5.2 describes the general synthesis of the organically-modified MCM 41 material by the post-synthetic grafting method.

In this case, most of the work involved functionalisation of Si-MCM 41 by post-synthetic grafting because the hexagonal structure of the as-synthesised material (synthesised by the one-step sol-gel method) collapsed on removal of the template using a solvent extraction technique.

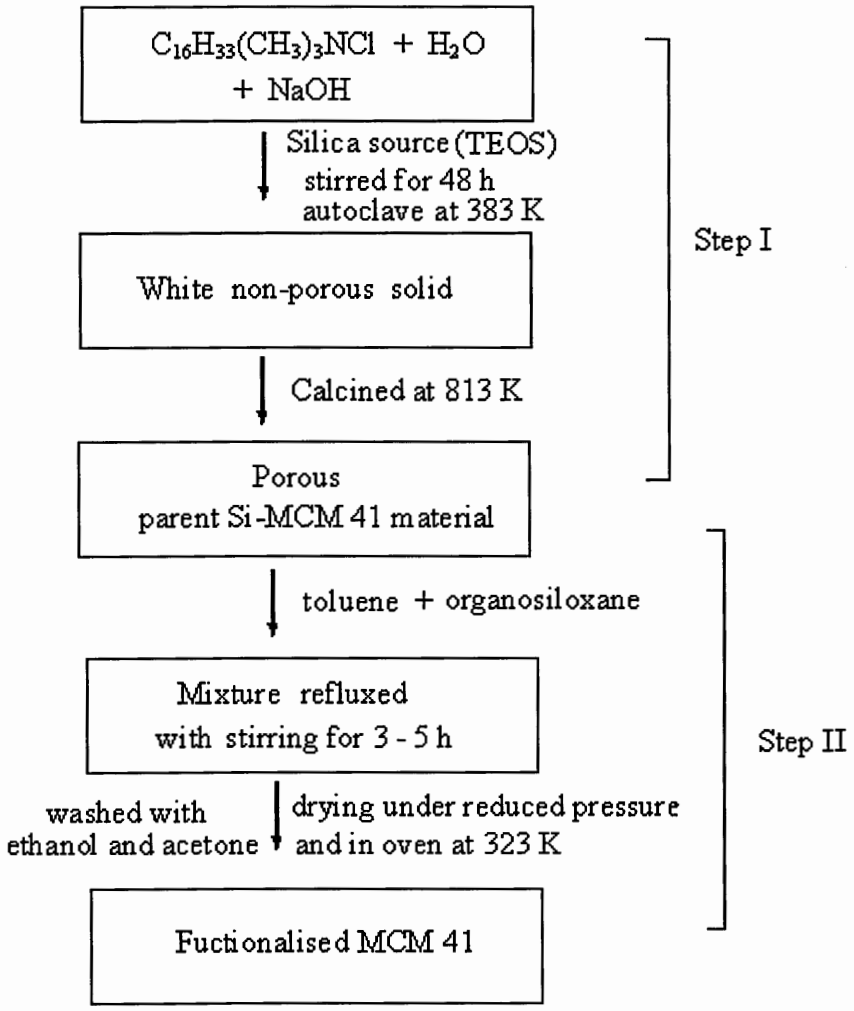

Figure 5.2 Flow diagram describing the general synthesis of the organically-functionalised MCM 41 material by the post-synthetic grafting method.

5.1.3 The Multi-step Method, Post-Functionalisation By Coupling With Existing Organic Surface Groups

In this method, the functionalisation was carried out by coupling of the organic species with the previously grafted organofunctional groups (3-aminopropyl-triethoxysilane).

The organic molecules immobilised by this method were Schiff base (Scheme 5.1) and the azodye (Scheme 5.2).

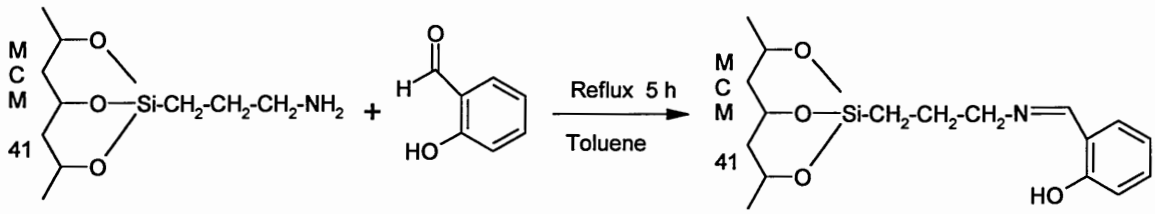

Scheme 5.1 Post-synthetic grafting of Schiff base triethoxysilane on Si-MCM 41 material (coupling of salicylaldehyde with previously grafted 3-aminopropyl groups).

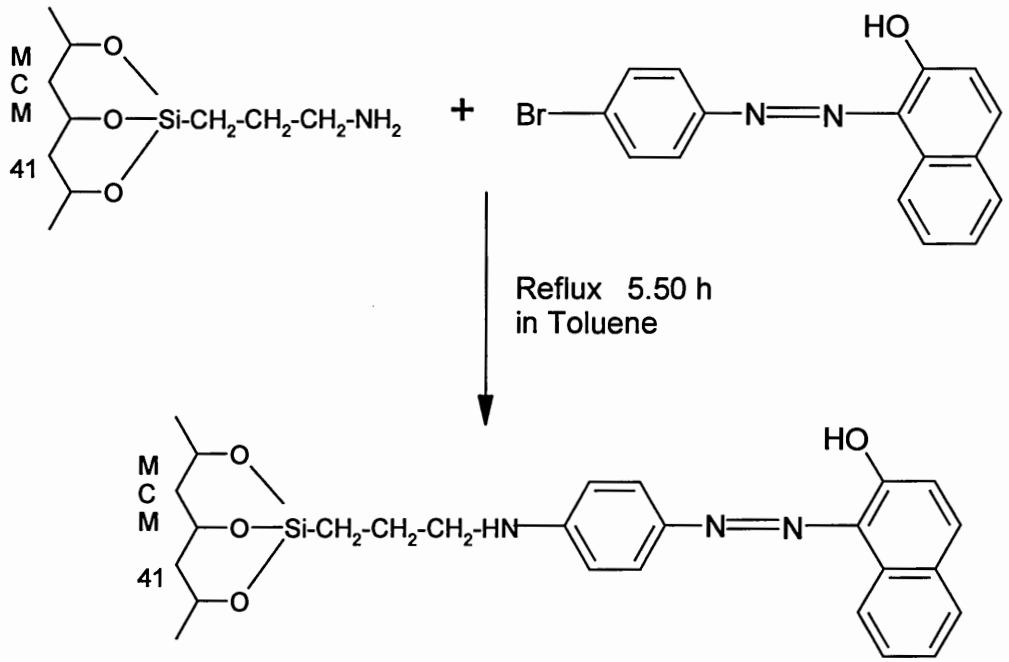

Scheme 5.2 Post-synthetic grafting of azodye on Si-MCM 41 material (coupling of azodye with previously grafted 3-aminopropyl groups).

Table 5.1 summarises the different organically-functionalised MCM 41 materials synthesised in this work and the analytical techniques used for their characterisation.

Table 5.1 Summary of the organically-functionalised MCM 41 materials synthesised, and the analytical techniques used for their characterisation

Materials	Abbreviations used	Physico-chemical Characterisation					V*
		XRD	IR	CHN	NMR	UV/Vis	
3-Aminopropyl MCM 41							
i) Sol-gel synthesised	NH_2-Ms-MCM-**s**	✓					
ii) Grafted MCM 41	NH_2-MCM-**g-0.5**	✓	✓	✓	✓		✓
	NH_2-MCM-**g-1.0**	✓	✓	✓	✓		✓
Schiff Base MCM 41							
i) Sol-gel synthesised	SB-MCM-**s**	✓					
ii) Grafted MCM 41	SB-MCM-**g-0.5**	✓	✓	✓	✓		✓
	SB-MCM-**g-1.0**	✓	✓	✓	✓		✓
iii) Coupling with previously grafted NH_2-MCM 41	SB-MCM-**c-0.5**	✓	✓	✓	✓		✓
	SB-MCM-**c-1.0**	✓	✓	✓	✓		✓
Azodye MCM 41							
Coupling of azodye with previously grafted NH_2-Ms-MCM 41	AZ-Ms-MCM-**c-3.0**	✓	✓	✓	✓	✓	✓

V = *Volumetric sorption of N_2 and CO_2, *CO_2 adsorption was carried out only on NH_2-MCM-**g** and SB-MCM-**c** samples. The numerical value gives the amount of organic moieties, in mmol g^{-1} used in the synthesis. Ms refers to the use of mesitylene-swollen materials.*

5.2 Synthesis

5.2.1 3-Aminopropyl-functionalised MCM 41

The synthesis of the 3-aminopropyl-functionalised MCM 41 material was carried out by two different methods *i.e.* the sol-gel synthesis method and by the post-synthetic

grafting method. The synthesis by each method is discussed below in following sub-sections.

*5.2.1.1 Sol-gel Synthesis (NH_2-MCM-**s**)*[9, 10, 11]

TEOS (3.06 g, 14.70 mmol) and 3-aminopropyltriethoxysilane (0.23 g, 1.04 mmol) were added to a solution of CTMACl (2.40 g, 1.90 mmol) and NaOH (0.37 g, 9.25 mmol) in 60 cm^3 of water. At the point where a white suspension started to form, mesitylene (2.00 g, 16.60 mmol g^{-1}) was added and the resulting mixture was stirred for 48 h and then heated in an autoclave for 24 h at 383 K. The white product obtained (Fig. 5.3) after filtration was washed with deionised water (250 cm^3) and dried at 323 K for 12 h. The solvent extraction method (Chapter 3, Section 3.1.1) was used rather than calcination for the removal of the template in order to avoid thermal decomposition of the 3-aminopropyl groups. The solvent used was concentrated HCl in ethanol (0.50 M solution).

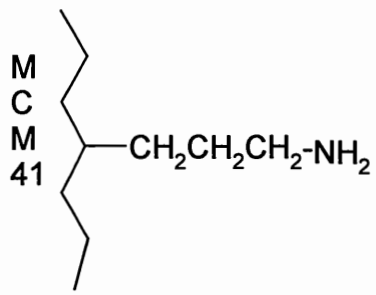

Figure 5.3 The structure of the 3-aminopropyl-functionalised MCM 41 material synthesised by the sol-gel method.

*5.2.1.2 Post-synthetic Grafting (NH_2-MCM-**g-1.0**)*[4,, 7, 8, 12]

Calcined Si-MCM 41 (1.00 g, preheated at 373 K for 2 h) was added to toluene (35 cm^3) followed by 3-aminopropyltriethoxysilane (0.22 g, 1.00 mmol) and the mixture was refluxed for 5 h with continuous stirring. The product (Fig. 5.4) was

cooled, filtered, and washed, first with ethanol (3 × 20 cm^3) and then with acetone (10 cm^3), dried initially under reduced pressure and finally at 323 K for 12 h.

For NH_2-MCM-**g-0.5** the synthesis procedure was similar to NH_2-MCM-**g-1.0** as described above, using half the amount of the 3-aminopropyltriethoxysilane (0.11 g, 0.50 mmol).

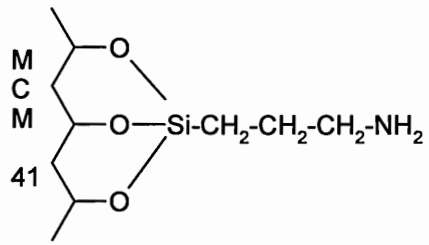

Figure 5.4 The structure of 3-aminopropyl-functionalised MCM 41 synthesised by the post-synthetic grafting method.

5.2.2 Schiff Base-fuctionalised MCM 41

The immobilization of Schiff base ligand on MCM 41 material was carried out by three different methods *i.e.* the sol-gel synthesis method, the post-synthetic grafting method and by coupling of salicylaldehyde with the previously grafted 3-aminopropyl groups on the MCM 41 surface.

The synthesis of the Schiff base ligand is described first, followed by synthesis of the Schiff base-modified MCM 41 materials by each method.

5.2.2.1 Synthesis of the Schiff Base Ligand

Salicylaldehyde (0.70 g, 5.73 mmol) was added to a solution of 3-aminopropyl-triethoxysilane (1.25 g, 5.65 mmol) in methanol (50 cm^3) *i.e.* in a 1:1 molar ratio. The resulting mixture was refluxed for 3 h with stirring[13, 14, 15] (reaction in Fig. 5.5). The Schiff base triethoxysilane ligand, a yellow viscous liquid, was isolated by evaporation of methanol under reduced pressure and was characterised by IR spectroscopy.

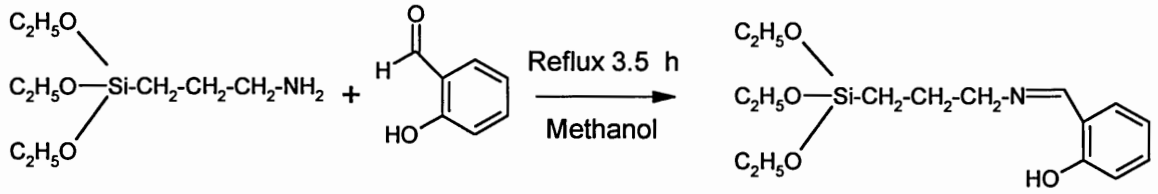

Figure 5.5 Synthesis of the Schiff base triethoxysilane ligand.

*5.2.2.2 Sol-gel Synthesis (SB-MCM-**s**)*

TEOS (2.68 g, 13 mmol) was added with stirring to a solution of CTMACl (2.40 g, 1.90 mmol) and NaOH (0.37 g, 9.25 mmol) in 60 cm^3 of water. At the point where a (after 5 min) white suspension started to form, Schiff base ligand (1.34 g, 4.30 mmol) was added and the resulting mixture were stirred for 3 h. The yellow suspension was heated in an autoclave for 24 h at 383 K. The resulting yellow solid (Fig. 5.6) was filtered washed with deionised water (250 cm^3) and then dried at 323 K for 12 h. The solvent extraction method (Chapter 3, Section 3.1.1) was used for the removal of a template in order to avoid thermal decomposition of the Schiff base. The solvent used was concentrated HCl in ethanol (0.50 M solution).

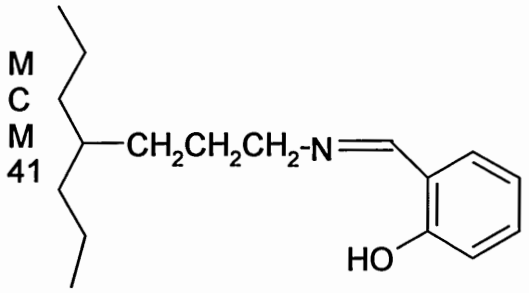

Figure 5.6 The structure of Schiff base-functionalised MCM 41 material synthesised by the sol-gel synthesis method.

*5.2.2.3 Post-synthetic Grafting (SB-MCM-**g-1.0**)*[7, 15]

Calcined Si-MCM 41 (1.00 g, preheated at 373 K for 2 h) was added to toluene (60 cm^3) followed by Schiff base triethoxysilane (0.34 g, 1.08 mmol) and the mixture

was refluxed for 6 h with continuous stirring. The resulting yellow product (Fig. 5.7) was cooled, filtered, and washed, first with ethanol (3 × 20 cm^3) and then with acetone (10 cm^3), dried initially under reduced pressure and finally at 323 K for 12 h.

For SB-MCM-**g-0.5** the synthesis procedure was similar to SB-MCM-**g-1.0** as described above, using half the amount of the Schiff base triethoxysilane ligand (0.17 g, 0.54 mmol).

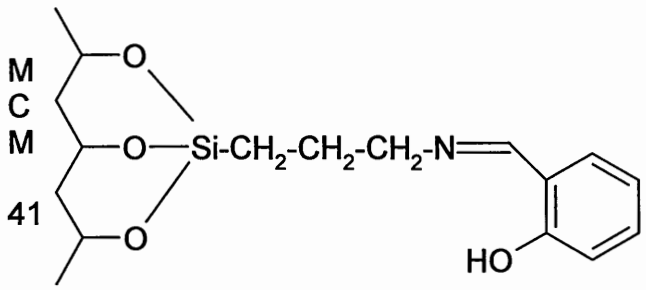

Figure 5.7 The structure of Schiff base-functionalised MCM 41 material synthesised by the post-synthetic grafting method.

*5.2.2.4 Coupling of Salicylaldehyde With Previously Grafted 3-Aminopropyl Groups on MCM 41 (SB-MCM-**c-1.0**)*[4, 16, 17]

The SB-MCM-**c-1.0** was obtained by coupling salicylaldehyde with previously grafted 3-aminopropyl groups of NH_2-MCM-**g-1.0**. The detailed procedure for the synthesis is as follows; NH_2-MCM-**g-1.0** (1.15 g) was added to methanol (40 cm^3), followed by a slight excess of salicylaldehyde (0.13 g, 1.06 mmol) to ensure complete reaction (required 1:1 molar ratio, salicylaldehyde:3-aminopropyl group) and the mixture was refluxed for 5 h with continuous stirring. The change in colour from white to yellow indicated the formation of imine (-C=N-).[15] The yellow product (Scheme 5.1) obtained was cooled, filtered, and washed, with methanol (4 × 20 cm^3), and then dried initially under reduced pressure and finally at 323 K for 12 h.

For SB-MCM-**c-0.5** the synthesis procedure was similar to SB-MCM-**g-1.0** as described above, using NH_2-MCM-**g-0.5** (1.10 g) and salicylaldehyde (0.07 g, 0.57 mmol).

5.2.3 Azodye-fuctionalised MCM 41

The immobilisation of azodye was carried out in three different steps:

- Step I: Azodye synthesis
- Step II: Grafting of 3-aminopropyltriethoxysilane onto Ms-MCM 41
- Step III: Coupling of azodye with previously grafted 3-aminopropyl groups of the NH_2-Ms-MCM 41 material.

5.2.3.1 Azodye {1-(4-bromo-phenylazo)-[2]naphthol} Synthesis[18, 19]

p-Bromoaniline (1.00 g) was dissolved in a solution of concentrated HCl (12 M, 4.65 cm^3) in water (11. 6 cm^3). The mixture was warmed (*ca.* 323 K) to dissolve the amine and then cooled in an ice-water bath, with constant stirring to a temperature less than 278 K.

A solution of sodium nitrite (0.47 g) in water (4.70 cm^3) was prepared and cooled to a temperature less than 278 K. 2-Naphthol (0.83 g) was dissolved in 1 M sodium hydroxide (10 cm^3) and then cooled to 278 K.

The cold sodium nitrite solution was added drop wise to the *p*-bromoaniline with swirling. The temperature of the solution was maintained below 278 K throughout the addition. The excess of nitrous acid was destroyed by adding urea. The diazonium salt solution obtained was added drop wise to the 2-naphthol solution and the resulting red dye (Fig. 5.8) was recovered by filtration. The recrystallisation was carried out in ethanoic acid and the purity was checked by TLC. The azodye obtained was characterised by ^{13}C NMR.

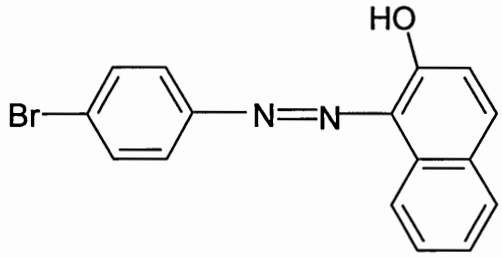

Figure 5.8 Structure of the pure azodye {1-(4-bromo-phenylazo)-[2]naphthol}.

5.2.3.2 Post-synthetic Grafting of 3-Aminopropyltriethoxysilane on Ms-MCM 41

Calcined Ms-MCM 41 (1.00 g, preheated at 373 K for 2 h) was added to toluene (50 cm^3), followed by 3-aminopropyltriethoxysilane (0.66 g, 2.99 mmol) and the mixture was refluxed for 5 h with continuous stirring. The product obtained was cooled, filtered, and washed, first with ethanol (3 × 20 cm^3) and then with acetone (10 cm^3), dried initially under reduced pressure and finally at 323 K for 12 h.

*5.2.3.3 Coupling of the Azodye With Previously Grafted 3-Aminopropyl Group on Mesitylene-swollen MCM 41 (AZ-Ms-MCM-**c-3.0**)*[4, 16, 17]

Calcined NH_2-Ms-MCM-**g-3.0** (0.50 g, with a 3-aminopropyl group of 3.00 mmol g^{-1}) was added to toluene (35 cm^3), followed by the azodye (0.3 g, in 1:1 molar ratio with respect to 3-aminopropyl group) and the resulting mixture was refluxed for 3 h with stirring. The red product (Scheme 5.2) obtained by filtration was washed, first with methanol (2 × 20 cm^3) and then with acetone (10 cm^3), and dried initially under reduced pressure and finally at 323 K for 12 h.

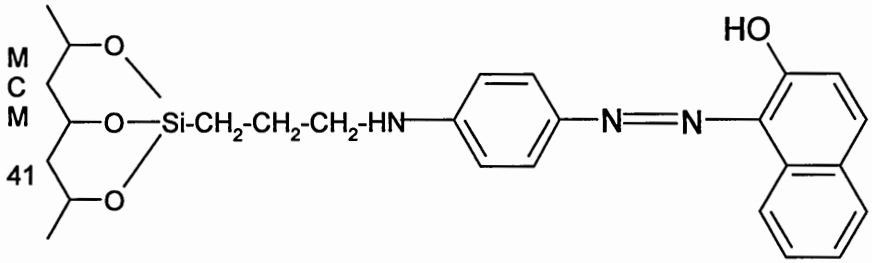

Figure 5.9 The azodye-functionalised MCM 41 material synthesised by the post-synthetic coupling method.

5.3 Results and Discussions: Physico-chemical Characterisation

The samples NH_2-MCM-**g-0.5** and NH_2-MCM-**g-1.0** are denoted as NH_2-MCM-**g**, samples SB-MCM-**g-0.5** and SB-MCM-**g-1.0** are denoted as SB-MCM-**g**, and samples SB-MCM-**c-0.5** and SB-MCM-**c-1.0** are denoted as SB-MCM-**c** for discussion of results.

5.3.1 Powder X-ray Diffraction (p-XRD)

The hexagonal periodicity of all the materials synthesised was confirmed by *p*-X-ray diffraction. The results obtained are summarised in Table 5.2.

Table 5.2 Powder-XRD results for the organically-modified MCM 41 materials

Sample	d_{100} **peaks**	d_{100}**-spacing / Å (A.S.)**	d_{100}***-spacing* / Å (S.E.)**	***a* / Å (S.E.)**
NH_2-Ms-MCM-**s***	1.9	48	--	--
NH_2-MCM-**g**	3.7	--	36	42
SB-MCM-**s**	4.1	32	--	--
SB-MCM-**g**	3.5	--	38	44
SB-MCM-**c**	3.7	--	36	42
AZ-Ms-MCM-**c-3.0**	2.6	--	50	58

A.S. = as-synthesised, S.E. = after template removal,
* *p-XRD pattern recorded using CuKα radiation (λ = 1.54 Å)*

The powder *p*-XRD patterns for NH_2-MCM-**s** and SB-MCM-**s** before and after removal of template are shown in Fig. 5.10 and Fig. 5.11, respectively. In both the cases, the XRD pattern displayed a d_{100} peak for the as-synthesised materials, indicating the hexagonal ordering of the material. However, the disappearance of the d_{100} in the XRD pattern of both the samples following template removal suggested the collapse of the hexagonal structure. This contrasts with the work reported by other workers.[2, 3, 4, 7]

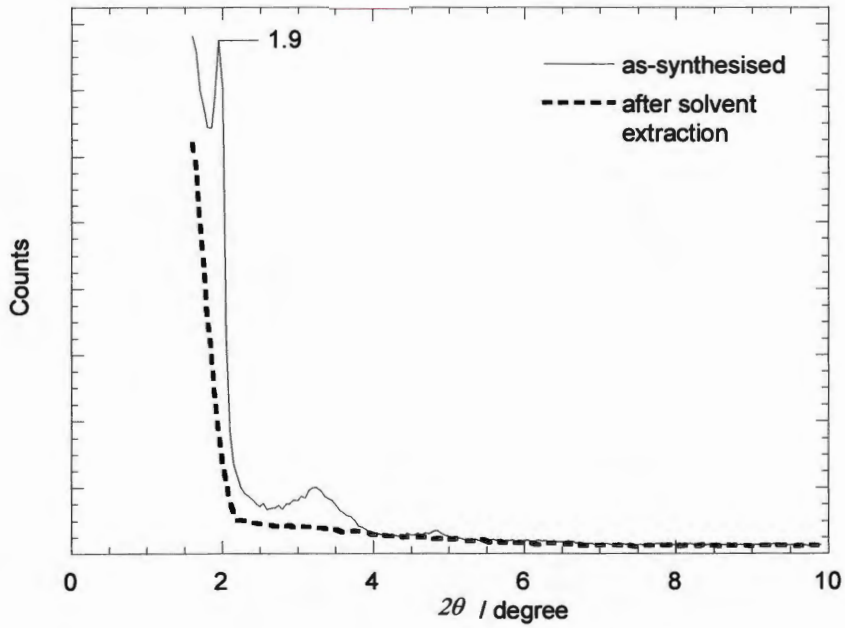

Figure 5.10 *p*-XRD pattern for NH_2-MCM-s, recorded using CuKα radiation (λ = 1.54 Å).

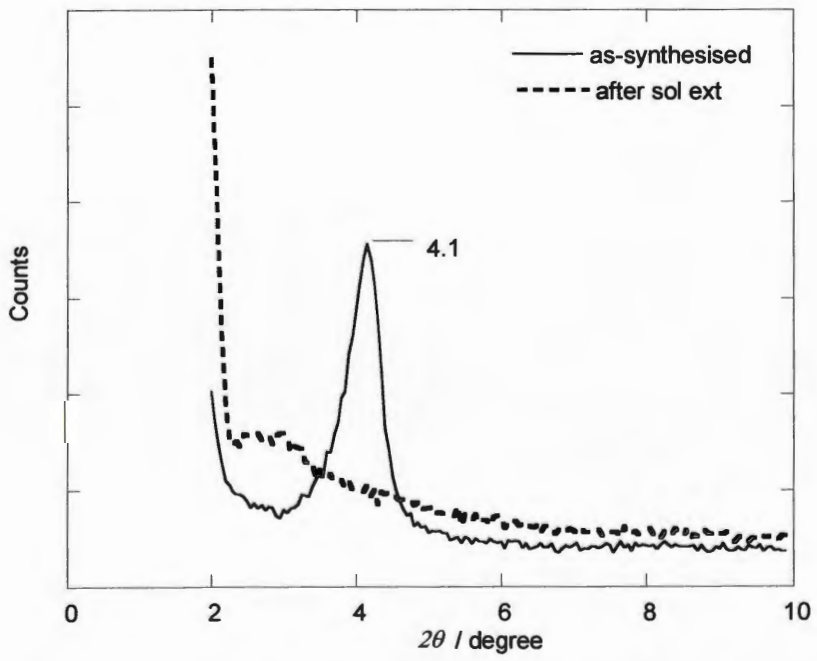

Figure 5.11 *p*-XRD pattern for SB-MCM-s, recorded using CrKα radiation (λ = 2.29 Å).

The d_{100} reflection for as-synthesised NH_2-MCM-**s** corresponds to a *d*-spacing of 48 Å, which was found to be larger than the *d*-spacing of unswollen MCM 41 (38 Å, Section 3.2.1). The addition of mesitylene resulted in an increase in the d_{100} spacing of this material, which is directly related to the increase in the pore diameter. Higher order Bragg reflections of the hexagonal structure can also be seen in the *p*-XRD pattern of the as-synthesised material.

SB-MCM-**s** (Fig. 5.11) showed only one broad d_{100} reflection for the as-synthesised sample, corresponding to a *d*-spacing of 32 Å. Other workers have suggested that the absence of higher order reflections is indicative of a disordered hexagonal mesophase.[2, 3, 11]

The *p*-XRD patterns for all the organically functionalised MCM 41 samples (NH_2-MCM-**g**, SB-MCM-**g,** SB-MCM-**c**) synthesised by post-synthetic grafting were similar to those of the parent Si-MCM 41 material, as shown by the *p*-XRD pattern for NH_2-MCM-**g** material in Fig. 5.12. The d_{100} peak positions and the corresponding *d*-spacings for all the samples are summarised in Table 5.2. The presence of the d_{100} reflection at 2θ *ca.* 3.7° and the higher order reflections at 2θ *ca.* 6.0° and 7.0° confirmed that the hexagonal mesophase of the Si-MCM 41 host was preserved following functionalisation. The *p*-XRD patterns of SB-MCM-**g** and SB-MCM-**c** are given in Appendix 3.

The presence of the d_{100} reflection and the higher order reflections in the *p*-XRD pattern of AZ-Ms-MCM-**c-3.0** (Fig. 5.13) suggested that there is no loss in the hexagonal ordering of mesoporous host even after treatment in different solvents and under different temperature conditions. This was similar to the work reported by other workers.[20, 21] The mesitylene-swollen material showed a large *d*-spacing (50 Å) and unit cell parameter (58 Å) compared with the unswollen Si-MCM 41 (38 Å and 44 Å, respectively).

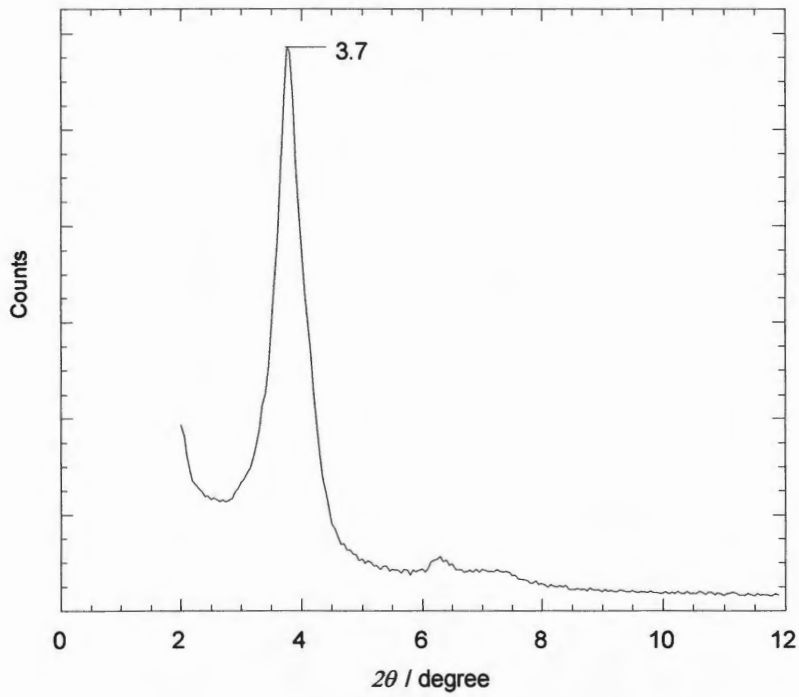

Figure 5.12 *p*-XRD pattern for NH_2-MCM-**g**, recorded using CrKα radiation (λ = 2.29 Å).

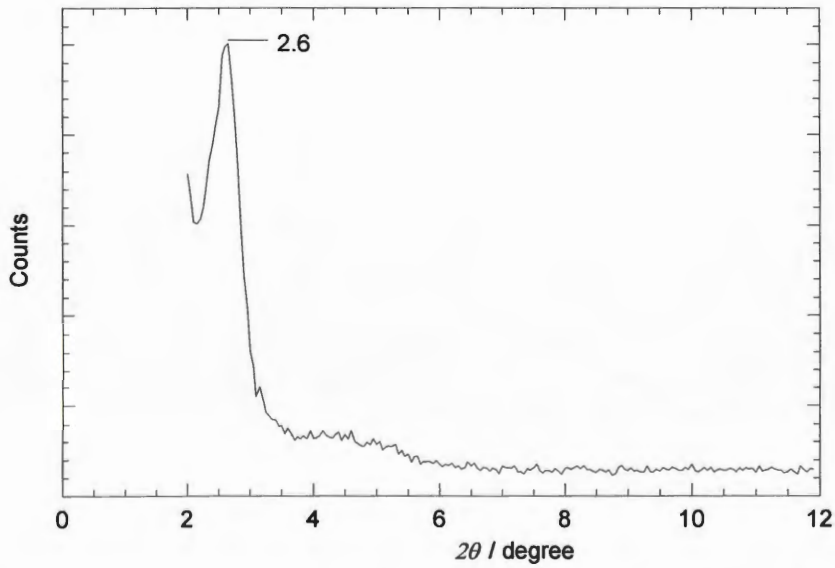

Figure 5.13 *p*-XRD pattern for AZ-Ms-MCM-**c-3.0**, recorded using CrKα radiation (λ = 2.29 Å).

5.3.2 Infrared Spectroscopy (IR)

Fourier Transform (FT) IR spectroscopy was used to confirm the presence of the organic moieties in the modified MCM 41 materials. It was also used to monitor the removal of the template from the sol-gel synthesised materials (NH_2-MCM-**s** and SB-MCM-**s**). However, due to the collapse of the hexagonal structure of these materials after template removal the IR results of these samples are not discussed in this work. The observed band assignments for different vibrations are summarised in Table 5.3.

Table 5.3 IR bands with assigned vibrations (approximate wavenumber / cm^{-1})[22, 23, 24, 25]

Observed IR bands / cm^{-1}			**Vibrations**
3-aminopropyl-fuctionalised MCM 41	**Schiff base-fuctionalised MCM 41**	**Azodye-fuctionalised MCM 41**	
--	730	730	Phenyl out-of-plane C-H_{def}
1450 – 1480	1450 – 1480	1450 – 1480	C-H_{def}
--	1485	1485	Phenyl C-C_{str}
1557*	--	--	N-H_{def}
--	1620*	--	C=N_{str}
1640	1650	1640	O-H_{def}
2830, 2960	2830, 2960	2930	C-H_{str}
--	--	1634*	N=N_{str}

def =deformation vibration, *str* = stretching vibration
** Poor signal/noise ratio was evident in the range 1400 cm^{-1} to 1650 cm^{-1} and the peaks for N-H, C=N and N=N are therefore tentatively assigned.*

5.3.2.1 3-Aminopropyl-modified MCM 41 Materials

The IR spectrum for 3-aminopropyl-modified MCM 41 (NH_2-MCM-**g**) is shown in Fig. 5.14. The peaks due to N-H_{def} vibrations are expected in the region 1550-1650 cm^{-1} but the poor signal to noise ratio in this region of the spectrum makes the band assignment very difficult. However, the band at *ca.* 1557 cm^{-1} was assigned to a N-H_{def} on the basis of NMR work (which is discussed in Section 5.3.4) and the results reported

by other workers.[9, 22, 26] The peaks due to the N-H_{str} vibrations from a primary amine, expected in the region 3350 - 3500 cm^{-1} are subsumed within the broad O-H absorption band. The C-H_{def} and C-H_{str} vibrations at *ca.* 1470 cm^{-1} and at *ca.* 2830 cm^{-1}, 2960 cm^{-1}, respectively,[22, 24, 25 27] present in the IR spectrum of the free 3-aminopropyl siloxane (Fig. 5.14-a) were also present in the spectrum of NH_2-MCM-**g** (Fig. 5.14-b). These bands were assigned to the propyl chains of the 3-aminopropyl groups. The presence of these bands in the IR spectrum of NH_2-MCM-**g** material suggested the successful immobilization of 3-aminopropyl functions on Si-MCM 41.

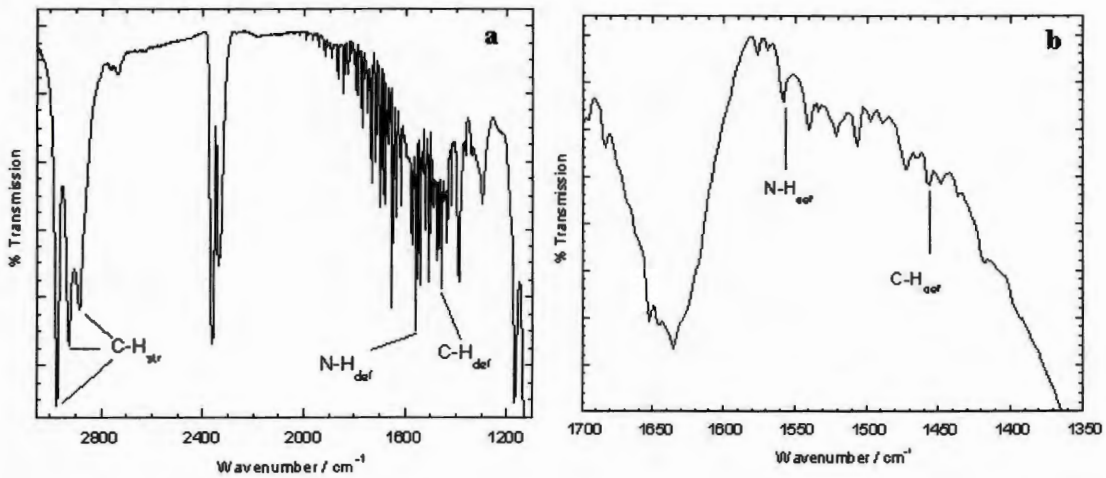

Figure 5.14 IR spectra of: (a) 3-aminopropyltriethoxysilane, and (b) 3-aminopropyl-modified MCM 41 (NH_2-MCM-**g**).

5.3.2.2 Schiff Base-modified MCM 41 Materials

The immobilization of Schiff base triethoxysilane on Si-MCM 41 surface was confirmed by IR spectroscopy. The IR spectra of the free Schiff base triethoxysilane, SB-MCM-**g** and SB-MCM-**c** (the Schiff base-modified MCM 41 materials) are presented in Fig. 5.15. The principal vibration bands observed in the modified samples are assigned in Table 5.3. The IR spectra for SB-MCM-**g** and SB-MCM-**c** show a band at 1650 cm^{-1} due to the O-H bending vibration. This band was found to be broad and

intense, which overlaps with the C=N band at *ca.* 1620 cm^{-1}. Hence the band due to the C=N stretching vibration appears as a shoulder. The IR spectrum of the free Schiff base triethoxysilane (Fig. 5.15-a) shows a band at *ca.* 1630 cm^{-1}, which was assigned to the C=N stretching vibration of the imine.[15, 25] A similar band at *ca.* 1620 cm^{-1} is also present in the spectrum of each of SB-MCM-**g** and SB-MCM-**c**.

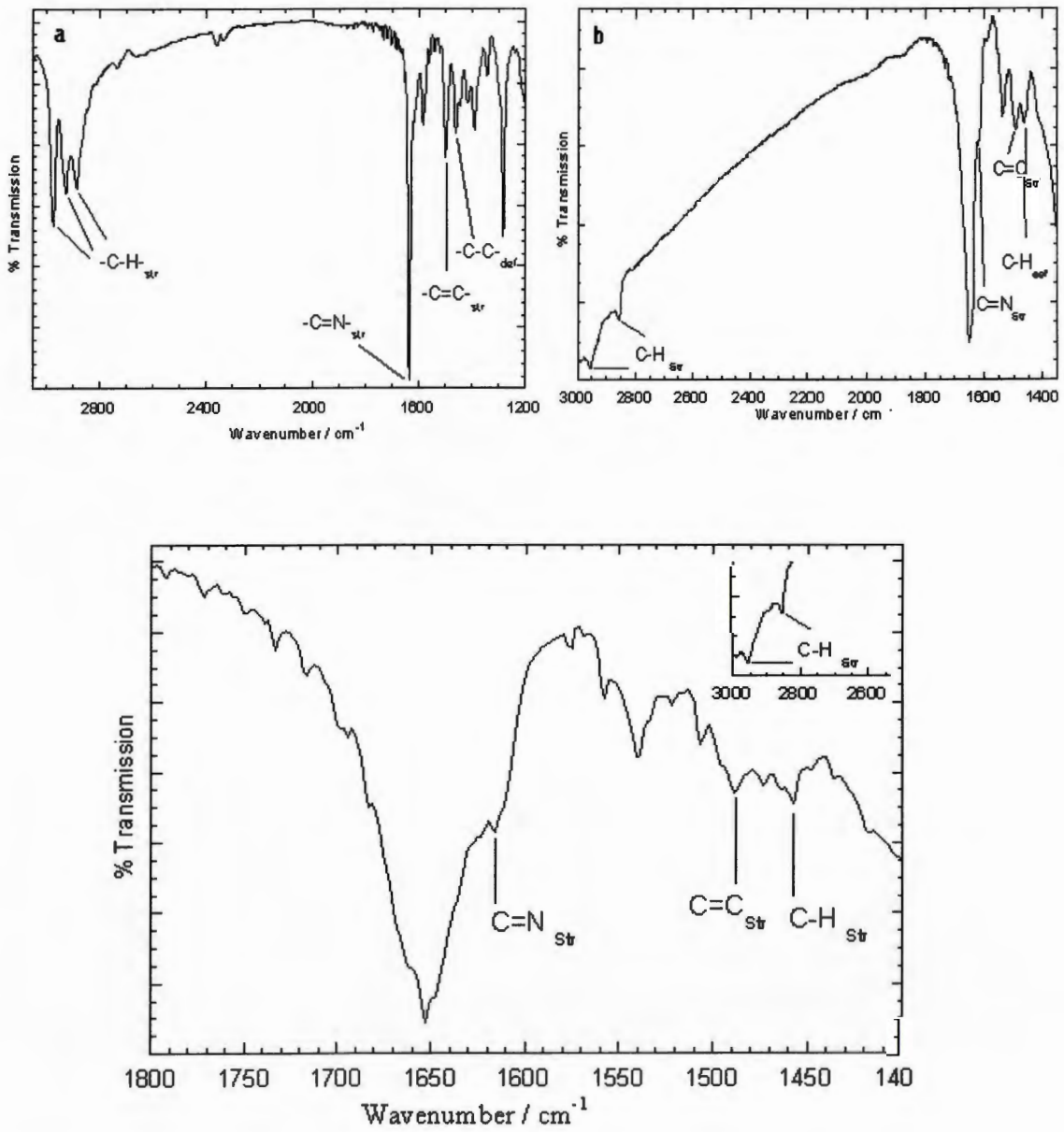

Figure 5.15 IR spectrum of: (a) Schiff base triethoxysilane ligand, (b) Schiff base-modified MCM 41 (SB-MCM-**g**), and (c) Schiff base-modified MCM 41 (SB-MCM-**c**).

The spectrum (Fig. 5.15-b) for SB-MCM-**g** shows peaks corresponding to C-H_{str} and C-H_{def} vibration frequencies at 2960 cm^{-1}, 2830 cm^{-1} and 1455 cm^{-1},[22, 27] respectively. These bands were due to the C-H vibrations from the propyl chain and were also found to be present in the spectrum of the free Schiff base ligand (Fig. 5.15-a). The IR absorption band at *ca.* 1485 cm^{-1},[22, 24, 25] which is assigned to C-C aromatic stretching vibration of the phenyl ring, was also found to be present in the spectra of SB-MCM-**g,** SB-MCM-**c** and the free Schiff base. The presence of C-C phenyl vibration bands in the IR spectrum of each of the Schiff base-modified materials confirmed the immobilisation of the Schiff base triethoxysilane on the Si-MCM 41 surface.

5.3.2.3 Azodye-modified MCM 41

The IR spectrum for the azodye-functionalised MCM 41 (AZ-Ms-MCM-**c-3.0**) is shown in Fig 5.16.

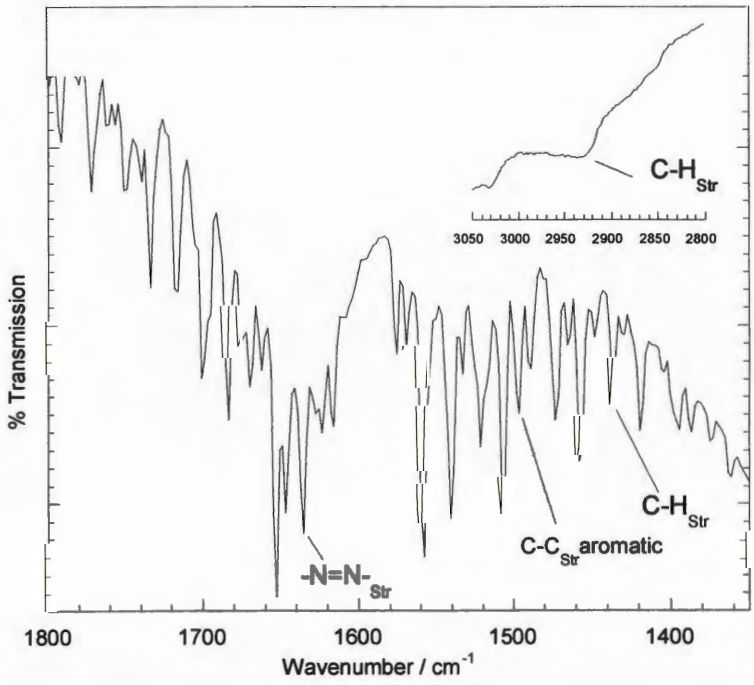

Figure 5.16 IR spectrum of azodye-functionalised MCM 41 (AZ-Ms-MCM-**c-3.0**).

The IR bands for the azo group (N=N) and the C-C aromatic stretching vibrations of the phenyl rings are located in the region 1400 – 1800 cm^{-1} but the poor signal to noise ratio makes the IR analysis difficult and inconclusive for this sample. However, the bands at *ca.* 1630 cm^{-1} and 1495 cm^{-1} were tentatively assigned to the azo group (N=N) and the C-C stretching of the aromatic rings, respectively,[24, 25] (These bands were not observed in the IR spectrum of the unmodified parent Ms-MCM 41 and the 3-aminopropyl-modified samples). The bands observed at *ca.* 2930 cm^{-1} and at 1430 cm^{-1} were assigned to C-H stretching, and deformation vibrations, respectively, of the $-CH_2-$ groups in the 3-aminopropyl chains, used to tether the azodye to the Si-MCM 41 surface.

The IR spectrum in the region 640 to 760 cm^{-1} (Fig. 5.17) for the azodye sample shows a sharp band at 730 cm^{-1} for the C-H deformation, aromatic out-of-plane, vibration.[22, 24, 25] This band was absent in the IR spectrum of the Ms-MCM 41 and in the spectrum of 3-aminopropyl-functionalised MCM 41, which confirmed the functionalisation of the Ms-MCM 41 material with azodye.

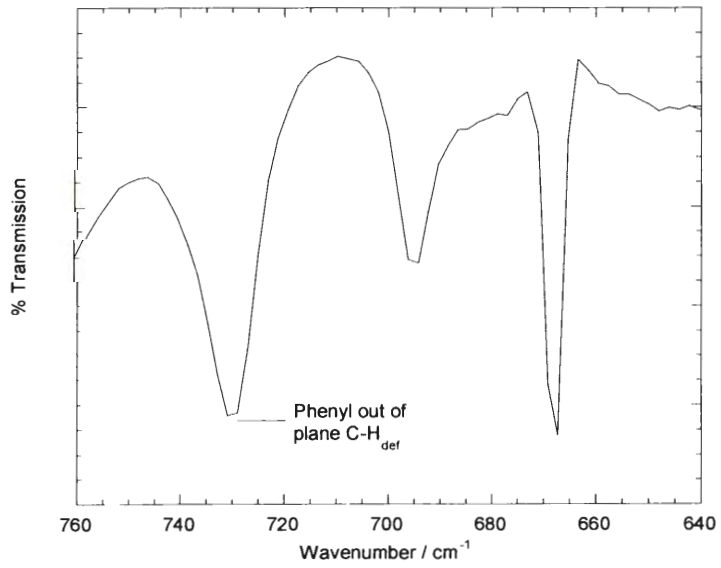

Figure 5.17 IR spectrum showing the peak due to C-H deformation (aromatic out-of-plane) vibration of azodye-functionalised MCM 41 (AZ-Ms-MCM-**c-3.0**).

5.3.3 CHN Microanalysis

The CHN microanalytical data for the organically-modified MCM 41 materials are summarised in Table 5.4.

Table 5.4 CHN microanalytical data for the organically-modified MCM 41 materials

Sample	Carbon / % by mass	Hydrogen / % by mass	Nitrogen / % by mass
NH_2-MCM-**g-0.5**	3.80	1.40	0.86
NH_2-MCM-**g-1.0**	5.40	1.70	1.40
SB-MCM-**g-0.5**	5.00	1.40	0.44
SB-MCM-**g-1.0**	6.50	1.60	0.64
SB-MCM-**c-0.5**	9.00	1.80	0.80
SB-MCM-**c-1.0**	11.50	2.00	1.30
AZ-Ms-MCM-**c-3.0**	6.80	2.00	1.20
Si-MCM 41	0.08	1.10	0.00

The data represents the average of two runs, which were in good agreement (± 0.07%).

The presence of a higher percentage of carbon, hydrogen and nitrogen in the organically-modified MCM 41 samples confirmed the immobilisation of organic moieties within the pores of the MCM 41. Higher loading of organic moieties was reflected by a higher percentage of carbon, hydrogen and nitrogen as expected.

Fig. 5.18 shows the possible structures for the grafted 3-aminopropyl-modified MCM 41 materials (NH_2-MCM-**g-0.5** and NH_2-MCM-**g-1.0**). It can be seen from Table 5.5, that the experimentally observed C:N ratio corresponded to the theoretical C:N ratio calculated for structure B. This suggested that structure B is predominantly present in the sample of grafted 3-aminopropyl-modified MCM 41 material (contributions from structure A and C are also possible though the ratio of these two structures would need to be in a 1:1 ratio in order to maintain the observed C:N ratio).

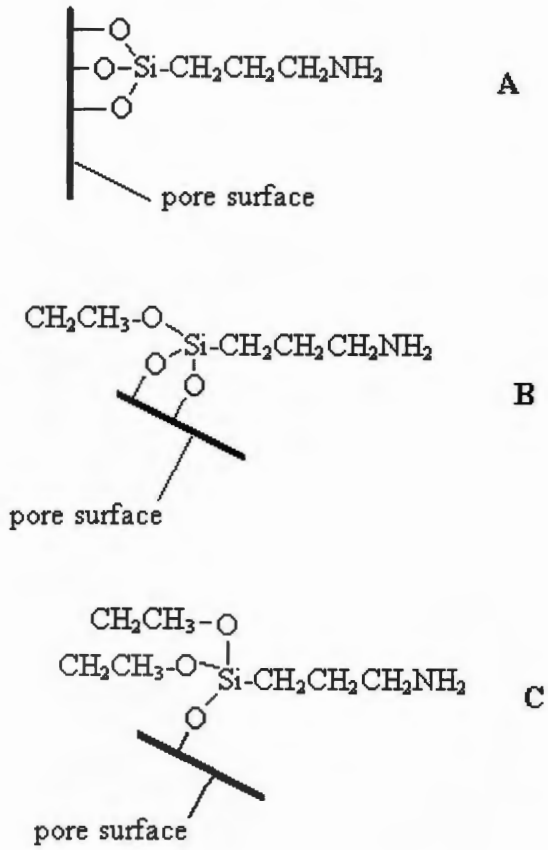

Figure 5.18 Possible structures for the grafted 3-aminopropyl-modified MCM 41 materials (NH_2-MCM-**g-0.5** and NH_2-MCM-**g-1.0**).

Table 5.5 Summary of the observed and theoretical C:N ratio for the possible structures of the 3-aminopropyl-modified MCM 41 material

Sample structure from Fig. 5.18	**Theoretical C:N ratio**	**Observed C:N ratio from CHN microanalysis**	**3-aminopropyl-modified samples**
A	3:1	5.1:1.0	NH_2-MCM-**g-0.5**
B	5:1	4.5:1.0	NH_2-MCM-**g-1.0**
C	7:1		

Comparing the results of the grafted (SB-MCM-**g**) and coupled (SB-MCM-**c**) Schiff base samples, SB-MCM-**c** shows a much higher percentage (nearly double) of

carbon, hydrogen and nitrogen than SB-MCM-**g**. This suggests that a higher loading of Schiff base was achieved by the coupling reaction (coupling with previously grafted organofunctional groups) compared with direct post-synthetic grafting reaction. It is possible that in the synthesis of SB-MCM-**g** the bulky nature of the pre-synthesised Schiff base siloxane restricts its access to the reactive surface sites within the pores. Again, the material (SB-MCM-**c**) retained its mesoporosity and there was no significant decrease in the surface area and pore volume as reflected by nitrogen sorption analysis (Section 5.4.1). This showed the advantage of coupling reaction method over the direct post-synthetic grafting method.

For the azodye functionalised MCM 41 material the immobilisation of azodye onto the Si-MCM 41 surface was supported by the CHN microanalysis results. The CHN microanalysis results for the azodye functionalised material yielded a C:N ratio of 6.5:1, which is in good agreement with the expected theoretical ratio of 6.3:1 for the azodye.

5.3.4 Nuclear Magnetic Resonance (NMR) Spectroscopy

5.3.4.1 ^{29}Si Cross-polarisation Magic Angle Spinning (CP MAS) NMR Spectroscopy

Silicon-29 cross polarisation magic angle spinning nuclear magnetic resonance (CP MAS NMR) spectroscopy of the 3-aminopropyl-modified MCM 41 and the Schiff base-modified MCM 41 samples was carried out by the solid-state NMR service at the University College London. The spectra obtained for NH_2-MCM 41 and SB-MCM-**c** (0.5 mmol g^{-1}) are shown in Figs. 5.19 and 5.20, respectively, and they indicate the various types of silicon species present in the sample. Other spectra are given in Appendix A3.

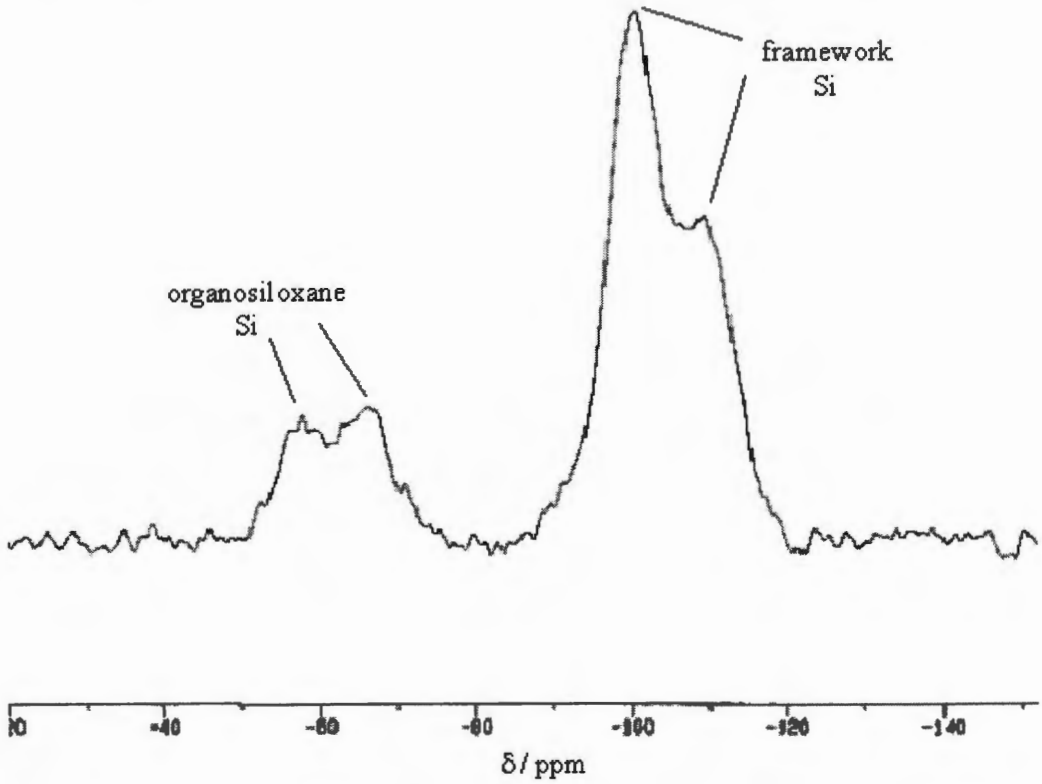

Figure 5.19 ^{29}Si CP MAS NMR spectrum of 3-aminopropyl-modified MCM 41 (NH_2-MCM-**g**).

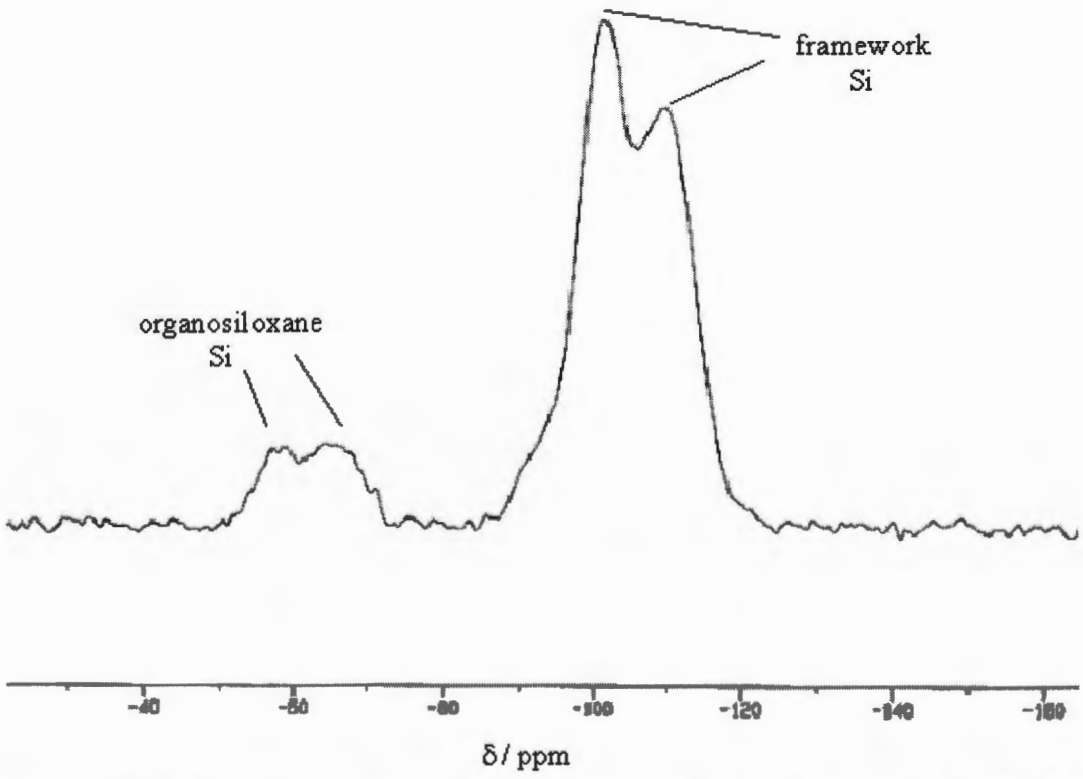

Figure 5.20 ^{29}Si CP MAS NMR spectrum of Schiff base-modified MCM 41 (SB-MCM-**g**).

The organically-modified samples show the presence of distinct resonances due to organosiloxane ($T^m = RSi(OSi)_m(OH)_{3-m}$, m = 1-3,) (Section 2.8.4), which are absent in the spectrum of the unmodified Si-MCM 41. The spectra also display resonances due to the siloxane unit [$Q^n = Si(OSi)_n(OH)_{4-n}$, n = 2-4) (Section 3.2.6), similar to those observed for Si-MCM 41. The chemical shifts of these resonances are summarised in Table 5.6.

Table 5.6 ^{29}Si CP MAS NMR chemical shifts for the organically-modified MCM 41 materials

	δ / ppm					
Sample	T^1	T^2	T^3	Q^2	Q^3	Q^4
NH_2-MCM-**g**	_ _	-57.8	-66.3	~ -92.0	-100.9	-109.7
SB-MCM-**g**	_ _	~ -59	~ -68	~ -92.0	-101.3	-109.7
SB-MCM-**c**	_ _	-58.6	-64.2	~ -92.0	-101.5	-109.5
Si-MCM-41	_ _	_ _	_ _	-91.9	-100.7	-109.3

The two main peaks observed, centred at *ca.* δ = -101 and -110 , assigned to Q^3 [$HOSi(OSi)_3$] and Q^4 [$Si(OSi)_4$] Si sites, respectively, represent the silica framework. The presence of a small contribution of Q^2 [$(HO)_2Si(OSi)_2$] Si site is evident from a weak and small peak, which appears as a small shoulder at *ca.* δ = -92 ppm. [28, 29]

Modification of the Si-MCM 41 with organosiloxane resulted in an increase in the peak intensity of the Q^4 sites relative to Q^3 sites (when compared with unmodified Si-MCM 41, see Fig. 3.10, Chapter 3). This indicated the replacement of surface silanol groups (Si-OH) by organosiloxane. [10, 22, 30]

The additional resonance peaks observed in the spectra of the modified samples between δ = -50 to -70 ppm were assigned to organosiloxane bonded on the silica surface *via* Si-O-Si linkages. The peak centred at *ca.* δ = -58 ppm for T^2,

$(SiO)_2Si(OC_2H_5)R$, and at *ca.* δ = -66 ppm for T^3, $(SiO)_3Si$-R, were indicative of bi- and tri-dentate binding, respectively.[10, 22, 31]

5.3.4.2 ^{13}C-{^1H}-Cross-polarisation Magic Angle Spinning (CP MAS) NMR Spectroscopy

Carbon-13-{^{1}H}-cross polarisation magic angle spinning (CP MAS) NMR spectroscopy on the 3-aminopropyl-modified MCM 41 and the Schiff base-modified MCM 41 samples was carried out by the solid-state NMR service at the University College London. The ^{13}C-{^{1}H}-CP MAS NMR spectroscopic analysis of the azodye and the azodye-functionalised MCM 41 material was carried out by Dr. Ashbrook (University of Exeter). The ^{13}C-{^{1}H}-CP MAS NMR results and spectra discussed in this Section are for samples with an organic compound loading of 0.5 mmol g^{-1}. The spectra for other samples with higher loading (1.0 mmol g^{-1}) are given in Appendix A3. The resonance frequencies and assigned carbon environments are summarised in Table 5.7.

Table 5.7 ^{13}C-{^{1}H}-CP MAS NMR chemical shifts for the organically-modified MCM 41 materials

	δ*/ ppm										
Sample	**Aliphatic carbon peak position**						**Aromatic carbon peak position**				
NH_2-MCM-**g**	8.8	19	22	29	43	60	--	--	--	--	--
SB-MCM-**g**	8.9	--	--	24	49	60	117	134	--	166	173
SB-MCM-**c**	9.2	--	--	24	49	61	118	131	162	166	175
AZ-Ms-MCM-**c-3.0**	9.2	--	--	22	43	--	124	127	130	131	140
Aromatic carbon peak position											
Azodye	116	124	129	132	135	141	145	174			

* *TMS as external standard*

The ^{13}C-{^{1}H}-CP MAS NMR spectra of all the organically-modified MCM 41 materials (Fig. 5.21 and Fig. 5.22) show three to five resonances in the aliphatic region, between 0 and 60 ppm.[16] Three peaks at *ca.* δ = 9, 22 and 43 ppm were assigned to the three different carbon atoms of the 3-aminopropyl groups (Fig. 5.23).[10, 16, 22, 31] The NH_2-MCM-**g** and AZ-Ms-MCM-**c-3.0** samples showed these peaks to be of approximately equal intensities as expected. The Schiff base modified samples shows three peaks in the aliphatic region at *ca.* δ = 9, 24 and 49 ppm. The peak at δ = 43 ppm in the 3-aminopropyl modified sample disappears and a new peak at δ = 49 ppm appears for the Schiff base modified sample, which confirms the formation of imine (-C=N-). This peak at *ca.* δ = 49 ppm is of twice the intensity of the other two peaks at δ = 8 and 24 ppm, which shows the presence of two different carbon atoms attached to the nitrogen atom of the imine functional groups. The metal-Schiff base modified samples showed the similar results (discussed in Chapter 6).

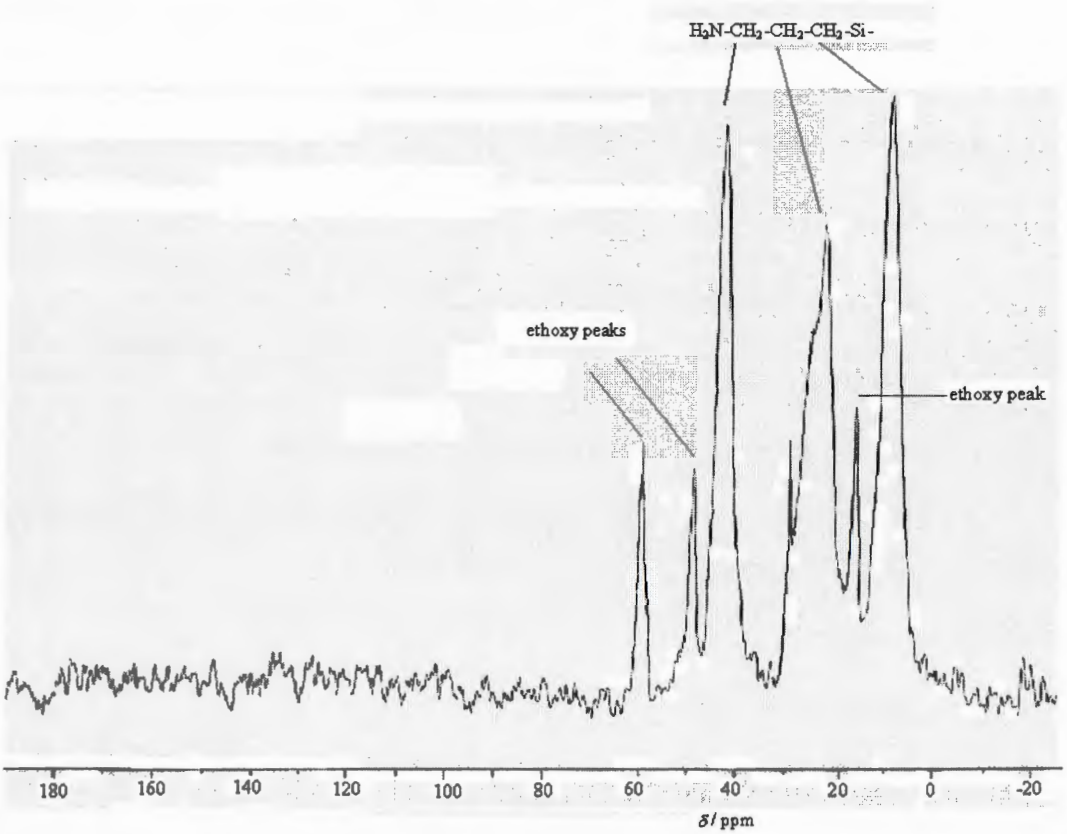

Figure 5.21 ^{13}C-{^{1}H}-CP MAS NMR spectrum of 3-aminopropyl-modified MCM 41 (NH_2-MCM-**g**).

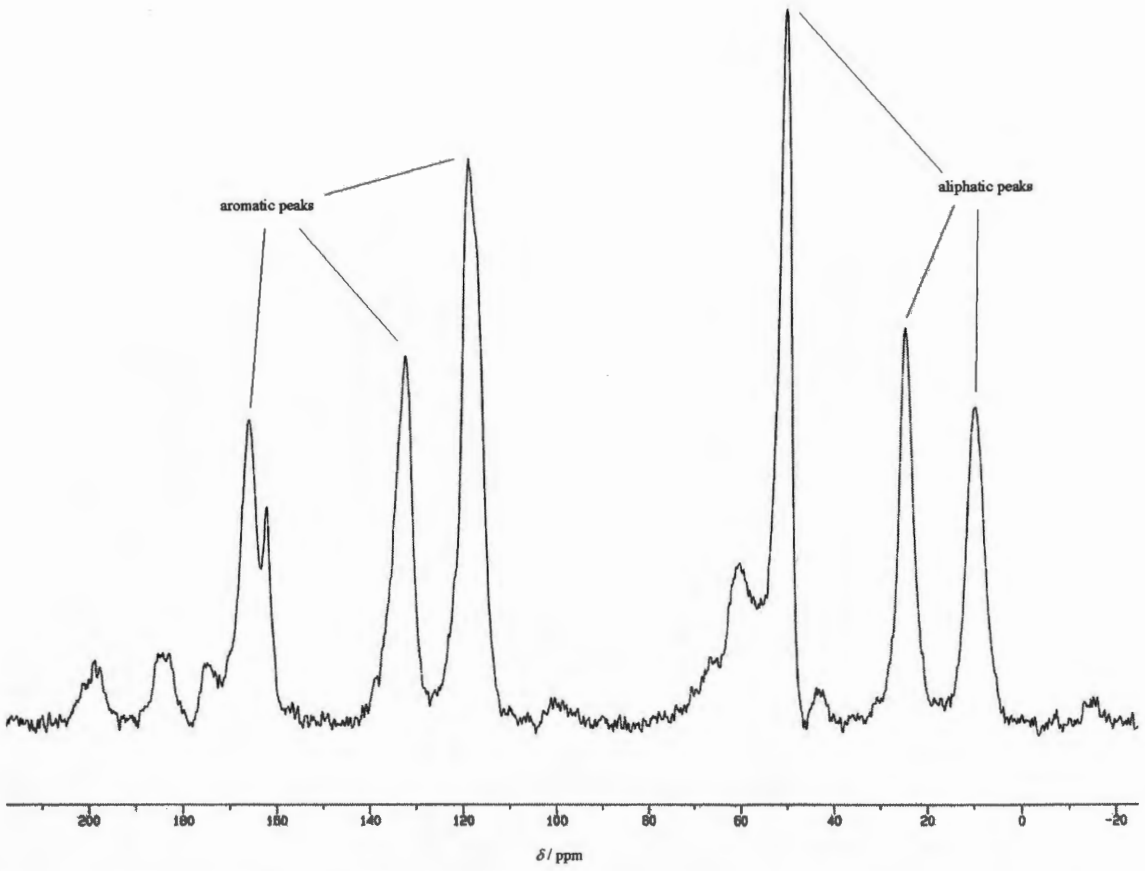

Figure 5.22 ^{13}C-{^{1}H}-CP MAS NMR spectrum of Schiff base-modified MCM 41 (SB-MCM-**g**).

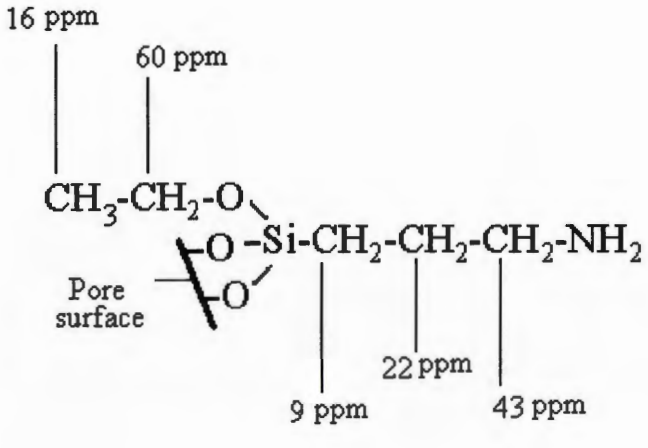

Figure 5.23 Diagram showing different carbon environments and their approximate chemical shift for the 3-aminopropyl-modified MCM 41 material (NH_2-MCM-**g**).

The NH_2-MCM-**g** sample showed three additional peaks at *ca.* δ = 16, 29, and 60 ppm (Fig. 5.21) possibly due to the ethoxy groups[16] present in two different environments *i.e.* on the MCM 41 surface and due to the incomplete reaction of ethoxy groups from 3-aminopropyl triethoxysiloxane (Fig 5.24). The Schiff base-modified samples showed only one peak at *ca.* δ = 60 ppm and this was assigned to the methylene carbon of the ethoxy groups. The peak at *ca.* δ = 16 ppm due to the methyl carbon of the ethoxy group is possibly obscured due to the overlapping with a broad peak at *ca.* δ = 22 ppm (from methylene carbon of 3-aminopropyl chain) and hence not seen in the spectrum of Schiff base MCM 41. The NMR spectrum of 3-aminopropyl triethoxysiloxane used for comparison is shown in Appendix A3.

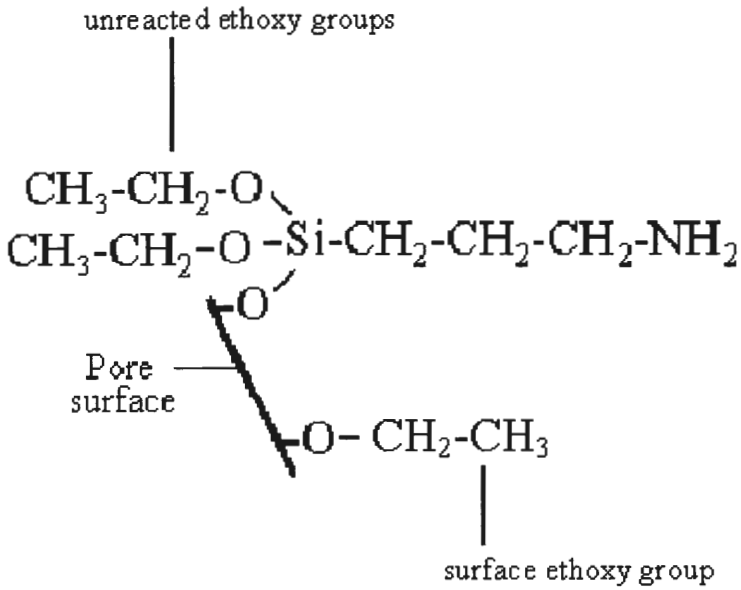

Figure 5.24 Diagram showing presence of two different types of ethoxy groups on MCM 41 surface.

The Schiff base-modified samples show NMR resonances in the aromatic region of the spectrum. These peaks were not present in the spectrum of 3-aminopropyl-modified MCM 41, and confirmed the immobilisation of Schiff base on the MCM 41 surface. The spectrum (Fig 5.21) shows resonance at *ca.* δ = 131 ppm for the quaternary

carbon atoms of the phenyl rings.[22, 33] The NMR peak at *ca.* δ = 170 ppm is attributed to the carbon atoms attached to the hydroxyl group. The other peaks observed due to the aromatic carbon atoms are summarised in Table 5.7.

Figs. 5.25 and 5.27 show the ^{13}C-{^{1}H}-CP MAS NMR spectra of the aromatic region, and Fig. 5.26 shows the assigned chemical shifts for the azodye and azodye-functionalised MCM 41 materials (AZ-Ms-MCM-**c-3.0**), respectively. The AZ-Ms-MCM-**c-3.0** sample shows resonances of the quaternary carbon atoms of the phenyl rings. However, it shows only four major peaks in the aromatic region compared with the nine resonances observed in the spectrum of the pure azodye. The smaller number of peaks in the spectrum of AZ-Ms-MCM-**c-3.0** suggested cleavage of the azo group in the dye might have occurred during the immobilisation process. The spectrum for AZ-Ms-MCM-**c-3.0** also shows peaks in the aliphatic region due to the 3-aminopropyl groups used to tether azodye to the MCM 41 surface. The NMR chemical shifts are summarised in Table 5.7.

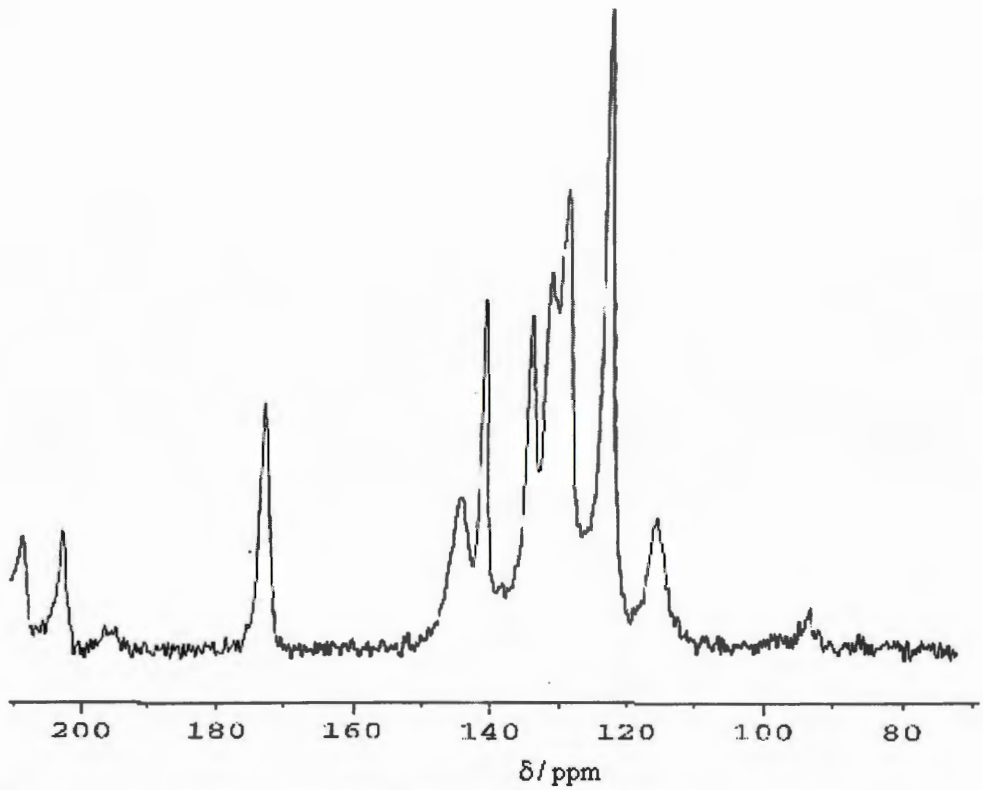

Figure 5.25 ^{13}C-{^{1}H}-CP MAS NMR spectrum of azodye.

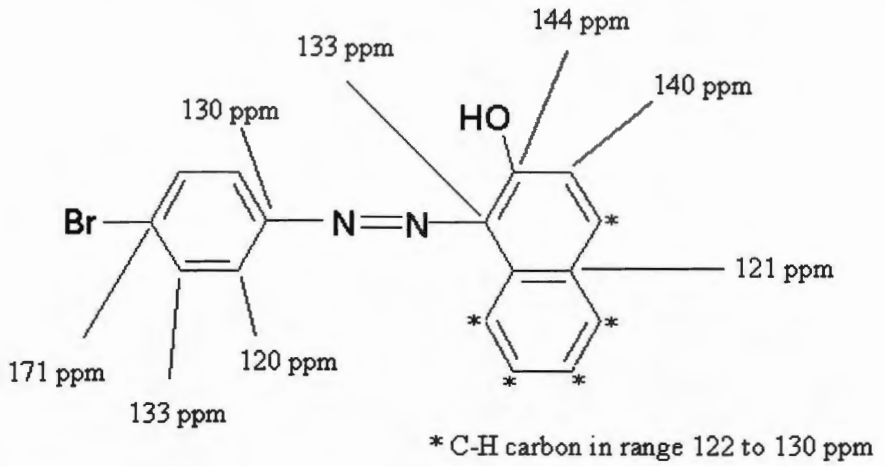

Figure 5.26 Diagram showing the different carbon environments and their approximate ^{13}C NMR chemical shifts observed for azodye in solution.

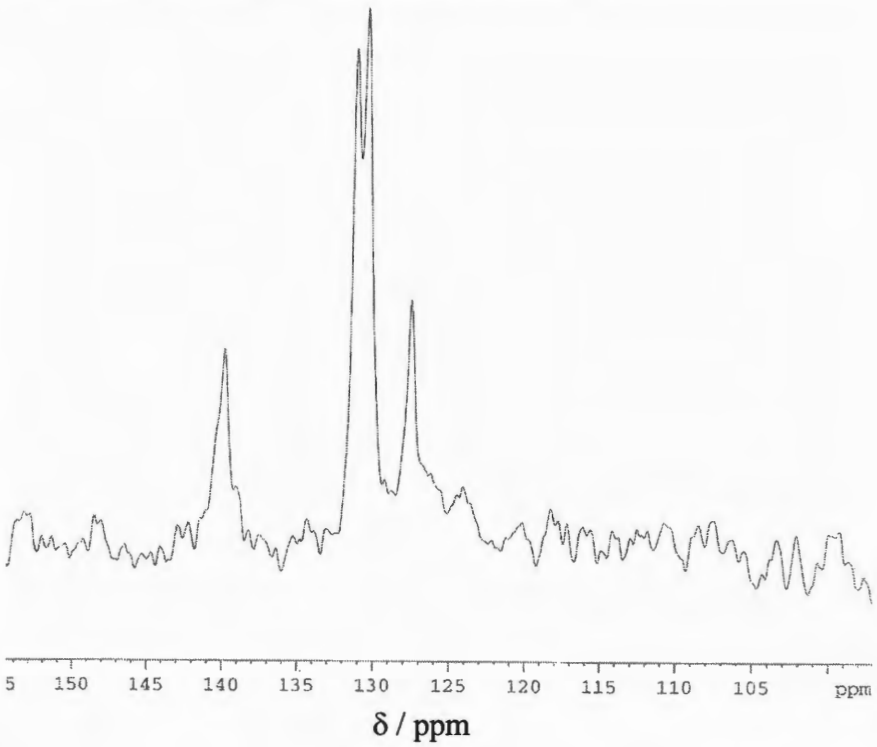

Figure 5.27 ^{13}C-{^{1}H}-CP MAS NMR spectrum of azodye-functionalised MCM 41 (AZ-Ms-MCM-**c-3.0**).

5.3.5 *UV/Visible Spectroscopy*

The UV/Visible spectroscopic analysis of AZ-Ms-MCM-**c-3.0** sample and the pure azodye was carried out at Actinic Technology, University of Surrey. The UV/Visible analysis was found to be inconclusive because not all the bands observed for the pure

azodye sample were visible in the spectrum of AZ-Ms-MCM-**c-3.0**. Fig. 5.28 shows the UV/Visible spectra of the azodye and the AZ-Ms-MCM-**c-3.0** samples. The azodye sample shows absorption maxima at 540 nm due to the azo group (-N=N-) involved in the conjugation with an aromatic system, whereas, the AZ-Ms-MCM-**c-3.0** sample shows absorption maxima at 488 nm. The shift in the absorption maximum in case of the AZ-Ms-MCM-**c-3.0** sample may be due to immobilisation of azodye on the silica surface or due to the interference of solid support *via* hydrogen bonding on the immobilised dye. The azodye sample shows strong bands near 1700 nm and 1150 nm corresponding to the C-H overtone-stretching vibration of the aromatics carbons.[34] These bands were very weak in AZ-Ms-MCM-**c-3.0**, which indicated that a very small amount of azodye is tethered to MCM 41 surface. The AZ-Ms-MCM-**c-3.0** sample showed a pronounced band at 1400 nm for the -OH feature of the Si-MCM 41, suggesting that not all the hydroxyl groups are involved in functionalisation.

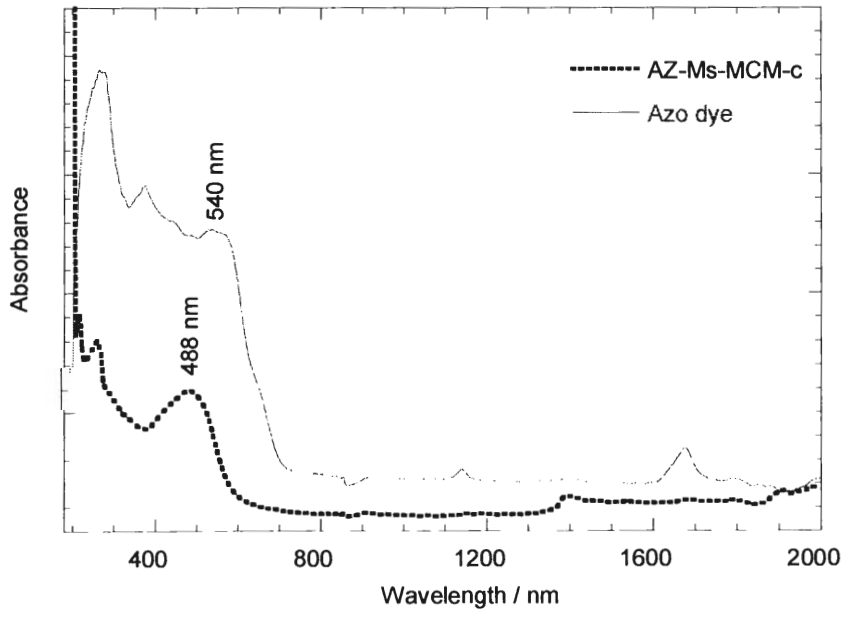

Figure 5.28 UV/Visible spectra of the pure azodye, and AZ-Ms-MCM-c-**3.0** sample.

5.4 Sorption Studies: Results and Discussions

This Section concerns the sorption studies of nitrogen (77 K) and carbon dioxide (195 K) on the organically-modified MCM 41 samples. Nitrogen was used as a standard probe to investigate the change in surface area and pore parameters after immobilization of the organic moieties on the Si-MCM 41 surface. Carbon dioxide was another adsorptive used, because of its high quadrupole moment, to investigate the change in surface characteristics following modification.

5.4.1 Nitrogen Sorption

The nitrogen sorption isotherms at 77 K for the organically-modified MCM 41 materials are shown in Figs. 5.29 to 5.32. All of the samples showed a Type IV isotherm, which is a typical of mesoporous MCM 41 material[35, 36] and similar to the parent MCM 41 material (Section 3.3.1). This suggests that the material retains its mesoporosity after modification. The adsorption data are summarised in Table 5.8. All of the modified materials showed a decrease in the average pore diameter, which is probably due to the pore narrowing from immobilisation of the organic moieties. However, for the AZ-Ms-MCM-c-**3.0** sample an increase in the average pore diameter was observed, though a decrease in pore diameter was expected. The result obtained was reproducible and may be explained by the loss of porosity arising from the blocking of the majority of the pores due to the immobilisation of azodye. This diameter represents the mean of the remaining unblocked pores and represents the weighted mean of pores with widths in the range 222 – 23 Å *i.e.* the resulting calculated mean has a significant uncertainty associated with the value.

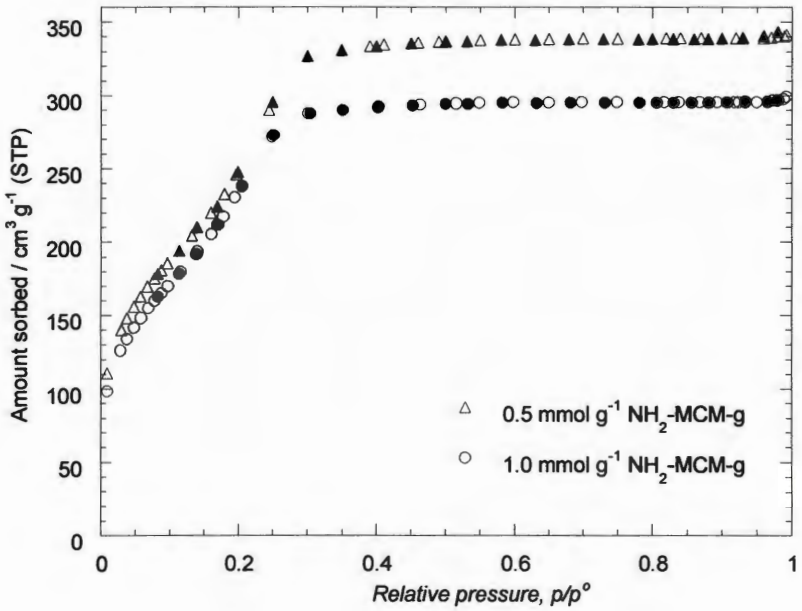

Figure 5.29 Nitrogen sorption isotherms (77 K) for NH_2-MCM-**g**. Filled symbols denote desorption points.

Table 5.8 Summary of the nitrogen sorption data for the organically-modified samples

Sample	**Type of Isotherm**	**Surface Area / $m^2 g^{-1}$**	**Pore volume / $cm^3 g^{-1}$**	**Average Pore diameter / Å**	
				†	‡
Si-MCM 41	Type IV	1150	0.74	27	25
NH_2-MCM-**g-0.5**	Type IV	940	0.53	25	22
NH_2-MCM-**g-1.0**	Type IV	900	0.46	26	20
SB-MCM-**c-0.5**	Type IV	900	0.42	23	19
SB-MCM-**c-1.0**	Type IV	830	0.35	22	17
SB-MCM-**g-0.5**	Type IV	910	0.47	24	21
SB-MCM-**g-1.0**	Type IV	855	0.43	23	20
Ms-MCM 41-**3.0**	Type IV	360	0.29	37	32
AZ-Ms-MCM-**c-3.0**	Type IV	60	0.05	42	35*

† *Pore diameter derived from BJH method*

‡ *Pore diameter derived from* $4V_p / S_{sp}$*(by BET)*

* *The uncertainty associated with this value is significant due to the minimal porosity of the sample.*

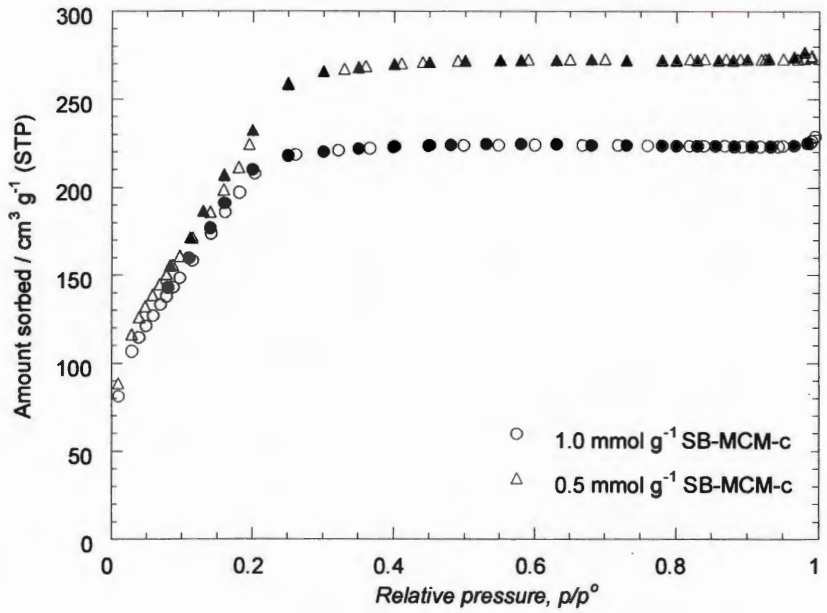

Figure 5.30 Nitrogen sorption isotherm (77 K) for SB-MCM-**c**. Filled symbols denote desorption points.

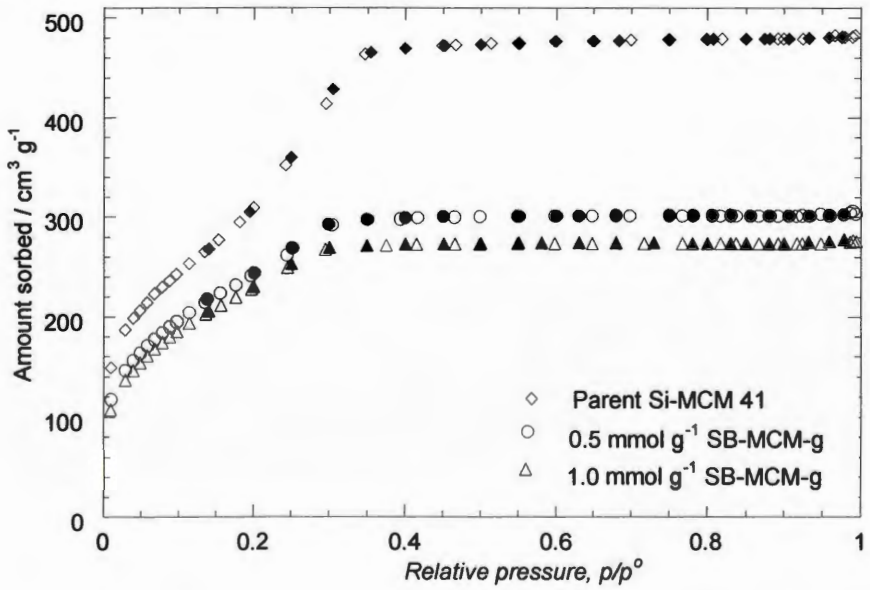

Figure 5.31 Nitrogen sorption isotherms (77 K) for SB-MCM-**g** and parent Si-MCM 41. Filled symbols denote desorption points.

The isotherms obtained for the 3-aminopropyl-modified and Schiff base modified materials were found to be reversible and reproducible with no hysteresis, similar to that of the parent Si-MCM 41 material (Chapter 3, Section 3.3.1). A decrease in surface area of the modified samples compared with the parent Si-MCM 41 was observed. Again, increasing the amount of organic moieties immobilized (from 0.5 mmol g^{-1} to 1.0 mmol g^{-1}) on to the MCM 41 surface resulted in a further decrease in the surface area of the modified-MCM 41 materials. A decrease in the surface area of up to *ca.* 300 m^2 g^{-1} following modification was observed for each of the sample. The results obtained are summarized in Table 5.8.

Gurvitsch pore volume, V_p, calculated from each of the isotherms from the final plateau, at high relative pressure. It can be noted from the Table 5.8 that the pore volumes of the modified samples were less than that of the parent MCM 41 material. A further decrease in the pore volume was observed for the higher loading of organic moieties immobilised on the Si-MCM 41 surface. The decrease in the pore volumes suggests that the organic moieties are immobilised in the pores of Si-MCM 41.

Comparing the nitrogen sorption results (see Table 5.8) of SB-MCM-**g** and SB-MCM-**c** (Schiff base materials synthesised by grafting and coupling, respectively, Section 5.2.2), it is evident that there is no significant difference between the surface area and pore volume of the material. However, the CHN microanalysis data (Section 5.3.3) indicated that higher loading of Schiff base was achieved by the coupling method *i.e.* for SB-MCM-**c**. This showed the superiority of the synthesis method "post- synthetic functionalisation by coupling with existing organic groups on surface" over " direct post-synthetic grafting".

Fig. 5.32 shows nitrogen sorption isotherm for the azodye-functionalised MCM 41 material. The AZ-Ms-MCM-**c-3.0** sample shows non-reversible Type IV isotherm similar to the parent Ms-MCM 41 material (mesitylene-swollen MCM 41).

The AZ-Ms-MCM-**c-3.0** sample shows a small degree of hysteresis throughout the isotherm, which was in contrast to the parent Ms-MCM 41, where the hysteresis was observed only in the capillary condensation region ($0.4 < p/p^o$ 0.7).

There was a significant decrease in the surface area and pore volume of the AZ-Ms-MCM-**c-3.0** sample (see Table 5.8). This indicated blocking of the pores by the bulky azodye.

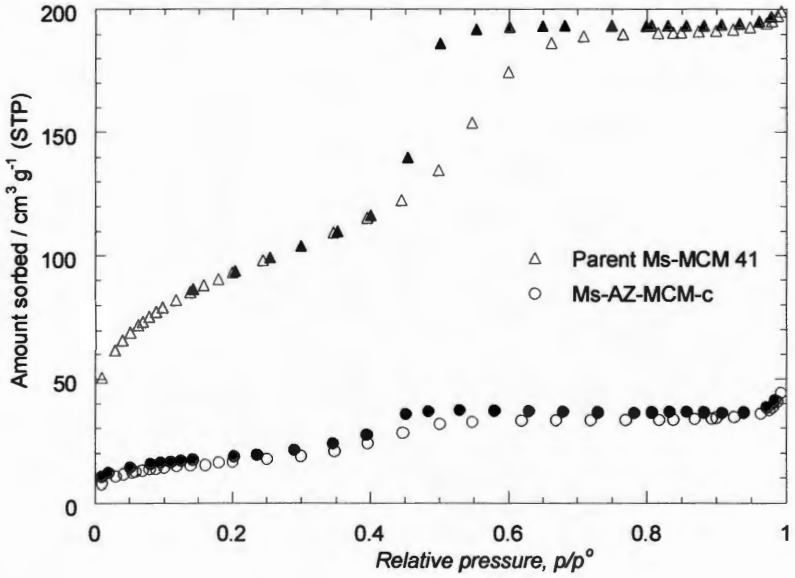

Figure 5.32 Nitrogen sorption isotherms (77 K) for AZ-Ms-MCM-**c-3.0** and parent Ms-MCM 41 materials. Filled symbols denote desorption points.

5.4.2 Carbon Dioxide Sorption

Carbon dioxide adsorption at 195 K on the 3-aminopropyl-modified MCM 41 (NH_2-MCM-**g-1.0**) and Schiff base-modified MCM 41 materials (SB-MCM-**c-1.0**) yielded Type IV isotherms (Fig. 5.33) in each case. The Type IV nature of the isotherms confirmed the mesoporosity of the materials and supported the results obtained from nitrogen sorption (Section 5.4.1). Both the isotherms show a rounded 'knee' at low relative pressure, and a condensation step commencing at p/p^o = 0.55, which levels off

at p/p^o = 0.75 indicating complete filling of pores by 'liquid CO_2'. However, the condensation step for CO_2 adsorption is not sharp and appears at higher relative pressure (between 0.55 < p/p^o 0.70) compared with nitrogen (0.20 < p/p^o< 0.30). The CO_2 derived surface areas were smaller (310 and 280 m^2 g^{-1}) compared with the nitrogen derived surface areas (900 and 855 m^2 g^{-1} for NH_2-MCM-**g-1.0** and SB-MCM-**c-1.0** samples, respectively). This indicated that the adsorption in case of CO_2 did not proceed *via* monolayer formation, which was supported by the observed rounded 'knee' at low relative pressure. A decrease in the surface area and pore volume following modification, similar to that of nitrogen sorption, was observed, and confirmed the immobilisation of organic moieties within the pores of the Si-MCM 41 material. The CO_2 adsorption results are summarised in Table 5.9.

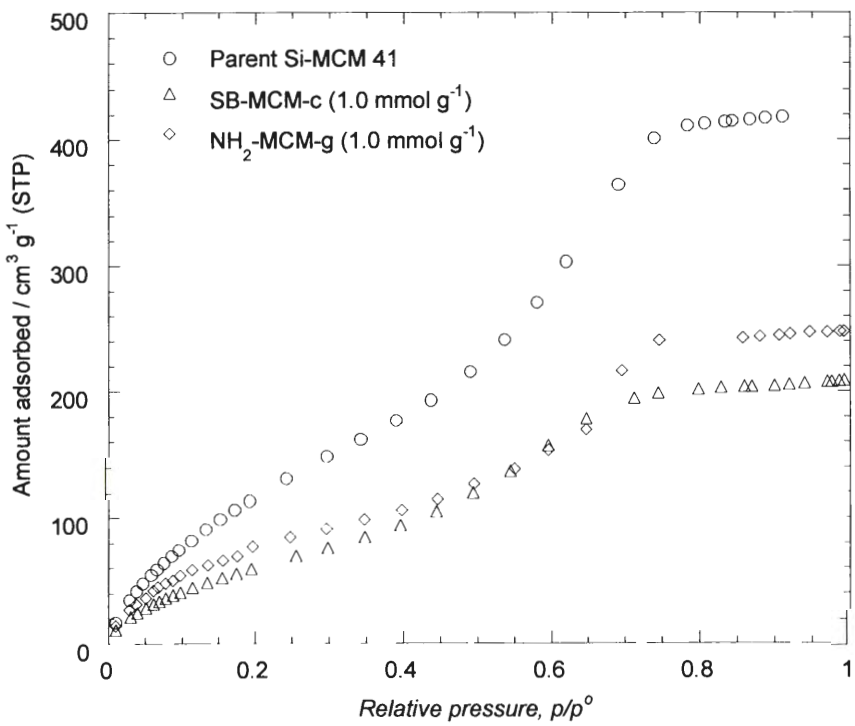

Figure 5.33 Carbon dioxide adsorption isotherms (195 K) for the NH_2-MCM-**g**, SB-MCM-**g** and parent Si-MCM 41 materials.

Table 5.9 Summary of carbon dioxide adsorption data for the organically-modified MCM 41 materials (N_2 derived values are given in brackets for comparison)

Sample	Organic moieties* /mmol g^{-1}	Type of Isotherm	CO_2 derived Surface Area / m^2 g^{-1}	Pore volume / cm^3 g^{-1}
Si-MCM 41	--	Type IV	580 (1150)	0.76 (0.74)
NH_2-MCM-**g-1.0**	1.0	Type IV	310 (900)	0.45 (0.46)
SB-MCM-**c-1.0**	1.0	Type IV	280 (830)	0.38 (0.35)

The molecular cross-sectional area for CO_2 = 17 $Å^2$

For each sample, the total pore volume derived from CO_2 adsorption was consistent with the value obtained from N_2 sorption. However, the CO_2 derived surface area was found to be much smaller than the surface area obtained from N_2 sorption (Table 5.8). The ratio of CO_2 surface area to nitrogen surface area was 1/2 for the unmodified (Si-MCM 41) sample and 1/3 for organically-modified samples. This may be explained by the decrease in the surface polarity of the modified samples on modification of the pore surface with the 3-aminopropyl groups and Schiff base ligand. The CO_2 adsorption occurs preferentially on polar surface groups and complete monolayer formation of CO_2 on the surface during adsorption was therefore not achieved.

5.5 Conclusions

Three organically-modified MCM 41 materials (3-aminopropyl modified, Schiff base ligand-modified and azodye-modified) were prepared by three different methods *i.e.* by sol-gel synthesis and post-synthetic grafting (direct grafting method, and grafting by a coupling method). The absence of the d_{100} peak in the *p*-XRD pattern of the organically-modified materials synthesised *via* the sol-gel synthesis method, following template removal, confirmed the collapse of the hexagonal structure. Hence, the post-synthetic

grafting method was used in the synthesis of the organically-modified MCM 41 materials.

The *p*-XRD patterns of the organically-modified materials, synthesised *via* post-synthetic grafting methods, each showed a d_{100} peak together with the less intense peaks at lower 2θ values (below 10^{o}) and confirmed that the hexagonal structure of the parent Si-MCM 41 material was retained following treatment at 383 K and 353 K in toluene and methanol, respectively.

The presence of organic moieties in the modified samples was confirmed by the presence of IR absorption bands at 1550 cm^{-1} ($N\text{-}H_{def}$) for the 3-aminopropyl-modified MCM 41, 1620 cm^{-1} ($C{=}N_{str}$) and 730 cm^{-1} (phenyl out-of-plane $C\text{-}H_{def}$) for the Schiff base-modified MCM 41, and 1634 cm^{-1} ($N{=}N_{str}$) and 730 cm^{-1} (phenyl out-of-plane $C\text{-}H_{def}$) for the azodye functionalised MCM 41 material. This conclusion was supported by CHN microanalysis, where high percentages of carbon, hydrogen and nitrogen were observed in the modified samples, and by NMR spectroscopic analysis, which shows the presence of organosiloxane silicon, aliphatic and aromatic carbons in the spectra of each of the modified samples.

The presence of ethoxy groups, due to incomplete hydrolysis of the organoalkoxysilane, in the modified samples was confirmed by the CHN microanalysis. This was supported by the $^{13}C\text{-}\{H\}$-CP MAS NMR spectroscopic analysis, which showed NMR resonances due to ethoxy groups in the spectrum of each of the modified samples at $\delta = 16$, 29 and 60 ppm.

The mesoporosity of the modified materials was demonstrated by the Type IV isotherms yielded from N_2 (77 K) and CO_2 (195 K) sorptions. The decrease in the surface areas (*ca.* 300 $m^2\ g^{-1}$) and the pore volumes (*ca.* 0.30 $cm^3\ g^{-1}$) following modification confirmed the immobilization of the organic moieties within the pores of the Si-MCM 41 host. The shape of the CO_2 sorption isotherm (presence of a rounded

'knee' at low relative pressure) and the smaller CO_2-derived surface areas suggested that the adsorption of CO_2 was by polar interaction rather than *via* monolayer formation.

The CHN microanalysis data indicated that a higher loading of the Schiff base ligand was achieved by the coupling method compared with the direct post-synthetic grafting method. However, the N_2 sorption studies showed that the surface areas (900 m^2 g^{-1} and 910 m^2 g^{-1} from the coupling and the direct grafting methods, respectively) and the pore volumes (0.42 cm^3 g^{-1} and 0.47 cm^3 g^{-1} from the coupling and the direct grafting methods, respectively) of the materials synthesised by these two methods were unaffected.

5.6 References

1. R. J. P. Corriu, E. Lancelle-Beltran, A. Mehdi, C. Reyé, S. Brandés and R. Guilard, *J. Mater. Chem.*, 2002, **12,** 1355.
2. R. J. P. Corriu, A. Mehdi and C. Reyé, *Acad. Sci. Paris, t. 2, Série II c*, 1999, 35.
3. S. L. Brukett, S. D. Sims and S. Mann, *J. Chem. Soc., Chem. Commun.*, 1996, 1367.
4. J. H. Clark and D. J. Macquarrie, *J. Chem. Soc., Chem. Commun.*, 1998, 853.
5. S. J. Bae, S. W. Kim, T. Hyeon and B. M. Kim, *J. Chem. Soc., Chem. Commun.*, 2000, 31.
6. S. Shyu, S. Cheng and D. Tzou, *J. Chem. Soc., Chem. Commun.*, 1999, 2337.
7. P. M. Price, J. H. Clark and D. J. Macquarrie, *J. Chem. Soc., Dalton Trans.*, 2000, 101.
8. J. S. Rafelt and J. H. Clark, *Catalysis Today*, 2000, **57**, 33.
9. D. J. Macquarrie, *Green Chemistry*, 1999, 195.
10. C. E. Fowler, S. L. Brukett and S. Mann, *J. Chem. Soc., Chem. Commun.*, 1997, 1769.
11. D. J. Macquarrie, D. B. Jackson, J. E. G. Mdoe and J. H. Clark, *New J. Chem.*, 1999, **23**, 539.
12. W. Kaleta and K. Nowinska, *J. Chem. Soc., Chem. Commun.*, 2001, 535.
13. A. R. Silva, C. Freire, B. de Castro, M. M. A. Freitas and J. L. Figueiredo, *Micropor. Mesopor. Mater.*, 2001, **46,** 211.
14. R. I. Kureshy, N. H. Khan. S. H. R. Abdi, S. T. Patel, P. Iyer, E. Suresh and P. Dastidar, *J. Mol. Catal. A: Chemical*, 2000, **160**, 217.
15. I. C. Chisem, J. Rafelt, M. T. Shieh, J. Chisem, J. H. Clark, R. Jachuck, D. J. Macquarrie, C. Ramshaw and K. Scott, *J. Chem. Soc., Chem. Commun.*, 1998, 1949.

16. H. Juvaste, E. I. Iiskola and T. T. Pakkanen, *J. Mol. Catal. A: Chemical*, 1999, **150**, 1.

17. D. Brunel, F. Fajula, J. B. Nagy, B. Deroide, M. J. Verhoef, L. Veum, J. A. Peters and H. van Bekkum, *Appl. Catal. A: General*, 2001, **213**, 73.

18. Science: SXR205: Exploring the Molecular World Study Book, The Open University press, Milton Keyenes, 2002.

19. D. Barton and W. D. Ollis, "*Comprehensive Organic Chemistry: The Synthesis and Reaction of Organic Compounds*", Volume 2, Pergamon Press, England, 1979.

20. P. Sutra and D. Brunel, *J. Chem. Soc., Chem. Commun.,* 1996, 2485.

21. S. J. Bae, S. W. Kim. T. Hyeon and B. M. Kim, *J. Chem. Soc., Chem. Commun.*, 2000, 31.

22. C. M. Bambrough, *PhD Thesis,* The Open University, 1998.

23. K. Nakamoto, "*Infrared and Raman Spectra of Inorganic and Coordination Compounds*", 4th Edition, John Wiley and Sons, USA, 1986.

24. C. J. Creswell, O. A. Runquist and M. M. Campbell, "*Spectral Analysis of Organic Compounds*", 2nd Edition, Longman Group Ltd., England, 1972.

25. K. Nakanishi, "*Infrared Absorption Spectroscopy*", 2nd Edition, Nankodo Company Ltd., Japan, 1964.

26. D. J. Macquarrie, *J. Chem. Soc., Chem. Commun.,* 1996, 1961.

27. D. Brunel, A. Cauvel, F. Di Renzo, F. Fajula, B. Fubini, B. Onida and E. Garrone, *New J. Chem.*, 2000, **24**, 807.

28. S. O'Brien, J. Tudor, S. Barlow, M. J. Drewitt, S. J. Heyes and D. O'Hare, *J. Chem. Soc., Chem. Commun.*, 1997, 641.

29. T. R. Pauly and T. J. Pinnavaia, *Chem. Mater.*, 2001, **13**, 987.

30. X.S. Zhao, G. Q. Lu and X. Hu, *Micropor. Mesopor. Mater.*, 2000, **41**, 37.

31. W. A. Carvalho, M. Wallau and U. Schuchardt, *J. Mol. Catal. A: Chemical*, 1999, **144**, 91.

32. B. Lindlar, M. Lüchinger, A. Röthlisberger, M. Haouas, G. Pirngruber, A. Kogelbauer and R. Prins, *J. Mater. Chem.*, 2002, 528.

33. L. M. H. Groenewoud, J. G. A. Terlingen, G. H. M. Engbers and J. Feijen, *Langmuir*, 1999, **15**(16), 5396.

34. Private communication, Henryk Herman, Actinic Technology, 2002.

35. S. Schacht, M. Janicke and F. Schuth, *Micropor. Mesopor. Mater.*, 1998, **22**, 485.

36. G. Øye, J. Sjöblom and M. Stöcker, *Adv. Colliod and Interface Sci.*, 2001, **89-90**, 439.

CHAPTER 6

METAL-SCHIFF BASE-MODIFIED MCM 41 MATERIALS

6.1 Introduction

It has been reported by other workers that metal-grafted MCM 41 materials, such as those discussed in Chapter 4, are prone to leaching during catalysis.[1, 2, 3, 4] As a result, recent developments such as the tethering of metal complexes onto the silica support[4, 5, 6, 7] have received much attention. In the synthesis of these types of materials, the immobilisation of metal complexes on the solid support is achieved by forming covalent bonds *via* reaction with surface silanol groups. The catalysts synthesised by this method have the metal ions firmly bound to a solid surface and this prevents leaching of the metal ions during catalysis. Thus, the catalysts synthesised are environmentally friendly, and they can be easily separated from a reaction mixture and recycled, which minimizes the large volumes of waste and toxic effluents produced during separation of catalysts from the reaction mixture.

This Chapter concerns the synthesis and characterisation of metal-Schiff base-modified MCM 41 materials. Table 6.1 summarises the metal-Schiff base complexes tethered on the Si-MCM 41 surface synthesised in this work and the techniques used for the characterisation of these materials. The volumetric sorption of N_2 and CO_2 gases and the gravimetric sorption of vapours [water, *n*-hexane, methanol (MeOH), *n*-butanol (*n*-BuOH) and *t*-butanol (*t*-BuOH)], were used in the characterisation of the surface characteristics and pore properties of these modified MCM 41 materials. This Chapter

also evaluates X-ray photoelectron spectroscopy (XPS) as an analytical tool to determine the distribution of copper complexes within the Si-MCM 41 material.

Table 6.1 Summary of the metal-Schiff base-modified MCM 41 materials synthesised and the analytical techniques used for their characterisation

Materials	Abbreviations used*	Physico-chemical Characterisation†					V	G
		XRD	IR	AAS	CHN	XPS		
Grafted Cu-Schiff base MCM 41	Cu-Schiff-MCM-**0.25** (8)	✓	✓	✓	✓	✓	✓	✓
	Cu-Schiff-MCM-**0.50** (8)	✓	✓	✓	✓	✓	✓	
	Cu-Schiff-MCM-**0.75** (8)	✓	✓	✓	✓	✓	✓	✓
	Cu-Schiff-MCM-**1.0** (8)	✓	✓	✓	✓	✓	✓	
	Cu-Schiff-MCM-**1.0** (20)	✓	✓	✓	✓	✓	✓	
Grafted Fe(II)-Schiff base MCM 41	Fe(II)-Schiff-MCM-**0.25**	✓	✓	✓	✓		✓	
	Fe(II)-Schiff-MCM-**0.50**	✓	✓	✓	✓		✓	
	Fe(II)-Schiff-MCM-**0.75**	✓	✓	✓	✓		✓	
	Fe(II)-Schiff-MCM-**1.0**	✓	✓	✓	✓		✓	
Grafted Fe(III)-Schiff base MCM 41	Fe(III)-Schiff-MCM-**0.25**	✓	✓	✓	✓		✓	
	Fe(III)-Schiff-MCM-**0.50**	✓	✓	✓	✓		✓	
	Fe(III)-Schiff-MCM-**0.75**	✓	✓	✓	✓		✓	
	Fe(III)-Schiff-MCM-**1.0**	✓	✓	✓	✓		✓	
Grafted Ni-Schiff base MCM 41	Ni-Schiff-MCM-**0.25**	✓	✓	✓	✓		✓	
	Ni-Schiff-MCM-**0.50**	✓	✓	✓	✓		✓	
	Ni-Schiff-MCM-**0.75**	✓	✓	✓	✓		✓	
	Ni-Schiff-MCM-**1.0**	✓	✓	✓	✓		✓	

** The numerical values show the amount of metal-Schiff base complex, in mmol g^{-1}, used in the synthesis of modified Si-MCM 41 materials i.e. the target loadings.*

*† ^{29}Si and ^{13}C NMR spectroscopic analysis were carried out on Cu-Schiff-MCM-**1.0** (8) Fe(III)-Schiff- MCM-**0.75** and Ni-Schiff-MCM-**1.0** samples.*

***V** = Volumetric sorption of nitrogen and CO_2, **G** = Gravimetric sorption of water, n-hexane, MeOH, n-BuOH and t-BuOH.*

6.2 Synthesis

The organically-modified materials synthesised by the sol-gel synthesis method (Chapter 5, Sections 5.1.1 and 5.1.2) show collapse of the hexagonal structure after template removal. Therefore, the post-synthetic grafting method was used in the synthesis of the metal-Schiff base-modified MCM 41 materials.[7, 8]

The post-synthetic grafting of metal-Schiff base complexes on the Si-MCM 41 material was carried out in three different steps:

- Step I, synthesis of the Schiff base ligand.[8, 9, 10]
- Step II, synthesis of the metal-Schiff base complexes.[7, 8]
- Step III, post-synthetic grafting of the metal-Schiff base complex on the Si-MCM 41 surface.[7, 8]

In step I, the Schiff base ligand was synthesised by reacting 3-aminopropyl-triethoxysilane with salicylaldehyde in 1:1 molar ratio, as shown in Scheme 1.

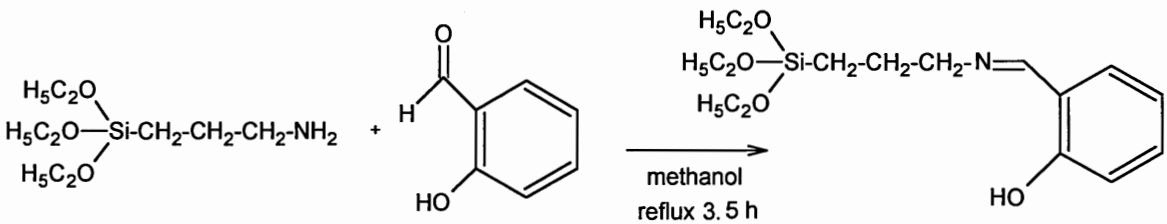

Scheme 1 Synthesis of the Schiff base triethoxysilane ligand.

Then, in step II, the metal-Schiff base complex was synthesised by refluxing the Schiff base ligand with metal acetate in an 2:1 molar ratio for 3 h, as shown in Scheme 2.

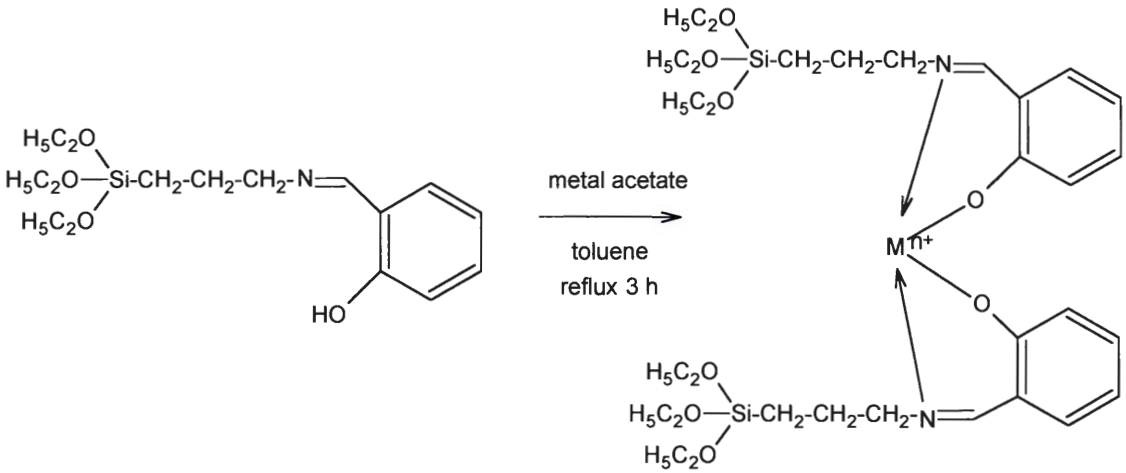

Scheme 2 Synthesis of the metal-Schiff base triethoxysilane complex.

Finally, in step III, the metal-Schiff base triethoxysilane complex was immobilised on the Si-MCM 41 surface by the post-synthetic grafting method, as shown in Scheme 3.

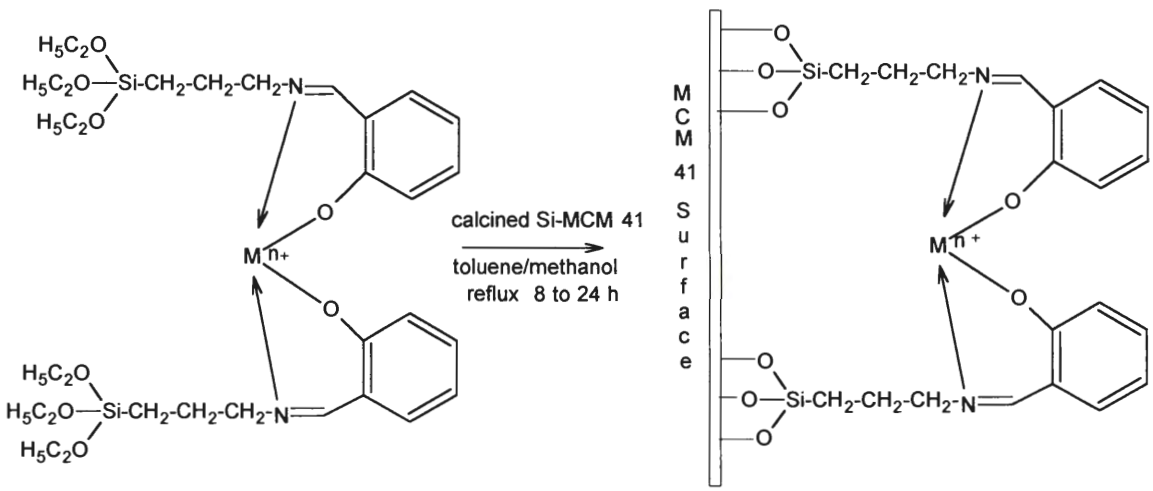

Scheme 3 Immobilisation of the metal-Schiff base triethoxysilane on calcined Si-MCM 41.

Fig. 6.1 shows the flow diagram for the general synthesis of the metal-Schiff base-modified MCM 41 material by the post-synthetic grafting method.

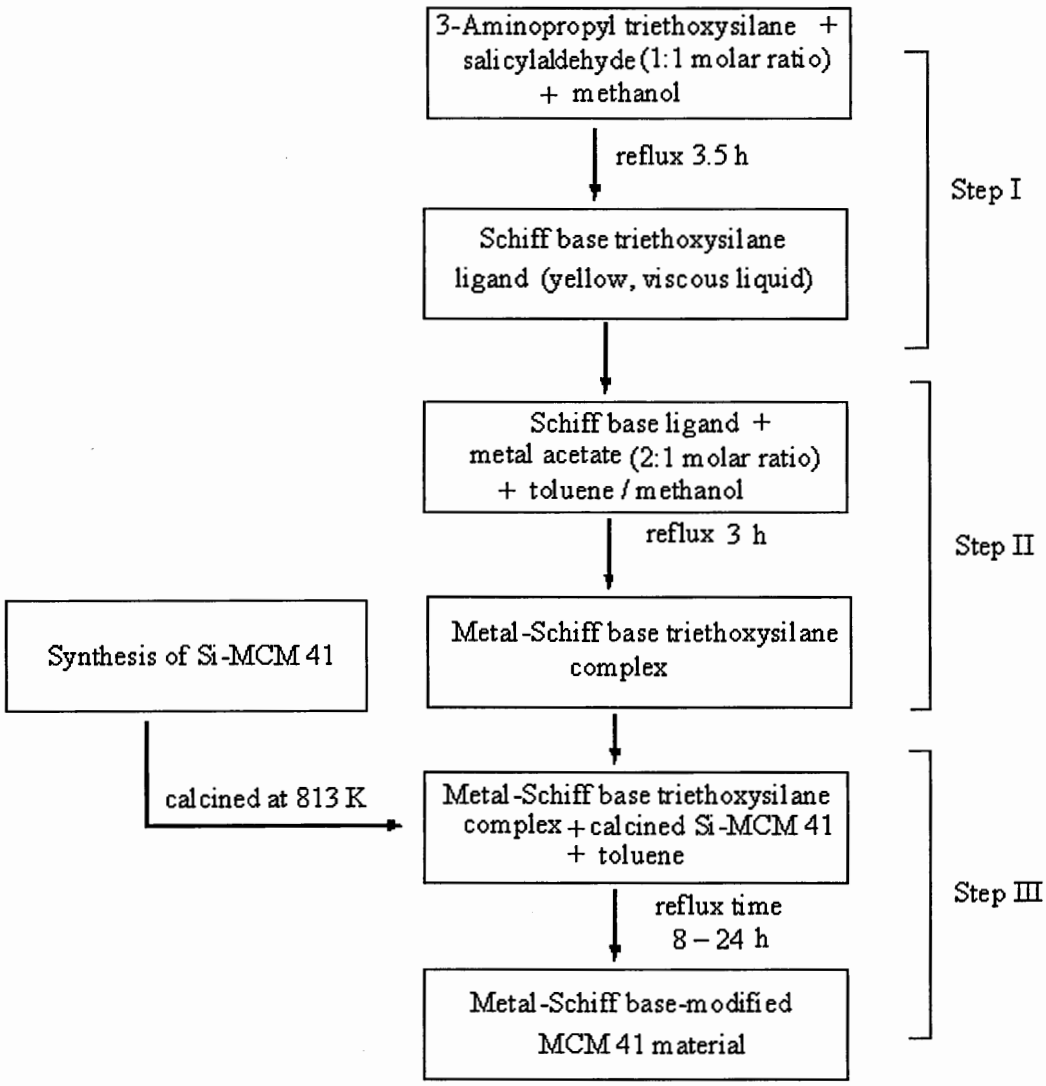

Figure 6.1 Flow diagram illustrating the general synthesis of the metal-Schiff base-modified MCM 41 material by the post-synthetic grafting method.

An attempt was also made to synthesise metal-Schiff base MCM 41 material by complexing metals with previously grafted Schiff base ligand on MCM 41 surface, as shown in Scheme 4. However, it was found that the metal was directly immobilised on the MCM 41 surface in addition to complexation with Schiff base ligand as determined by AAS and CHN microanalysis. The detail of this work is not reported here.

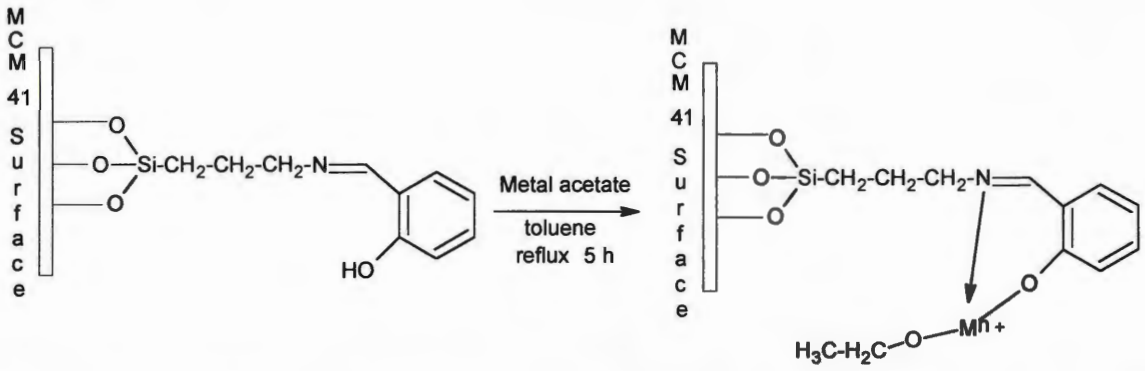

Scheme 4 Complexation of metal ions with previously grafted Schiff base ligand on MCM 41 Surface.

Table 6.2 summarises the synthesis conditions and the solvents used in the synthesis of different metal-Schiff base-modified MCM 41 materials.

Table 6.2 Summary of the synthesis conditions and the solvents used in the synthesis of different metal-Schiff base-modified MCM 41 materials

Sample	Schiff base complex with metal	Solvents used	Total reaction time / h
Cu-Schiff-MCM-**0.25** to **1.0** (8)†	Copper (II)	toluene	8
Cu-Schiff-MCM-**1.0** (20)*	Copper (II)	toluene	20
Fe(II)-Schiff-MCM-**0.25** to **1.0** †	Iron (II)	methanol	15
Fe(III)-Schiff-MCM-**0.25** to **1.0** †	Iron (III)	methanol	15
Ni-Schiff-MCM-**0.25** to **1.0** †	Nickel (II)	methanol	27

** Only one sample with a target copper loading of 1.0 mmol g^{-1} on Si-MCM 41 was synthesised with a reaction time of 20 h.*
† Four samples with a target metal loading of 0.25, 0.50, 0.75 and 1.0 mmol g^{-1} on the Si-MCM 41 were synthesised.

The synthesis of the Schiff base ligand is described first, followed by synthesis of each of the metal-Schiff base-modified MCM 41 materials.

6.2.1 Synthesis of the Schiff Base Triethoxysilane Ligand

Salicylaldehyde (1.40 g, 11.47 mmol) was added to a solution of 3-aminopropyl-triethoxysilane (2.50 g, 11.31 mmol) in methanol (50 cm^3). The resulting mixture was

refluxed for 3 h with stirring. The Schiff base triethoxysilane ligand was isolated as a yellow viscous liquid by evaporation of the methanol under reduced pressure, and was characterised by IR spectroscopy.

6.2.2 Post-synthetic Grafting of the Copper(II)-Schiff Base Complex on Si-MCM 41, Cu-Schiff-MCM-1.0 (8)

The Schiff base triethoxysilane ligand (0.75 g, 2.30 mmol) was added to a solution of copper acetate (0.23 g, 1.15 mmol) in toluene (40 cm^3). The resulting mixture was refluxed for 3 h with stirring. Calcined Si-MCM 41 (1.00 g) (preheated at 373 K for 2 h) was then added and the refluxing continued for a further 5 h. The resulting green solid was filtered, washed, first with ethanol (2 × 25 cm^3) and then with acetone (10 cm^3), and dried, initially under reduced pressure and finally at 323 K for 12 h.

The synthesis procedures for the Cu-Schiff-MCM-**0.25** (8), Cu-Schiff-MCM-**0.50** (8) and Cu-Schiff-MCM-**0.75** (8) materials were similar to that for Cu-Schiff-MCM-**1.0** (8) as described above. Table 6.3 summarises the amounts of Schiff base triethoxysilane ligand and copper(II) acetate used in the syntheses.

Table 6.3 Summary of the amounts of the Schiff base triethoxysilane ligand and copper acetate used per gram of Si-MCM 41 in the synthesis of the copper-Schiff base-modified MCM 41 materials

Sample	**Schiff base triethoxysilane / g (mmol)**	**Copper acetate / g (mmol)**	**Total reaction time / h**
Cu-Schiff-MCM-**0.25** (8)	0.16 (0.49)	0.05 (0.25)	8
Cu-Schiff-MCM-**0.50** (8)	0.33 (1.01)	0.10 (0.50)	8
Cu-Schiff-MCM-**0.75** (8)	0.50 (1.53)	0.15 (0.75)	8
Cu-Schiff-MCM-**1.0** (20)	0.75 (2.30)	0.23 (1.15)	20

6.2.3 Post-synthetic Grafting of the Iron(II)-Schiff Base Complex[11] on Si-MCM 41, Fe(II)-Schiff-MCM-1.0

Triethylamine (0.10 g, 1.06 mmol) was added to a solution of iron(II) acetate (0.18 g, 1.03 mmol) in methanol (60 cm^3) and the mixture was stirred for 5 min. The Schiff base triethoxysilane ligand (0.66 g, 2.02 mmol) was then added and the mixture was refluxed for 3 h with stirring. Calcined Si-MCM 41 (1.00 g) (preheated at 373 K for 2 h) was added and the refluxing continued for a further 12 h. The resulting brown solid was filtered, washed, first with methanol (2 × 25 cm^3) and then with acetone (10 cm^3), and dried, initially under reduced pressure and finally at 323 K for 12 h.

The synthesis procedures for the Fe(II)-Schiff-MCM-**0.25,** Fe(II)-Schiff-MCM-**0.50** and Fe(II)-Schiff-MCM-**0.75** materials were similar to that for Fe(II)-Schiff-MCM-**1.0** as described above. Table 6.4 summarises the amounts of Schiff base triethoxysilane ligand and iron(II) acetate used in the syntheses.

Table 6.4 Summary of the amounts of the Schiff base triethoxysilane ligand and iron(II) acetate used per gram of Si-MCM 41 in the synthesis of the iron(II)-Schiff base-modified MCM 41 materials

Sample	**Schiff base triethoxysilane / g (mmol)**	**Iron(II) acetate / g (mmol)**	**Triethyl-amine/ g (mmol)**	**Total reaction time / h**
Fe(II)-Schiff-MCM-**0.25**	0.16 (0.49)	0.05 (0.25)	0.03 (0.29)	15
Fe(II)-Schiff-MCM-**0.50**	0.33 (1.01)	0.10 (0.50)	0.06 (0.59)	15
Fe(II)-Schiff-MCM-**0.75**	0.50 (1.53)	0.15 (0.75)	0.08 (0.79)	15

6.2.4 Post-synthetic Grafting of Iron(III)-Schiff Base Complex[11] on Si-MCM 41, Fe(III)-Schiff-MCM-1.0

Triethylamine (0.11 g, 1.08 mmol) was added to a solution of anhydrous iron(III) chloride (0.18 g, 1.03 mmol) in methanol (60 cm^3) and stirred for 5 min. The Schiff base triethoxysilane ligand (0.66 g, 2.02 mmol) was added and the resulting mixture was refluxed for 3 h with stirring. Calcined Si-MCM 41 (1.00 g) (preheated at 373 K for 2 h) was then added and the refluxing continued for a further 12 h. The resulting brown solid was filtered, washed, first with methanol (2 × 25 cm^3) and then with acetone (10 cm^3), and dried, initially under reduced pressure and finally at 323 K for 12 h.

The synthesis procedures for the Fe(III)-Schiff-MCM-**0.25,** Fe(III)-Schiff-MCM-**0.50** and Fe(III)-Schiff-MCM-**0.75** materials were similar to that for Fe(III)-Schiff-MCM-**1.0** as described above. Table 6.5 summarises the amounts of Schiff base triethoxysilane ligand and iron(III) acetate used in the syntheses.

Table 6.5 Summary of the amounts of the Schiff base triethoxysilane ligand and iron(III) chloride used per gram of Si-MCM 41 in the synthesis of the iron(III)-Schiff base-modified MCM 41 materials

Sample	**Schiff base triethoxysilane / g (mmol)**	**Iron(III) chloride / g (mmol)**	**Triethyl – amine / g (mmol)**	**Total reaction time / h**
Fe(III)-Schiff-MCM-**0.25**	0.16 (0.49)	0.04 (0.25)	0.05 (0.49)	15
Fe(III)-Schiff-MCM-**0.50**	0.33 (1.01)	0.08 (0.49)	0.11 (1.08)	15
Fe(III)-Schiff-MCM-**0.75**	0.50 (1.53)	0.12 (0.74)	0.15 (1.48)	15

6.2.5 Post-synthetic Grafting of Nickel(II)-Schiff Base Complex on Si-MCM 41, Ni-Schiff-MCM-1.0

The Schiff base triethoxysilane ligand (0.66 g, 2.02 mmol) was added to a solution of nickel(II) acetate (0.25 g, 1.00 mmol) in methanol (60 cm^3). The resulting mixture was refluxed for 3 h with stirring.[9, 10, 12] Calcined Si-MCM 41 (1.00 g) (preheated at 373 K for 2 h) was then added and the refluxing continued for a further 24 h. The resulting yellowish green solid was filtered, washed, first with methanol (2 × 25 cm^3) and then with acetone (10 cm^3), and dried, initially under reduced pressure and finally at 323 K for 12 h.

The synthesis procedures for the Ni-Schiff-MCM-**0.25,** Ni-Schiff-MCM-**0.50** and Ni-Schiff-MCM-**0.75** materials were similar to that for the Ni-Schiff-MCM-**1.0** as described above. Table 6.6 summarises the amounts of the Schiff base triethoxysilane ligand and the nickel(II) acetate used in the syntheses.

Table 6.6 Summary of the amounts of the Schiff base triethoxysilane ligand and nickel(II) acetate used per gram of Si-MCM 41 in the synthesis of the nickel-Schiff base-modified MCM 41 materials

Sample	**Schiff base triethoxysilane / g (mmol)**	**Nickel acetate / g (mmol)**	**Total reaction time / h**
Ni-Schiff-MCM-**0.25**	0.16 (0.49)	0.06 (0.24)	27
Ni-Schiff-MCM-**0.50**	0.33 (1.01)	0.13 (0.52)	27
Ni-Schiff-MCM-**0.75**	0.50 (1.53)	0.19 (0.76)	27

6.3 Results and Discussions: Physico-chemical Characterisation

The copper-Schiff base-modified samples are denoted as Cu-Schiff-MCM-41, the Fe(II)-Schiff base-modified samples as Fe(II)-Schiff-MCM 41, the Fe(III)-Schiff base-modified samples as Fe(III)-Schiff-MCM 41 and the nickel-Schiff base-modified samples as Ni-Schiff MCM 41 for the discussion of the results.

6.3.1 Powder-X-ray Diffraction (p-XRD)

The hexagonal periodicity of all the metal-Schiff base-modified MCM 41 materials synthesised was confirmed by powder X-ray diffraction. The *p*-XRD results obtained for the metal-Schiff base-modified MCM 41 samples are summarised in Table 6.7.

Table 6.7 *p*-XRD results for the metal-Schiff base-modified MCM 41 materials

Sample	d_{100} **peaks**	d_{100}**-spacing / Å**	***a* / Å**
Cu-Schiff-MCM-41	3.5	38	44
Fe(II)-Schiff-MCM-41	3.6	37	43
Fe(III)-Schiff-MCM-41	3.6	37	43
Ni-Schiff-MCM-41	3.6	37	43

The *p*-XRD patterns for all the metal-Schiff base-modified MCM 41 samples synthesised by post-synthetic grafting were similar to the parent Si-MCM 41 material (Chapter 3, Fig. 3.2). Due to similar *p*-XRD patterns, only the *p*-XRD pattern of Cu-Schiff-MCM-**1.0** material is shown in Fig. 6.2 and the d_{100} peak positions and the corresponding *d*-spacings for all the samples are summarised in Table 6.7.

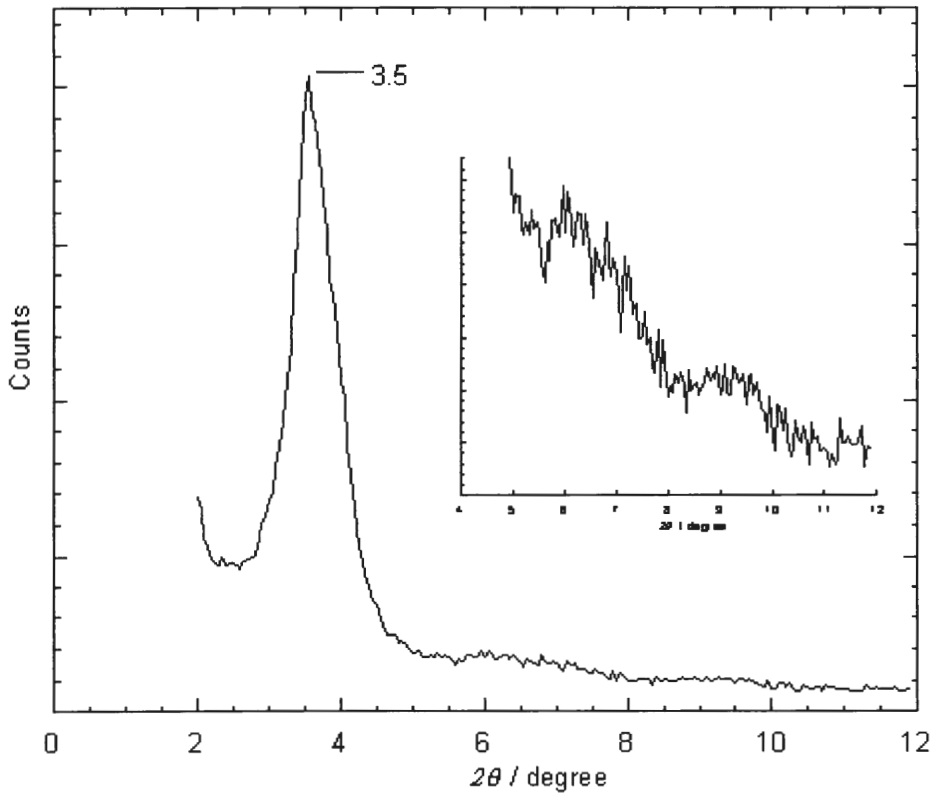

Figure 6.2 *p*-XRD pattern of the Cu-Schiff-MCM-**1.0** material.

The *p*-XRD confirmed that the hexagonal periodicity of the Si-MCM 41 host was preserved after treatment in different solvents and under different temperature conditions following functionalisation. This was indicated by the presence of the d_{100} reflection at 2θ *ca.* 3.5 and the higher order reflections between 2θ *ca.* 6 .0 and 7.0.[13]

6.3.2 Infrared (IR) Spectroscopy

Fourier Transform (FT) IR spectroscopy was used to confirm the presence of the metal-Schiff base complex in the Si-MCM 41 material for all of the samples. The observed IR bands and the vibrations assigned to them are summarised in Table 6.8.

Table 6.8 Principal IR bands with assigned vibrations (approximate wavenumber / cm^{-1})[8, 14, 15, 16]

Free Cu-Schiff base complex	Cu-Schiff-MCM-41	Fe(II)-Schiff-MCM-41	Fe(III)-Schiff-MCM-41	Ni-Schiff-MCM-41	Vibrations
760	760	760	760	755	Phenyl out-of-plane $C\text{-}H_{def}$
1450	1450	1450	1447	1454	$C\text{-}H_{def}$
1475	1475	1475	1475	1475	Phenyl $C\text{-}C_{str}$
1622	1625	1623	1623	1630	$C{=}N_{str}$
		1652	1650	1654	$O\text{-}H_{def}$
2960, 2830	2960, 2830	2960, 2830	2960, 2830	2960, 2830	$C\text{-}H_{str}$
	3400-3500	3400-3500	3400-3500	3400-3500	$O\text{-}H_{str}$

def =*deformation vibration,* str = *stretching vibration*

The IR spectra of the free copper-Schiff base triethoxysilane complex and the metal-Schiff base-modified MCM 41 materials (for 1.0 mmol g^{-1} samples) are presented in Figs. 6.3 to 6.5. All of the principal bands observed in the spectrum of the metal-Schiff base triethoxysilane complex [Fig. 6.3(a)], were also found to be present in the spectrum of each of the metal-Schiff base-modified MCM 41 materials. This confirmed the functionalisation of Si-MCM 41 with the metal-Schiff base complexes.

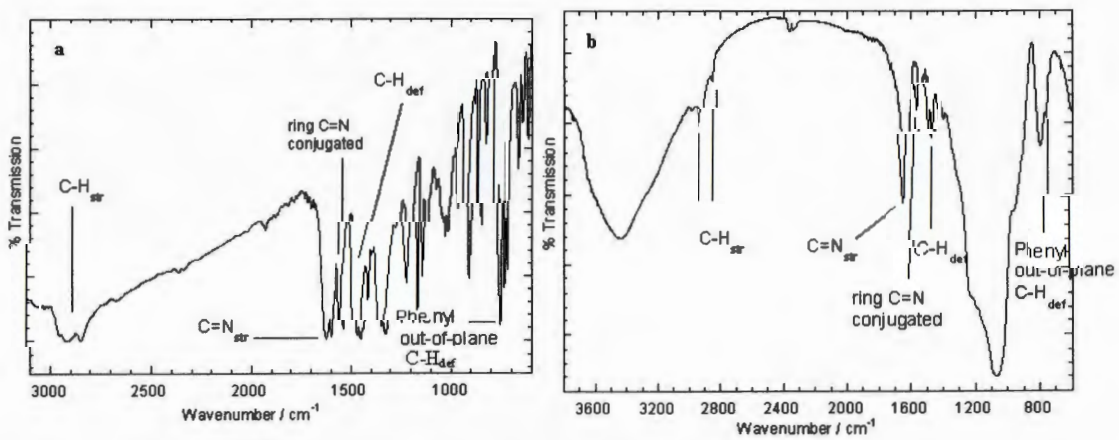

Figure 6.3 IR spectra of: (a) free copper-Schiff base triethoxysilane complex, and (b) copper-Schiff base-modified MCM 41 (Cu-Schiff-MCM-**1.0**).

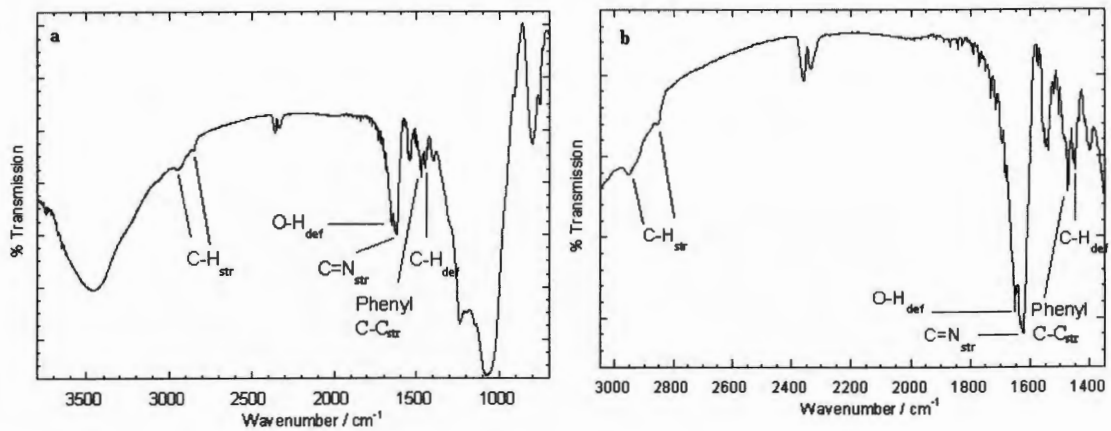

Figure 6.4 IR spectra of: (a) iron(II)-Schiff base-modified MCM 41 [Fe(II)-Schiff-MCM-**1.0**], and (b) iron(III)-Schiff base-modified MCM 41 [Fe(III)-Schiff-MCM-**1.0**].

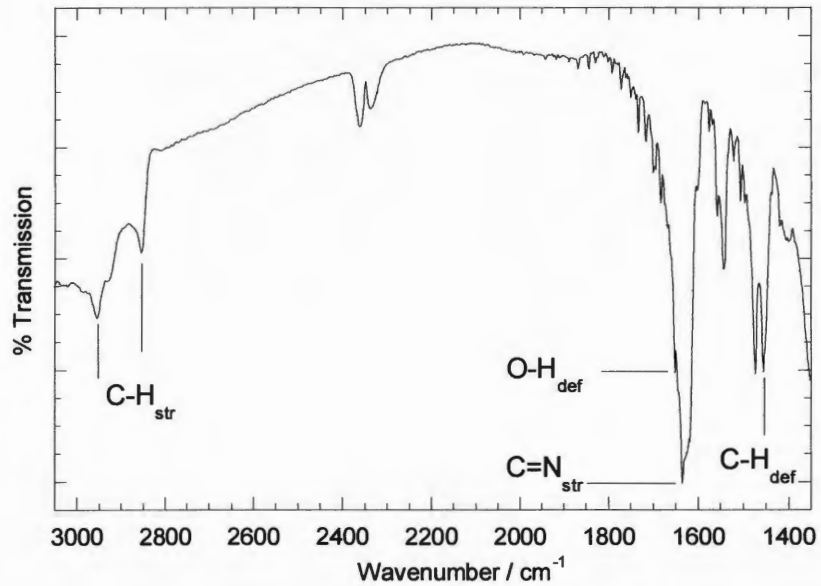

Figure 6.5 IR spectrum of the nickel-Schiff base-modified MCM 41 material (Ni-Schiff-MCM-**1.0**).

The IR spectrum of each of the metal-Schiff base-modified samples shows a peak at *ca.* 1625 cm^{-1} for the stretching vibration of C=N.[6, 8, 10] A similar band in the free copper-Schiff base complex appears at *ca.* 1622 cm^{-1}. Spectra for all of the metal-Schiff base-modified MCM 41 samples show peaks assigned to $C\text{-}H_{str}$ and $C\text{-}H_{def}$ vibrations at *ca.* 2960 cm^{-1}, 2830 cm^{-1}, and 1450 cm^{-1},[14, 15, 16, 17] respectively. These

bands are due to the C-H vibrations from the propyl chain of the metal-Schiff base triethoxysilane complex. The IR absorption bands at *ca.* 1475 cm^{-1},[14, 15, 16] and 760 cm^{-1} are assigned to a C-C stretching vibration of the phenyl ring and an aromatic out-of-plane C-H deformation vibration,[14, 15, 16] respectively. Both of these bands were also found to be present in the IR spectrum of the free copper-Schiff base complex.

6.3.3 Nuclear Magnetic Resonance (NMR) Spectroscopy

The ^{29}Si and ^{13}C cross-polarisation magic angle spinning nuclear magnetic resonance (CP MAS NMR) spectroscopic analysis of the Ni-Schiff-MCM-**1.0**, Fe(III)-Schiff-MCM-**0.75** and Cu-Schiff-MCM-**1.0** (8) samples were carried out by Dr. A. Herve, using the solid-state NMR service at the University College London. The ^{29}Si and ^{13}C CP MAS NMR spectra of the Cu-Schiff-MCM-**1.0** (8), Fe(III)-Schiff-MCM-**0.75** and Ni-Sciff-MCM-**1.0** samples were similar and, hence, the ^{29}Si and ^{13}C CP MAS NMR spectra of only the Ni-Schiff-MCM-**1.0** sample are discussed below in detail.

6.3.3.1 ^{29}Si Cross-polarisation Magic Angle Spinning (CP MAS) NMR Spectroscopy

The ^{29}Si CP MAS NMR chemical shifts for the metal-Schiff base-modified MCM 41 materials are summarised in Table 6.9 and the ^{29}Si CP MAS NMR spectrum of the Ni-Schiff-MCM-**1.0** sample is shown as an example in Fig. 6.6.

Table 6.9 ^{29}Si CP MAS NMR chemical shifts for the metal-Schiff base-modified MCM 41 materials

	δ / ppm					
Sample	T^1	T^2	T^3	Q^2	Q^3	Q^4
Ni-Schiff-MCM-**1.0**	_ _	-57.9	-66.0	_ _	-101.8	-109.3
Fe(III)-Schiff-MCM-**0.75**	_ _	-58.0	-66.0	_ _	-101.5	-109.0
Cu-Schiff-MCM-**1.0** (8)	_ _	-58.5	-67.1	_ _	-100.6	-108.8
Parent Si-MCM-41	_ _	_ _	_ _	-91.9	-100.7	-109.3

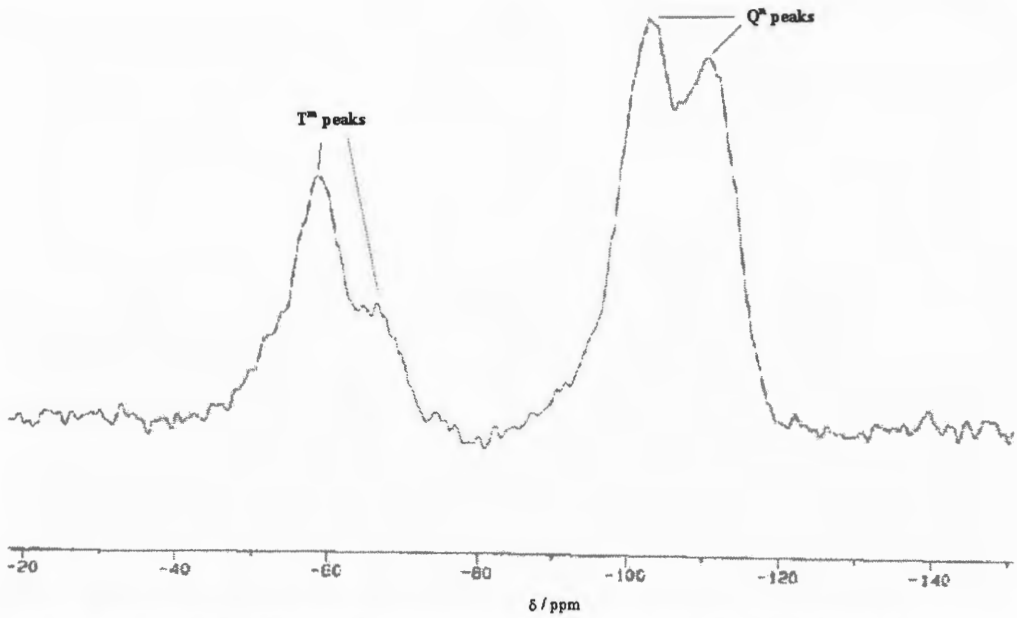

Figure 6.6 ^{29}Si CP MAS NMR spectrum of nickel-Schiff base-modified MCM 41 (Ni-Schiff-MCM-**1.0**).

The ^{29}Si CP MAS NMR spectrum for the Ni-Schiff-MCM-**1.0** shows the presence of two different types of silicon (T^m and Q^n) in the material, which confirmed the immobilisation of nickel-Schiff base complex on the Si-MCM 41 material. The NMR peaks at *ca.* δ = -57.9 and -66.0 ppm[18, 19, 20, 21, 22] were assigned as T^m peaks, which were due to the organosiloxanes [T^m = $RSi(OSi)_m(OH)_{3-m}$, m = 1-3, Section 2.8.4] and found to be present in the modified materials. These peaks were absent in the ^{29}Si CP MAS NMR spectrum of the parent Si-MCM 41 material.

The NMR peaks at *ca.* δ = -101.8 and -109.3 ppm[18, 19, 20, 21, 22] due to the framework silicon [siloxane unit, Q^n = $Si(OSi)_n(OH)_{4-n}$, n = 2-4, Section 3.2.6] were similar to those observed for the Si-MCM 41 material (Chapter 3, Fig. 3.11). These peaks are assigned to the Q^3 [$HOSi(OSi)_3$] and Q^4 [$Si(OSi)_4$] silicon sites, respectively, present in the MCM 41 framework. The immobilisation of the nickel-Schiff base complex resulted in an increase in the peak intensity of the Q^4 sites relative to Q^3 sites compared with the unmodified Si-MCM 41. This indicated the replacement of the surface silanol groups (Si-OH) by the nickel-Schiff base triethoxysilane complex.[21]

6.3.3.2 ^{13}C-{^{1}H}-Cross-polarisation Magic Angle Spinning (CP MAS) NMR Spectroscopy

The ^{13}C-{^{1}H}-CP MAS NMR chemical shifts and assigned carbon environments for the metal-Schiff base-modified samples are summarised in Table 6.10 and the ^{13}C-{^{1}H}-CP MAS NMR spectrum of the Ni-Schiff-MCM-**1.0** sample is shown in Fig. 6.7.

Table 6.10 ^{13}C-{^{1}H}-CP MAS NMR chemical shifts for the metal-Schiff base-modified MCM 41 materials

	Approximate δ / ppm							
Sample	**Aliphatic carbon peak position**					**Aromatic carbon peak position**		
Ni-Schiff-MCM-**1.0**	10	--	25	50	60	120	133	163
Fe(III)-Schiff-MCM-**0.75**†	9	--	24	49	59	118	139	--
Cu-Schiff-MCM-**1.0** (8) †	7	17	23	49	59	119	133	--

† *The signal-to-noise ratio in the spectrum of this sample was poor so not all the peaks were clearly visible.*

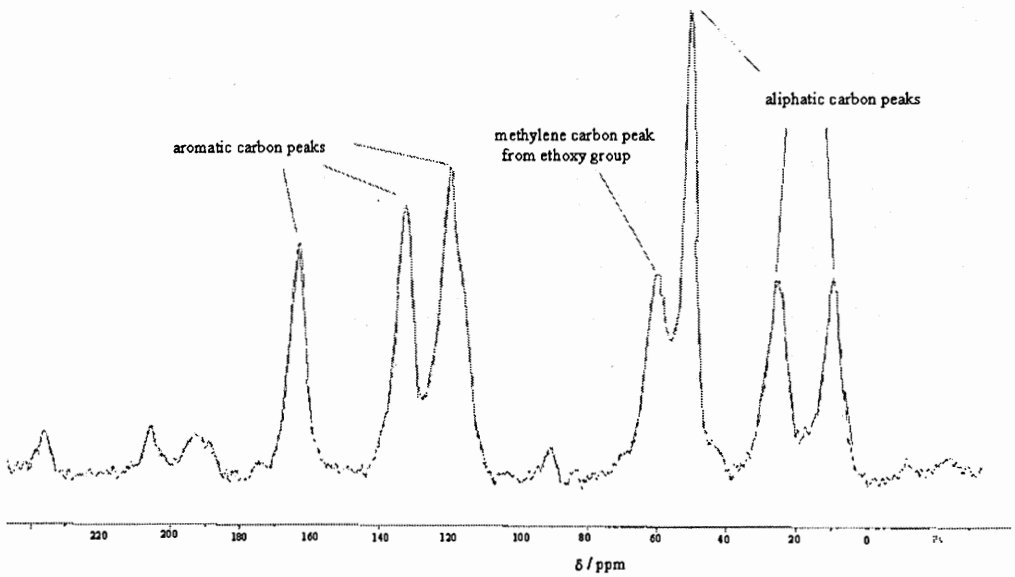

Figure 6.7 ^{13}C-{^{1}H}-CP MAS NMR spectrum of nickel-Schiff base-modified MCM 41 (Ni-Schiff-MCM-**1.0**).

The spectrum shows the presence of both the aliphatic and aromatic carbons, which confirms the immobilisation of nickel-Schiff base complex on the Si-MCM 41 surface. The ^{13}C-{^{1}H}-CP MAS NMR spectrum of the nickel-Schiff base-modified

MCM 41 material shows three NMR peaks in the aliphatic region at *ca.* δ = 10, 25 and 50 ppm,[20, 23, 24, 25] and these were assigned to the three different carbon atoms of the 3-aminopropyl groups, which link the metal-Schiff base complex to the MCM 41 surface. The NMR peak at *ca.* δ = 60 ppm[23] in all the three samples (Table 6.10) and the peak at *ca.* δ = 17 ppm[23] were assigned to the methylene carbon and methyl carbon, respectively, of the ethoxy groups. This confirmed the presence of ethoxy groups in the sample and supported the results obtained from the CHN analysis (Section 6.3.5).

The NMR spectra for all the three samples also showed peaks (Table 6.10) in the aromatic region at *ca.* δ = 120, 135 and 163 ppm for the carbon atoms of the phenyl rings (Fig. 6.8).[23] The NMR peak at *ca.* δ = 163 ppm was attributed to the phenyl carbon atoms attached to the oxygen and the carbon attached to nitrogen (-C=N-), *i.e.* carbons attached to both electronegative atoms. Six NMR peaks from the phenyl ring was expected, however, the resolution of these peaks in solid state NMR was not achieved under the analysis conditions and the spectrum of Ni-Schiff-MCM-**1.0** (Fig. 6.7) showed three broad peaks in the aromatic region. Some of these peaks were not clearly visible in the ^{13}C NMR spectra of Cu-Schiff-MCM-**1.0** and Fe-Schiff-MCM-**0.75** samples due to poor signal-to-noise ratio (Appendix A4).

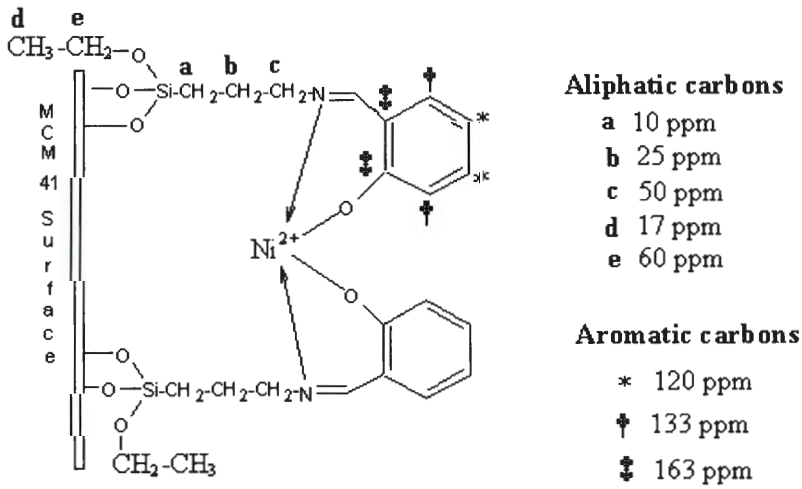

Figure 6.8 Diagram showing different carbon environments with approximate chemical shift for the nickel Schiff base-modified MCM 41 material (Ni-Schiff-MCM-**1.0**).

6.3.4 Atomic Absorption Spectroscopy (AAS)

The metal contents of the metal-Schiff base-modified MCM 41 materials synthesised were determined by atomic absorption spectroscopy (AAS) and the results are summarised in Table 6.11. The Table reveals that the materials synthesised using increasing initial amounts of metal-Schiff base complex possess a higher metal content. The results show that there was an increase in the immobilisation of metal-Schiff base complex (with target loading from 0.25 to 0.75 mmol g^{-1}) on the Si-MCM 41 surface. However, a maximum loading of *ca.* 0.50 mmol g^{-1} was achieved at a target loading of 0.75 mmol g^{-1} and further attempts to increase the immobilisation of metal-Schiff base complex *i.e.* 1.0 mmol g^{-1} (under control conditions) resulted in no significant increase in the amount of metal detected.

Table 6.11 AAS results for the metal-Schiff base-modified MCM 41 materials

Sample	**Metal loading / mmol g^{-1}**
Cu-Schiff-MCM-**0.25** (8)	0.25
Cu-Schiff-MCM-**0.50** (8)	0.35
Cu-Schiff-MCM-**0.75** (8)	0.45
Cu-Schiff-MCM-**1.0** (8)	0.47
Cu-Schiff-MCM-**1.0** (20)	0.65
Fe(II)-Schiff-MCM-**0.25**	0.24
Fe(II)-Schiff-MCM-**0.50**	0.36
Fe(II)-Schiff-MCM-**0.75**	0.49
Fe(II)-Schiff-MCM-**1.0**	0.47
Fe(III)-Schiff-MCM-**0.25**	0.20
Fe(III)-Schiff-MCM-**0.25**	0.30
Fe(III)-Schiff-MCM-**0.75**	0.47
Fe(III)-Schiff-MCM-**1.0**	0.52
Ni-Schiff-MCM-**0.25**	0.20
Ni-Schiff-MCM-**0.50**	0.37
Ni-Schiff-MCM-**0.75**	0.45
Ni-Schiff-MCM-**1.0**	0.48

The Cu-Schiff-MCM-1.0 (20) material synthesised using toluene as the solvent and with a reaction time of 20 h, showed a maximum 0.65 mmol g^{-1} loading of copper grafted onto the Si-MCM 41 surface compared with a 0.50 mmol g^{-1} loading for the material synthesised using a reaction time of 8 h (Table 6.11). This suggests that the immobilisation of the metal-complex on the MCM 41 surface increases with longer reaction time. However, the material subjected to the longer reaction time (20 h) lost mesoporosity through pore blocking in addition to the pore narrowing as indicated by the N_2 sorption results (Section 6.4.1). For this reason, a series of copper-Schiff base MCM 41 materials with different loadings were synthesised using the shorter reaction time (8 h) to achieve maximum loading of Cu-Schiff base complex whilst maintaining the mesoporosity of the synthesised materials.

The copper samples synthesised using toluene as the solvent with a reaction time of 8 h showed similar loadings of metal when compared with iron and nickel samples, which were synthesised using methanol as the solvent and with reaction times of 15 h and 27 h, respectively. This suggests that toluene is a good solvent for post-synthetic grafting of metal-Schiff base complex. However, problems arose when using toluene as a solvent in the synthesis of the Fe-Schiff base-MCM 41 samples, due to the insolubility of the $FeCl_3$ salt in toluene. In the case of the nickel-Schiff base MCM 41 material, the nickel-Schiff base triethoxysilane complex precipitated out in toluene and hence methanol was used as a solvent coupled with longer reaction times to achieve maximum loadings.

6.3.5 CHN Microanalysis

The presence of a higher percentage of carbon, hydrogen and nitrogen in the metal-Schiff base-modified samples confirmed the immobilisation of the metal-Schiff base complex on the surface of the MCM 41. The CHN microanalytical data for the metal-

Schiff base-modified MCM 41 materials are summarised in Table 6.12. The higher initial loading of the metal-Schiff base complex used in the preparation of a sample is reflected by a higher percentage of carbon, hydrogen and nitrogen, as expected.

The N/metal molar ratio (metal content determined from AAS) observed in each of the metal-Schiff base-modified materials was found to be in the range 1.7 to 2.5 (Table 6.12). This ratio was in reasonable agreement with the expected ratio of 2.0, which confirmed the complexation of the metal with the Schiff base ligand in a 1:2 ratio. This suggested that the immobilisation of metal on the MCM 41 surface occurs *via* complexation with the Schiff base ligand.

Table 6.12 CHN microanalytical data for the metal-Schiff base-modified MCM 41 materials

Sample	**Carbon / % mass**	**Hydrogen / % mass**	**Nitrogen / % mass**	**N / Metal (by AAS) mol ratio**
Si-MCM 41	0.08	1.10	0.00	--
Cu-Schiff-MCM-**0.25** (8)	7.16	1.67	0.59	1.7
Cu-Schiff-MCM-**0.50** (8)	9.42	2.01	0.86	1.8
Cu-Schiff-MCM-**0.75** (8)	10.96	2.20	1.11	1.8
Cu-Schiff-MCM-**1.0** (8)	11.46	2.24	1.16	1.8
Cu-Schiff-MCM-**1.0** (20)	14.59	1.96	1.65	1.8
Fe(II)-Schiff-MCM-**0.25**	9.59	1.73	0.60	1.8
Fe(II)-Schiff-MCM-**0.50**	13.04	2.27	1.03	2.0
Fe(II)-Schiff-MCM-**0.75**	15.69	2.46	1.36	2.0
Fe(II)-Schiff-MCM-**1.0**	17.06	2.71	1.62	2.5
Fe(III)-Schiff-MCM-**0.25**	7.39	1.66	0.51	1.8
Fe(III)-Schiff-MCM-**0.25**	9.99	1.84	0.89	2.1
Fe(III)-Schiff-MCM-**0.75**	11.88	2.02	1.10	1.7
Fe(III)-Schiff-MCM-**1.0**	14.56	2.40	1.49	2.0
Ni-Schiff-MCM-**0.25**	8.82	1.74	0.60	2.1
Ni-Schiff-MCM-**0.50**	12.59	2.05	1.04	2.0
Ni-Schiff-MCM-**0.75**	15.34	2.32	1.42	2.3
Ni-Schiff-MCM-**1.0**	17.77	2.59	1.70	2.5

The data are averaged for two analyses, which were in good agreement of ca. ± 0.07 %.

Reaction of the ethanol, liberated during the immobilization of metal-Schiff base triethoxysilane complex, with surface silanol groups may be ruled out. Since, carrying out the reaction in ethanol/methanol as a solvent would result in only very small amount of immobilisation of the complex on the surface.

Fig. 6.9 shows some possible structures for the grafted metal-Schiff base-modified MCM 41 samples in which a variable number of ethoxy groups have been lost on immobilisation. The hydrogen from the surface silanol groups interferes with the hydrogen value derived from CHN analysis and hence only the C:N ratios are compared. It can be seen from the Table 6.13 that the experimentally observed C:N ratios for the Cu-Schiff-MCM 41 materials are between the calculated theoretical C:N ratio of structure B and structure C (Fig. 6.9). This suggests that the structures B and C or combination, *i.e.* those with two, three and four unreacted ethoxy groups, are predominantly present in the samples of grafted metal-Schiff base-modified MCM 41 materials. Thus, CHN microanalysis in combination with AAS enabled the prediction of possible structures of the metal-Schiff base-modified samples.

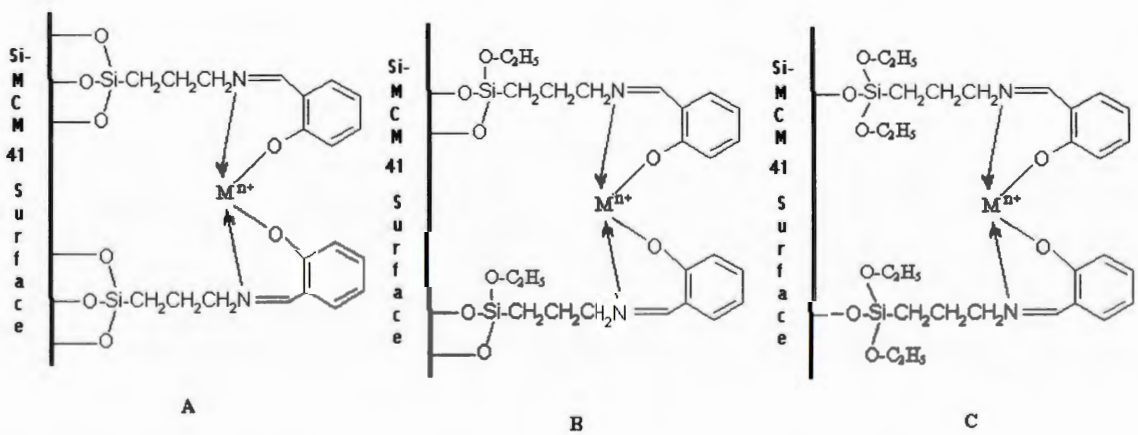

Figure 6.9 Some possible structures for the grafted metal-Schiff base modified-MCM 41 materials.

Table 6.13 Summary of the theoretical and observed C:N ratios for some possible structures of the metal-Schiff base-modified MCM materials

Sample structure from Fig. 6.6	Theoretical C:N ratio	Observed C:N ratio from CHN microanalysis	Cu-Schiff base-modified MCM 41 samples
A	10:1	14:1	Cu-Schiff-MCM-**0.25**
B	12:1	13:1	Cu-Schiff-MCM-**0.50**
		11:1	Cu-Schiff-MCM-**0.75**
C	14:1	12:1	Cu-Schiff-MCM-**1.0**

The observed C:N ratio for only the Cu-Schiff base MCM 41 samples are shown.

Table 6.13 shows a trend of decrease in the number of unreacted ethoxy groups with increase in the amount of metal-Schiff base complex present in the modified samples *i.e.* more of structure B is present in the material.

6.3.6 X-ray Photoelectron Spectroscopy (XPS)

In this project, one key aim was to evaluate XPS as an analytical tool to determine the distribution of metal-Schiff base complexes on the surface of the Si-MCM 41 material. X-ray photoelectron spectroscopic analyses were carried out on the range of copper-Schiff base-modified MCM 41 materials by the Interface Analysis Centre, University of Bristol.

The XPS results are discussed in two sub-sections: First, the XPS results for the Cu-Schiff-MCM-**1.0** (20) material (Cu-Schiff base complex target loading of 1.0 mmol g^{-1} using a reaction time of 20 h) are discussed. Second, the results of the range of Cu-Schiff-MCM-**0.25, -0.50, -0.75, -1.0** (8 h) materials are discussed.

*6.3.6.1 Cu-Schiff-MCM-**1.0** (20)*

The wide-scan XPS spectrum for the Cu-Schiff-MCM-**1.0** (20) sample is shown in Fig. 6.10. The spectrum of the Cu-Schiff-MCM-**1.0** (20) sample shows peaks for C, N and Cu in addition to the Si and O, which confirms the presence of the copper-Schiff base complex on the Si-MCM 41 surface.

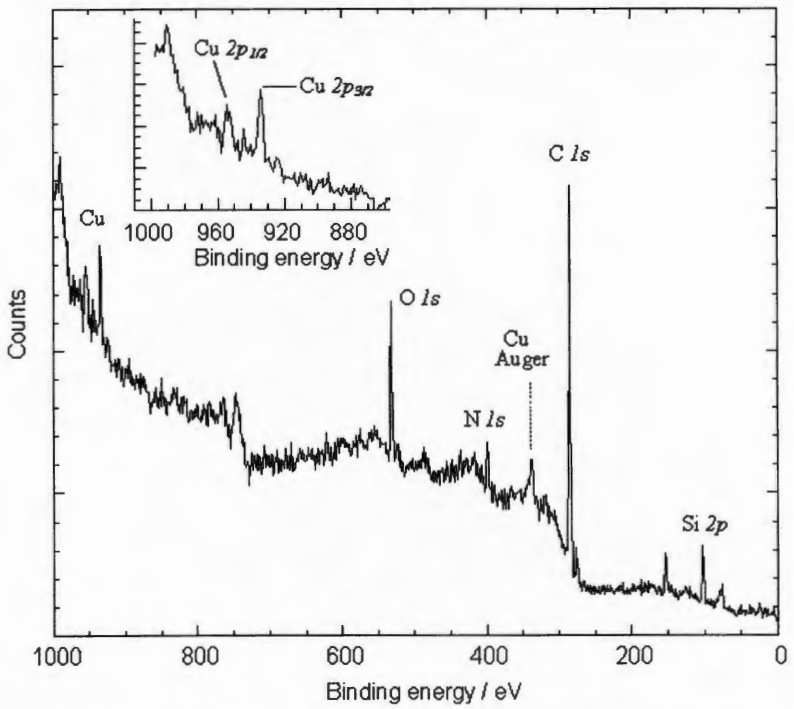

Figure 6.10 Wide-scan XPS spectrum of the Cu-Schiff-MCM-**1.0** (20) material.

The peak positions were corrected for sample charging by reference to the adventitious hydrocarbon peak at 284.8 eV binding energy.[26, 27] The O *1s* peak position at 532.8 eV was as expected for alpha-quartz, SiO_2. The Si *2p* peak position (102.8 eV) in the modified sample was observed at a slightly lower binding energy compared with the parent Si-MCM 41 material (103.8 eV), which indicated the presence of silicate in the modified samples. The peak positions did not change significantly upon tilting the sample to reduce the analysis depth, as shown in Fig. 6.11 (shallow take-off analysis).

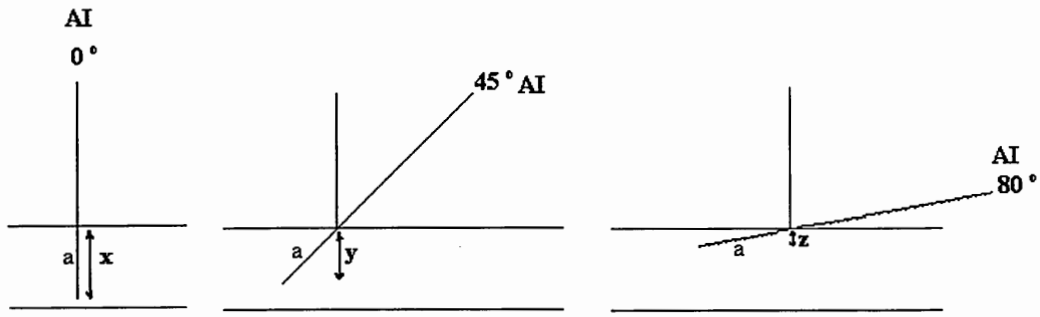

Figure 6.11 Schematic representation of shallow take-off angle analysis, where AI is the position of analyser input at angle 0°, 45° and 80° and x, y and z are the distance from the sample surface from which the emitted electrons were analysed.

Table 6.14 summarises the measured binding energy peak positions for the various elements and assigned chemical environments as determined by XPS.

Table 6.14 Binding energies and assigned chemical environments for the Cu-Schiff-MCM-**1.0** (20) material determined by XPS

Elements	**Binding energy / eV**		
	*Cu-Schiff-MCM-**1.0** (20)*	*Cu-Schiff-MCM-**1.0** (20) (Shallow take-off angle analysis)*†	*Cu-Schiff-MCM-**1.0** (20) (after argon etching)*‡
Carbon	284.8 (HC)* 286.2 (carbon with nitrogen)	284.8 (HC) 286.4 (carbon with nitrogen)	284.8 (HC) 286.7 (alcohol / ether)
Nitrogen	399.4 (amines / cyanides / organic matrices)	399.3 (amines / cyanides / organic matrices)	399.6 (amines / cyanides / organic matrices)
Oxygen	532.8 (SiO_2-type)	532.3 (silicate / SiO_2-type)	532.5 (silicate / SiO_2-type)
Silicon	102.8 (silicate)	102.7 (silicate)	102.1 (silicate)
Copper	932.9 (Cu-I) 934.5 (Cu-II)	933.1 (Cu-I) 934.7 (Cu-II)	933.1 (Cu-I)

**HC = adventitious hydrocarbon[26] and –CH_2– groups*
† Shallow take-off angle = 45°
The results obtained using shallow-take-off angle of 80° were similar to that of 45° and hence results of shallow take-off of 45° are shown and discussed here.
‡ at a rate of ca. 1 nm min^{-1}, equivalent to ca. 4.5 nm depth

The 399.4 eV binding energy measured for N *1s* was as expected for nitrogen containing organic compounds,[26, 27] and the peak was attributed to the C=N species present in the sample. This N *1s* peak was absent in the spectrum of the parent

Si-MCM 41 material. Although Cu(II) was the expected oxidation state [as the reduction of Cu(II) to Cu(I) during the synthesis process is unlikely], the spectrum showed two copper peaks at binding energies of 932.9 and 934.5 eV for Cu(I) and Cu(II),[26, 27] respectively. This suggests that the copper in the material was present in two different oxidation states. However, further investigation of the effects of X-ray radiation exposure under ultra-high vacuum conditions on the sample showed reduction of Cu(II) to Cu(I). This involved a series of experiments using a succession of short exposure times for a period of 2.5 h on freshly prepared samples and it was noted that reduction was seen to occur even after short exposure times. Fig. 6.12 illustrates the effect of X-ray exposure on the oxidation state of the detected copper. In addition to a shift in the peaks to lower binding energies, there is also a reduction in the intensity of the satellite peaks, which are both indicative of a reduction of Cu(II) to Cu(I). It was, therefore, concluded that the presence of two oxidation states in the modified MCM 41 material was a function of the analysis conditions rather than a fundamental property of the material.

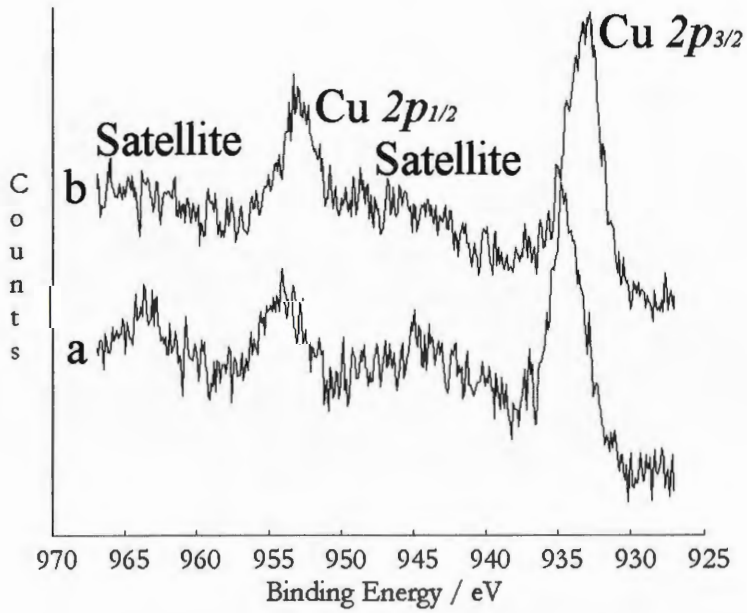

Figure 6.12 An example of the X-ray induced reduction effect on copper for the Cu-Schiff-MCM-**1.0** (20) material. (a) initial XPS spectrum, (b) XPS spectrum following X-ray exposure time of 2.5 h.

Table 6.15 summarises the quantified surface atomic concentrations for the Cu-Schiff-MCM-**1.0** (20) material determined using XPS. The material showed higher carbon concentrations compared with the unmodified-Si-MCM 41 material. Nitrogen and copper were observed in the modified material, which were not present prior to modification. The reduced silicon and oxygen levels in the modified sample were indicative of the presence of the Schiff base masking the siliceous surface.

Table 6.15 Quantified surface atomic concentrations determined by XPS for the parent Si-MCM 41 and Cu-Schiff-MCM-**1.0** (20) materials

Sample	**Surface Concentration / Atomic % (at%)**				
	Carbon	Nitrogen	Oxygen	Silicon	Copper
Parent Si-MCM 41	3.3	--	68.5	28.3	--
Parent Si-MCM 41 (shallow take-off angle)	6.4	--	65.5	28.0	--
Parent Si-MCM 41 (after Ar^+ etching)	32.1	--	45.8	22.1	--
Cu-Schiff-MCM-**1.0** (20)	71.0	5.8	16.2	5.6	1.5
Cu-Schiff-MCM-**1.0** (20) (shallow take-off angle)	71.8	5.3	15.5	6.2	1.2
Cu-Schiff-MCM-**1.0** (20) (after Ar^+ etching)	85.7	3.0	6.6	4.1	0.5

The results of parent Si-MCM 41 are reproduced here for comparison.
Shallow take-off angle = 45°, Argon etching = 270 s (at a rate of ca. 1 nm min^{-1}, equivalent to ca. 4.5 nm depth)

XPS gave a copper concentration of 1.5 at% present in the Cu-Schiff-MCM-**1.0** (20) material, whereas AAS measurements showed a copper concentration of 0.65 mmol g^{-1} (41.34 mg g^{-1}), which was equivalent to a copper concentration of 1.29 at%. Thus, the copper concentration determined using XPS was in good agreement with that measured by AAS.

Argon ion etching[26] for a total of 270 s (at a rate of *ca.* 1 nm min^{-1}, equivalent to *ca.* 4.5 nm depth) brought about an increase in the carbon concentration for both the parent and the modified materials, which was probably due to the ion beam redistributing carbon-containing material from the adhesive tab. The oxygen concentration decreased upon etching for both of the samples. For the modified materials, the Si:Cu ratio increased on etching, suggesting that the copper was predominantly on the surface and preferentially removed by the ion etching.[27] The copper concentration decreased to a third after argon etching (see Table 6.15), which suggested that the Cu-Schiff base complex was at or near a surface in the mouth of the pores and that a significant proportion (approximately two thirds) was immobilised on the external surface and very little (one third) goes into the pores.[27] The nitrogen sorption analysis discussed later in Section 6.4.1 suggests that the Cu-Schiff base is blocking the pores of this particular material.

*6.3.6.2 Cu-Schiff-MCM-**0.25** to -**1.0** Materials (Synthesised with Reaction Time of 8 h)*

XPS was carried out on the four copper-Schiff base-modified samples synthesised with a reaction time of 8 h: Cu-Schiff-MCM-**0.25** (8), Cu-Schiff-MCM-**0.50** (8), Cu-Schiff-MCM-**0.75** (8) and Cu-Schiff-MCM-**1.0** (8). The XPS spectra for all four samples were similar and only the XPS spectrum of Cu-Schiff-MCM-**1.0** (8) is shown here (Fig. 6.13). Table 6.14 summarises the measured binding energy peak positions and assigned chemical environments for the various elements.

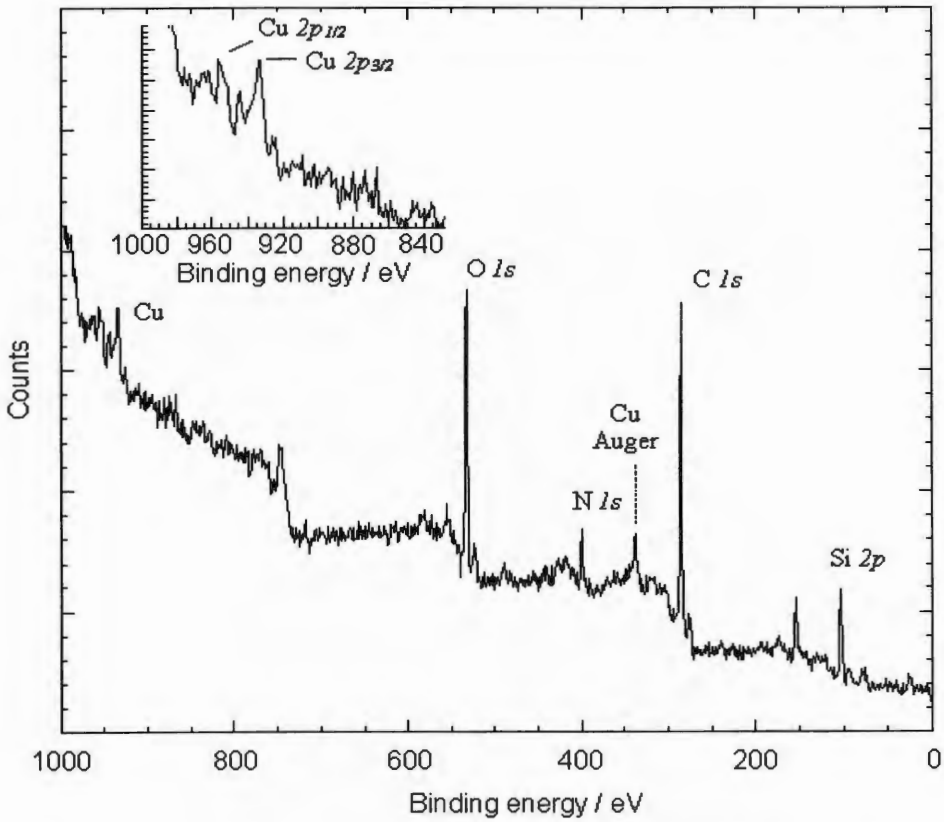

Figure 6.13 Wide-scan XPS spectrum of the Cu-Schiff-MCM-**1.0** (8) material.

Table 6.16 Binding energies and chemical environments for the Cu-Schiff-MCM 41 (8) materials determined by XPS.

Elements	**Binding energy for / eV**		
	*Cu-Schiff-MCM-**1.0** (8)*	*Cu-Schiff-MCM-**1.0** (8) (Shallow take-off angle analysis)* †	*Cu-Schiff-MCM-**1.0** (8) (after argon etching)* ‡
Carbon	284.8 (HC)* 286.3 (carbon with nitrogen)	284.8 (HC) 286.4 (carbon with nitrogen)	284.8 (HC)
Nitrogen	399.3 (amines / cyanides / organic matrices)	399.1 (amines / cyanides / organic matrices)	398.7 (amines / cyanides / organic matrices)
Oxygen	531.0 532.8 (SiO_2-type)	531.7 532.3 (silicate / SiO_2-type)	532.5 (silicate / SiO_2-type)
Silicon	103.1 (silicate)	103.0 (silicate)	102.7 (silicate)
Copper	933.2 (Cu-I) 934.8 (Cu-II)	932.9 (Cu-I) 934.2 (Cu-II)	933.6 (Cu-I)

Elements	Binding energy for / eV		
	Cu-Schiff-MCM-0.75 (8)	*Cu-Schiff-MCM-0.75 (8) (Shallow take-off angle analysis)* †	*Cu-Schiff-MCM-0.75 (8) (after argon etching)* ‡
Carbon	284.8 (HC) 286.4 (carbon with nitrogen)	284.8 (HC) 286.3 (carbon with nitrogen)	284.8 (HC)
Nitrogen	399.3 (amines / cyanides / organic matrices)	399.3 (amines / cyanides / organic matrices)	398.6 (amines / cyanides / organic matrices)
Oxygen	531.3 532.8 (SiO_2-type)	530.8 532.7 (silicate / SiO_2-type)	532.6 (silicate / SiO_2-type)
Silicon	103.1 (silicate)	103.1 (silicate)	101.2 102.9 (silicate)
Copper	933.2 (Cu-I) 934.7 (Cu-II)	933.0 (Cu-I) 934.7 (Cu-II)	932.6 (Cu-I) 935.5 (Cu-II)
Elements	**Binding energy for / eV**		
	Cu-Schiff-MCM-0.50 (8)	*Cu-Schiff-MCM-0.50 (8) (Shallow take-off angle analysis)* †	*Cu-Schiff-MCM-0.50 (8) (after argon etching)* ‡
Carbon	284.8 (HC) 286.3 (carbon with nitrogen)	284.8 (HC) 286.4 (carbon with nitrogen)	284.8 (HC) 290.5 (alcohol / ether)
Nitrogen	399.3 (amines / cyanides / organic matrices)	399.3 (amines / cyanides / organic matrices)	398.5 (amines / cyanides / organic matrices)
Oxygen	531.2 532.9 (SiO_2-type)	530.8 532.8 (silicate / SiO_2- type)	532.7 (silicate / SiO_2-type)
Silicon	103.3 (silicate)	103.3 (silicate)	100.9, 103.0 (silicate)
Copper	933.1 (Cu-I) 934.8 (Cu-II)	932.9 (Cu-I) 934.3 (Cu-II)	933.5 (Cu-I) 934.9 (Cu-II)
Elements	**Binding energy for / eV**		
	Cu-Schiff-MCM-0.25 (8)	*Cu-Schiff-MCM-0.25 (8) (Shallow take-off angle analysis)* †	*Cu-Schiff-MCM-0.25 (8) (after argon etching)* ‡
Carbon	284.8 (HC) 286.3 (carbon with nitrogen)	284.8 (HC) 286.3 (carbon with nitrogen)	284.8 (HC)
Nitrogen	399.3 (amines / cyanides / organic matrices)	399.3 (amines / cyanides / organic matrices)	398.7 (amines / cyanides / organic matrices)
Oxygen	531.1 532.9 (SiO_2-type)	530.8 532.9 (silicate / SiO_2-type)	532.6 (silicate / SiO_2-type)
Silicon	103.4 (silicate)	103.4 (silicate)	100.8 102.9 (silicate)
Copper	933.1 (Cu-I) 935.5 (Cu-II)	933.1 (Cu-I) 935.2 (Cu-II)	933.6 (Cu-I) 935.4 (Cu-II)

**HC = adventitious hydrocarbon[26] and $-CH_2-$ groups, † Shallow take-off angle = 45° The results obtained using shallow-take-off angle of 80° were similar to that of 45° and hence results of shallow take-off of 45° are shown and discussed here.*

‡ At a rate of ca. 1 nm min^{-1}, equivalent to ca. 4.5 nm depth.

All of the modified samples show a carbon peak at *ca.* 286.4 eV due to the C=N species.[26] The intensity of this peak tends to decrease with argon ion etching indicating the removal of the C=N (Schiff base) following etching. The N *1s* peak observed at *ca.* 399.3 eV was as expected for the nitrogen containing organic compounds.[26, 27] The presence of these peaks in the modified samples and their absence following argon etching confirmed the immobilisation of the copper-Schiff base complex on the MCM 41 surface.

The modified samples show an O *1s* peak at 532.8 eV and a Si *2p* peak at *ca.* 103.1 eV for the Si-MCM 41 framework, which were as expected for alpha-quartz, SiO_2.[27] The O *1s* peak observed at *ca.* 531.1 eV is assigned to oxygen from the Schiff base ligand. This peak was found to be absent in the spectrum after argon etching, which indicated the removal of the organics (Schiff base ligand) after etching. The appearance of a peak at *ca.* 101 eV[26] suggests the formation of some carbides and/or nitrides of silicon by the etching process.

The two copper peaks at binding energies 933.1 eV and 935.5 eV[26, 27] observed in the spectrum of each of the modified samples were assigned to Cu(I) and Cu(II), respectively. The Cu(I) peak was due to reduction on exposure of the samples to the X-rays under high vacuum, as discussed earlier in Section 6.3.6.1.

The Table 6.17 summarises the quantified surface atomic concentrations for the copper-Schiff base-modified samples (reaction time 8 h) determined using XPS. The modified samples showed higher carbon concentrations compared with the unmodified Si-MCM 41, which indicated the presence of the copper-Schiff base complex on the MCM 41 surface. The shallow take-off angle analysis showed no significant change in the measured carbon, nitrogen and copper concentrations of the modified samples, indicating that there was little change in the sample surface between *ca.* 2 and 4 nm. The silicon concentration remained unchanged with shallow take-off angle analysis. This may be because the higher kinetic energy of these photoelectrons (lower binding

energy) mean that they are less affected by any contamination overlayers. A slight increase in the silicon concentration was observed in the samples with decrease in the initial amount of copper-Schiff base complex loading. This probably indicates that the Si-MCM 41 surface is covered by the copper-Schiff base complex.[27]

Table 6.17 Quantified surface atomic concentrations for the copper-Schiff base materials (reaction time 8 h) as determined by XPS.

Sample	Surface Concentration / Atomic % (at%)				
	Carbon	Nitrogen	Oxygen	Silicon	Copper
Cu-Schiff-MCM-**1.0** (8)	65.0	4.7	21.2	8.2	0.9
Cu-Schiff-MCM-**1.0** (8) (shallow take-off angle)	64.4	5.0	20.6	9.1	0.9
Cu-Schiff-MCM-**1.0** (8) (after Ar^+ etching)	50.6	3.3	28.0	17.8	0.3
Cu-Schiff-MCM-**0.75**	61.8	5.1	22.6	9.5	1.0
Cu-Schiff-MCM-**0.75**) (shallow take-off angle)	60.9	5.2	23.0	10.1	0.8
Cu-Schiff-MCM-**0.75** (after Ar^+ etching)	48.9	1.8	30.2	18.8	0.3
Cu-Schiff-MCM-**0.50**	54.1	4.4	28.6	12.0	0.9
Cu-Schiff-MCM-**0.50** (shallow take-off angle)	54.8	4.0	28.3	12.2	0.8
Cu-Schiff-MCM-**0.50** (after Ar^+ etching)	45.1	1.5	32.5	20.6	0.2
Cu-Schiff-MCM-**0.25**	48.3	3.9	33.1	13.8	0.9
Cu-Schiff-MCM-**0.25** (shallow take-off angle)	48.7	4.0	32.6	13.9	0.8
Cu-Schiff-MCM-**0.25** (after Ar^+ etching)	46.5	1.0	32.3	20.0	0.2

Shallow take-off angle = 45°, Argon etching = 270 s (at a rate of ca. 1 nm min^{-1}, equivalent to ca. 4.5 nm depth)

Argon ion etching tended to reduce the detected carbon, nitrogen and copper concentrations on the modified samples whilst increasing those of the oxygen and silicon. This confirmed the immobilisation of the copper-Schiff base complex on the Si-MCM 41 surface. The silicon-to-copper ratio increased upon etching, which suggested that the copper-Schiff base complex was predominantly on the surface and

preferentially removed by argon ion etching.[27] However, the presence of copper in the sample after argon ion etching suggested that some of the copper-Schiff base complex was also immobilised within the pores of the Si-MCM 41 material.

6.3.6.3 Conclusion

The XPS analysis of the Cu-Schiff base MCM 41 materials (both the 8 h and the 20 h reaction time samples) proves that the copper-Schiff base complex was present both on the external surface and within the pores of the Si-MCM 41 material. The argon ion etching (4.5 nm from surface) showed that between 1/3 and 1/4 of the copper-Schiff base complex goes into the pores whilst the rest was either on the external surface or blocking the pores.

The copper concentration of 1.50 at% estimated by XPS for the Cu-Schiff-MCM-**1.0** (20) sample was in good agreement with the copper concentration determined using AAS (1.29 at%). However, the amount of copper detected for the Cu-Schiff-MCM-**0.25, -0.50, -0.75** and **-1.0** (8) samples were not found to vary with the Cu-Schiff base complex loading. Thus, XPS showed poor reproducibility in quantitative estimation, which made the investigation inconclusive with respect to quantitative determination of copper.

6.4 Sorption Studies: Results and Discussions

Sorption studies on each of the metal-Schiff base-modified samples were carried out to investigate changes in the surface characteristics and pore properties upon modification. Table 6.18 summarises the adsorptives, and the sorption conditions used to study the sorption properties of the modified samples.

Table 6.18 The adsorptives used for the measurement of sorption isotherms on the metal-Schiff base-modified samples

Adsorptive	Technique used for sorption	Molecular cross-sectional area of adsorptive / Å^2	Sorption temperature / K	Degassing time / h at 423 K
Nitrogen	Volumetric	16.2*	77	6
CO_2	Volumetric	17.0*	195	6
H_2O	Gravimetric	10.5*	303	1.5
MeOH	Gravimetric	18.0*	303	1.5
n-BuOH	Gravimetric	31.0†	303	1.5
t-BuOH	Gravimetric	31.9†	303	1.5
n-Hexane	Gravimetric	39.3†	303	1.5

* *Literature values*[28, 29, 30]

† *Derived from equation 2.9 (Chapter 2, Section 2.9.4)*

The sorption isotherms of nitrogen and carbon dioxide were measured on each of the metal-Schiff base-modified MCM 41 samples. In addition, the sorption isotherms of water, alcohols (MeOH, *n*-BuOH and *t*-BuOH) and *n*-hexane were obtained on two of the copper-Schiff base-modified MCM 41 samples. Table 6.19 summarises the different adsorptives used to study the sorption properties of each of the synthesised metal-Schiff base-modified MCM 41 materials. The sorption results of copper-Schiff base samples are discussed first followed by the results and discussion of iron- and nickel-Schiff base samples.

Table 6.19 Summary of the adsorptives used to study the sorption properties of each of the metal-Schiff base-modified MCM 41materials

Abbreviations used*	Volumetric sorption		Gravimetric sorption				
	N_2	CO_2	H_2O	*n*-Hexane	MeOH	*n*-BuOH	*t*-BuOH
Cu-Schiff-MCM-**0.25** (8)	✓	✓	✓	✓	✓	✓	✓
Cu-Schiff-MCM-**0.50** (8)	✓	✓					
Cu-Schiff-MCM-**0.75** (8)	✓	✓	✓	✓	✓	✓	✓
Cu-Schiff-MCM-**1.0** (8)	✓	✓					
Cu-Schiff-MCM-**1.0** (20)	✓	✓					
Fe(II)-Schiff-MCM-**0.25**	✓	✓					
Fe(II)-Schiff-MCM-**0.50**	✓	✓					
Fe(II)-Schiff-MCM-**0.75**	✓	✓					
Fe(II)-Schiff-MCM-**1.0**	✓	✓					
Fe(III)-Schiff-MCM-**0.25**	✓	✓					
Fe(III)-Schiff-MCM-**0.50**	✓	✓					
Fe(III)-Schiff-MCM-**0.75**	✓	✓					
Fe(III)-Schiff-MCM-**1.0**	✓	✓					
Ni-Schiff-MCM-**0.25**	✓	✓					
Ni-Schiff-MCM-**0.50**	✓	✓					
Ni-Schiff-MCM-**0.75**	✓	✓					
Ni-Schiff-MCM-**1.0**	✓	✓					

6.4.1 Copper-Schiff Base-modified Materials

Sorption isotherms were obtained on both the material synthesised with a reaction time of 20 h [Cu-Schiff-MCM-**1.0** (20)], and the materials synthesised with a reaction time

of 8 h [Cu-Schiff-MCM-**1.0** (8), Cu-Schiff-MCM-**0.75** (8), Cu-Schiff-MCM-**0.50** (8) and Cu-Schiff-MCM-**0.25** (8)] using different adsorptives (Table 6.19). The sorption results are summarised in Table 6.20.

Table 6.20 Sorption isotherm results for the Copper-Schiff base MCM 41 materials

Sample	**Adsorptive**	**Type of Isotherm**	**S_{BET} / $m^2 g^{-1}$**	**V_{pore} / $cm^3 g^{-1}$**	**Average pore diameter/ Å**	
					§	†
Si-MCM 41*	Nitrogen	IV	810	0.39	24	24
Cu-Schiff-MCM-**1.0** (20)	Nitrogen	I / IV	332	0.09	16	37
	CO_2	IV	294	0.20	--	--
Si-MCM 41	Nitrogen	IV	1150	0.74	26	--
	CO_2	IV	580	0.76	53	--
	H_2O	V	72	0.54	--	--
	MeOH	IV	640	0.70	--	--
	n-BuOH	IV	672	0.68	--	--
	t-BuOH	IV	840	0.69	--	--
	n-Hexane	?	800	0.57	--	--
Cu-Schiff-MCM-**1.0** (8)	Nitrogen	IV	825	0.34	17	20
	CO_2	IV	310	0.39	47	--
Cu-Schiff-MCM-**0.75** (8)	Nitrogen	I / IV	850	0.36	17	20
	CO_2	IV	280	0.32	43	--
	H_2O	V	--	0.26	--	--
	MeOH	IV	300	0.29	--	--
	n-BuOH	IV	450	0.33	--	--
	t-BuOH	IV	360	0.31	--	--
	n-Hexane	I	240	0.29	--	--
Cu-Schiff-MCM-**0.50** (8)	Nitrogen	IV	950	0.42	18	22
	CO_2	IV	325	0.45	53	--
Cu-Schiff-MCM-**0.25** (8)	Nitrogen	IV	1010	0.49	19	23
	CO_2	IV	425	0.58	51	--
	H_2O	V	--	0.32	--	--
	MeOH	IV	360	0.33	--	--
	n-BuOH	IV	575	0.48	--	--
	t-BuOH	IV	465	0.46	--	--
	n-Hexane	I	350	0.29	--	--

§ = *Pore diameter derived from Eq. 4V/(S_{sp} by BET),* † = *BJH mean pore diameter (Chapter 2, Section 2.10.7).*

* *Parent Si-MCM 41 material for the Cu-Schiff-MCM-**1.0** (20) was from different synthesis batch compared with the other Cu-Schiff base complex modified samples.*

6.4.1.1 Nitrogen Sorption

Nitrogen sorption isotherms at 77 K for the Cu-Schiff-MCM-**1.0** (20) material, the Cu-Schiff-MCM-**0.25**, -**0.50**, -**0.75** and -**1.0** (8) materials and the corresponding parent Si-MCM 41 materials are shown in Figs. 6.14 and 6.15, respectively.

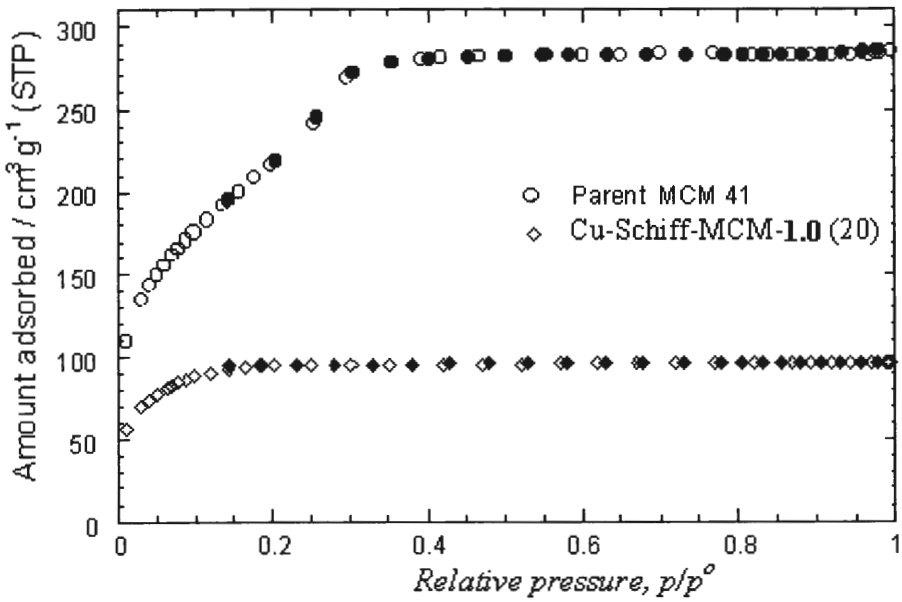

Figure 6.14 Nitrogen sorption isotherms (77 K) for the parent Si-MCM 41 and the Cu-Schiff-MCM-**1.0** (20) materials. Filled symbols denote desorption points.

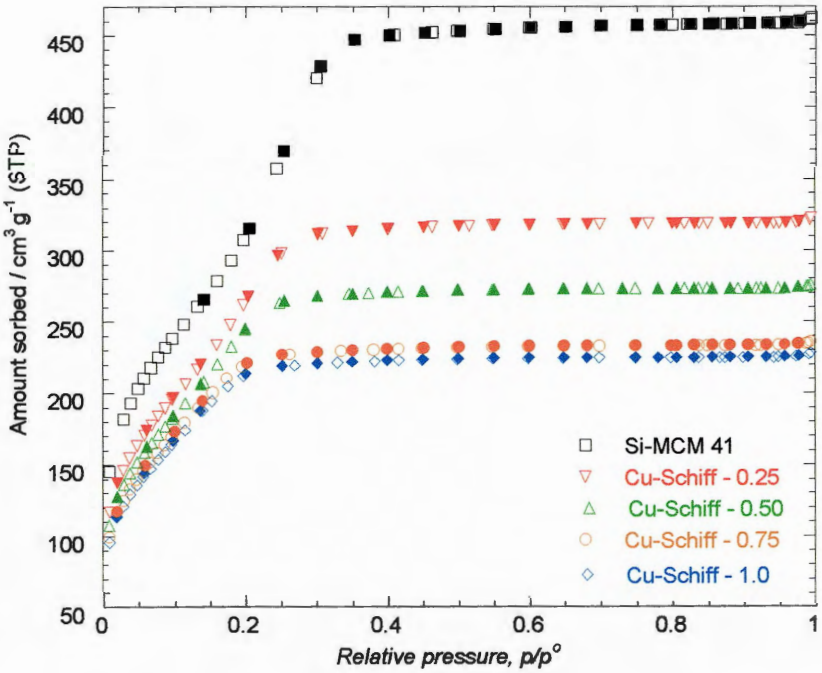

Figure 6.15 Nitrogen sorption isotherms (77 K) for the parent Si-MCM 41 and the copper-Schiff base-modified MCM 41 materials (reaction time 8 h). Filled symbols denote desorption points.

The Cu-Schiff-MCM-**1.0** (20) material yielded a Type I isotherm compared with the Type IV isotherm shown by the parent Si-MCM 41 material (Fig. 6.14). This suggests that modification of the material synthesised resulted in pore narrowing. The result was similar to that reported by Bambrough *et al.*[31, 32] for phenyl modified MCM 41 material. The step-wise rise in the amount of adsorbed nitrogen, caused by condensation in the mesopores was evident for the parent Si-MCM 41 material in the range $0.3 < p/p^o < 0.4$. In contrast, the Cu-Schiff-MCM-**1.0** (20) material shows no condensation step and showed a significant decrease in the surface area, pore volume and average pore diameter, summarised in Table 6.20.

On modification the average pore diameter (derived from $4V/S_{sp}$) was found to decrease from 24 Å to 16 Å. Assuming a cylindrical pore shape this would be expected

to correspond to a predicted decrease in pore volume from 0.39 cm^3g^{-1} to 0.17 cm^3g^{-1} on modification. However, the measured pore volume for the modified sample was only 0.09 cm^3g^{-1}, which suggested that a considerable pore-blocking has occurred in the Cu-Schiff-MCM-**1.0** (20) material.[27] Hence, a series of copper-Schiff base-modified materials were synthesised with short reaction time, *i.e.* 8 h in order to avoid pore blocking whilst achieving reasonable loading of the copper-Schiff base complex.

The average pore diameter determined by the BJH method was found to increase upon modification from 24 Å for the parent Si-MCM 41 material to 37 Å for the modified material. This was possibly due to the small pores, which contributed to the BJH pore diameter becoming blocked and the resulting pore diameter obtained corresponding to the average for unblocked and/or narrowed larger pores.

The materials with the target copper-Schiff base complex loadings of 0.25 and 0.50 mmol g^{-1} show Type IV isotherms, whereas the materials with 0.75 mmol g^{-1} and 1.0 mmol g^{-1} target loadings show isotherms to be intermediate between Type I and Type IV (Fig. 6.15). This suggested that increasing the amounts of immobilised copper-Schiff base complex led to a change in the nature of the porosity of the material. The complete filling of pores with adsorptive in the modified samples was achieved at lower p/p^o as compared with the parent Si-MCM 41, the greatest shift in p/p^o corresponds to the sample with the highest complex loading *i.e.* 1.0 mmol g^{-1}. This indicates a progressive narrowing of pores upon modification with increasing amounts of the immobilised copper-Schiff base complex.

A decrease in the surface areas and pore volumes with increasing amounts of copper complex loading was observed (Table 6.20), which suggested that more of the copper complex was immobilised within the pores of the samples with a higher copper-Schiff base complex loading.

A decrease in the average pore diameter (derived from $4V/S_{sp}$) upon modification (Table 6.20), which decreases further with increasing copper-Schiff base

complex loading, confirmed the narrowing of the pores as a result of immobilisation of complex within the pores. Although, the average pore diameters derived from BJH method were slightly higher than those obtained from *Eq. 4V/S*$_{sp}$ for the modified samples, a similar trend of a decrease in the average pore diameter with increasing copper complex loading was observed.

Fig. 6.16 shows a plot of the surface area and pore volume against actual copper loading as determined by AAS. The plot shows a reasonably linear relationship where an increase in the copper-Schiff base complex loading on the Si-MCM 41 material resulted in a decrease in the surface area and pore volume and confirmed that no significant pore blocking occurred in samples synthesised with a reaction time of 8 h. These changes in the pore parameters were expected because of the replacement of surface silanol groups[4, 33, 34] with the bulky copper-Schiff base complex.[27]

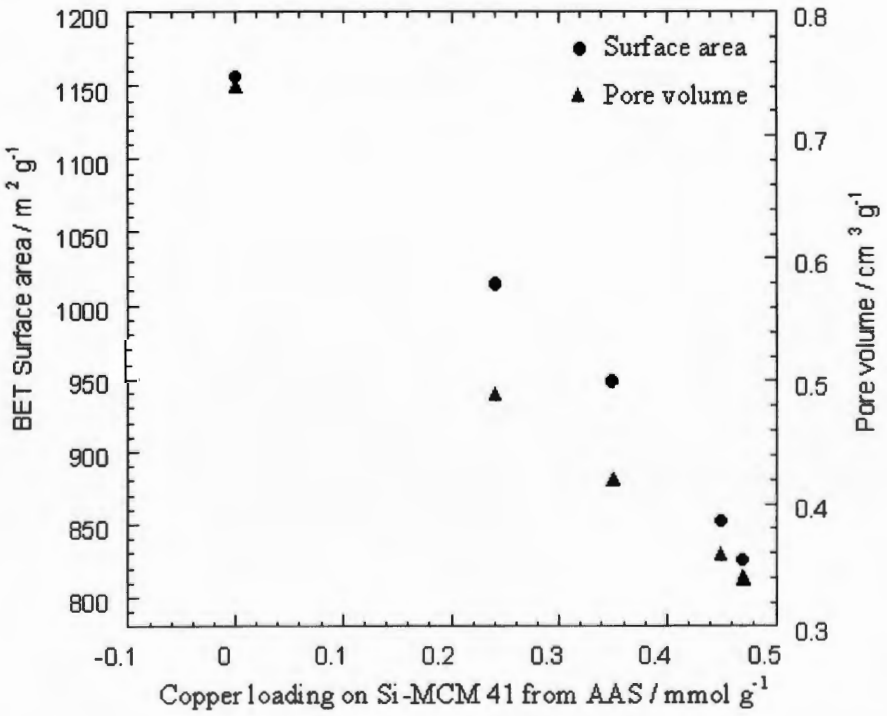

Figure 6.16 A plot showing the effect on the surface area and pore volume following functionalisation of the Si-MCM 41 surface with the copper-Schiff base complex.

α_s-Plot for the Nitrogen Sorption

The N_2 α_s-plots for the copper-Schiff base-modified samples are shown in Fig. 6.17.

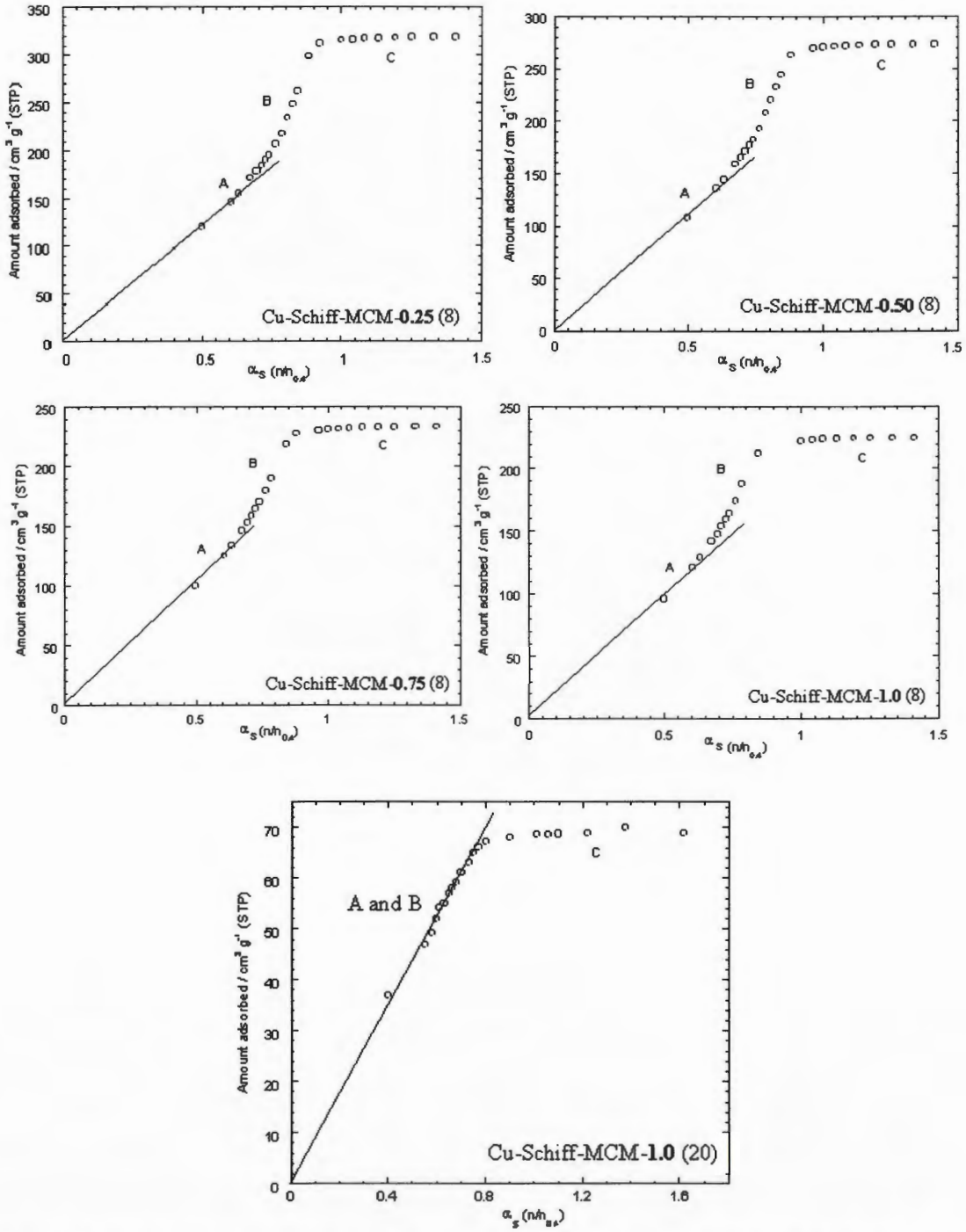

Figure 6.17 Nitrogen sorption α_s-plots for the copper-Schiff base-modified MCM 41 materials.

The α_s-plots for the Cu-Schiff-MCM-**0.25**, **-0.50**, **-0.75** and **-1.0** (8) exhibit three well-defined regions similar to that of the parent Si-MCM 41 material (see Chapter 3, Fig. 3.14):

- Region *A*, a linear region from 0.4 to 0.7 on a α_s scale, due to the monolayer-multilayer adsorption on the pore walls and the external surface.
- Region *B*, region between 0.75 to 1.0 on a α_s scale, which shows deviation from the standard isotherm, due to the capillary condensation in the mesopores.
- Region *C*, a linear region of the plot between 1.0 to 1.6 on a α_s scale, which corresponds to multilayer adsorption on the external surface.

The extrapolation of region *A* to the origin confirmed the absence of any detectable micropore filling in the samples at low p/p^o.[28, 35, 36] This indicated that even after immobilisation of the copper-Schiff base complex the pores present in the material are in mesoporous range. The shallow slope of region *C* compared with region *A* confirmed that the material had little external surface.

The α_s-plot for the Cu-Schiff-MCM-**1.0** (20) material was different from the other Cu-Schiff base modified samples. Regions *A* and *B* in the α_s-plot for the Cu-Schiff-MCM-**1.0** (20) were found to merge indicating the absence of significant condensation in the pores. This confirmed that the pores had become blocked with complex in this sample.

6.4.1.2 Carbon Dioxide Sorption

Carbon dioxide sorption isotherms at 195 K for the Cu-Schiff-MCM-**0.25**, **-0.50**, **-0.75** and **-1.0** (8) materials and the parent Si-MCM 41 material, and the Cu-Schiff-MCM-**1.0** (20) material are shown in Figs. 6.18 and 6.19, respectively.

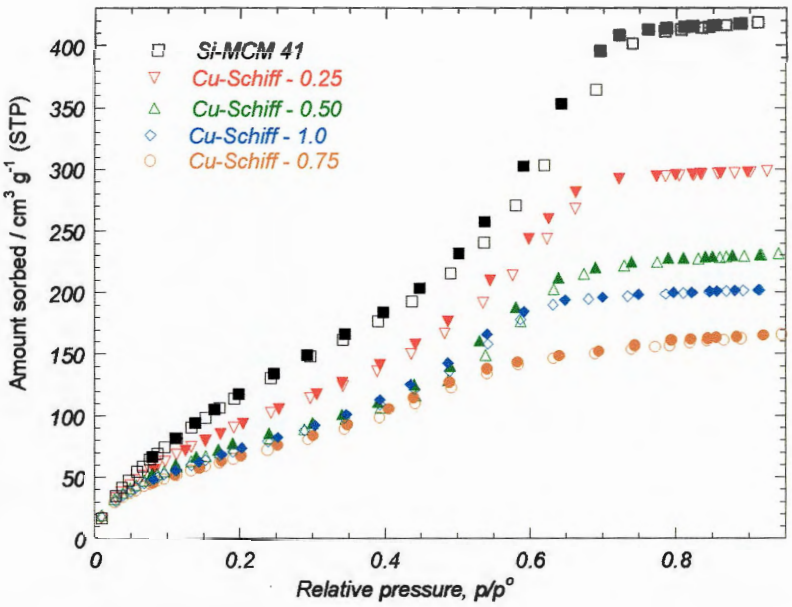

Figure 6.18 Carbon dioxide sorption isotherms (195 K) for the parent Si-MCM 41 and the copper-Schiff base-modified MCM 41 materials (reaction time 8 h). Filled symbols denote desorption points. Sample Cu-Schiff-0.75 was used from water sorption and hence shows smaller amount of total CO_2 adsorbed compared with Cu-Schiff-1.0.

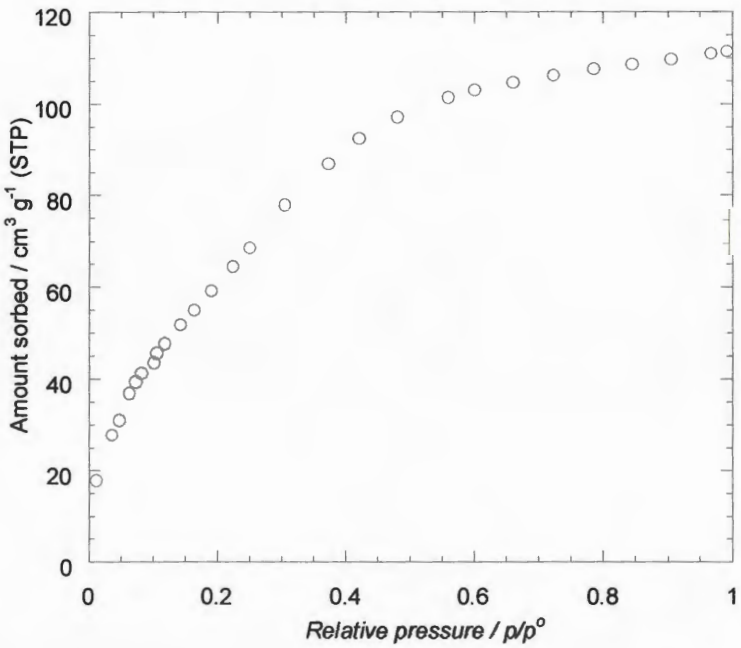

Figure 6.19 Carbon dioxide sorption isotherm (195 K) for the Cu-Schiff-MCM-**1.0** (20) material.

The carbon dioxide sorption for the Cu-Schiff-MCM-**0.25**, **-0.50**, **-0.75** and **-1.0** (8) materials yielded Type IV isotherms (Fig. 6.18), which indicated that the materials synthesised were in the mesoporous range. A shift in the capillary condensation step towards a high relative pressure (p/p^o *ca.* between 0.5 and 0.7) compared with that of the nitrogen sorption (p/p^o = between 0.2 and 0.3) was observed. The complete filling of pores shifts towards lower p/p^o as the copper-Schiff base complex loading increases from 0.25 to 1.0 mmol g^{-1}. This confirmed the narrowing of pores upon modification. The CO_2 sorption isotherm displays a Type H1 hysteresis loop[37] (Chapter 2, Section 2.9.2) in contrast to the nitrogen sorption isotherm, where no hysteresis was observed.

The CO_2 sorption isotherms for the 8 h reaction time samples were obtained with an increased equilibration time of 15 s as the isotherms obtained with an equilibration time of 5 s showed improbable negative hysteresis (not shown here). This indicated that sorption of CO_2 may be diffusion controlled, possibly due to the slower diffusion of the CO_2 molecules in the smaller pores or due to its affinity for the polar sites present on the surface. In the case of nitrogen sorption, isotherms obtained with equilibration times of 5 s were identical to those measured with an equilibration time of 15 s.

The carbon dioxide sorption isotherm for the Cu-Schiff-MCM-**1.0** (20) sample (Fig. 6.19) was difficult to classify according to the IUPAC classification[35] and is intermediate between Type II and Type IV. Although, no sharp condensation step is observed, the isotherm shows a gradual increase in the adsorbed CO_2 with increasing pressure, in the range $0.15 < p/p^o < 0.45$, which levels off at p/p^o of 0.60.

Similar to the nitrogen sorption, a decrease in surface area and pore volume upon modification was observed, which decreases further with increasing amounts of the copper-Schiff base complex loading. The results are summarised in Table 6.20. The Gurvitsch pore volumes derived from the CO_2 sorption for each of the samples

were in good agreement with the N_2 derived pore volumes. However, it should be noted that the CO_2 density at 273 K was used in the calculation. The Cu-Schiff-MCM-**1.0** (20) sample showed a higher CO_2 derived Gurvitsch pore volume compared with the N_2 derived value. This may possibly be explained by the activated adsorption of CO_2 at 195 K into the narrowed pores, which N_2 at 77 K cannot access. The sample Cu-Schiff MCM-**0.75** was used from water sorption and hence shows smaller Gurvitch pore volume compared with Cu-Schiff MCM-**1.0**.

The CO_2 derived surface areas were all found to be much smaller than the surface area derived from N_2 sorption (Table 6.20). This may be due to the polar interaction of CO_2 with the MCM 41 surface, which resulted in site-specific adsorption rather than monolayer formation.[35] This was supported by the occurrence of the capillary condensation within pores at higher p/p^o compared with nitrogen sorption. The results obtained were similar to those observed for the organically-modified samples (Chapter 5, Section 5.3.2).

The ratio of CO_2 surface area to nitrogen surface area was 1:2 for the unmodified (Si-MCM 41) sample and between 1:3 and 1:4 for the copper-Schiff base-modified samples. This difference may be explained as, upon modification, some of the surface hydroxyl groups being used up in tethering of the copper-Schiff base complex and hence the surface polarity changes, which affects the adsorption of CO_2 on surface. This may tentatively be explained as the change in surface polarity decreasing the initial adsorption of CO_2, thus, the 'monolayer formation', which resulted in a decrease in the calculated surface area. This explanation is supported by the q^{st} (isosteric heat of adsorption) data (Table 6.21) and the plot (Fig.6.22), which shows higher q^{st} values at low CO_2 coverage for the modified samples compared with unmodified samples. The q^{st} value remains constant at high CO_2 coverage.

α_s-Plot for the Carbon Dioxide Sorption

The α_s-plots for the carbon dioxide sorption by copper-Schiff base modified MCM 41 materials are shown in Fig. 6.20. The plots show three well-defined regions corresponding to the initial adsorption of CO_2 on a surface due to "monolayer formation" (region *A*), an increase in the adsorbed CO_2 due to capillary condensation in the mesopores (*B*), and multilayer formation (*C*) after complete filling of the pores, similar to that of the parent Si-MCM 41 material (Chapter 3, Fig. 3.14).

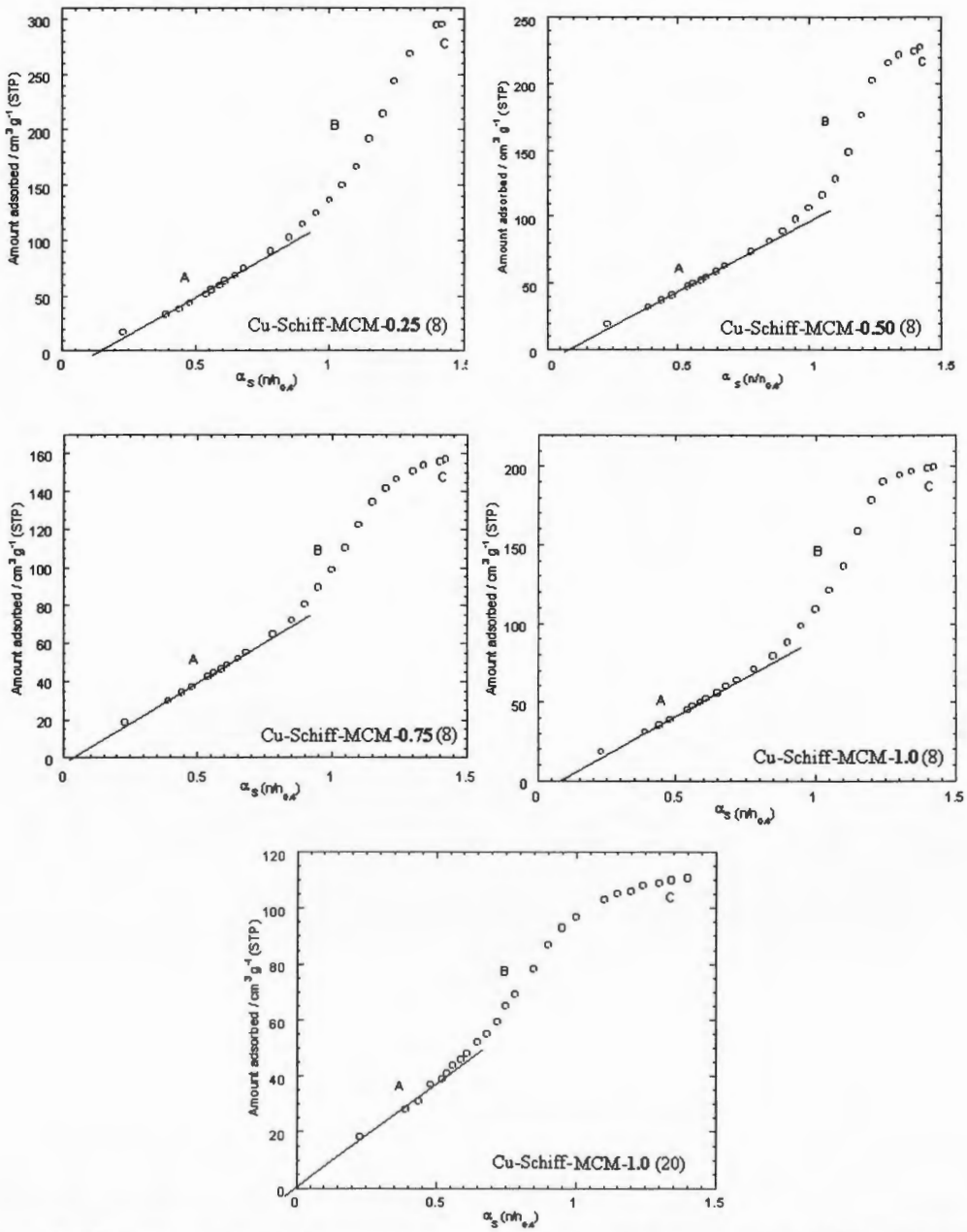

Figure 6.20 Carbon dioxide sorption α_s-plots for the copper-Schiff base-modified MCM 41 materials.

The presence of region *B* in the α_s-plot for each of the samples confirmed the presence of mesopores in the material.[28, 35, 36] However, the inflection due to capillary condensation is not as sharp as that observed in the nitrogen α_s-plots (Fig 6.17). The linear region *A*, when extrapolated (to $\alpha_s = 0$) passes through the origin for Cu-Schiff-MCM-**1.0** (20) sample though a small negative intercept on the y-axis is observed for the 8 h Cu-Schiff base MCM 41 material. This near zero intercepts suggests the lack of micropores in the materials, whereas the negative intercept usually indicates lack of monolayer formation.[35]

iii) Isosteric Heat of Adsorption

CO_2 adsorption isotherms at elevated temperatures of 273 K and 286 K for the Cu-Schiff-MCM-**1.0** (8) and Cu-Schiff-MCM-**0.25** (8) samples are shown in Fig. 6.21.

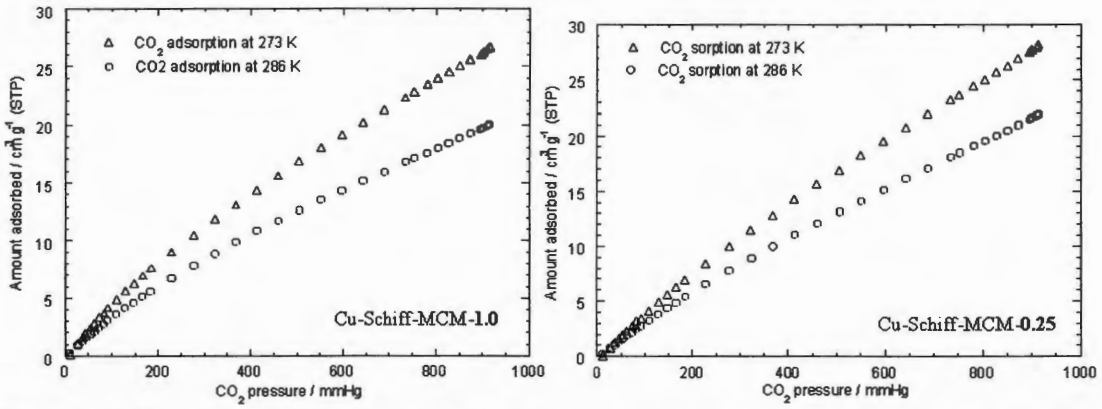

Figure 6.21 CO_2 adsorption isotherms (273 K and 286 K) for the Cu-Schiff-MCM-**1.0** (8) and Cu-Schiff-MCM-**0.25** (8) samples.

At these elevated temperatures the isotherms correspond to only a narrow low relative pressure range, $0 < p/p^o$ 0.03, of the CO_2 sorption isotherm obtained at 195 K. A decrease in CO_2 uptake with increase in temperature (from 273 to 286 K) was observed as expected.

The isosteric heat of adsorption data are summarised in Table 6.21. Fig. 6.22 shows a plot of the variation of the isosteric heat of adsorption, q^{st}, with surface coverage for the adsorption of CO_2 on the Si-MCM 41, Cu-Schiff-MCM-**0.25** (8) and Cu-Schiff-MCM-**1.0** (8) materials.

Table 6.21 Isosteric heat of adsorption values at different surface coverage of CO_2 on the parent Si-MCM 41, Cu-Schiff-MCM-**0.25** (8) and Cu-Schiff-MCM-**1.0** (8) samples.

Surface coverage of CO_2 / mmol g^{-1}	0.018	0.04	0.115	0.148	0.165
q^{st} / kJ mol^{-1} for Si-MCM 41	7.5	12.5	15.0	15.5	15.6
q^{st} / kJ mol^{-1} for Cu-Schiff-MCM-0.25	11.4	14.3	14.7	15.0	16.2
q^{st} / kJ mol^{-1} for Cu-Schiff-MCM-1.0	14.4	17.8	18.4	19.7	17.6

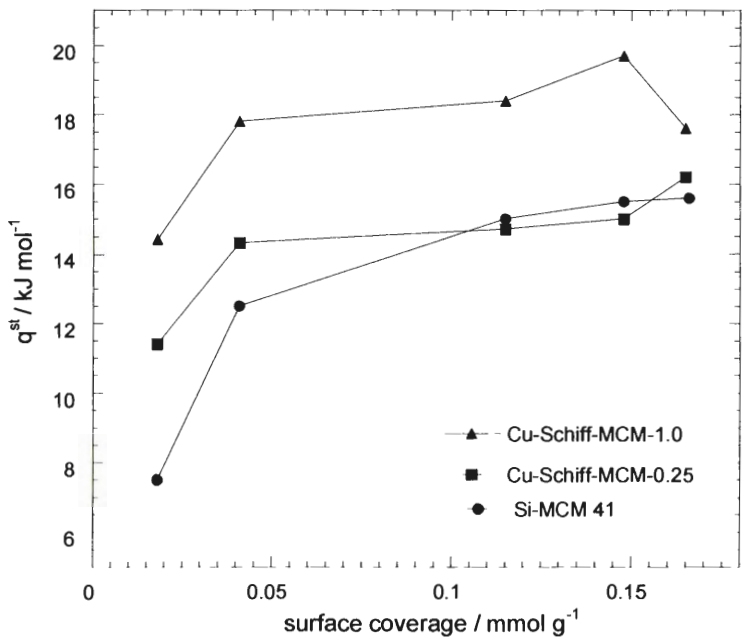

Figure 6.22 Variation of isosteric heat of adsorption, q^{st}, with surface coverage for the adsorption of CO_2 on the parent Si-MCM 41, Cu-Schiff-MCM-**0.25** (8) and Cu-Schiff-MCM-**1.0** (8) samples.

The isosteric heat of adsorption for Cu-Schiff-MCM-**1.0** (8) was higher as compared with those for the Cu-Schiff-MCM-**0.25** (8) and the unmodified MCM 41 materials. This suggested stronger interaction of CO_2 molecules with the sorption sites for surface coverage of up to 0.15 mmol g^{-1} in the Cu-Schiff-MCM-**1.0** (8) sample. However, at the higher CO_2 coverage of 0.165 mmol g^{-1} the isosteric heat of adsorption for all the samples approached values in the range 15 to 18 kJ mol^{-1} (Table 6.21) due to the interaction between CO_2 molecules. The q^{st} values obtained are lower than the theoretically estimated value of 28 kJ mol^{-1} for silicalite.[38] A drop in the heat of sorption from 28 to 22 kJ mol^{-1} and from 28 to 20 kJ mol^{-1} at a low loading of 0.12 mmol g^{-1} was reported by Graham *et al.*[39] and Choudhary *et al.*[40], respectively. However, it should be noted that in this work the CO_2 adsorption was measured at pressures less than one atmosphere compared with the high-pressure adsorption reported by other workers.[39, 40]

6.4.1.3 Water Sorption

The water sorption isotherms (303 K) on the Cu-Schiff-MCM-**0.25** (8) and Cu-Schiff-MCM-**0.75** (8) materials were of Type V similar to that observed for the parent Si-MCM 41 material as shown in Fig. 6.23. This confirmed the hydrophobic nature of the surface. The isotherms show low initial adsorption due to weak adsorbent-adsorbate interaction in the range $0 < p/p^o$ 0.45. However, the adsorption of water in this pressure range was higher for the modified samples compared with the parent Si-MCM 41 material. This suggested that there was a slight decrease in the hydrophobicity upon modification. As for the parent material, capillary condensation was observed at higher relative pressure in the range $0.45 < p/p^o < 0.70$ compared with N_2 sorption, which confirmed the mesoporosity of the material. However, a decrease in the pore volume (Table 6.20) upon modification was observed, which suggested that the copper-Schiff

base complexes were immobilised within the pores. The water derived Gurvitsch pore volumes were found to be lower than the nitrogen derived pore volumes similar to that reported by other workers.[28, 29, 36] This behaviour may be explained[35] as the adsorbed water within the pores may exist in a less dense form compared with the ordinary water due to the differences in hydrogen bonding arrangements.

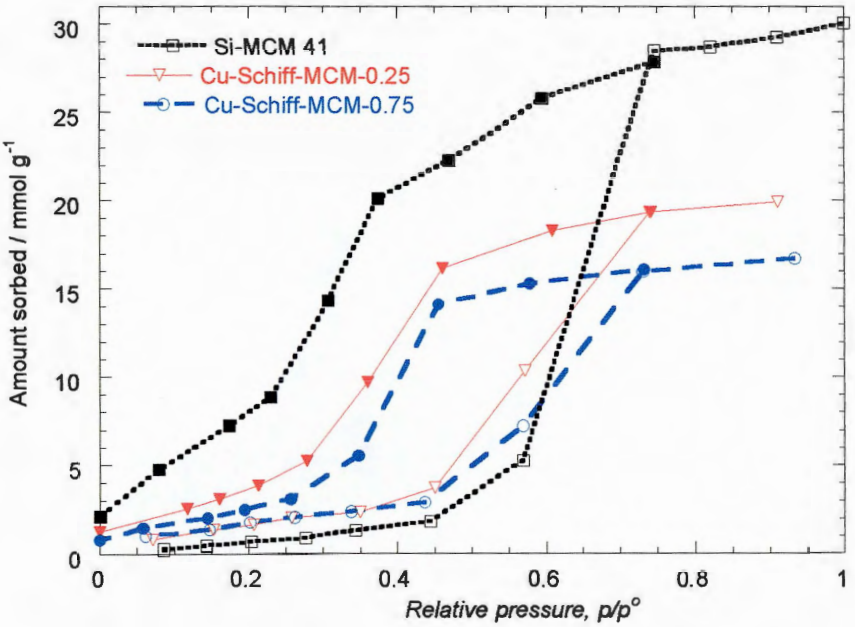

Figure 6.23 Water sorption isotherms (303 K) for the Cu-Schiff-MCM-**0.25** (8), Cu-Schiff-MCM-**0.75** (8) and parent Si-MCM 41 materials. Filled symbols denote desorption points.

The modified samples show non-reversible isotherms similar to that of the parent Si-MCM 41 material, with a hysteresis extending over a low-pressure region, which does not close even after exposing the samples to vacuum (*ca.* 10^{-5} torr). This suggested that the water remains on the surface probably as a result of rehydroxylation of the surface *i.e.* chemisorption of the water on the sample surface. The extent of this chemisorption of water was found to decrease with increase in the copper-Schiff base complex loading. This suggested that with increasing amounts of the copper-Schiff base

complex loading, the number of hydroxyl groups present on the surface decreased (Table 6.22) as a result of reaction *i.e.* by chemical tethering of the metal complex.

A slight increase in the BET monolayer capacity of the modified samples compared with that of parent-Si-MCM 41 was observed (Table 6.22). This was thought to be due to the copper-Schiff base complex masking the silica surface of the modified samples giving rise to a slight increase in the hydrophilic property of the surface of the modified samples.

Table 6.22 Summary of the water derived values of chemisorption, number of hydroxyl groups and monolayer capacity for the parent Si-MCM 41, Cu-Schiff-MCM-**0.25** (8) and Cu-Schiff-MCM-**0.75** (8) samples

Sample	**Chemisorption* / mmol g^{-1}**	**Number of –OH groups / nm^2**		**Monolayer† capacity / mmol g^{-1}**
		§	‡	
Si-MCM 41	2.0	1.0	0.63	1.2
Cu-Schiff-MCM-**0.25** (8)	1.2	0.7	1.1	1.9
Cu-Schiff-MCM-**0.75** (8)	0.8	0.6	1.3	1.8

* *Value after complete desorption and exposing to a vacuum of* $< 10^{-5}$ *torr.*
‡ *Hydroxyl groups derived from monolayer capacity.*
§ *Hydroxyl groups derived from chemisorption of the adsorptive.*
† *Water sorption derived monolayer capacity calculated from the BET plot.*

6.4.1.4 n-Hexane Sorption

The sorption isotherms of the *n*-hexane at 303 K on the Cu-Schiff-MCM-**0.25** (8), Cu-Schiff-MCM-**0.75** (8) and parent Si-MCM 41 materials are shown in Fig. 6.24.

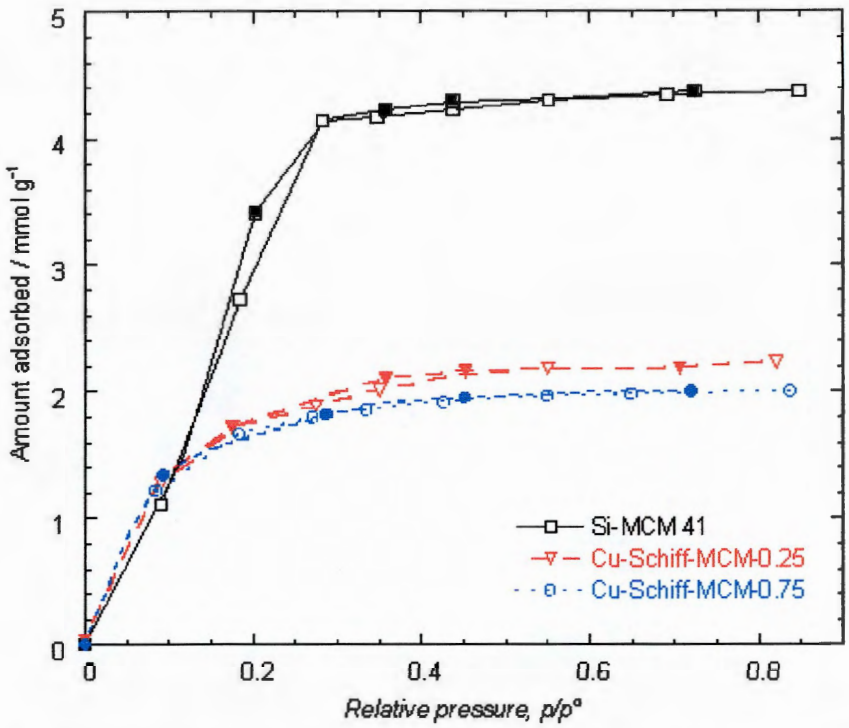

Figure 6.24 *n*-Hexane sorption isotherms (303 K) for the Cu-Schiff-MCM-**0.25** (8), Cu-Schiff-MCM-**0.75** (8) and parent Si-MCM 41 materials. Filled symbols denote desorption points.

The isotherms of the modified materials were found to be of Type I, whereas the isotherm of the parent Si-MCM 41 material was difficult to classify according to the IUPAC[35] classification. The isotherm for the parent Si-MCM 41 shows low initial uptake of the *n*-hexane in the range $0 < p/p^o < 0.15$, although a Type I isotherm with high initial uptake was expected. This indicated the restricted diffusion of *n*-hexane on the hydrophobic surface within the pores of the Si-MCM 41 material and was similar to the work reported by other workers.[37] The initial adsorption in the range $0 < p/p^o < 0.1$ was found to be similar for both the parent Si-MCM 41 and the modified samples, which indicated increase in the organophilic nature of the surface following modification.[41] The lower uptake of the *n*-hexane in the range $0.10 < p/p^o < 0.25$ and the smaller pore volumes for the modified samples compared with the parent Si-MCM 41 material confirmed the immobilisation of the copper-Schiff base complex within the pores.

All the isotherms were found to be reversible with no evident hysteresis loop, similar to that of the parent Si-MCM 41 material. No chemisorption of *n*-hexane on the surface was observed, as expected. The Gurvitsch pore volume obtained was lower than those derived from other adsorptives apart from water (See Table 6.20). A possible explanation for this could be that the adsorption of *n*-hexane molecules is sterically hindered, *i.e.* the size and the shape (long chain) of hexane might restrict easy access of the molecules into the pores and affect the close packing of the molecules. The validity of the BET derived parameters from hexane adsorption are unreliable, since the BET plots were non-linear in the range 0.05 p/p^o 0.35, and therefore it was not possible to determine the n_m values accurately nor the corresponding surface areas. The calculated BET surface areas shown in Table 6.20 should therefore be interpreted with caution.

6.4.1.5 Sorption of Alcohols (MeOH, n-BuOH and t-BuOH)

Sorption of alcohols at 303 K was carried out on the Cu-Schiff-MCM-**0.25** (8) and Cu-Schiff-MCM-**0.75** (8) materials and the sorption data are summarised in Table 6.20.

The alcohol isomers, *n*-BuOH and *t*-BuOH, a long chain molecule and a 'spherical shape' molecule, respectively, are useful sorption probes for both shape sensitivity and whether the adsorption proceeds *via* the organophilic or hydrophilic interaction with the surface. The alcohols sorption isotherms are compared with the two 'extremes' *i.e.* water sorption isotherms showing the extent of hydrophilic interaction and *n*-hexane sorption isotherm showing organophilic interaction.

i) Methanol (MeOH) Sorption

Methanol sorption (303 K) on the Cu-Schiff-MCM-**0.25** (8) and Cu-Schiff-MCM-**0.75** (8) samples yielded a Type IV isotherm (Fig. 6.25), similar to that of the parent Si-MCM 41 material.

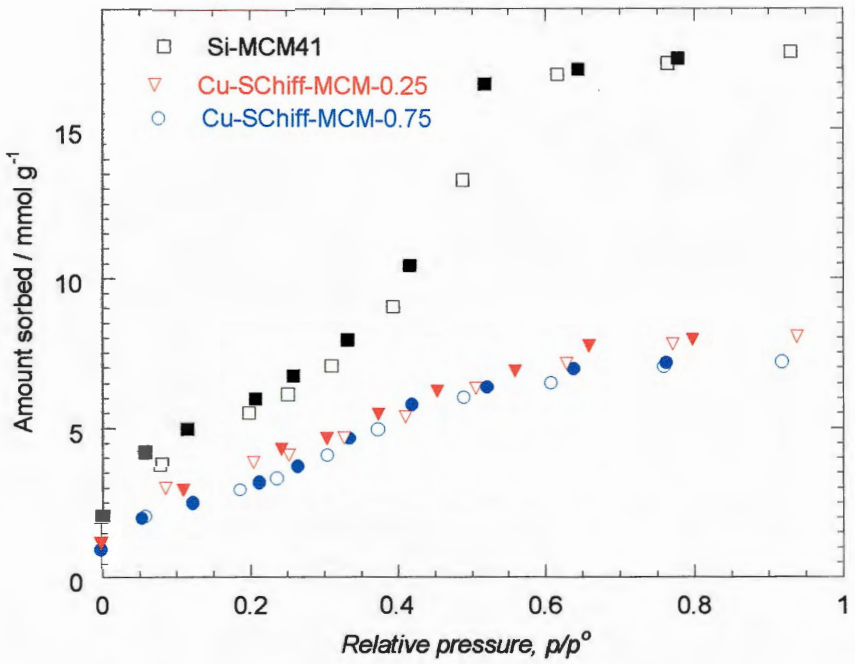

Figure 6.25 Methanol sorption isotherms (303 K) for the Cu-Schiff-MCM-**0.25** (8), Cu-Schiff-MCM-**0.75** (8) and parent Si-MCM 41 materials. Filled symbols denote desorption points.

The isotherms for the modified samples showed a significant decrease in the total uptake of MeOH compared with the parent Si-MCM 41 material, which confirmed the immobilisation of the copper-Schiff base complex within the pores. A sharp capillary condensation step is evident in the isotherm of the parent Si-MCM 41 material, whereas the modified samples showed a gradual increase in the adsorbed methanol with increasing pressure. All the isotherms level off at p/p^o *ca.* 0.6 indicating complete filling of pores by methanol adsorbate.

The isotherm for each of the samples shows a well defined knee at p/p^o *ca.* 0.05, and the calculated BET monolayer capacity, n_m, (Table 6.23) was found to be higher than those obtained from the water sorption. The isotherms were reversible with no hysteresis loop, which was in contrast to the water sorption isotherm where a large degree of hysteresis was observed throughout the isotherm. These results suggested that

the sorption of methanol involved predominantly organophilic interaction leading to monolayer formation.

Table 6.23 Summary of the amount of chemisorption, monolayer capacity and number of hydroxyl groups calculated for different sorptives on the Cu-Schiff-MCM-**0.25** (8), Cu-Schiff- MCM-**0.75** (8) and Si-MCM 41 materials

Sample	**Adsorptive**	**Chemisorption* / mmol g^{-1}**	**Monolayer† capacity / mmol g^{-1}**	**Number of -OH groups / nm^2**	
				‡	§
Si-MCM 41	Nitrogen	no	11.9	--	--
	H_2O	2.0	1.2	0.63	1.0
	MeOH	2.0	5.9	3.0♦	1.0
	n-BuOH	2.8	3.6	1.9♦	1.5
	t-BuOH	2.0	4.4	2.3♦	1.0
	n-Hexane	no	3.4	--	--
Cu-Schiff-MCM-**0.25** (8)	Nitrogen	no	10.4	--	--
	H_2O	1.2	1.9	1.1	0.7
	MeOH	1.2	3.3	1.9♦	0.7
	n-BuOH	1.6	2.5	1.5♦	1.0
	t-BuOH	1.0	3.0	1.8♦	0.7
	n-Hexane	no	1.5	--	--
Cu-Schiff-MCM-**0.75** (8)	Nitrogen	no	8.7	--	--
	H_2O	0.8	1.8	1.3	0.6
	MeOH	1.0	2.8	2.0♦	0.7
	n-BuOH	1.2	1.9	1.3♦	0.8
	t-BuOH	0.9	2.4	1.7♦	0.6
	n-Hexane	no	1.0	--	--

* *Value after complete desorption and exposing to a vacuum of* $< 10^{-5}$ *torr.*
† *Monolayer capacity derived from the BET plot.*
‡ *Hydroxyl groups derived from the monolayer capacity.*
♦ *Values assumes both organophilic and hydroxyl group interactions.*
§ *Hydroxyl groups derived from the chemisorption of adsorptive.*

Using the BET n_m values, the methanol derived specific surface area (Table 6.20) was found to be significantly lower than that obtained from nitrogen

sorption. This indicated that the sorption of methanol on a sample surface was highly specific giving rise to a lower BET derived surface area. The desorption branch of the isotherms did not close even after exposing the samples to high vacuum (10^{-5} torr), indicating chemisorption of methanol on the sample surface. The number of hydroxyl groups (*i.e.* the total number of –OH groups present after sorption) calculated from the chemisorption values for each of the samples was in good agreement with the number of hydroxyl groups derived from the water sorption (Table 6.23). A decrease in the number of hydroxyl groups upon modification indicated that some of the surface -OH / siloxane groups had been used up in immobilization of metal-Schiff base complex.

ii) n-Butanol (n-BuOH) Sorption

The sorption isotherms of *n*-BuOH (303 K) on the Cu-Schiff-MCM-**0.25** (8), Cu-Schiff-MCM-**0.75** (8) and Si-MCM 41 materials yielded Type IV isotherm as shown in Fig. 6.26. Similar to the results obtained from other adsorptives, the isotherms of the modified samples yielded a significant decrease in the surface area and pore volume (Table 6.20), confirming the immobilisation of the copper-Schiff base complex within the pores of the Si-MCM 41 material. The isotherms show a large degree of hysteresis extending to the low-pressure region, which does not close. This is similar to the hysteresis observed in the water sorption isotherms and is in contrast with the methanol sorption isotherms, where no hysteresis was observed. The similarity with water sorption suggested that the adsorption of *n*-BuOH occurred predominantly *via* polar interaction with the surface hydroxyls.

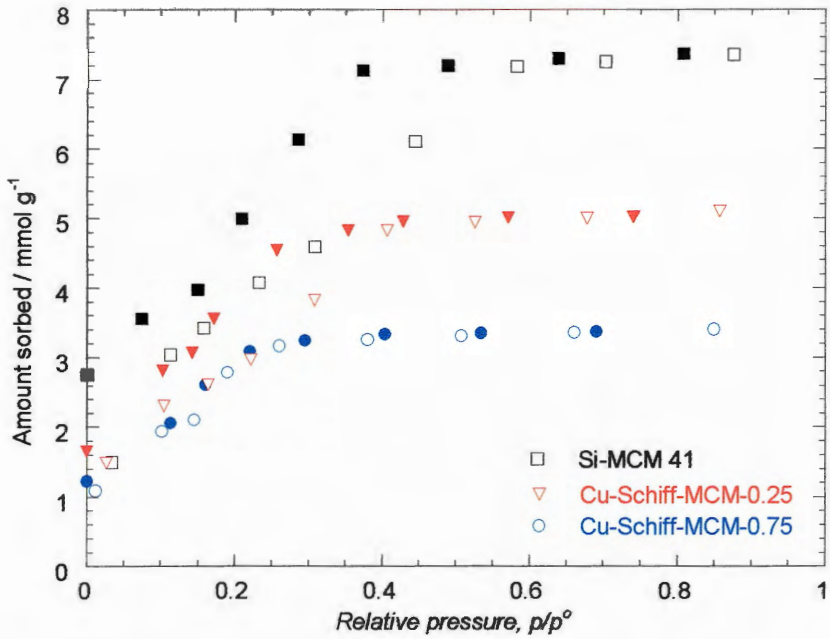

Figure 6.26 *n*-Butanol sorption isotherms (303 K) for the Cu-Schiff-MCM-**0.25** (8), Cu-Schiff-MCM-**0.75** (8) and parent Si-MCM 41 materials. Filled symbols denote desorption points.

The *n*-BuOH derived BET surface area was found to be smaller than the nitrogen derived surface area. It is important to note that in this instance the calculation of specific surface area was performed using a calculated value for the molecular area, a_m = 31 Å^2, (Chapter 2, *Eq.* 2.14). This equation assumes spherical molecules and hexagonal packing, which is inaccurate in the case of *n*-BuOH (a long chain alcohol).[29, 42] For this reason, it is the monolayer capacity, which is of real interest here. The *n*-butanol derived n_m values (Table 6.23) for each of the samples were smaller than the methanol derived n_m values. This may be because the larger size (long chain) of the *n*-butanol molecule hinders access to adsorption sites by lying across them preventing further adsorption.[42] However, the n_m values were higher than the water derived n_m values, which suggested that the organic end of the molecule was also involved in adsorption of *n*-BuOH on the sample surface. The amount of *n*-BuOH chemisorbed on

the surface and the number of hydroxyl groups calculated from the chemisorption, assuming that one *n*-BuOH will adsorb on one surface hydroxyl / siloxane groups, were unexpectedly higher for each of the samples than those obtained from the other adsorptives (Table 6.23).

iii) t-Butanol (t-BuOH) Sorption

The sorption of *t*-BuOH at 303 K on the Cu-Schiff-MCM-**0.25** (8), Cu-Schiff-MCM-**0.75** (8) and Si-MCM 41 samples yielded Type IV isotherms (Fig. 6.27), which confirmed the mesoporosity of the material.

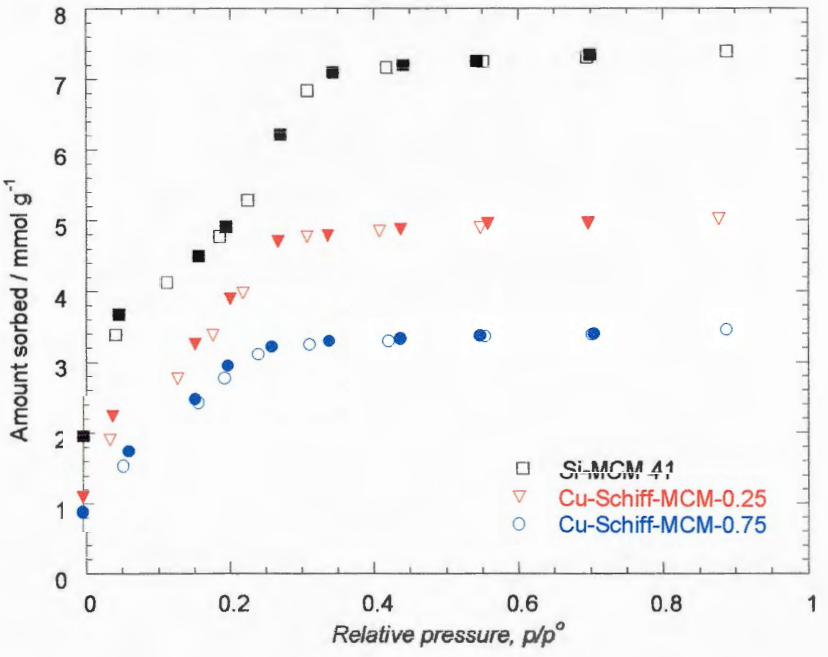

Figure 6.27 *t*-Butanol sorption isotherms (303 K) for the Cu-Schiff-MCM-**0.25** (8), Cu-Schiff-MCM-**0.75** (8) and parent Si-MCM 41 materials. Filled symbols denote desorption points.

The modified samples showed a decrease in the surface area and pore volume (Table 6.20), similar to that observed from other adsorptives, which confirmed the immobilisation of the copper-Schiff base complex within the pores of the Si-MCM 41

material. The complete filling of the pores, in the modified samples, was achieved at low relative pressure compared with the unmodified Si-MCM 41 material, which indicated narrowing of the pores upon modification.

The isotherms for each of the materials show a well-defined knee at low p/p^o *ca.* 0.05 and the corresponding BET surface areas (Table 6.20) are much higher than those derived from methanol adsorption, despite the bulky size of *t*-BuOH molecule. This suggested that the sorption of *t*-BuOH was predominantly favored *via* the organic part of the molecule as the -OH groups in *t*-BuOH are embedded in the bulky methyl groups and are not readily available for the polar interaction with the surface hydroxyls. However, the *t*-BuOH derived surface areas were found to be smaller when compared with the nitrogen-derived values. This may be explained by the larger size and cross-sectional area of the *t*-BuOH molecule resulting in steric hindrance in the close packing of the molecules.

The isotherms for each of the samples were reversible with no hysteresis, similar to the methanol isotherms but were in contrast with the sorption isotherms of water and *n*-butanol, where a large degree of hysteresis was observed. However, the desorption branch of the isotherm does not close and shows chemisorption of *t*-BuOH on the surface hydroxyls, as shown by other adsorptives (water, MeOH and *n*-BuOH). The number of surface hydroxyl groups derived from the chemisorption of *t*-BuOH was in good agreement with the water and MeOH derived values (Table 6.23). A decrease in number of surface hydroxyl groups upon modification suggested that some of the hydroxyl groups were used in chemical tethering of the copper complex on the surface. However, the key factor to note is that the chemisorption value (1.0 nm^2) derived from *t*-BuOH was similar to those derived from water and methanol. This may be explained as following its initial adsorption on surface *via* organophilic interaction the *t*-BuOH molecule hydrophillicaly interacts with the surface hydroxyls / siloxane groups and showed chemisorption.

The *t*-BuOH derived BET n_m values for each of the samples were only slightly lower than those obtained from MeOH, possibly due to the bulky size of the *t*-BuOH molecule, but were higher than those obtained from the *n*-BuOH. This indicated that the initial adsorption of *t*-BuOH on a surface predominantly occurred *via* organophilic interaction compared with the *n*-BuOH (where a polar interaction with the surface hydroxyls was assumed) as the –OH groups in the *t*-BuOH molecules are sterically hindered within the bulky methyl groups for polar interaction.[42] The lower n_m values of *n*-BuOH compared with other adsorptives also indicated that the sorption of *n*-BuOH is more sterically hindered.

The comparison plot of all the adsorptives, water, MeOH, *n*-BuOH, *t*-BuOH and *n*-hexane, for the Si-MCM 41 material is shown in Fig. 6.28.

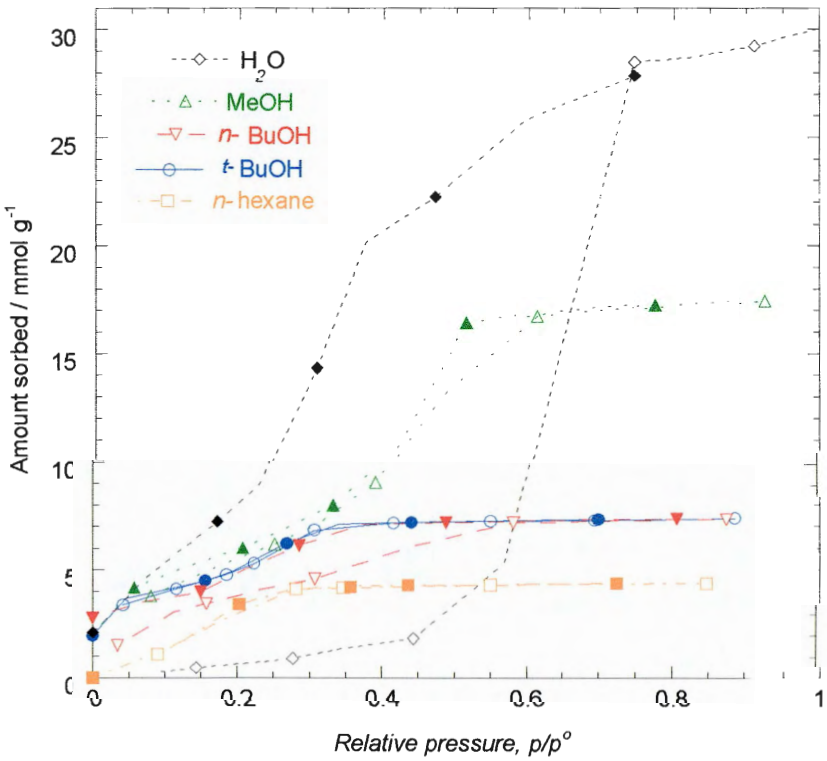

Figure 6.28 Water, MeOH, *n*-BuOH, *t*-BuOH and *n*-hexane sorption isotherms (303 K) for the Si-MCM 41 material. Filled symbols denote desorption points.

In conclusion, the sorption isotherms of all the adsorptives confirmed the immobilisation of the copper-Schiff base complex within the pores of the Si-MCM 41 material. The adsorption of water molecules on the surface was found to occur initially *via* polar interaction with the surface hydroxyls. In contrast, the nature of the *n*-hexane sorption confirmed the high organophilic character of the surface. The adsorptions of MeOH, *n*-BuOH and *t*-BuOH were found to be intermediate in character between water and *n*-hexane sorption *i.e.* showing adsorption both by interaction of –OH groups, leading to some chemisorption on a surface, and adsorption involving the interaction of the alkyl groups with the surface. The higher monolayer capacity and absence of hysteresis observed in case of both the *t*-BuOH and MeOH sorption compared with both water and *n*-BuOH sorption indicated that *t*-BuOH adsorption occurred predominantly *via* organophilic interactions.

6.4.2 Iron-Schiff Base-modified Materials

The sorption of nitrogen (77 K) and carbon dioxide (195 K) was carried out on both the Fe(II)- and Fe(III)-Schiff base-modified MCM 41 materials to investigate the changes in the surface and pore parameters upon modification.

6.4.2.1 Nitrogen Sorption

Nitrogen sorption isotherms (77 K) on both the Fe(III)- and Fe(II)-Schiff base-modified MCM 41 materials (Fe-Schiff base complex target loading of 0.25, 0.50, 0.75 and 1.0 mmol g^{-1} of Si-MCM 41) are shown in Fig. 6.29 and Appendix A4, respectively. The sorption isotherm data are summarised in Table 6.24.

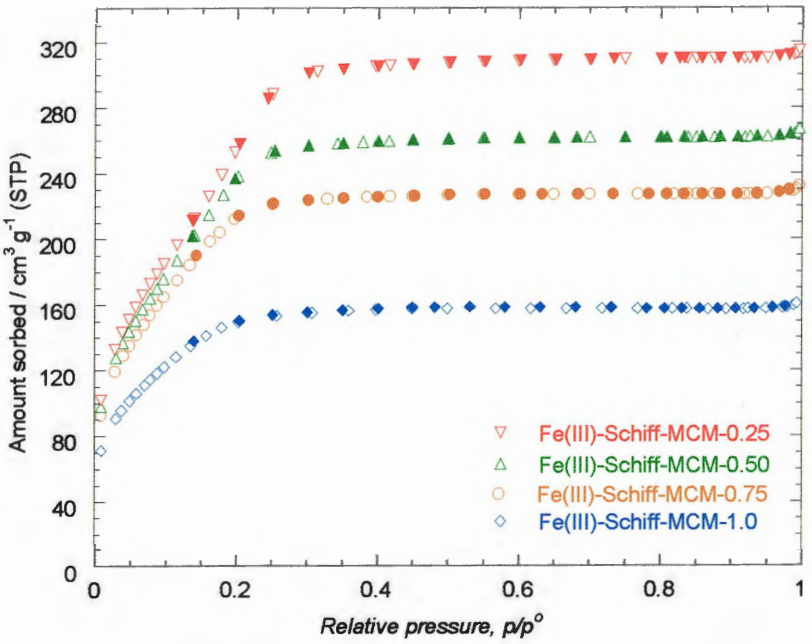

Figure 6.29 Nitrogen sorption isotherms (77 K) for the Fe(III)-Schiff base-modified materials. Filled symbols denote desorption points.

Table 6.24 Summary of the nitrogen sorption results for the iron-Schiff base MCM 41 materials

Sample	Type of isotherm	S_{BET} / m^2 g^{-1}	V_{pore} / cm^3 g^{-1}	Average pore diameter / Å	
				§	†
Si-MCM 41	IV	1140	0.72	25	25
Fe(II)-Schiff-MCM-**0.25**	IV	920	0.45	19	23
Fe(II)-Schiff-MCM-**0.50**	IV	840	0.38	18	23
Fe(II)-Schiff-MCM-**0.75**	IV	730	0.32	18	24
Fe(II)-Schiff-MCM-**1.0**	I	360	0.15	17	24
Fe(III)-Schiff-MCM-**0.25**	IV	1000	0.48	19	23
Fe(III)-Schiff-MCM-**0.50**	IV	930	0.40	18	22
Fe(III)-Schiff-MCM-**0.75**	IV	830	0.35	17	23
Fe(III)-Schiff-MCM-**1.0**	I	560	0.24	17	23

§ *Pore diameter derived from Eq. 4V/(S_{sp} by BET),* † *= BJH pore diameter*

The Type IV isotherms for the samples with Fe-Schiff base complex with a target loading of 0.25, 0.50 and 0.75 mmol g^{-1}, indicate the samples to be mesoporous. However, the sample with Fe-Schiff base complex target loading of 1.0 mmol g^{-1} showed Type I isotherms, indicating microporosity. A progressive decrease in the surface area and total pore volume (Table 6.24) observed with increased loading for the modified samples compared with the unmodified sample confirmed the immobilisation of the Fe-Schiff base complex within the pores of the Si-MCM 41 material. Both the Fe(II) and Fe(III) materials with a target loading of 1.0 mmol g^{-1} showed a significant decrease in the surface area and pore volume (Table 6.24), which suggested that the pores in these materials are either completely filled by a complex or may be blocked.

The complete filling of the pores is achieved at low relative pressure for the modified samples compared with the unmodified sample, which indicated a narrowing of the pores. However, the condensation step in the modified samples was not sharp, which suggested that the materials did not retain the narrow pore size distribution of the parent material. A slight decrease in the average pore diameter (derived from $4V/S_{sp}$) upon modification (Table 6.24), which decreases with increase in Fe-Schiff base complex loading, confirmed the immobilisation of complex within the pores leading to narrowing of pores. A decrease in the BJH average pore diameter (from 25 to 23 Å) upon modification was also observed. However, the average BJH pore diameters for the modified samples were found to be the same (Table 6.24).

6.4.2.2 Carbon Dioxide Sorption

The carbon dioxide sorption data are summarized in Table 6.25 and the sorption isotherms at 195 K for the Fe(III)-Schiff base-modified MCM 41 samples are shown in Figs 6.30. The CO_2 sorption isotherms for the Fe(II)-Schiff-MCM 41 samples are presented in Appendix A4.

Table 6.25 CO_2 sorption isotherm results for the iron-Schiff base MCM 41 materials

Sample	Type of isotherm	S_{BET} / m^2 g^{-1}	V_{pore} / cm^3 g^{-1}	Average pore Diameter / Å§
Si-MCM 41	IV	580	0.76	53
Fe(II)-Schiff-MCM-**0.25**	IV	300	0.52	70
Fe(II)-Schiff-MCM-**0.50**	IV	300	0.42	56
Fe(II)-Schiff-MCM-**0.75**	IV	300	0.35	46
Fe(II)-Schiff-MCM-**1.0**	IV	290	0.30	42
Fe(III)-Schiff-MCM-**0.25**	IV	360	0.60	64
Fe(III)-Schiff-MCM-**0.50**	IV	340	0.50	57
Fe(III)-Schiff-MCM-**0.75**	IV	340	0.44	50
Fe(III)-Schiff-MCM-**1.0**	IV	280	0.33	47

§ *Pore diameter derived from Eq. 4V/(S_{sp} by BET)*

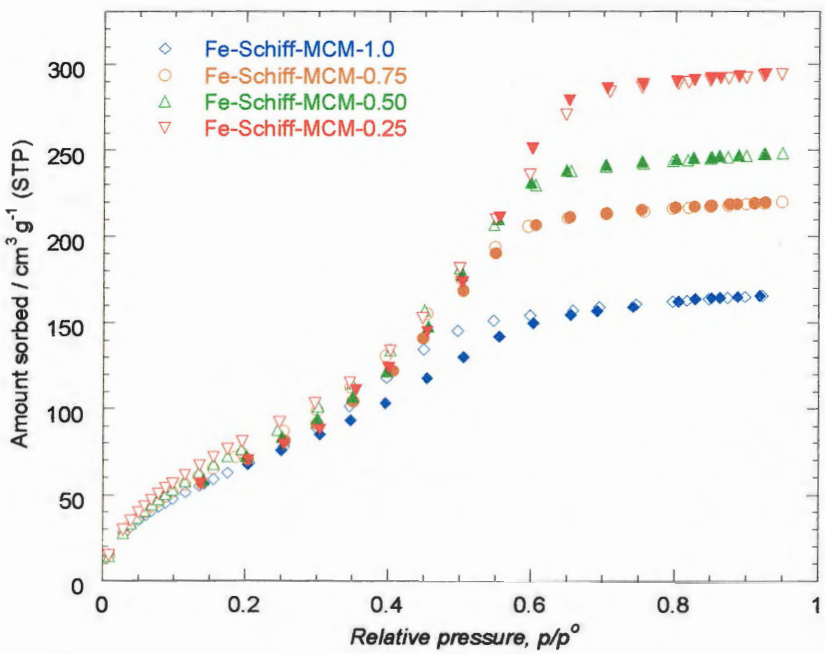

Figure 6.30 Carbon dioxide sorption isotherms (195 K) for the Fe(III)-Schiff base-modified MCM 41 materials. Filled symbols denote desorption points.

The isotherms are Type IV, indicating mesoporosity, similar to the isotherms obtained from nitrogen sorption, except for the 'rounded knee' at low p/p^o (> 0.1) and a shift in the capillary condensation step towards higher p/p^o between *ca.* 0.5 and 0.6.

The CO_2 sorption isotherms on the Fe(III)-Schiff-MCM 41 samples (Fig. 6.30) unexpectedly show a negative hyteresis. However, the isotherms in this case were obtained with an equilibration time of 5 s compared with 15 s in the case of the Fe(II)-Schiff-MCM 41 samples (where no hysteresis was observed) and Cu-Schiff-MCM 41 (positive hysteresis), Fig. in Appendix A4 and Fig. 6.18, respectively, indicating equilibration of CO_2 requires > 5 s.

The CO_2 derived surface areas (Table 6.25) for all the samples were found to be smaller than those obtained from N_2 sorption (Table 6.24). However, the Gurvitsch pore volumes for all the samples were found to be in good agreement with the nitrogen derived pore volumes except for 1.0 mmol g^{-1} samples where CO_2 values were higher. The CO_2 derived surface areas for all the modified samples were constant at around 300 m^2 g^{-1}. However, a decrease in surface area and pore volume compared with the parent Si-MCM 41 material was observed, which confirmed the results obtained from nitrogen sorption that the Fe-Schiff base complex was immobilised within the pores of the Si-MCM 41 material.

The rounded 'knee' observed in the CO_2 sorption isotherms and the lower CO_2 derived surface areas compared with the nitrogen sorption suggested that the sorption mechanism of CO_2 on the surface was probably *via* site-specific adsorption rather than *via* complete monolayer formation.

6.4.3 Nickel-Schiff Base-modified Materials

The adsorptives used to study the sorption characteristics of the nickel-Schiff base-modified MCM 41 materials (samples with nickel-Schiff base complex target loadings of 0.25, 0.50, 0.75 and 1.0 mmol) were nitrogen at 77 K and CO_2 at 195 K.

6.4.3.1 Nitrogen Sorption

The nitrogen sorption isotherms on the nickel-Schiff base modified samples are shown in Fig. 6.31. The Ni-Schiff-MCM-**0.25** and Ni-Schiff-MCM-**0.50** materials yielded Type IV isotherms, which suggested that the materials synthesised were in the mesoporous range. However, the condensation steps for these samples are not sharp and suggested that the modified materials have not retained the narrow pore size distribution of the parent material. On the other hand the Type I isotherm observed for the Ni-Schiff-MCM-**0.75** and Ni-Schiff-MCM-**1.0** samples confirmed that the materials with the higher loading of complex are microporous.

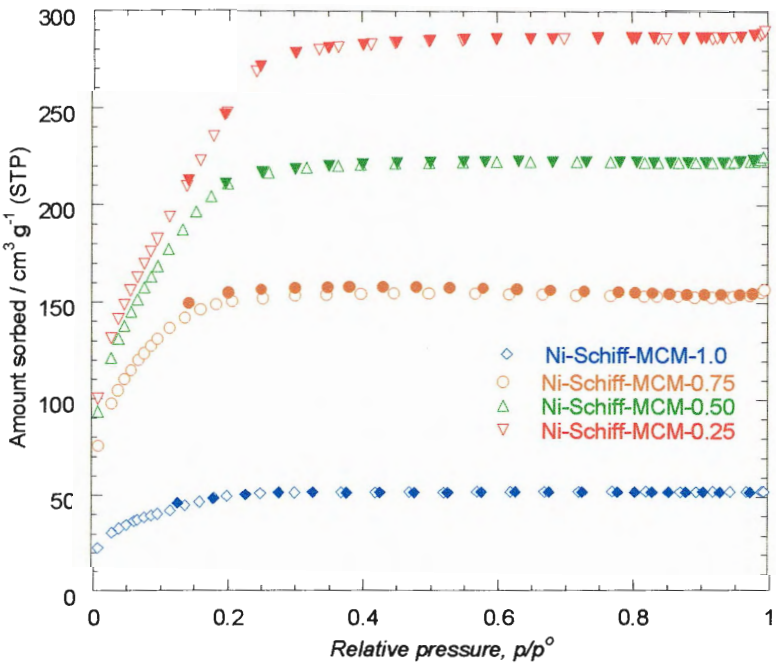

Figure 6.31 Nitrogen sorption isotherms (77 K) for the nickel-Schiff base-modified MCM 41 materials. Filled symbols denote desorption points.

The Ni-Schiff-MCM-**0.25** and Ni-Schiff-MCM-**0.50** samples showed a small decrease in the surface area and pore volume (Table 6.26) due to the immobilisation of the Ni-Schiff base complex within the pores of the Si-MCM 41 material. However, a

significant decrease in the surface area and pore volume (Table 6.26) of the Ni-Schiff-MCM-**0.75** and Ni-Schiff-MCM-**1.0** samples may be due to the blocking of pores. The CHN microanalysis and the results obtained from AAS (Table 6.11, Section 6.3.4) for the Ni-Schiff-MCM-**1.0** sample showed that the amount of Ni-Schiff base complex immobilised (0.48 mmol g^{-1}) on the surface of Si-MCM 41 material was similar to that of the Cu-Schiff-MCM-**1.0** (0.47 mmol g^{-1}) and Fe-Schiff-MCM-**1.0** (0.47 mmol g^{-1}) materials (isotherm intermediate between Type I and Type IV). Thus with the similar type of loading the Ni-Schiff-MCM-**0.75** and Ni-Schiff-MCM-**1.0** samples showed a Type I isotherm and a significant decrease in the surface area and pore volume, which confirmed the pore blocking. In this case, the nickel-Schiff base MCM 41 materials were synthesised with reaction time of 24 h and the solvent used was methanol, which suggested that a long reaction time and higher initial loading of the complex was more likely to result in considerable pore blocking.

Table 6.26 Summary of nitrogen sorption results for the nickel-Schiff base-modified MCM 41 materials

Sample	**Type of isotherm**	**S_{BET} / $m^2 g^{-1}$**	**V_{pore} / $cm^3 g^{-1}$**	**Average pore diameter / Å**	
				§	**†**
Si-MCM 41	IV	1140	0.72	25	25
Ni-Schiff-MCM-**0.25**	IV	970	0.45	18	23
Ni-Schiff-MCM-**0.50**	IV	800	0.34	17	22
Ni-Schiff-MCM-**0.75**	IV	540	0.24	18	23
Ni-Schiff-MCM-**1.0**	I	160	0.05	12	--

§ = *Pore diameter derived from Eq. 4V/(S_{sp} by BET) and,* † = *BJH pore diameter*

6.4.3.2 Carbon Dioxide Sorption

The CO_2 sorption isotherms at 195 K (Fig. 6.32) for the nickel-Schiff base-modified MCM 41 samples yielded Type IV isotherms. The isotherms were non-reversible with a

negative hysteresis loop similar to that of the Fe(III)-Schiff- MCM 41 samples (Fig. 6.30). It is important to note that the isotherms were obtained with equilibration time of 5 s. A shift in the capillary condensation step towards higher relative pressure (in the range $0.45 < p/p^o < 0.60$) is observed compared to the nitrogen sorption isotherm (in the range $0.15 < p/p^o < 0.25$). The capillary condensation step in the isotherm is not sharp, which indicated that the material had a broad pore size distribution.

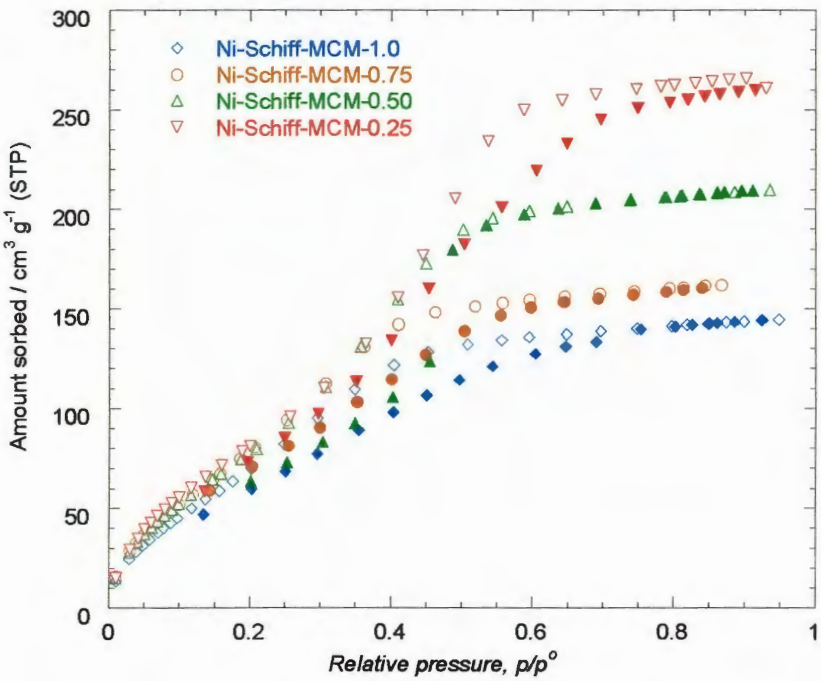

Figure 6.32 Carbon dioxide sorption isotherms (195 K) for the nickel-Schiff base-modified MCM 41 materials. Filled symbols denote desorption points.

The CO_2 derived surface areas for each of the nickel-Schiff base-modified samples were constant (Table 6.27). However, a decrease in the surface areas and pore volumes compared with the parent Si-MCM 41 material was observed following modification. The results were similar to those obtained from nitrogen sorption and confirmed the immobilisation of the Ni-Schiff base complex within the pores of the Si-MCM 41 material. The Ni-Schiff-MCM-**1.0** sample showed a Type IV CO_2 sorption

isotherm compared with the Type I obtained from the nitrogen sorption, and the CO_2 derived Gurvitsch pore volume for this sample was unexpectedly higher than the N_2 derived pore volume. This higher observed pore volume may be due to activated adsorption of CO_2 at higher sorption temperature (195 K) compared with N_2 sorption (77 K).

A decrease in CO_2 derived pore diameter upon modification was observed, which was mainly due to the narrowing of pores and confirmed the immobilisation of the Ni-Schiff base complex within the pores of the Si-MCM 41 material.

The rounded 'knee' observed in the CO_2 sorption isotherms and the lower CO_2 derived surface areas (except for Ni-Schiff-MCM-**1.0**) compared with the nitrogen sorption confirmed that the sorption mechanism of CO_2 on the surface was probably *via* site-specific adsorption rather than *via* complete monolayer formation.

Table 6.27 Summary of carbon dioxide sorption results for the nickel-Schiff base-modified MCM 41 materials

Sample	**Type of isotherm**	**S_{BET} / $m^2\ g^{-1}$**	**V_{pore} / $cm^3\ g^{-1}$**	**Average pore diameter / Å §**
Si-MCM 41	IV	580	0.76	53
Ni-Schiff-MCM-**0.25**	IV	375	0.53	55
Ni-Schiff-MCM-**0.50**	IV	365	0.42	45
Ni-Schiff-MCM-**0.75**	IV	375	0.30	32
Ni-Schiff-MCM-**1.0**	IV	330	0.26	38

§ *Pore diameter derived from Eq. $4V/(S_{sp}$ by BET)*

6.5 Conclusions

Metal[Cu, Fe(II), Fe(III) and Ni]-Schiff base-modified MCM 41 materials with five different loadings (*ca.* 0.25, 0.35, 0.45, 0.48 and 0.65 mmol g^{-1}) were successfully synthesised by a post-synthetic grafting method. The functionalised samples showed *p*-XRD patterns similar to that of the parent Si-MCM 41 material, which confirmed that

the hexagonal periodicity of the Si-MCM 41 host was preserved after treatment at 383 K and 353 K in toluene and methanol, respectively.

The presence of the metal-Schiff base complex on the Si-MCM 41 surface was confirmed by IR and NMR spectroscopy. The IR spectrum for each of the modified samples shows IR bands at *ca.* 1625 cm^{-1} for the imine group, at *ca.* 1450 cm^{-1} for C-H_{def}, at *ca.* 2960 and 2830 cm^{-1} for C-H_{str}, and at *ca.* 1475 cm^{-1} for phenyl C-C_{str}. The ^{13}C-{^{1}H}-CP MAS NMR spectra of the modified samples showed peaks due to the presence of both the aliphatic and aromatic carbon atoms. The ^{29}Si CP MAS NMR spectra of the modified samples showed the presence of both the organosiloxanes (T^m) and the framework silicon (Q^n).

AAS demonstrated that a maximum loading of *ca.* 0.50 mmol g^{-1} of metal-Schiff base complex was achieved. Increasing the reaction time (from 8 h to 20 h) increased the amount immobilised (up to 0.65 mmol g^{-1}) of the metal (copper)-Schiff base complex. However, the material thus formed lost mesoporosity by pore blocking and pore narrowing as indicated by N_2 sorption.

The complexation of metal with the Schiff base ligand in a 1:2 ratio was confirmed by the AAS and the CHN microanalysis. The results obtained by these techniques revealed that the N/metal molar ratio for each of the modified samples is in between 1.7 and 2.5, which was in a good agreement with the expected ratio of 2.0. This suggested that the immobilisation of metal on the MCM 41 surface occurred *via* complexation with the Schiff base ligand.

The presence of unreacted ethoxy groups in the modified samples was confirmed by ^{13}C-{^{1}H}-CP MAS NMR spectroscopy and CHN microanalysis. The ^{13}C-{^{1}H}-CP MAS NMR spectra of the modified samples showed the presence of peaks at *ca.* δ = 60 and 17 ppm from the ethoxy groups. The CHN microanalytical data showed that the number of unreacted ethoxy groups in the modified samples decreased with increase in the amount of metal-Schiff base complex loading.

The mesoporosity of the synthesised materials was confirmed by the Type IV isotherms yielded from nitrogen (77 K), CO_2 (195 K) and alcohols (303 K) sorption. The Cu-Schiff-MCM-**1.0** (20), Fe(II)-Schiff-MCM-**1.0**, Fe(III)-Schiff-MCM-**1.0** and Ni-Schiff-MCM-**1.0** materials showed Type I nitrogen sorption isotherms, which suggested that the materials synthesised with higher metal loading and longer reaction times lost mesoporosity by pore blocking and pore narrowing.

The Type V isotherm obtained from water sorption confirmed the adsorption of the water molecules on the surface occurred *via* interaction with the surface hydroxyls. The CO_2 sorption yielded lower surface areas (between 580 and 310 $m^2\ g^{-1}$) whereas the Gurvitsch pore volumes (between 0.76 and 0.39 $cm^3\ g^{-1}$) obtained were in good agreement with the nitrogen-derived values (surface areas between 1150 and 825 $m^2\ g^{-1}$, pore volumes between 0.72 and 0.34 $cm^3\ g^{-1}$). The occurrence of condensation within the pores at higher p/p^o confirmed that the CO_2 sorption occurred by a different mechanism to N_2 sorption *i.e. via* interaction with polar groups on the surface rather than *via* monolayer formation. In contrast, the nature of the *n*-hexane sorption indicated the high organophilic character of the surface.

The adsorption of alcohols (MeOH, *n*-BuOH and *t*-BuOH) was found to be intermediate in character between water and *n*-hexane sorption. This suggested that adsorption occurred both by hydrophilic interaction involving –OH groups and organophilic interaction involving the alkyl groups with the surface.

The immobilisation of the metal-Schiff base complex within the pores of the Si-MCM 41 host was supported by a decrease in the surface area and the pore volume following modification. A progressive decrease in both the surface area and pore volume with increase in the loading of the metal-Schiff base complex was observed.

XPS was evaluated as an analytical technique to investigate the distribution of copper complexes within the pores and on the external surface. The presence of the copper-Schiff base complex on the Si-MCM 41 surface was confirmed by the observed

C, N and Cu peaks in the XPS spectrum of each of the copper-Schiff base-modified MCM 41 materials. Argon etching of the surface to a depth of 4.5 nm demonstrated that the copper-Schiff base complex was distributed both on the external surface and within the pores of the Si-MCM 41 material. The argon etching showed that between 1/3 and 1/4 of the copper-Schiff base complex was located in the pores, whereas the remainder was present on the external surface or blocking some of the pores. This was attributed to the bulky nature of the complex, which restricted access to the pores. AAS gave copper loadings of 0.25, 0.35, 0.45 and 0.48 mmol g^{-1}, whereas the amounts of copper detected from XPS were constant (*ca.* 0.90 at%). Thus, the quantitative information obtained from XPS was not reliable for this type of material.

6.6 References

1. J. M. Fraile, J. I. Garaía, J. A. Mayoral, E. V. Ispe, D. R. Brown and M. Naderi, *J. Chem. Soc., Chem. Commun.,* 2001, 1510.
2. V. Parvulescu and B. L. Su, *Catal. Today*, 2001, **69**, 315.
3. A. Corma, H. Garcia and A. Leyva, *Appl. Catal. A: General*, 2002, **236**, 179.
4. P. M. Price, J. H. Clark and D. J. Macquarrie, *J. Chem. Soc., Dalton Trans.,* 2001, 101.
5. D. Brunel, F. Fajula, J. B. Nagy, B. Deroide, M. J. Verhoef, L. Veum, J. A. Peters and H. van Bekkum, *Appl. Catal. A: General*, 2001, **213**, 73.
6. C. Baleizao, B. Gigante, M. Jose Sabater, H. Garcia and A. Corma, *Appl. Catal. A: General*, 2002, **228**, 279.
7. P. Sutra and D. Brunel, *J. Chem. Soc., Chem. Commun.,* 1996, 2485.
8. I.C. Chisem, J. Rafelt, M.T. Shieh, J. Chisem, J.H. Clark, R. Jachhuck, D.J. Macquarrie, C. Ramshaw and K. Schott, *J. Chem. Soc., Chem. Commun.*, 1998, 1949.
9. A. R. Silva, C. Freire, B. de Castro, M. M. A. Freitas and J. L. Figueiredo, *Micropor. Mesopor. Mater.*, 2001, **46,** 211.
10. R. I. Kureshy, N. H. Khan. S. H. R. Abdi, S. T. Patel, P. Iyer, E. Suresh and P. Dastidar, *J. Mol. Catal. A: Chemical*, 2000, **160**, 217.
11. A. Bottcher, M. W. Grinstaff, J. A. Labinger and H. B. Gray, *J. Mol. Catal. A: Chemical,* 1996, **113**, 191.
12. R. H. Holm, G. W. Everett, A. Chakravorty, *Prog. Inorg. Chem.,* 1996, **7**, 183.
13. J. C. Vartuli, K. D. Schmitt and C. T. Kresge, *Chem. Mater.*, 1994, **6**, 2317.
14. K. Nakamoto, "*Infrared and Raman Spectra of Inorganic and Coordination Compounds*", 4th Edition, John Wiley and Sons, USA, 1986.
15. C. J. Creswell, O. A. Runquist and M. M. Campbell, "*Spectral Analysis of Organic Compounds*", 2nd Edition, Longman Group Ltd., England, 1972.

16. K. Nakanishi, "*Infrared Absorption Spectroscopy*", Second Edition, Nankodo Company Ltd., Japan, 1964.

17. D. Brunel, A. Cauvel, F. Di Renzo, F. Fajula, B. Fubini, B. Onida and E. Garrone, *New J. Chem.*, 2000, **24**, 807.

18. D. J. Macquarrie, D. B. Jackson, J. E. G. Mdoe and J. H. Clark, *New, J. Chem.*, 1999, **23**, 539.

19. C. E. Fowler, S. L. Brukett and S. Mann, *J. Chem. Soc., Chem. Commun.*, 1997, 1769.

20. H. Kosslick, I. Mönnich, E. Patezold, H. Fuhrmann, R. Fricke, D. Müller and G. Oehme, *Micropor. Mesopor. Mater.*, 2001, **44-45**, 537.

21. X.S. Zhao, G. Q. Lu and X. Hu, *Micropor. Mesopor. Mater.*, 2000, **41**, 37.

22. R. C. T. Slade, C. M. Bambrough and R. T. Williams, *Phys. Chem. Chem. Phys.*, 2002, **4**, 5394.

23. H. Juvaste, E. I. Iiskola and T. T. Pakkanen, *J. Mol. Catal. A: Chemical*, 1999, **150**, 1.

24. W. A. Carvalho, M. Wallau and U. Schuchardt, *J. Mol. Catal. A: Chemical*, 1999, **144**, 91.

25. M. Pillinger, I. Goncalves, A. D. Lopes, J. Madureira, P. Ferreira, A. Valente, T. M. Santos, J. Rocha, J. F. S. Menezes and L. D. Carlos, *J. Chem. Soc., Dalton Trans.*, 2001, 1628.

26. J. F. Moulder, W. F. Stickle, P. E. Sobol and K. D. Bomben, "*Handbook of X-Ray Photoelectron Spectra- A Reference Book of Standard Spectra for Identification and Interpretation of XPS Data*", ed. J. Chastain, Perkin-Elmer Corporation, Eden Prairie, Minnesota, USA, 1992.

27. U. Singh, R. T. Williams, I. D. Salter, K. R. Hallam and G. C. Allen, *Studies in Surface Science and Catalysis 144*, Elsevier Science, 2002, p-639.

28. P. J. Branton, *PhD Thesis*, University of Exeter, 1994.

29. C. M. Bambrough, *PhD Thesis,* The Open University, 1998.

30. A. M. James and M. P. Lord, "*Macmillan's Chemical and Physical data*", The Macmillan Press Ltd., London, 1992.

31. C. M. Bambrough, R. C. T. Slade and R. T. Williams, *J. Mater. Chem.*, 1998, **8**, 569.

32. C. M. Bambrough, R. C. T. Slade, R. T. Williams, S. L. Brukett, S. D. Sims and S. Mann, *J. Colloid and Interface Sci.,* 1998, 201, 220.

33. S. Shyu, S. Cheng and D. Tzou, *J. Chem. Soc., Chem. Commun.*, 1999, 2337.

34. J. H. Clark and D. J. Macquarrie, *Chem. Soc. Rev.,* 1996, 303.

35. S. J. Gregg and K. W. Sing, *Adsorption Surface Area and Porosimetry*, 2nd Edition, Academic Press, London, 1982.

36. P. J. Branton, P. G. Hall and K. S. W. Singh, *J. Chem. Soc., Chem. Commun.*, 1993, 1257.

37. F. Courivaud, E. W. Hansen, A. Karlson, S. Kolboe and M. Stöcker, *Micropor. Mesopor. Mater.*, 2000, **35-36**, 327.

38. A. V. Kiselev, A. A. Lopatkin and A. A. Shugla, *Zeolites*, 1985, **5**, 261.

39. P. Graham, A. D. Hughes and L. V. C. Rees, *Gas Separation Technology*, Elsevier Science Publisher, Amsterdam, 1990, p. 215.

40. V. R. Choudhary and S. Mayadevi, *Zeolites*, 1996, **13**, 501.

41. X. S. Zhao, G. Q. Lu and X. Hu, *Colloids and Surface Sci. A: Physiochem. Eng. Aspects*, 2001, **179**, 261.

42. C. M. Bambrough, R. C. T. Slade and R. T. Williams, *Phys. Chem. Chem. Phys.*, 2000, **2**, 3499.

CHAPTER 7

SUMMARY

7.1 Introduction

A range of chemically-tailored mesoporous MCM 41 materials has been synthesised by sol-gel synthesis, and by post-synthetic grafting methods. Purely siliceous-MCM 41, a series of mesitylene-swollen MCM 41, metal-containing MCM 41 (Fe and Ti) and organically-modified (3-aminopropyl and Schiff base) MCM 41 were synthesised by the sol-gel synthesis method. Metal-grafted (Fe and Ti) MCM 41, organically-modified (3-aminopropyl, Schiff base and azodye) MCM 41 and the metal(Cu, Fe and Ni)-Schiff base-modified MCM 41 were prepared by post-synthetic grafting method.

The materials were characterised using a number of techniques including *p*-X-ray diffraction (*p*-XRD), infrared spectroscopy, CHN microanalysis, atomic absorption spectroscopy, nuclear magnetic resonance spectroscopy, X-ray photoelectron spectroscopy, transmission electron microscopy, and by the sorption of gases (N_2 and CO_2) and vapours (water, *n*-hexane, methanol, *n*-butanol, *t*-butanol).

The effect of heat-treatment (under reduced pressure of $< 10^{-5}$ torr, at 623 K) on the sorption characteristics of Ru-MCM 41 by the adsorption of nitrogen (77 K), 1-hexene and 3,3-dimethyl-1-butene (303 K) was also studied. This chapter summarises the conclusions from these work.

7.2 Si-MCM 41 materials

Standard methods were used to synthesise the Si-MCM 41 materials. Mesitylene was used as a pore-swelling agent in the synthesis of larger pore MCM 41 materials.

The hexagonal periodicity of the synthesised materials was confirmed by *p*-XRD, which shows an intense d_{100} peak and three less intense peaks below $2\theta = 10^{o}$. The shift in the d_{100} peak towards lower 2θ values in the *p*-XRD pattern of the mesitylene swollen MCM 41 reflected the incremental addition of mesitylene and this confirmed that the materials with larger pore diameters were formed.

The IR spectrum of the calcined Si-MCM 41 material showed a weak band at 947 cm^{-1} from siloxane groups present on the surface, suggesting that the surface dehydroxylates on calcination. The TEM analysis showed that the synthesised material has a tubular structure. The CHN microanalysis confirmed that the material was free from any organic contaminants.

The mesoporosity of the synthesised materials was confirmed by the Type IV isotherms obtained for nitrogen (77 K), CO_2 (195 K), MeOH, *n*-BuOH and *t*-BuOH (303 K) sorptions, and Type V isotherm for water sorption (303 K). The Type V nature of the water sorption isotherm (303 K) confirmed that the material has a predominantly hydrophobic surface and adsorption of water is *via* polar interaction with the surface. The large degree of hysteresis extending in the low-pressure range ($0 < p/p^{o}$ 0.60) is due to rehydroxylation of the Si-MCM 41 surface following the chemisorption of water. The sorption isotherm of *n*-hexane is difficult to classify according to the IUPAC classification, which suggests restricted diffusion over the hydrophobic surface. The shape of the *n*-hexane sorption isotherm indicates the high organophilic character of the surface. The adsorption of alcohols was found to be intermediate in character between water and *n*-hexane. This suggests that adsorption of the alcohols takes place both by

hydrophilic interactions involving –OH groups, and by organophilic interactions involving the alkyl groups with the surface.

The materials synthesised yielded high nitrogen-derived surface areas (*ca.* 1150 $m^2 g^{-1}$), pore volumes (*ca.* 0.74 $cm^3 g^{-1}$) and average pore diameter (*ca.* 26 Å), which are typical for mesoporous materials. The larger pore (39 Å) MCM 41 material (synthesised using 33.4 mmol of mesitylene/synthesis batch) showed an expected decrease in the surface area (360 $m^2 g^{-1}$) and pore volume (0.3 $cm^3 g^{-1}$) as the number of pores per unit area decreases with increase in the pore diameter.

The CO_2 adsorption showed a lower surface area (580 $m^2 g^{-1}$) and a shift in capillary condensation towards higher p/p^o (*ca.* 0.60) compared with the nitrogen sorption (p/p^o *ca.* 0.30). This suggests that the adsorption of CO_2 proceeds *via* polar interaction with the MCM 41 surface, resulting in site-specific adsorption rather than *via* monolayer formation.

7.3 Metal-functionalised MCM 41 materials

7.3.1 Fe- and Ti-MCM 41 Materials

Fe and Ti were each incorporated into the Si-MCM 41 material to form Fe-MCM 41 and Ti-MCM 41, respectively. Fe-MCM 41 and Ti-MCM 41 were successfully synthesised by two different methods *i.e.* by the sol-gel method, and by the post-synthetic grafting method. Both Fe(II) and Fe(III) precursors were used for the synthesis of Fe-MCM 41. The ^{57}Fe Mössbauer spectrum of each sample shows a doublet with a quadrupole splitting of *ca.* 0.86 mms^{-1}, which demonstrated that Fe(III)-MCM 41 was synthesised irrespective of the initial source of iron [Fe(II) or Fe(III) salts] used in the synthesis. The surfaces of the Ti-MCM 41 samples were modified by amnolysis. The presence of a d_{100} peak in the *p*-XRD pattern of each of the metal-functionalised MCM 41 materials confirms that the material synthesised exhibits hexagonal

periodicity. The incorporation of Fe and Ti in the silica framework of the Fe-MCM-**a** and Ti-MCM-**e** (sol-gel synthesised materials), respectively, was confirmed by the bands at 974 cm^{-1} and 962 cm^{-1}, respectively, in the IR spectra due to metal-oxygen stretching. The IR band at *ca.* 947 cm^{-1} for surface hydroxyls was not present in the grafted samples, which confirms the grafting of Fe and Ti involves reaction with the surface hydroxyls on the surface.

The mesoporosity of each of the synthesised materials was confirmed by the Type IV isotherms yielded by nitrogen sorption (77 K). A small decrease in both the surface area and total pore volume observed following grafting was attributed to the immobilisation of the Fe and Ti species on the pore surface. The grafted Fe- and Ti-MCM 41 materials showed an increase in the pore wall thickness upon grafting but this was not the case with the sol-gel synthesised samples. This increase in the pore wall thickness (from 19 Å to 21 Å) was attributed to a smearing layer formed by metals grafted on the pore walls.

Incorporation of metal-functionalities resulted in a reduction in the surface areas (from 1160 to 1097 $m^2\ g^{-1}$, and from 1160 to 800 $m^2\ g^{-1}$, for the grafted and sol-gel synthesised samples, respectively) and pore volumes (from 0.74 to 0.45 $cm^3\ g^{-1}$) of the modified samples. The loss in surface area was more pronounced for the sol-gel synthesised samples compared with the grafted samples. The grafted samples showed a reduction in the average pore diameter (from 26 Å to 18 Å) following functionalisation, whereas the sol-gel synthesised samples had pore diameters (*ca.* 25 Å) comparable with those of the parent Si-MCM 41 (26 Å). A significant decrease in the surface area (from 1160 $m^2\ g^{-1}$ to 770 $m^2\ g^{-1}$) and a slight increase in the average pore diameter (from 23 to 26 Å) for the grafted amnolysed Ti-MCM-**h** sample suggested sintering of Ti during amnolysis. However, for the sol-gel synthesised Ti-MCM-**g** sample, there was a slight decrease in the surface area (from 800 $m^2\ g^{-1}$ to 690 $m^2\ g^{-1}$) and no change in the pore

diameter. This suggests that in the sol-gel synthesised sample the Ti was incorporated in the framework and was less likely to undergo sintering under amnolysis conditions compared with the grafted samples.

The condensation steps in the CO_2 sorption isotherms of all the modified samples were observed at higher relative pressures compared with N_2 sorption, and the CO_2 derived surface areas (between 130 and 580 $m^2 g^{-1}$) were found to be much smaller than the N_2 derived surface areas (between 690 and 1160 $m^2 g^{-1}$). This suggests that the CO_2 sorption occurs *via* a different mechanism to N_2 sorption *i.e.* by interaction with polar groups on the surface rather than monolayer formation.

The presence of titanium nitride in the amnolysed Ti-MCM 41 samples was suggested by the XPS. The detection of this compound by the IR spectroscopy was not possible as the bands arising from the framework SiO_2 mask the expected Ti-N bands. The presence of adsorbed NH_4^+ and NH_2 groups in the amnolysed Ti-MCM 41 samples was confirmed by the IR spectroscopy.

7.3.2 Ru-MCM 41 Materials

The ruthenium-MCM 41 (Ru-MCM 41) material was supplied by Bruce *et al.*[5] The effect of heat-treatment (under reduced pressure of $< 10^{-5}$ torr, at 623 K) on the sorption characteristics of Ru-MCM 41 by the adsorption of nitrogen (77 K), 1-hexene and 3,3-dimethyl-1-butene (303 K) was studied. Heat-treatment of Ru-MCM 41 was shown to alter the surface characteristics of the material with respect to the sorption of both nitrogen and hexene isomers, 1-hexene and 3,3-dimethyl-1-butene, though the changes are more marked for 1-hexene. Nitrogen adsorption yields a Type IV isotherms before and after heat-treatment, with hysteresis observed in the isotherm of the heat-treated sample. A slight decrease in the BET surface area (330 to 282 m^2g^{-1}) and pore volume (0.19 to 0.16 cm^3g^{-1}) as a result of the heat-treatment was observed for nitrogen

adsorption. However, adsorption of 1-hexene yields a Type I isotherm and doubling of the monolayer uptake of 1-hexene was observed following heat-treatment, which was equivalent to an increase in both BET surface area and (144 to 295 m^2g^{-1}) and pore volume (0.12 to 0.16 $cm^3 g^{-1}$). For this sample, the heat-treatment resulted in improved accessibility of 1-hexene molecules to the surface and the pores. This increase in 1-hexene uptake without a corresponding change in nitrogen BET surface area partly explains the observed increase in catalytic activity for 1-hexene isomerisation following heat-treatment of the Ru-MCM 41 sample. The adsorption of the hexene isomer 3,3-dimethyl-1-butene (303 K) after heat-treatment showed a Type I isotherm and yielded a BET surface area of 161 m^2g^{-1}, *i.e.* about half of the value derived from 1-hexene (295 m^2g^{-1}) measured value. The pore volume (0.13 cm^3g^{-1}) derived was also lower that that of 1-hexene (0.16 $cm^3 g^{-1}$) on the heat-treated sample. The lower uptake of 'spherical' 3,3-dimethyl-1-butene, compared with the 'long chain' 1-hexene suggests that the 3,3-dimethyl-1-butene was more sterically hindered on the adsorption sites of the Ru-MCM 41 sample.

7.4 Organically-modified MCM 41 materials

Three organically-modified MCM 41 materials (3-aminopropyl modified, Schiff base ligand modified and azodye modified) were prepared by three different methods *i.e.* by sol-gel synthesis and post-synthetic grafting (direct grafting method, and grafting by a coupling method). The absence of the d_{100} peak in the *p*-XRD pattern of the organically-modified materials synthesised *via* the sol-gel synthesis method, following template removal, confirmed the collapse of the hexagonal structure. Hence, the post-synthetic grafting method was used in the synthesis of the organically-modified MCM 41 materials.

The *p*-XRD patterns of the organically-modified materials, synthesised *via* post-synthetic grafting methods, each showed a d_{100} peak together with the less intense peaks at lower 2θ values (below 10^{o}) and confirmed that the hexagonal structure of the parent Si-MCM 41 material was retained following treatment at 383 K and 353 K in toluene and methanol, respectively.

The presence of organic moieties in the modified samples was confirmed by the presence of IR absorption bands at 1550 cm^{-1} ($N\text{-}H_{def}$) for the 3-aminopropyl-modified MCM 41, 1620 cm^{-1} ($C{=}N_{str}$) and 730 cm^{-1} (phenyl out-of-plane $C\text{-}H_{def}$) for the Schiff base-modified MCM 41, and 1634 cm^{-1} ($N{=}N_{str}$) and 730 cm^{-1} (phenyl out-of-plane $C\text{-}H_{def}$) for the azodye functionalised MCM 41 material. This conclusion was supported by CHN microanalysis, where high percentages of carbon, hydrogen and nitrogen were observed in the modified samples, and by NMR spectroscopic analysis, which showed the presence of organosiloxane silicon, aliphatic carbons and aromatic carbons in the spectra of each of the modified samples.

The presence of ethoxy groups, due to incomplete hydrolysis of the organoalkoxysilane, in the modified samples was confirmed by the CHN microanalysis. This was supported by the $^{13}C\text{-}\{H\}$-CP MAS NMR spectroscopic analysis, which showed NMR resonances due to the ethoxy groups in the spectrum of each of the modified samples at $\delta = 16$, 29 and 60 ppm.

The mesoporosity of the modified materials was demonstrated by the Type IV isotherms yielded from N_2 (77 K) and CO_2 (195 K) sorptions. The decrease in the surface areas (*ca.* 300 $m^2\ g^{-1}$) and the pore volumes (*ca.* 0.30 $cm^3\ g^{-1}$) following modification confirmed the immobilization of the organic moieties within the pores of the Si-MCM 41 host. The shape of the CO_2 sorption isotherm (presence of a rounded 'knee' at low relative pressure) and the smaller CO_2-derived surface area suggested that the adsorption of CO_2 was by polar interaction rather than *via* monolayer formation.

The CHN microanalysis data indicated that a higher loading of the Schiff base ligand was achieved by the coupling method compared with the direct post-synthetic grafting method. However, the N_2 sorption studies showed that the surface areas (900 m^2 g^{-1} and 910 m^2 g^{-1} from the coupling and the direct grafting methods, respectively) and the pore volumes (0.42 cm^3 g^{-1} and 0.47 cm^3 g^{-1} from the coupling and the direct grafting methods, respectively) of the materials synthesised by these two methods were unaffected.

7.5 Metal Schiff base-modified MCM 41 materials

Metal[Cu, Fe(II), Fe(III) and Ni]-Schiff base-modified MCM 41 materials with five different loadings (*ca.* 0.25, 0.35, 0.45, 0.48 and 0.65 mmol g^{-1}) were successfully synthesised by a post-synthetic grafting method. The functionalised samples showed *p*-XRD patterns similar to that of the parent Si-MCM 41 material, which confirmed that the hexagonal periodicity of the Si-MCM 41 host was preserved after treatment at 383 K and 353 K in toluene and methanol, respectively.

The presence of the metal-Schiff base complex on the Si-MCM 41 surface was confirmed by IR and NMR spectroscopy. The IR spectrum for each of the modified samples showed bands at *ca.* 1625 cm^{-1} for the imine group, at *ca.* 1450 cm^{-1} for C-H_{def}, at *ca.* 2960 and 2830 cm^{-1} for C-H_{str}, and at *ca.* 1475 cm^{-1} for phenyl C-C_{str}. The ^{13}C-{^1H}-CP MAS NMR spectra of the modified samples showed peaks due to the presence of both the aliphatic and aromatic carbon atoms. The ^{29}Si CP MAS NMR spectra of the modified samples showed the presence of both the organosiloxanes (T^m) and the framework silicon (Q^n).

AAS demonstrated that a maximum loading of *ca.* 0.50 mmol g^{-1} of metal-Schiff base complex was achieved. Increasing the reaction time (from 8 h to 20 h) increased the amount immobilised (up to 0.65 mmol g^{-1}) of the metal (copper)-Schiff base

complex. However, the material thus formed lost mesoporosity by pore blocking and pore narrowing as indicated by N_2 sorption.

The complexation of metal with the Schiff base ligand in a 1:2 ratio was confirmed by the AAS and the CHN microanalysis. The results obtained by these techniques revealed that the N/metal molar ratio for each of the modified samples was between 1.7 and 2.5, which was in a good agreement with the expected ratio of 2.0. This suggested that the immobilisation of metal on the MCM 41 surface occurred *via* complexation with the Schiff base ligand.

The presence of unreacted ethoxy groups in the modified samples was confirmed by ^{13}C-{^{1}H}-CP MAS NMR spectroscopy and CHN microanalysis. The ^{13}C-{^{1}H}-CP MAS NMR spectra of the modified samples showed the presence of peaks at *ca.* δ = 60 and 17 ppm from the ethoxy groups. The CHN microanalytical data showed that the number of unreacted ethoxy groups in the modified samples decreased with increase in the amount of metal-Schiff base complex loading.

The mesoporosity of the synthesised materials was confirmed by the Type IV isotherms yielded from nitrogen (77 K), CO_2 (195 K) and alcohols (303 K) sorption. The Cu-Schiff-MCM-**1.0** (20), Fe(II)-Schiff-MCM-**1.0**, Fe(III)-Schiff-MCM-**1.0** and Ni-Schiff-MCM-**1.0** materials showed Type I nitrogen sorption isotherms, which suggested that the materials synthesised with higher metal loading and longer reaction times lost mesoporosity by pore blocking and pore narrowing.

The Type V isotherm obtained from water sorption confirmed the adsorption of the water molecules on the surface occurred *via* interaction with the surface hydroxyls. The CO_2 sorption yielded lower surface areas (between 580 and 310 $m^2\ g^{-1}$), whereas the Gurvitsch pore volumes (between 0.76 and 0.39 $cm^3\ g^{-1}$) obtained were in good agreement with the nitrogen-derived values (surface areas between 1150 and 825 $m^2\ g^{-1}$, pore volumes between 0.72 and 0.34 $cm^3\ g^{-1}$). The occurrence of condensation within

the pores at higher p/p^o confirmed that the CO_2 sorption occurred by a different mechanism to N_2 sorption *i.e. via* interaction with polar groups on the surface rather than *via* monolayer formation. In contrast, the nature of the *n*-hexane sorption indicated the high organophilic character of the surface.

The adsorption of alcohols (MeOH, *n*-BuOH and *t*-BuOH) was found to be intermediate in character between water and *n*-hexane sorption. This suggested that adsorption occurred both by hydrophilic interaction involving –OH groups and organophilic interaction involving the alkyl groups with the surface.

The immobilisation of the metal-Schiff base complex within the pores of the Si-MCM 41 host was supported by a decrease in the surface area and the pore volume following modification. A progressive decrease in both the surface area and pore volume with an increase in the loading of the metal-Schiff base complex was observed.

XPS was evaluated as an analytical technique to investigate the distribution of copper complexes within the pores and on the external surface. The presence of the copper-Schiff base complex on the Si-MCM 41 surface was confirmed by the observed C, N and Cu peaks in the XPS spectrum of each of the copper-Schiff base-modified MCM 41 materials. Argon etching of the surface to a depth of 4.5 nm demonstrated that the copper-Schiff base complex was distributed both on the external surface and within the pores of the Si-MCM 41 material. The argon etching showed that between 1/3 and 1/4 of the copper-Schiff base complex was located in the pores, whereas the remainder was present on the external surface or blocking some of the pores. This was attributed to the bulky nature of the complex, which restricted access to the pores. AAS gave copper loadings of 0.25, 0.35, 0.45 and 0.48 mmol g^{-1}, whereas the amounts of copper detected from XPS were constant (*ca.* 0.90 at%). Thus, the quantitative information obtained from XPS was not reliable for this type of material.

Appendix A1

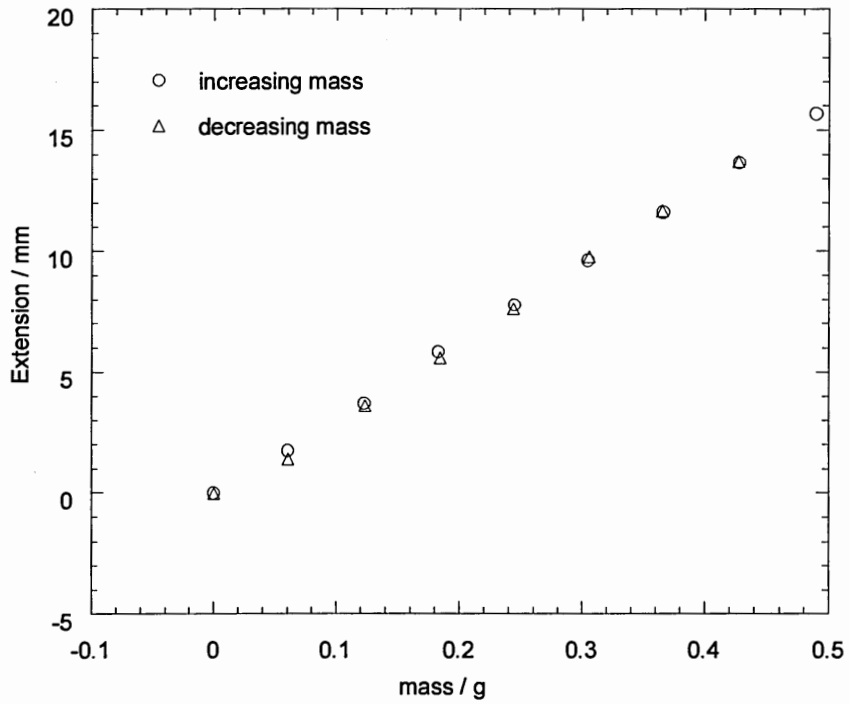

Figure A1.1 Calibration of the spring

$$\text{Slope} = 32.0 \text{ mm g}^{-1}$$

$\therefore$ The sensitivity of the spring is 32.0 microscope units g^{-1}.

APPENDIX A2

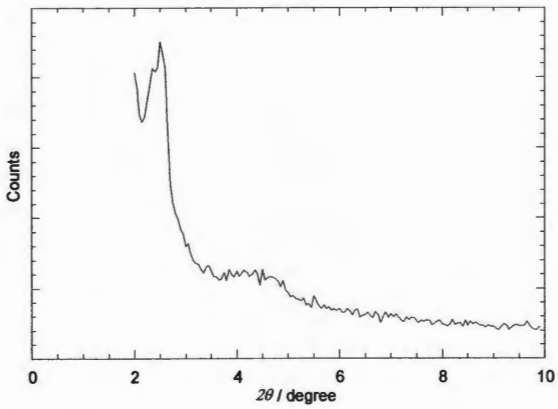

Figure A2.1 XRD pattern of sol-gel synthesised Fe(III)-MCM 41(Fe-MCM-**c**), obtained using CuKα radiation.

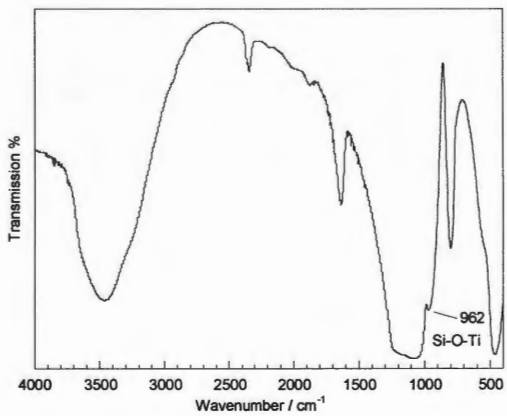

Figure A2.2 FT-IR spectrum of sol-gel synthesised Ti-MCM 41 (Ti-MCM-**e**).

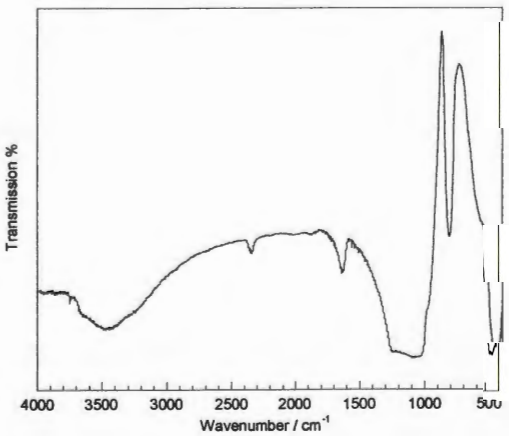

Figure A2.3 FT-IR spectrum of grafted Ti-MCM 41 (Ti-MCM-**f**).

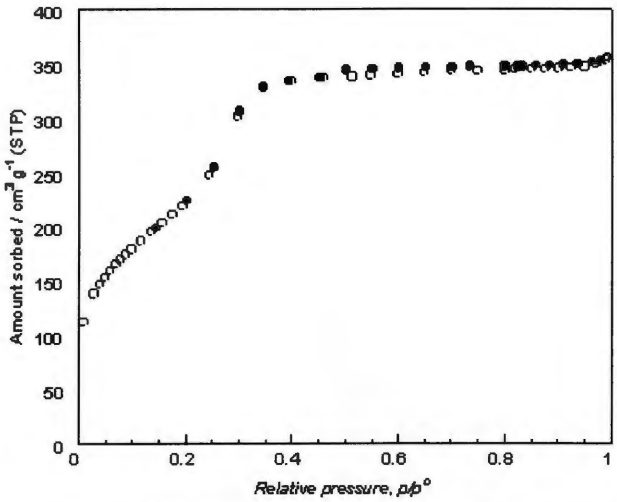

Figure A2.4 Nitrogen sorption (77 K) isotherm for sol-gel synthesised Fe(II)-MCM 41 (Fe-MCM-**a**). Filled symbols denote desorption points.

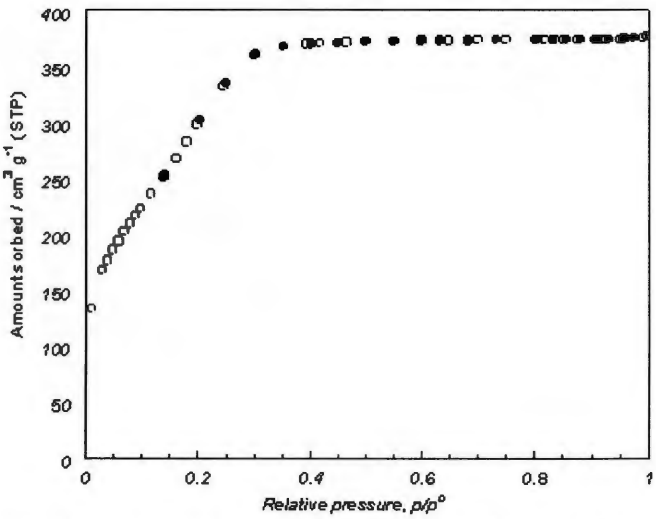

Figure A2.5 Nitrogen sorption (77 K) isotherm for grafted Ti-MCM 41 (Ti-MCM-**f**). Filled symbols denote desorption points.

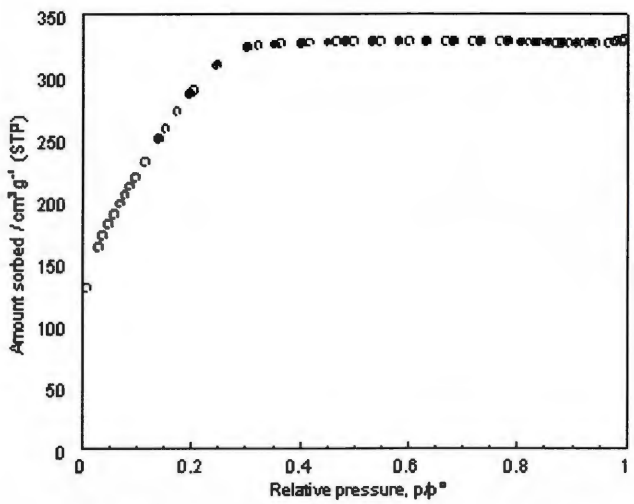

Figure A2.6 Nitrogen sorption (77 K) isotherm for grafted Fe(II)-MCM 41 (Fe-MCM-**b**). Filled symbols denote desorption points.

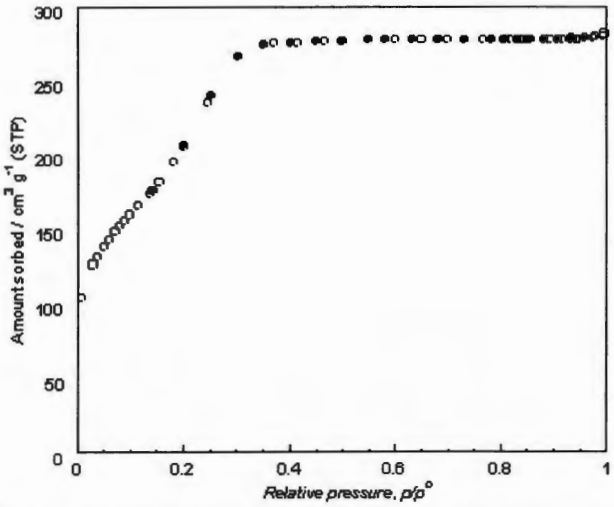

Figure A2.7 Nitrogen sorption (77 K) isotherm for grafted Ti-MCM 41 following amnolysis (Ti-MCM-**h**). Filled symbols denote desorption points.

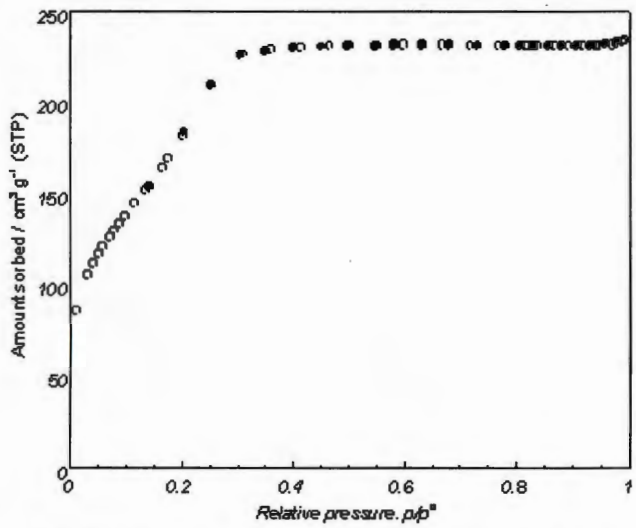

Figure A2.8 Nitrogen sorption (77 K) isotherm for sol-gel synthesised Ti-MCM 41 following amnolysis (Ti-MCM-**h**). Filled symbols denote desorption points.

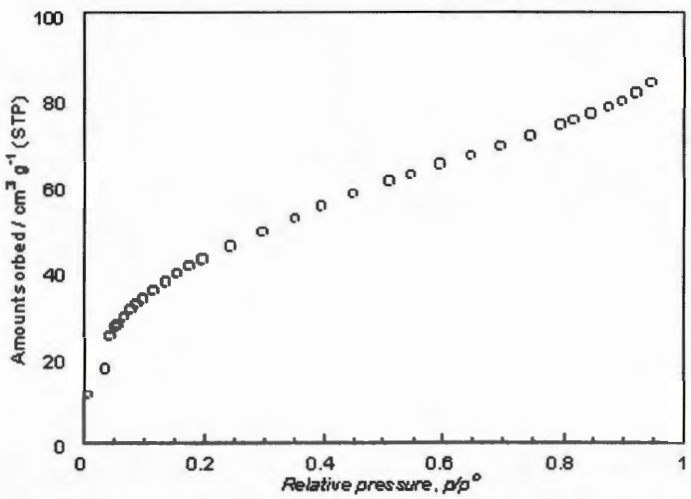

Figure A2.9 Carbon dioxide sorption (195 K) isotherm for sol-gel synthesised Ti-MCM 41 (Ti-MCM-**e**).

APPENDIX 3

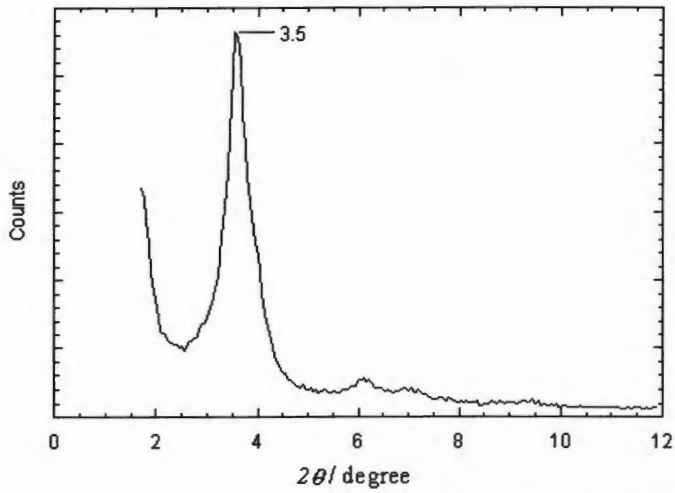

Figure A3.1 *p*-XRD pattern of the SB-MCM-**g** material.

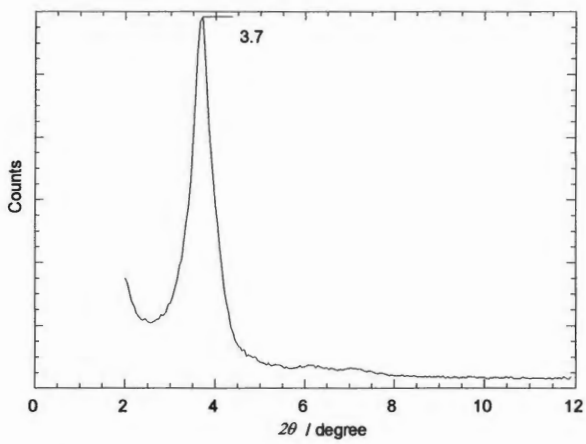

Figure A3.2 *p*-XRD pattern of the SB-MCM-**c** material.

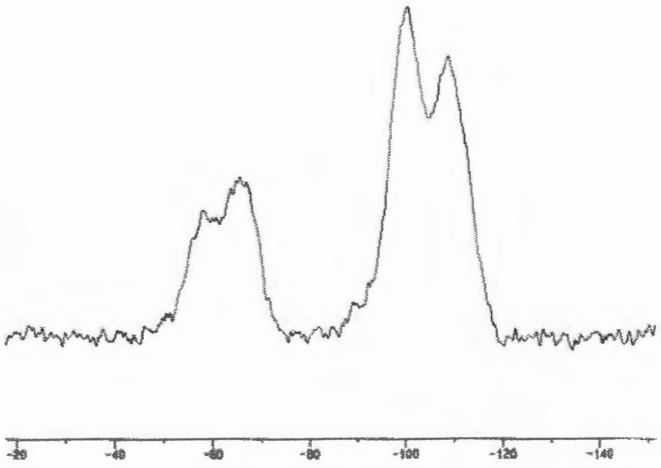

Figure A3.3 ^{29}Si CP MAS NMR spectrum of the SB-MCM-**g** (1.0 mmol g^{-1}).

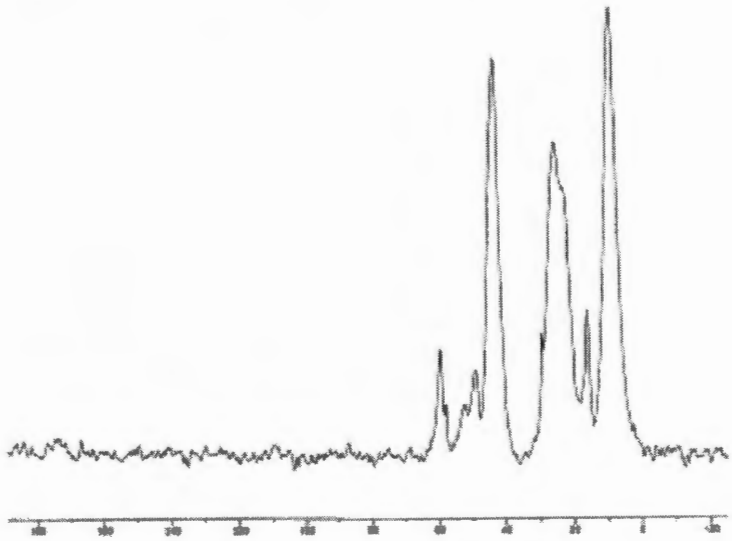

Figure A3.4 ^{13}C CP MAS NMR spectrum of NH_2-MCM-**g** (1.0 mmol g^{-1}).

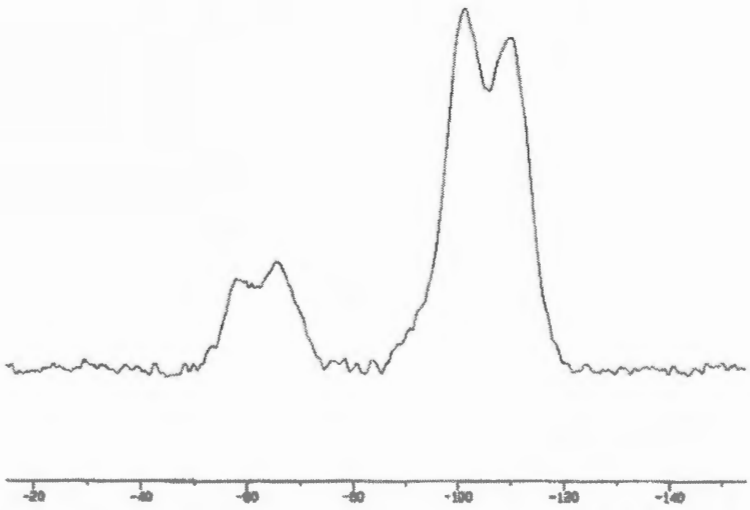

Figure A3.5 ^{29}Si CP MAS NMR spectrum of SB-MCM-**g** ((1.0 mmol g^{-1}).

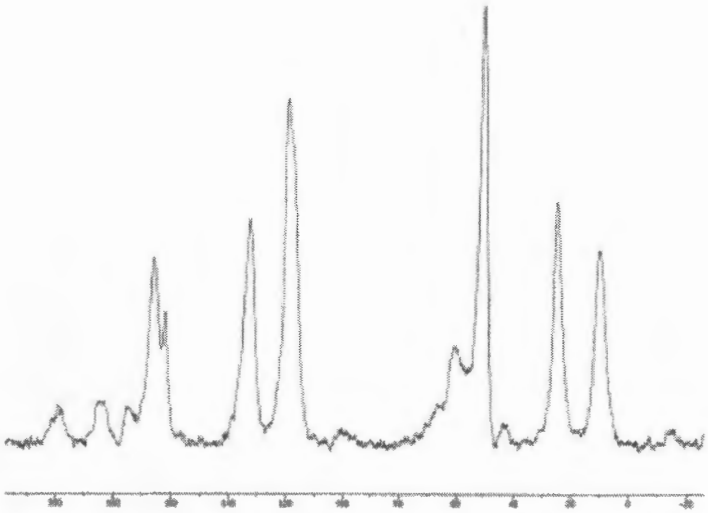

Figure A3.6 ^{13}C CP MAS NMR spectrum of the SB-MCM-**c** material (1.0 mmol g^{-1}).

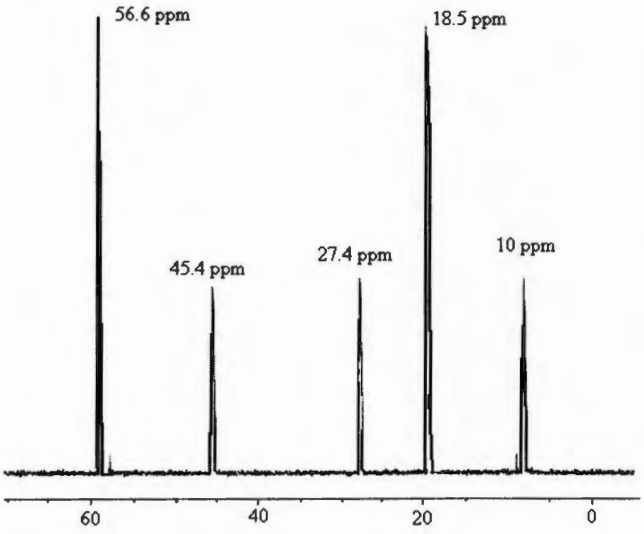

Figure A3.7 ^{13}C NMR spectrum of the 3-aminopropyltriethoxy silane.

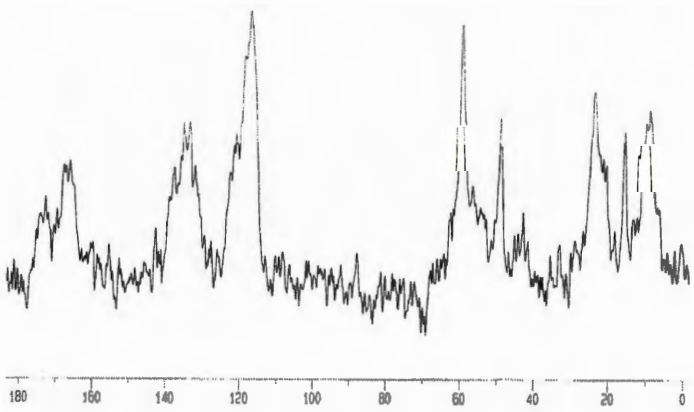

Figure A3.8 ^{13}C CP MAS NMR spectrum of the SB-MCM-**g** material (1.0 mmol g^{-1}).

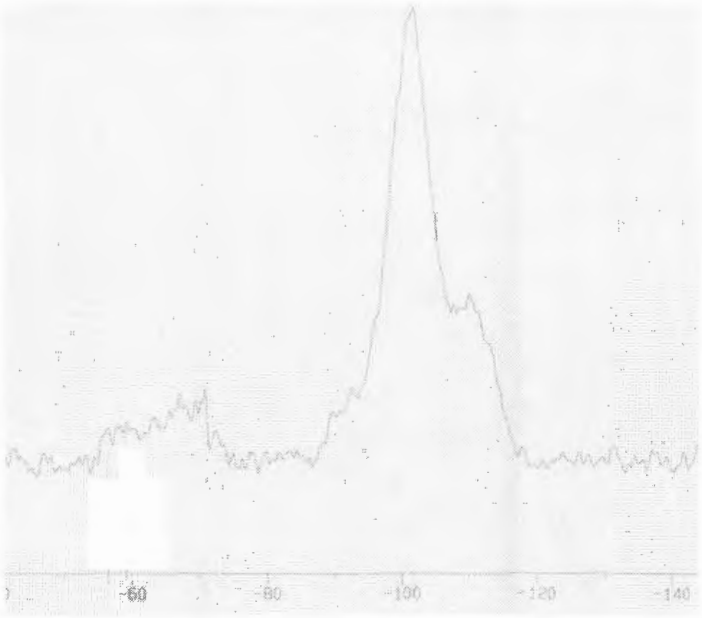

Figure A3.9 ^{29}Si CP MAS NMR spectrum of the SB-MCM-**g-1.0** material.

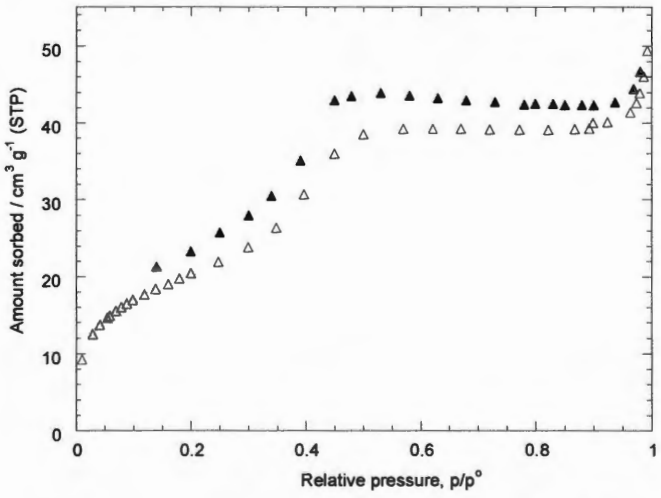

Figure A3.10 N_2 sorption isotherm (77 K) for the NH_2-Ms-MCM 41-**3.0** material.

APPENDIX 4

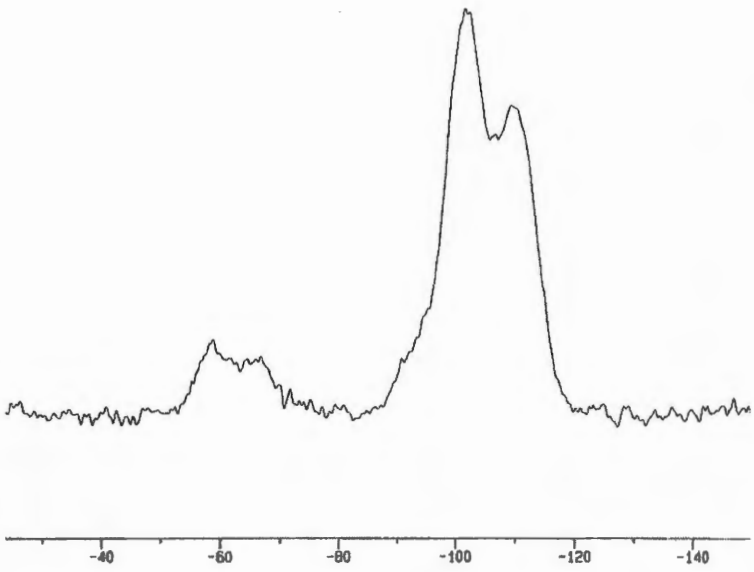

Figure A4.1 ^{29}Si CP MAS NMR spectrum of the Fe-Schiff-MCM-**0.75** material.

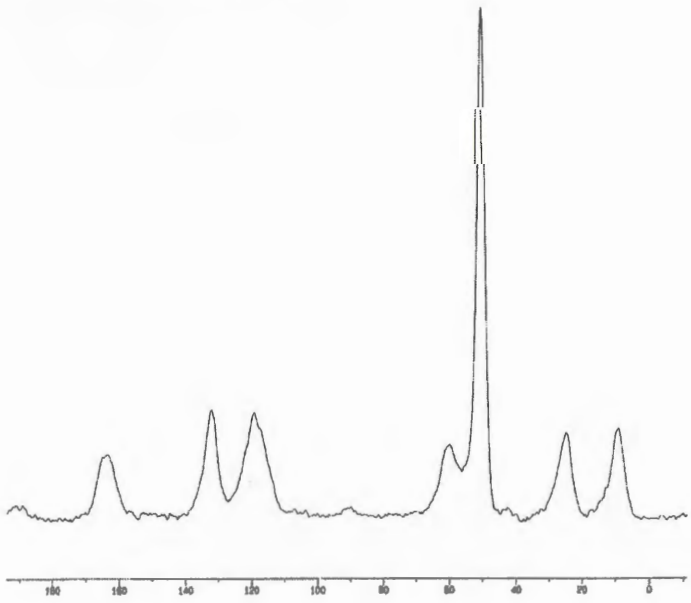

Figure A4.2 ^{13}C CP MAS NMR spectrum of the Fe-Schiff-MCM-**0.75** material.

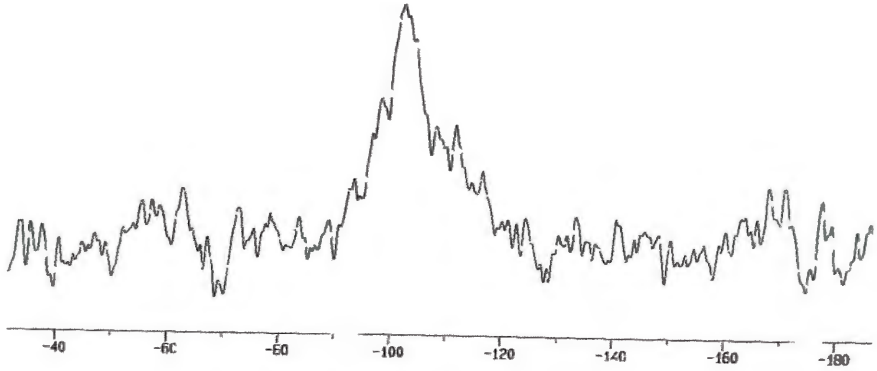

Figure A4.3 ^{29}Si CP MAS NMR spectrum of the Cu-Schiff-MCM-**1.0** (8) material.

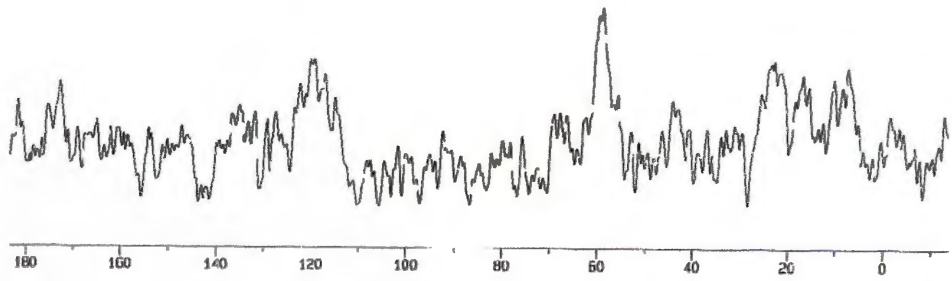

Figure A4.4 ^{13}C CP MAS NMR spectrum of the Cu-Schiff-MCM-**1.0** (8) material.

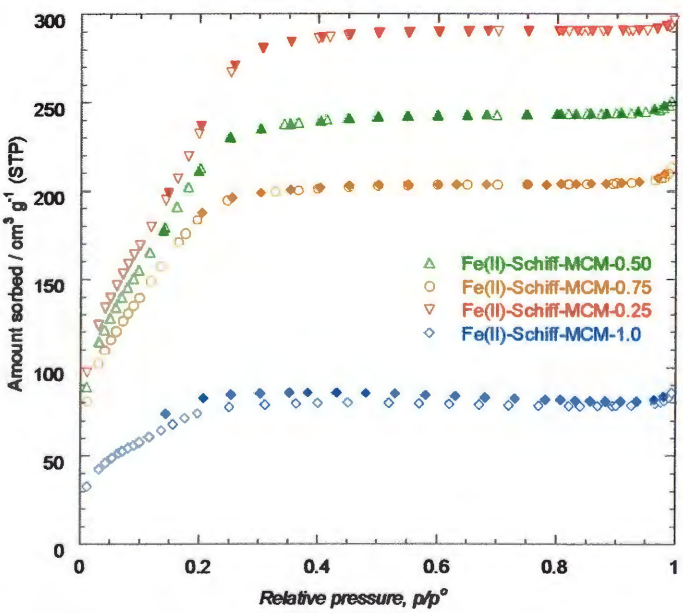

Figure A4.5 N_2 sorption isotherms (77 K) for the Fe(II)-Schiff base-modified MCM 41 materials. Filled symbols denote desorption points.

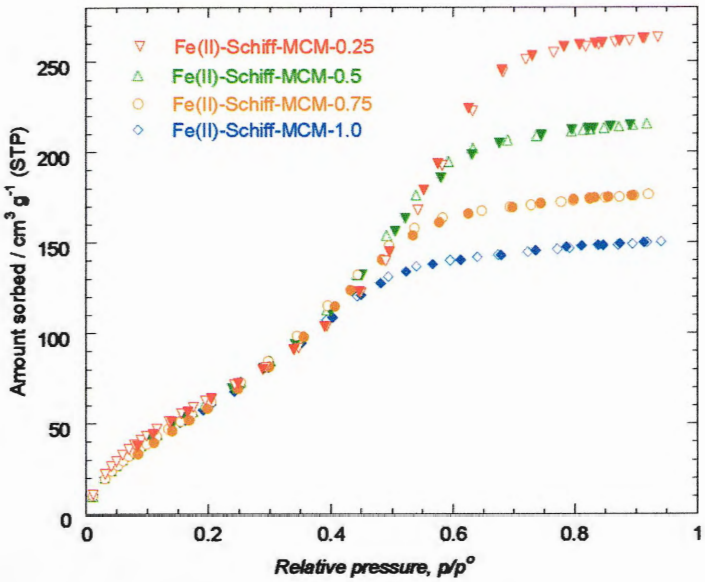

Figure A4.6 CO_2 sorption isotherms (195 K) for the Fe(II)-Schiff base-modified MCM 41 materials. Filled symbols denote desorption points.